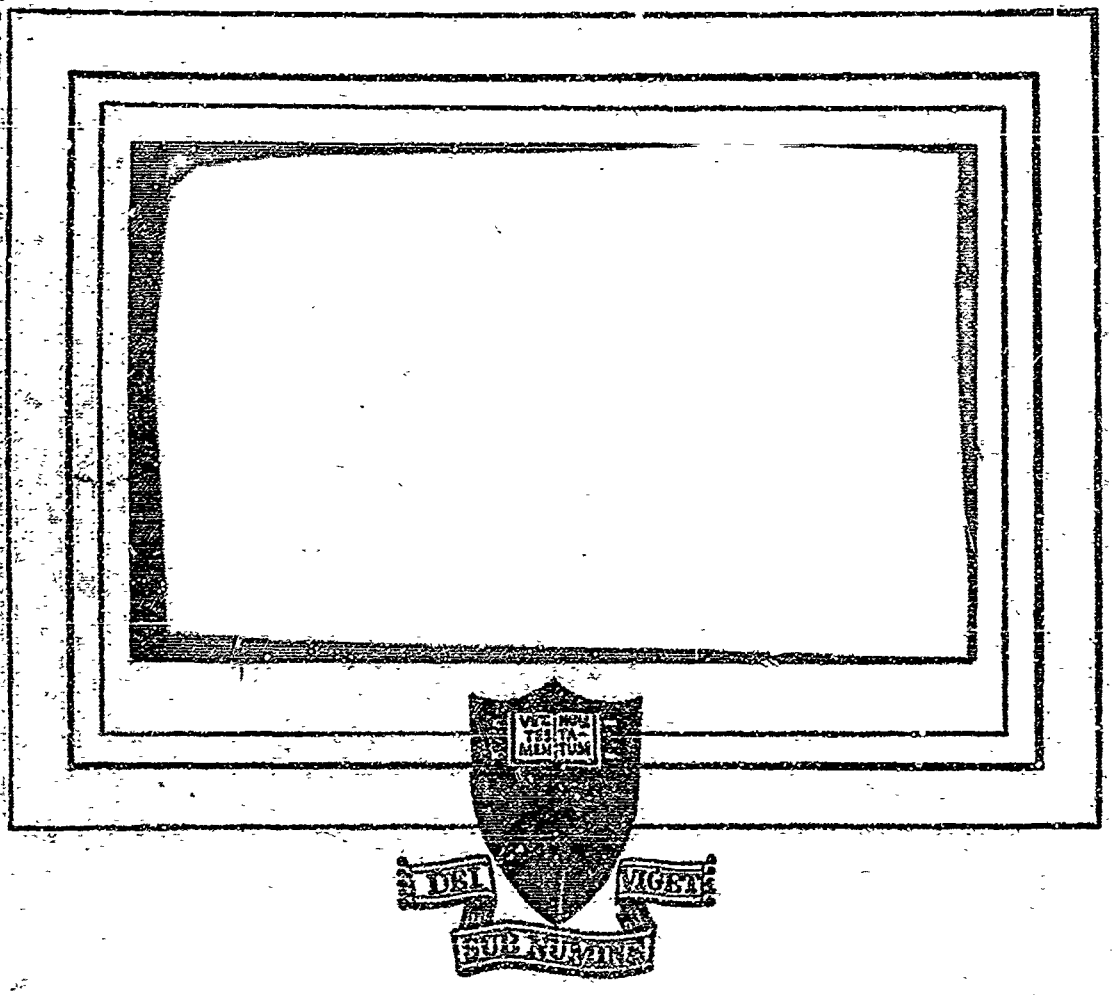

PRINCETON UNIVERSITY

DEPARTMENT OF

AEROSPACE AND MECHANICAL SCIENCES

DEPARTMENT OF THE NAVY
OFFICE OF NAVAL RESEARCH

Contract USN-Nonr 1858(29)
NR 094-200

A STUDY OF THE MECHANISMS OF HEAT TRANSFER IN OSCILLATING FLOW

Technical Report No. 483-f
Department of Aerospace and Mechanical Sciences

Submitted by: David W. Bogdanoff
David W. Bogdanoff

Approved by: Luigi Crocco
Luigi Crocco
Robert H. Goddard Professor
of Jet Propulsion

and David T. Harrje
David T. Harrje
Sr. Research Engineer & Lecturer

October 1967

Guggenheim Laboratories for the Aerospace Propulsion Sciences
Department of Aerospace and Mechanical Sciences
PRINCETON UNIVERSITY
Princeton, New Jersey

ABSTRACT

The mechanisms of heat transfer in oscillating flow are the subject of this report. Most of the work relates to the more restricted topic of heat transfer in turbulent gas pipe flow with superimposed longitudinal standing-wave oscillations.

The important non-dimensional parameters of the unsteady heat transfer problem are determined and known mechanisms by means of which oscillations can affect heat transfer are discussed, e.g., viscous dissipation, acoustic streaming, and changes of the turbulence structure. A quasi-steady analysis is also presented. Heat transfer and (hot-wire) velocity profile measurements from this investigation of pipe flow with superimposed oscillations are compared with the results of other studies to determine the importance of acoustic streaming and viscous dissipation. These phenomena appear to be unimportant in many cases of interest. The present experimental work is then reexamined, with a view to studying the effects of the oscillations on the turbulence structure. Total (eddy plus molecular) viscosity plots give some indication of regions of generation by the oscillation of 'abnormal' turbulence, and subsequent diffusion and decay of this turbulence. These effects of the oscillation on the turbulence structure are also qualitatively supported by heat transfer and peak-to-peak velocity profile data. From this analysis, it appears that the principal mechanism of the effect of the oscillations on heat transfer is through changes in the turbulence structure. An attempt was then made to correlate the heat transfer data of this investigation with other studies. Evidence suggests that in certain cases the data may be approximately correlated using only 2 of the 4 main parameters. In a certain parameter range, the heat transfer data appears to approach the theoretical quasi-steady values remarkably; it appears that here regions of the flow near the wall may be approaching the quasi-steady state. Recommendations for further work are given, and the possible applications of oscillations to heat exchanger design is discussed; the latter appear very limited.

ACKNOWLEDGEMENTS

The author wishes to express his indebtedness to Professor L. Crocco and Mr. D. T. Harrje for much useful advice and many stimulating discussions throughout the period of this investigation. With respect to specific aspects of the research, discussions with Professors R. Eichhorn, W. O. Criminale, G. L. Mellor and W. A. Sirignano were invaluable. The computer work was done with the aid of Mr. L. L. Hoffman and in building and operating the experimental apparatus and instrumentation systems, the able assistance of Messrs. J. Semler, F. Willis, J. Cooper, M. Drobnek and S. Marquardt is acknowledged. Thanks are also due to Mrs. E. Olsen and Miss D. Morris for the secretarial work involved in the preparation of this thesis. The work was supported by the Office of Naval Research, Contract No. USN-NONR 1858 (29).

TABLE OF CONTENTS

NOMENCLATURE

Some symbols defined in the text and used in a very restricted region of the text near the definition are not given here. Symbols used with different meanings in different places in the text have all meanings given here; the use in the text should make it obvious which meaning is intended at a particular point in the text. To save space, for some symbols which are defined in the text, we merely give the location of that definition in the list below. We here use the abbreviations:

E. - Equation
S. - Section
p. - page or pages
def. - definition

A (1) constant
(2) see discussion, S. 5.5, p. 275-277

$A(\hat{h})$ amplitude of heat transfer coefficient fluctuation

$A(\hat{R})$ amplitude of wire resistance fluctuation

A_1, A_2 defined in Figure 54, S. 4.7, p. 108

a (1) defined by E. (59), S. 4.9, p. 120
(2) velocity in x-direction

$\bar{a}, a'$ time-average and time-varying components of a (2nd def.)

$\overline{a'^2}$ time-average value of a'^2

$\bar{\bar{a}}$ mean time-average flow velocity in pipe

a_τ defined by $\rho a_\tau^2 = \tau_w$

$\overline{a'b'}$ time-average value of $a'b'$

b velocity in r-direction

$\bar{b}, b'$ time-average and time-varying components of b

$\overline{b'^2}$ time-average value of b'^2

C_f' $\dfrac{\tau_w}{\frac{1}{2}\rho \bar{u}^2}$ (for flat plate)

C_p (1) specific heat at constant pressure of fluid
(2) specific heat at constant pressure of hot-wire

c speed of sound

c_b speed of sound in duct based on $\bar{T}_{b,s}$

D (1) diameter of pipe

(2) " " hot-wire

$D' = 2\delta$, see discussion, S. 5.5., p. 292

DK,DHW see discussion, S. 4.11, p. 133

E = Eckert No. = $\bar{U}^2/C_p(T - T_w)$

$E_{Fhl} = (h_{lw} - h_{lF})/h_{lF}$

E_{m1}, E_{m2} defined, Figure 55, S. 4.7, p. 110

E_r see discussion, S. 5.3, p. 246

$E_{s,1}$ defined, E. (134), S. 5.7, p. 310

E_o defined, Figure 55, S. 4.7, p. 110

$E_o, E_{o,1}$ defined, E. (132),(133), S. 5.7, p. 309

$E_{1r} = E_r/\bar{a}$

$E_{2r} = E_{1r}/\bar{a}D$

$F_v = v_{p,ss}/v_{hw,ss}$

$F_{2r} = \ln(10)\, kEr/\bar{a}^2$

f (1) frequency of oscillation

(2) general function

$f_c = \omega_c/2\pi$

g general function

$\bar{H}_p$ parameter used in Ref. 6, see S. 2, p. 29

h (1) heat transfer coefficient

(2) general function

$\bar{h}$ average heat transfer coefficient at hot-wire surface

h_l heat transfer coefficient at hot-wire surface

h_{lC} h_l under standard conditions

h_{lF} see discussion, S 4.9, p. 121

h_{lS} h_l under measurement conditions

h_{lw} see discussion, S. 4.9, p. 121

I		hot-wire current
I_1	(1)	defined, E. (51), S. 4.7, p. 111
	(2)	see discussion, S. 4.12, p. 138
I_1, I_2		see discussion, S. 4.12, p. 141
K	(1)	thermal conductivity
	(2)	parameter used in Ref. 31, see S.2, p. 60
	(3)	total voltage gain of amplifiers in feedback loop of hot-wire anemometer circuit
K_F		air thermal conductivity (evaluated at T_F)
K_{FC}		K_F under standard conditions
K_{FS}		" " measurement conditions
K_e		'eddy thermal conductivity'
K_t		molecular plus eddy conductivity
K_w		thermal conductivity of hot-wire
K_1, K_2		individual voltage gains of amplifiers in feedback loop of hot-wire anemometer circuit
k		wave number
k_1, k_2		specific values of k
L	(1)	length of pipes in heat exchanger
	(2)	see discussion, S. 5.5, p. 275-277
	(3)	length of heat transfer section of pipe
	(4)	hot-wire length
L'		see discussion, S. 4.9, p. 123
M	=	Mach number = $\bar{U}/\sqrt{\gamma RT}$
M_a		M calculated as given in S. 3.4, p. 80
M_b	=	$\bar{U}_b/c_b$
$\dot{m}$		mass flow in heat exchanger
N		number of pipes in heat exchanger
Nu	(1)	= local Nusselt number = hD/K
	(2)	unsteady flow Nusselt number based on D
$\hat{Nu}$		Nusselt number as a function of x/D
$\left[\frac{Nu-Nu_o}{Nu_o}\right]_{max}$		see discussion, S. 5.2, p. 199

Nu_n normalized Nusselt number, see S. 3, p. 76

$Nu_{n,s}$ steady flow value of Nu_n

$Nu_{n,u}$ unsteady " " " "

Nu_x Nusselt number based on distance from leading edge of heated wall, or leading edge of flat plate

$Nu_{x,o}$ Nu_x under steady flow conditions

Nu_o (1) steady flow Nusselt number based on D

(2) Nu under steady flow conditions

n (1) an integer

(2) general exponent

P (1) pressure

(2) defined by E. (57), S. 4.9, p. 120

ΔP pressure drop in oscillating flow

P' parameter used in Ref. 5, see S. 2, p. 36

$\bar{P}$ time-average fluid pressure in pipe

$\hat{P}$ peak-to-peak fluid pressure in pipe

$\left(\frac{\Delta P}{P}\right)_o$ parameter used in Reference 31, see S. 2, p. 62

P_C freestream pressure under standard conditions

$\hat{P}_N$ peak-to-peak pressure in pipe at velocity node (pressure antinode)

$\tilde{P}_N$ r.m.s. pressure in pipe at velocity node

$\bar{P}_x$ time-average value of P_x

ΔP_o pressure drop in steady flow

Pr = Prandtl number = $\mu C_p/K$

$(Pr)_\tau = y \frac{\overline{a'b'}}{a_\tau \frac{4}{}} \frac{d\bar{a}}{dr}$

Q defined by E. (58), S. 4.9, p. 120

ΔQ heat transferred in oscillating flow

ΔQ_T total heat transferred in heat exchanger

Q_c typically experimentally observed heat transfer rate

ΔQ_c difference between heat transfer deviations from the steady flow values at the maxima and minima of heat transfer under oscillating conditions

Q_v defined, E. (16), S. 1, p. 12

$Q_{v,A}$		Q_v at velocity antinode
ΔQ_o		heat transferred in steady flow
R	(1)	resistance of hot-wire
	(2)	gas constant
R'		wire resistance ratio - average operating resistance of wire (electrically heated) divided by resistance of unheated wire
$\bar{R}$		average value of R (1st def.), see Fig. 51, S. 4.6, p. 104
R_c		resistance of cable, wire support needles, etc., associated with hot-wire, see S. 4.7, p. 110, 111 and Fig. 56
R'_{cal}		see discussion, S. 4.12, p. 138
R_f		defined, S. 4.6, p. 107
R_w		resistance of hot-wire
$R_{w,c}$		resistance of hot-wire when unheated
$R_{w,h}$		average resistance of hot-wire when electrically heated
R_o		resistance of hot-wire at 68^oF
R'_1		see discussion, S. 4.12, p. 138
R_1, R_2, R_3		resistances in hot-wire bridge circuit, see S. 4.7, p. 104 (Fig. 51), p. 108 (Fig. 53), p. 111 (Fig. 56)
Re	=	Reynolds number = $\rho\bar{U}D/\mu$
Re'		Re based on D' instead of D
Re_L		Reynolds number based on length of flat plate
Re_a		Re calculated as given in S. 3.4, p. 80
Re_x		Reynolds number based on distance from leading edge of flat plate
Re_δ		Reynolds number based on boundary layer thickness
r		coordinate measured radially outward from center-line of pipe
r(subscript)		differentiation with respect to r
S	=	Strouhal number = $\omega D/\bar{U}$
S'		S based on D' instead of D
S_a		S calculated as given in S. 3.4, p. 80
S_L		Strouhal number based on length of flat plate
S_x		Strouhal number based on distance from leading edge of flat plate

St = Stanton number = $h/\rho C_p \bar{U}$

T (1) temperature

(2) bulk temperature of fluid

(3) period of oscillation

ΔT temperature difference

T_B bulk temperature of fluid

ΔT_B see S. 1, p. 8

T_{CL} temperature at center-line of pipe

T_E free stream temperature

T_{EC} T_E under standard conditions

T_{ES} T_E " measurement "

T_F film temperature = ½(free stream temperature + wire temperature)

T_{FC} T_F under standard conditions

T_{FS} T_F " measurement conditions

T_R gas temperature in ^oR

$T_{R,b}$ T_b measured in ^oR

$\bar{T}_a$ defined, S. 3, p. 77

$\bar{T}_b$ air temperature in duct at exit of heated section, a function of r (^oF)

$\bar{T}_{b,s}$ defined, S. 3, p. 77

T_w (1) wall temperature

(2) a specific constant wall temperature

$(T_w-T_B)_{typ}$ see S. 1, p. 8

$T_{w,av}$ time-averaged value of T_w(def. 1)

T_o, T_1 specific constant wall temperatures

T_1 see discussion, S. 5.3, p. 256, 257

t time

Δt defined, Figure 54, S. 4.7, p. 108

t_a, t_b, t_c times such that $t_a < t_b < t_c$

t(subscript) differentiation with respect to t

U velocity in x-direction

$\bar{U}$ mean time-average flow velocity in pipe or in free stream

$\tilde{U}'$ defined, E. (78), S. 5.2, p. 193

$\tilde{U}$ (1) r.m.s. velocity at pipe center-line

(2) r.m.s. x-velocity

$\hat{U}$ (1) peak-to-peak velocity at pipe center-line, or in free stream

(2) peak-to-peak x-velocity

$\hat{U}_A$ peak-to-peak velocity in pipe at center-line at velocity antinode

$\tilde{U}_A$ r.m.s. velocity in pipe at center-line at velocity antinode

$\bar{U}_a$ mean time-average flow velocity in duct upstream of heated section, see S. 3.4, p. 80

$\bar{U}_b$ mean time-average flow velocity in duct downstream of heated section

U_m center-line velocity in pipe

$U_{y,s}, U_{y,a}$ defined, S. 1, p. 13

U_τ defined by $\tau_\omega = \rho U_\tau^2$

$\hat{U}_o$ $\hat{U}$ (def. 2) far from wall

$\tilde{U}_o$ $\tilde{U}$ (def. 2) far from wall

u velocity in x-direction

$u^+ = u\sqrt{\frac{\tau_w}{\rho}}$

$\bar{u}_r, \tilde{u}_r'$ time-average and time-varying components of u_r

V (1) average flow velocity through pipes in heat exchanger

(2) velocity in y-direction

v (1) x-velocity of fluid in pipe

(2) air velocity

$\bar{v}$ (1) mean x-velocity of fluid in pipe

(2) defined, S. 4.13, p. 146

$\tilde{v}'$ defined, E. (62), S. 4.12, p. 140, and in S. 4.13, p. 146

$\hat{v}$ peak-to-peak velocity, see S. 4.13, p. 146

v_C air velocity under standard conditions

v_J, v_K, v_L, v_M see discussion, S. 4.12, p. 138

v_S air velocity under measurement conditions

$\bar{v}_c' = \bar{v}' F_v$

$v_{c1}, \bar{v}_{c1}$ defined, S. 1, p. 4

$v_{hw,ss}$ defined, S. 5.3, p. 209

v_m x-velocity in pipe at center-line

$v_{p,ss}$ defined, S. 5.3, p. 209

v_1, v_2, v_4, v_5 - see discussion, S. 4.12, p. 136

$w = \left[\frac{Nu - Nu_o}{Nu_o}\right]_{max}$

w_e w estimated from experimental data

w_x, w_y see discussion, S. 5.2, p. 204

x (1) distance downstream of heated section entrance

(2) position of traversing hot-wire test section, see discussion, S. 4.13, p. 146

(3) coordinate parallel to flat plate, or wall of pipe

x(subscript) differentiation with respect to x

$\hat{x}$ (1) $\hat{U}/\omega$

(2) peak-to-peak displacement of flat plate

x_A, x_B specific values of x(def. 1)

x_A distance of velocity antinode downstream of heated section entrance

x_o unheated length of flat plate (upstream of heat-transfer section)

x_1 specific value of x (def. 1)

y distance measured away from and perpendicular to flat wall, or pipe wall

$y' = \nu/U_\tau$

$y^+ = \frac{y}{\nu}\sqrt{\frac{\tau_w}{\rho}}$

y(subscript) differentiation with respect to y

$y_s = 45\nu/U_\tau$

y_1 defined by $5 = y_1^+ = \frac{y_1}{\nu}\sqrt{\frac{\tau_w}{\rho}}$

y_1^+, y_2^+ specific values of y^+, $y_1^+ = 5$, $y_2^+ = 30$

ZM,ZN,ZJ see discussion, S. 4.11, p. 133

α (1) $= \sqrt{\omega/2\nu}$

(2) temperature coefficient of resistance of hot-wire at 68°F

(3) damping coefficient for wave travelling in a circular tube, see S. 5.7, p. 308

γ	(1)	$2y/D$
	(2)	ratio of specific heats
δ	(1)	a small number ($\delta \ll 1$)
	(2)	boundary layer thickness
δ_A	=	$1/\alpha$ (1st def. of α)
δ_A^+	=	$\frac{y_1^+}{y_1}$ (δ_A)
δ_{AC}, δ_{ac}	=	δ_A
ϵ		kinematic 'eddy viscosity'
$\bar{\epsilon}$		'average' kinematic 'eddy viscosity' see discussion, S. 5.2, p. 200, 204
ζ	=	$S/\lambda Re$
ζ'	=	$S'/\lambda' Re'$
θ		dummy variable in integration
λ	(1)	wave length of oscillation
	(2)	friction factor defined by $\tau_w = \frac{1}{8}\lambda\rho\bar{U}^2$
λ'		friction factor λ based on Re' instead of on Re
λ_1		friction factor defined by $\tau_w = \frac{1}{2}\lambda_1\rho\bar{U}^2$
μ		viscosity
$\bar{\mu}, \mu'$		time-average and time-varying components of μ
μ_F		air viscosity (evaluated at T_F)
μ_{FC}		μ_F under standard conditions
μ_{FS}		μ_F " measurement conditions
μ_t		'eddy' plus molecular viscosity
$\overline{\mu' u_r'}$		time average value of $\mu' u_r'$
$\overline{\mu u_r}$		time average value of μu_r
ν		kinematic viscosity
ν_2	=	$\log_{10}(k\bar{a}D/\bar{\bar{a}})$
ν_{21}, ν_{22}		specific values of ν_2
ρ	(1)	density of fluid
	(2)	density of hot-wire

$\bar{\rho}$ time-average value of ρ (def. 1)

ρ_F air density (evaluated at T_F and the free stream static pressure near the wire)

ρ_{FC} ρ_F under standard conditions

ρ_{FS} ρ_F under measurement conditions

$\overline{\rho U}$ time-average value of ρU in free stream

$\widetilde{\rho U}$ r.m.s. value of ρU in free stream

τ shear stress

τ_w shear stress at wall

ϕ see discussion, S. 5.5, p. 275-277

ω (1) angular frequency

(2) angular frequency of oscillations

(3) angular frequency of heat-transfer coefficient fluctuation

$\omega_c = 4\bar{h}/(R' \rho C_p D)$ critical angular frequency of hot-wire

ω_c' defined in S. 4.6, p. 107

$\omega_s = U\tau/y'$

$\omega_2 = k\bar{a}D/\bar{\bar{a}}$

LIST OF FIGURES

- continued next page

INTRODUCTION

In recent years a number of fields have been confronted with problems associated with unsteady heat transfer. Classic examples have involved the burnout problems associated with the heat transfer increases experienced with unstable rocket motor operation and with other similar combustion devices. Heat transfer increases, at times approaching an order of magnitude change, have been measured in the presence of high amplitude combustion instability. It is important that an understanding of the governing mechanisms be achieved.

Another reason for studying the mechanisms of heat transfer with oscillating flow is to possibly control such heat transfer increases and thereby enhance heat fluxes. With this control, techniques might be employed to improve the performance of size-limited heat transfer systems including propulsion devices like the nuclear rocket.

For such reasons, this study into the basic mechanisms of heat transfer with oscillating flow was undertaken. Only with a knowledge of the mechanisms can the phenomenon be controlled and accurate predictions of the effects be made. These non-combustion studies were conducted in a turbulent, unsteady environment provided within a duct, which was placed in resonance by a siren arrangement. Another research program (also conducted at Princeton) on combustion instability in liquid propellant rocket motors provided data for a limited number of comparisons with this study and added factors such as combustion, shock-type waves, and extremely high amplitudes. However, only through analysis and via carefully controlled tests, such as those described in this report, is it possible to isolate the mechanisms that are responsible for such heat transfer increases due to this complex gas dynamic phenomenon in turbulent flow.

1. DIMENSIONAL ANALYSIS, SOME IMPORTANT PARAMETERS OF THE PROBLEM, AND DISCUSSION OF SOME PHENOMENA IN HEAT TRANSFER IN OSCILLATING FLOW

To gain some insight into the important parameters in the problem of heat transfer in oscillating flow, the following simple dimensional analysis can be performed . Considering first the case of steady flow (no oscillations), that situation is sketched in Figure 1. (All symbols are defined in the nomenclature, p.vii).

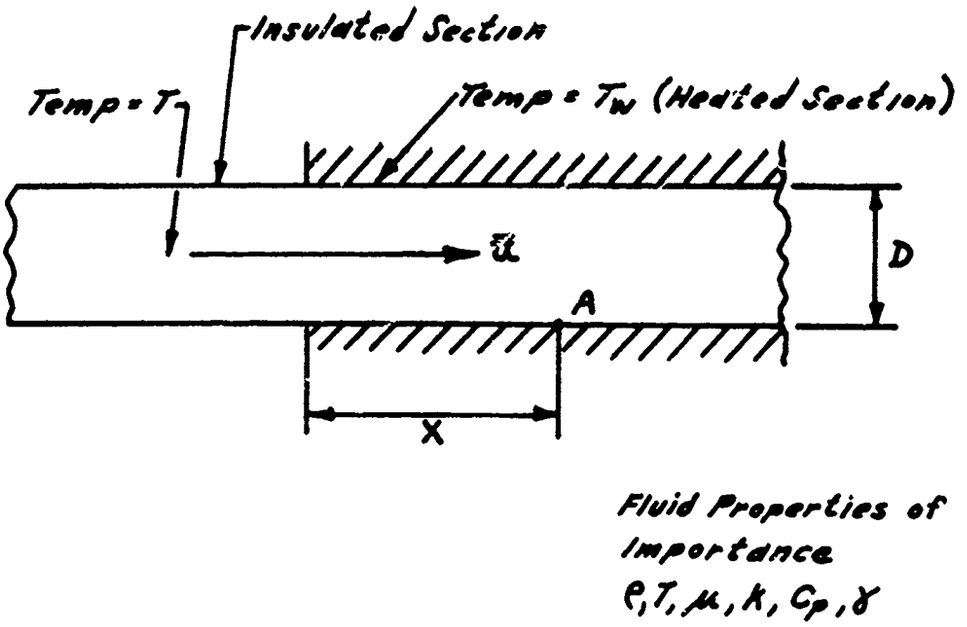

FIGURE 1

We consider flow of a gas in a circular pipe with the following assumptions:

- the pipe is hydrodynamically smooth
- natural convection effects are absent
- the flow is fully developed hydrodynamically upstream of the heated section
- the equation of state, $P = \rho RT$, applies and hence P is not an independent variable in the dimensional analysis (also $R = \frac{\gamma-1}{\gamma} C_p$).

We then consider the heat transfer coefficient (h) at point A, and write the following relationship:

$$h = f(\rho, T, \mu, K, C_p, \gamma, T_w, \bar{U}, x, D) \tag{1}$$

(f represents a function in general, not any particular function). Here, we consider the quantities ρ, μ, K, C_p, γ, $\bar{U}$ to be defined by their values upstream of the heated section, to simplify the analysis. For a gas with moderate $(T - T_w)/T$ and low Mach number, these quantities remain nearly constant throughout the flow field. We have an equation relating eleven quantities containing four fundamental dimensions (mass, length, time, and temperature), hence we expect (1) to reduce to a relation among seven dimensionless groups. A common way of selecting these groups is:

$$\frac{hD}{K} = f\left(\frac{\rho \bar{U} D}{\mu}, \frac{\mu C_p}{K}, \frac{\bar{U}}{\sqrt{\gamma RT}}, \frac{x}{D}, \gamma, \frac{T_w}{T}\right) \tag{2}$$

or:

$$Nu = f\left(Re, Pr, M, \frac{x}{D}, \gamma, \frac{T_w}{T}\right) \tag{3}$$

We now consider the comparison of two cases, with different values of Re, Pr, M, γ, and T_w/T. Therefore, the overall (over all values of x/D) heat transfer characteristics of two cases being compared (which we shall represent by $\hat{Nu} = \hat{Nu}(x/D)$, a function whose form depends on Re, Pr, M, γ, and T_w/T) may be written as:

$$\hat{Nu} = f\left(Re, Pr, M, \gamma, \frac{T_w}{T}\right) \tag{4}$$

Since we are dealing with gases, the ranges of variation of the quantities Pr and γ are small, and these groups may be dropped as a first approximation from Equations (2), (3) and (4). Hence, we can write, approximately,

$$\hat{Nu} = f\left(Re, M, \frac{T_w}{T}\right) \tag{5}$$

We now consider the addition of periodic longitudinal oscillations of the gas flow to the problem. The oscillation can be viewed as being made up of a right-travelling and a left-travelling wave. The pressure is approximately uniform across the cross-section of the pipe at given values of x and time. For most cases of concern, (important exceptions are some cases of unstable rocket motors) the amplitude of the oscillations are such that $\hat{P}/2\bar{P} \leq .15$ and hence the left and right-travelling waves are approximately linear in character and as a first approximation, do not interact. Therefore, the oscillation can be specified by giving (at a fixed value of x) the pressure variations due to the right and left travelling waves, as a function of time. Due to the constraint of the equations of motion of the fluid, the oscillations could equally well be specified by giving the velocity fluctuations on the pipe center-line at a fixed value of x as a function of time due to the right and left-travelling waves. Clearly, we could have an infinite number of different cases, corresponding to the infinite number of possible wave-shapes. To proceed with the analysis, the assumption is made, which is a good approximation in many cases of interest, that the right and left-travelling of waves (defined by either pressure fluctuations or pipe center-line velocity fluctuations) are sine waves of the same frequency. A further approximation also applicable to many cases of interest is that the strength of the right and left travelling waves are $\sim$ equal (i.e., that, to an approximation, only standing waves are present). Under these approximations, the oscillation can be described by two parameters, the angular frequency, ω, and the peak-to-peak velocity at the pipe center-line at a velocity antinode, $\hat{U}_A$. When we superimpose the standing-wave pattern on the heat-transfer configuration pictured in Fig. 1, we see that another parameter, the distance of a velocity antinode from the upstream edge of the heated section (x_A), is required to specify the situation. (See Fig. 2 next page.) We now must consider $\hat{Nu}$ (see Eqn. (5)), to be a function of three additional parameters, ω, $\hat{U}_A$, x_A. Forming non-dimensional groups, we replace Eqn. (5) by, for the case with oscillations;

$$\hat{Nu} = f\left(\frac{\rho \bar{U} D}{\mu}, \frac{\bar{U}}{\sqrt{gRT}}, \frac{T_w}{T}, \frac{\omega D}{\bar{U}}, \frac{\hat{U}_A}{\bar{U}}, \frac{x_A}{D}\right) \tag{6}$$

or:

$$\hat{Nu} = f\left(M, Re, \frac{T_w}{T}, S, \frac{\hat{U}_A}{\bar{U}}, \frac{x_A}{D}\right) \tag{7}$$

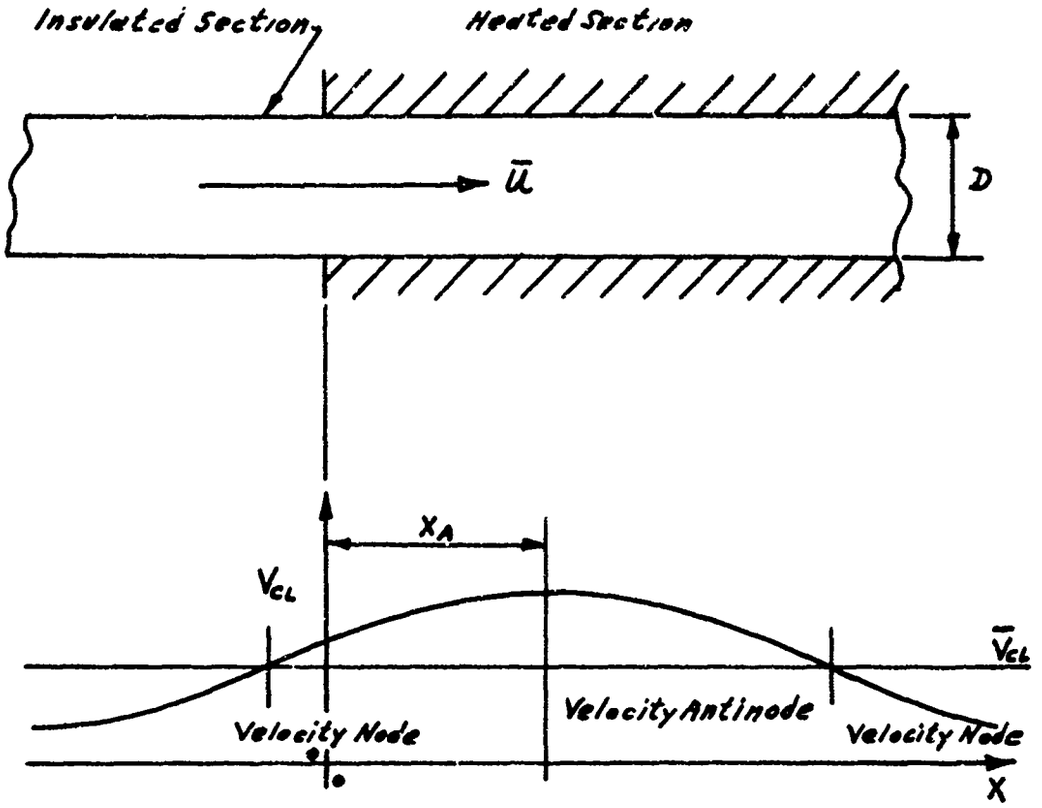

v_{cl} = instantaneous center-line velocity

$\bar{v}_{cl}$ = time-average center-line velocity

FIGURE 2

We now briefly discuss some aspects of these dimensionless groups and a few other combinations of the group which may be used. In experimental work the parameter $\hat{P}_N/\bar{P}$ is often used to specify the oscillation strength. Using the simple wave relations for unsteady flow, we can show that

$$\frac{\hat{P}_N}{\bar{P}} = \frac{\gamma \hat{U}_A}{c} = \gamma \frac{\hat{U}_A}{\bar{U}} \frac{\bar{U}}{c} = \gamma \frac{\hat{U}_A}{\bar{U}} M \qquad (8)$$

In theoretical solutions for laminar channel and pipe flow with superimposed longitudinal standing-wave oscillations, References 1 and 2 show (within the range of applicability of their solutions) that the time-averaged secondary flows induced by the oscillation (acoustic streaming) are of order of magnitude

$$\frac{\hat{U}_A^2}{\bar{U}^2} \frac{\bar{U}}{c} = \frac{\hat{U}_A^2}{\bar{U}^2} M$$

as compared to the undisturbed flow (no oscillations).

By combining the parameter Re and S , one can obtain the parameter

$$\frac{\rho \bar{U} D}{\mu} \times \frac{\omega D}{\bar{U}} = \frac{\rho}{\mu} \omega D^2 = \frac{\omega D^2}{\nu}$$

which has the following significance: we consider a two dimensional flow field as sketched in Figure 3 and governed by Eqns. (9) and (10).

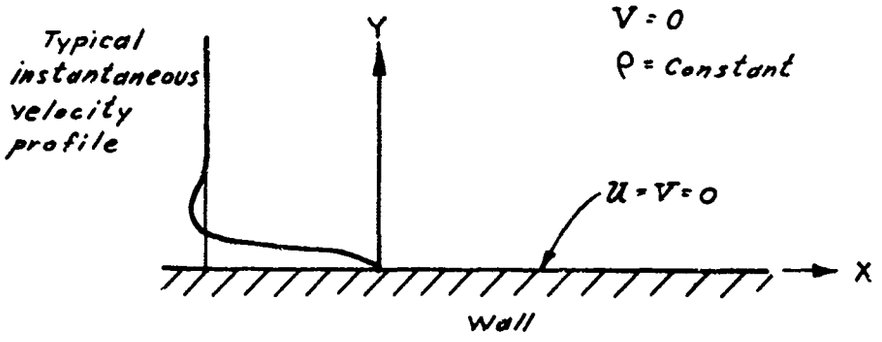

FIGURE 3

$$U_t = -\frac{1}{\rho} P_x + \nu U_{yy} \qquad (9)$$

$$P_x = A\sin\omega t \tag{10}$$

This simplified system approximately reproduces the behavior of the time-varying component of longitudinal velocity near the wall for the case of laminar pipe flow with superimposed longitudinal oscillations. In this case the time-mean U velocity is zero. The well known solution to this problem is

$$U = \frac{A}{\omega\rho}\left[\cos\omega t - e^{-\alpha y}\cos(\omega t - \alpha y)\right] \tag{11}$$

$$\alpha = \sqrt{\frac{\omega}{2\nu}} \tag{12}$$

where $\frac{1}{\alpha}$ is the e-folding distance for the decaying sinusoid part of the solution. $\delta_A = 1/\alpha$ is sometimes referred to as the thickness of the A.C. boundary layer. The combination of parameters ReS can then be written as:

$$ReS = \frac{\omega D}{\bar{U}} \times \frac{\rho \bar{U} D}{\mu} = \frac{\omega D^2}{\nu} = 2\alpha^2 D^2 = \frac{2D^2}{\delta_A^2} \tag{13}$$

which is twice the square of the ratio of the pipe diameter to the A.C. boundary layer thickness. In many cases of interest, the parameter ReS may have much the same significance even in turbulent flow; since in these cases the thickness of the A.C. boundary layer is so small that it lies within and near what would normally be the laminar sub-layer, and hence the 'eddy viscosity' in the A.C. boundary layer is relatively close to the molecular value, μ .

One reason for the importance of the parameter T_w/T in Equation 7 is the fact that the properties of the fluid (μ, K , C_p , ρ) may vary considerably between the wall (T_w) and the central portion of the flow (where the temperature may range from T to T_w). However, in cases where the fluid properties are almost constant throughout the flow field (e.g. gas

flows with $T_w/T \approx 1$), this parameter still may be of importance for some cases of oscillating flow as discussed below. Under some conditions (though usually unimportant, see p. 190), viscous dissipation caused by the instantaneously very high shear values near the wall due to the imposed oscillations can contribute significantly to the heat transfer to or from the wall. A measure of the wave energy per unit mass available for possible dissipation is $\hat{U}_A^2$. A measure of the thermal energy available per unit mass for possible heat transfer to the walls is:

$$C_p(T - T_w)$$

One parameter of significance in estimating the importance of viscous dissipation is then:

$$\frac{\hat{U}_A^2}{C_p(T-T_w)} = \left(\frac{\hat{U}_A}{\bar{U}}\right)^2 \frac{\bar{U}^2}{C_p(T-T_w)} = \left(\frac{\hat{U}_A}{\bar{U}}\right)^2 E \qquad (14)$$

which may be written as:

$$\left(\frac{\hat{U}_A}{\bar{U}}\right)^2 \frac{\bar{U}^2}{C_p(T-T_w)} = \left(\frac{\hat{U}_A}{\bar{U}}\right)^2 \frac{\bar{U}^2(\gamma-1)}{\gamma RT\left(1-\frac{T_w}{T}\right)} = \left(\frac{\hat{U}_A}{\bar{U}}\right)^2 M^2 \frac{(\gamma-1)}{\left(1-\frac{T_w}{T}\right)} \qquad (15)$$

which shows again, the appearance of the parameter T_w/T .

It appears likely that when both the variations of fluid properties throughout the flow field, and the effects of viscous dissipation are unimportant, T_w/T may be dropped, as a first approximation, from Equation (7).

In comparing the literature reports among themselves and with the work presented here, the parameters presented in Equation (7) will be used. However, in making such comparisons the following possible differences from the situation analyzed above must be considered:

(1) Pressure (and/or center-line velocity) wave shapes differing from sinusoidal.

(2) Non-equality of the strengths of the right and left travelling waves (i.e. travelling waves as well as standing waves in the pipe).

(3) Variation of the wall temperature in the heated section of the pipe (Fig. 1, T_w). (A pipe heated by condensing steam will usually have $T_w \approx$ constant and hence will approximate the model presented above, while an electrically heated pipe ($\sim$ constant heat input per unit area) will have a wall temperature usually rising in the downstream direction.)

(4) A heated section so short that it cannot be regarded as extending to infinity in the downstream direction (this point is discussed further on p.18,19).

(5) Flow which is not hydrodynamically developed at the entrance to the heated section. (Many references deal with flow which starts to hydrodynamically develop at or near the heated section entrance.)

(6) Also, for some cases (e.g., in rocket motors with $T_w/T \not\ll 1$), it may not be permissible to drop T_w/T from Equation (7) as was discussed on p.7 .

(7) Geometry differences; in many cases very severe, such as flows over flat plates. Any comparisons between flows over flat plates and pipe flows must be made with great caution.

In the author's opinion, comparisons may tentatively be made on the basis of the parameters of Equation (7) alone, even in the cases where differences (3) and (5) listed above apply in restricted cases as discussed below. Considering difference (3) first, we refer to Figure 4 on the next page. We compare electrically and steam-heated cases. If ΔT_B is much smaller than a typical value of $T_w - T_B$, say $\Delta T_B < 0.1(T_w - T_B)_{typ}$, the electrically and steam-heated cases are almost identical except near the entrance to the heated section. In this case, comparison using the parameters of Equation (7) only should be quite satisfactory, except near the thermal entrance. Even with $\Delta T_B \approx 0.4(T_w - T_B)_{typ}$ or higher, the author feels that comparisons on the basis of Equation (7) may be tentatively made, though with less confidence than for smaller values of ΔT_B. (See cases I and II, Figure 4.) With respect to difference (5), we compare the case where the flow is hydrodynamically developed at the entrance to the

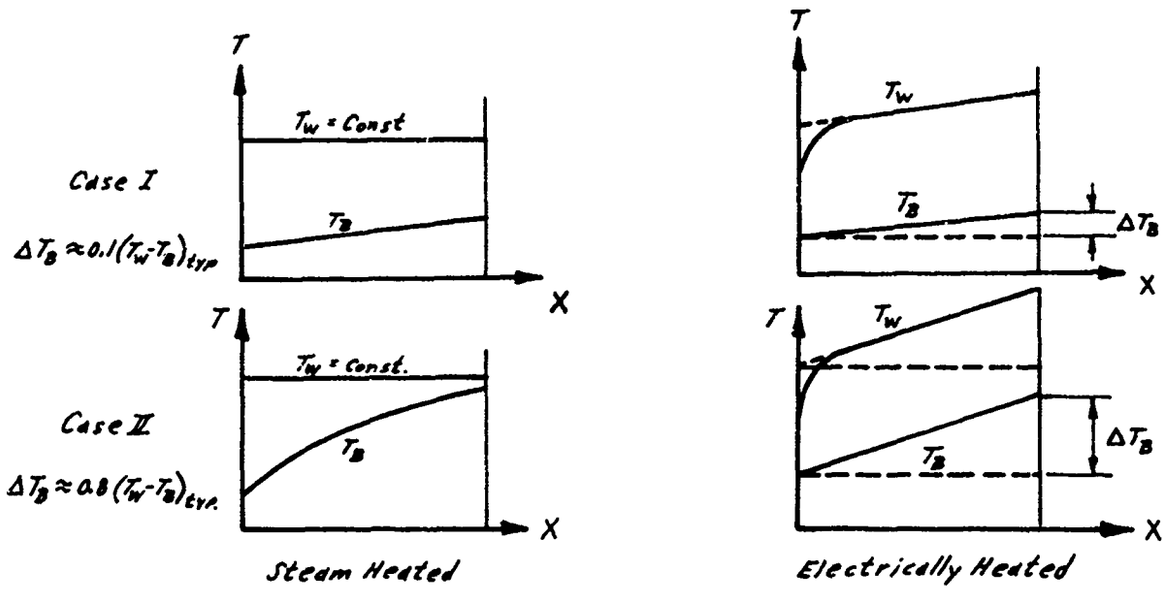

FIGURE 4

heated section with that where the hydrodynamic development starts at this point. The author feels that for distances greater than ~ 20 diameters downstream from the entrance of the heated section (for turbulent flow) where the flow is approaching hydrodynamic development in the latter case mentioned above, again, comparisons of the two cases may tentatively be made on the basis of Equation (7). For distances of 10-20 diameters or less from the thermal entrance these comparisons get progressively more dangerous.

We now discuss briefly some of the phenomena involved in heat transfer in oscillating flow systems. We consider here mainly the case of pipe flow, but the discussions are also applicable to flow over flat plates.

(1) Acoustic Streaming

We consider here the case of laminar flow. It has been shown (Refs. 1 and 2) that the presence of longitudinal standing-wave oscillations superimposed on a time-average laminar pipe flow, can produce deviations of the time-average gas velocities from those of the corresponding flow with no oscillations. In particular, the time-average U-velocity profile across the pipe diameter will be distorted. This generation of time-average secondary flow velocities is acoustic streaming. An analysis presented in Ref. 3 shows that these distortions of the velocity profiles can produce local deviations of the heat transfer coefficient from the corresponding steady-state values, as would be expected. This phenomena will be further described in the survey of the literature in which Refs. 1, 2 and 3 are discussed. Acoustic streaming can also occur in turbulent flow, for which to the author's knowledge, no analysis has been done to date.

(2) Variation in the Turbulence Exchange Properties of the Fluid Due to the Imposed Oscillations

This effect can be subdivided into 2 types of phenomena. One is the oscillation-induced transition from laminar to turbulent flow (i.e. the flow is laminar under conditions of no applied oscillations, but turbulent when oscillations are applied); the other is the alteration of the turbulence exchange properties of a flow already turbulent in the steady state. Refs. 4 and 5 show that the transition Reynolds number on a flat plate may be reduced by the application of longitudinal oscillations, whereas Reference 6 suggests that turbulence may be induced in pipe flow for $Re = 1{,}000 - 2{,}100$ by longitudinal flow oscillations. These references, also, will be further discussed in the literature survey. A large number of references dealing with turbulent flows seem, from heat transfer data, to imply deviations of the turbulence exchange properties from those of the corresponding steady flows. This follows from the tentative elimination of the phenomena described in paragraphs (1), (3) and (4) of this discussion as accountable for the observed changes in heat transfer. These elimination calculations are given in Section 5 and the references discussed in detail in the literature survey. It is to be noted, that for the case of turbulent

flow, both acoustic streaming and changes in the turbulence exchange properties induced by oscillation may alter the time-average velocity profiles from the corresponding steady-state values thus presenting a complex picture for analysis. Heat transfer deviations due to both these processes, acoustic streaming and variations in the turbulence exchange properties, are due only to changes (produced by oscillations) in the exchange processes between the central regions of the pipe and the wall, and hence differ from heat transfer deviations caused by viscous dissipation (discussed in the next paragraph) of wave energy near the wall, which involve another heat energy source, the wave. Heat transfer deviations (from the corresponding steady flow values) due to these two phenomena may be regarded as somewhat indirect. That is, the heat transfer deviations may be regarded in each case as caused by the oscillations through a two-stage process: (1) the time-average secondary flow velocities and alterations in the time-average turbulence exchange properties are produced directly by the oscillations, then (2) using the steady flow energy equation the above mentioned changes in time-average velocities and turbulence exchange properties will generate the observed deviations in heat transfer.

(3) Viscous Dissipation

For the case of laminar 'flow' in a pipe with a sinusoidally time-varying pressure gradient, an A.C. boundary layer thickness much less than the pipe diameter and no mean flow, the viscous dissipation may be calculated using the value of U_y obtained from Equation (11). Where there is a mean flow (which would be Poiseuille flow, neglecting the acoustic streaming velocities), the viscous dissipation as calculated above gives the additional dissipation due to the unsteady motion over and above that caused by the steady flow. For many cases of interest, this method of calculating dissipation may at least give an order of magnitude estimate even in turbulent flow, for the following reasons:

(1) If the frequency of oscillation is fairly high, the regions of high A.C. shear, where most of the dissipation takes place, will be very close to the wall (see p. 6) and hence in or near the laminar sub-

layer. Thus the effective 'eddy viscosity' will be relatively near to the molecular value in the dissipation regions.

(2) The dissipation analysis shows that for constant viscosity the dissipation per unit surface area is

$$Q_v = \frac{1}{8} \hat{U}^2 \sqrt{\frac{\omega \rho \mu}{2}} \tag{16}$$

and hence, for given values of $\hat{U}$, ω and ρ, $Q_v \propto \sqrt{\mu}$. Thus, even if the areas of high A.C. shear include regions where the 'eddy viscosity' is up to, say 10 times the molecular value, one would expect the dissipation to be not more than $\sim 3 \sim \sqrt{10}$ times the value as calculated from Equation (16). In most of the experimental data presented in the literature survey, it appears that the magnitude of the deviations of heat transfer caused by viscous dissipation are very small (of the order of a few percent of the steady-state heat transfer value, at most). The dissipation calculations for some of the experimental literature are presented in Section 5.

(4) Effects Directly Due to the Time-Varying Velocity Profiles

We consider here the case where viscous dissipation is negligible, the flow is always laminar and there are no deviations in the time-average velocity profile caused by the oscillations. These restrictions eliminate any of the effects of the oscillations on heat transfer described in paragraphs (1), (2) and (3) above. There are still effects due to the time-varying velocity profile as described below. We consider the case sketched on the next page (pipe flow). First we consider the non-realistic case where $T_w = 0$ for $x < 0$, and $T_w = T_1$ for $x > 0$. Here one expects an increase in heat transfer under oscillating conditions in the region of A, since, because of the oscillating motion, the fluid near the heated wall at A has, one half cycle earlier been in close contact with the cool wall in the B region. The rate of heat transfer away from regions A during the positive part of the velocity cycle can be quite large compared to corresponding steady flow value on account of the very steep instantaneous slope of the velocity profile near the wall. If, during the

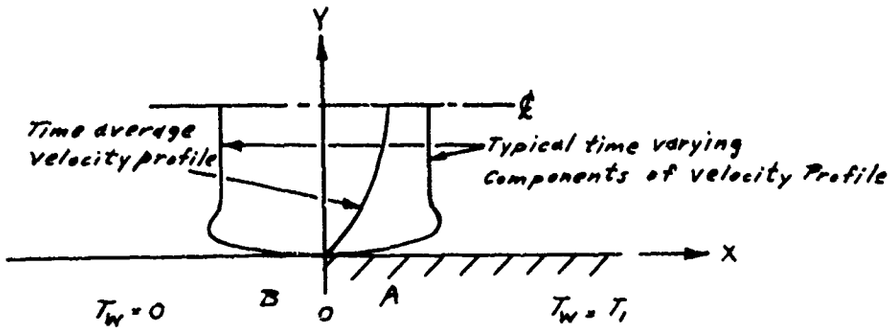

FIGURE 5

positive part of the velocity cycle the fluid which sweeps over the leading edge of the heated section were truly unheated, one would expect large increases in heat transfer as discussed below. In the region very close to the leading edge, the thermal boundary layer will lie within the approximately linear region of the unsteady velocity profile. For this region the unsteady and steady heat transfer rates will be related by

$$\frac{Nu_x}{Nu_{x,o}} \propto \left(\frac{U_{y,u}}{U_{y,s}}\right)^{1/3} \tag{17}$$

where $U_{y,u}$ = velocity gradient at wall in unsteady flow

$U_{y,s}$ = " " " " " steady flow

according to Lévêque's (7) solution for heat transfer in a flow with a linear velocity profile. Farther downstream, where the thermal boundary layer extends well into the flat portion of the unsteady velocity profile, the heat transfer in the unsteady case would be given closely by the slug flow solu-

tion; there heat transfer rates are still considerably higher than the rates for the steady flow case, though not as much so as in the region where Lévêque's solution applies. Now, the heat transfer increases, of course, cannot be explained simply on the basis of the above arguments, since (1) the flow which sweeps over the leading edge of the plate during the positive part of the velocity cycle is not totally unheated and (2) the heat transfer over the leading edge section will be reduced during the negative part of the velocity cycle as the fluid which has been in contact with the heated section further downstream sweeps back over the leading edge section. We now consider the effects of points (1) and (2) mentioned above. Point (1): when the fluid heated in contact with the leading edge section is first swept back over the $T_w = 0$ area, its temperature profile will appear as sketched in Figure 6 (a)

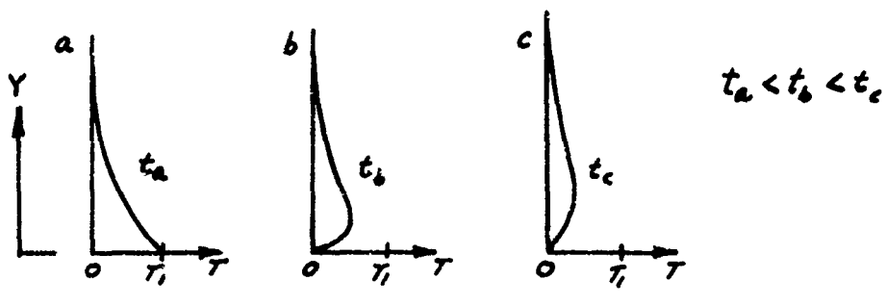

FIGURE 6

However, while the fluid remains in the $x < 0$ region heat will be conducted both towards the wall and further outwards into the flow as indicated in Figure 6 (a), (b) and (c). Hence, when the fluid again sweeps into the $x > 0$ region, its temperature profile will be similar to that of Figure 6 (c) at $x = 0$, and hence to a considerable extent, the fluid may now be regarded as unheated. With respect to point (2), the general argument that there still may be a time-average increase in heat transfer in the case of oscillating flow despite the decrease during the negative part of the velocity cycle is as follows. At least for the case of $T_w = T_1 = \text{constant}$ (which approximates the case of a steam-heated pipe), the heat transfer rate

cannot become less than zero on the negative part of the velocity cycle, while on the positive part of the velocity cycle, if the unsteady velocity gradients and the magnitude of the unsteady velocities are large enough, the heat transfer rates may be increased many fold over the corresponding steady flow values. From the above discussion it appears that heat transfer increases due to oscillations may be expected in the leading edge regions under the conditions described above ($T_w = 0$ for $x < 0$) . An important criteria for these increases at a given x-position (say, x_1) is that fluid which is in the region of x_1 on the maximum positive part of the velocity cycle was in the region $x < 0$ one-half cycle earlier. Hence beyond roughly $x_1 = \hat{x} = \frac{\hat{U}}{\omega}$, the above mentioned effects should disappear.

We now describe the modifications to the above discussion which are necessary when a more realistic wall condition is prescribed for $x < 0$. (At this point, we are still considering a hydrodynamically developed velocity profile at the entrance to the heated section.) A more realistic condition neglecting axial conduction along the wall itself would appear to be that the time-average heat flux to the wall is zero for $x < 0$. Neglecting axial wall conduction, this might be a fairly accurate description for the type of experimental apparatus sketched below

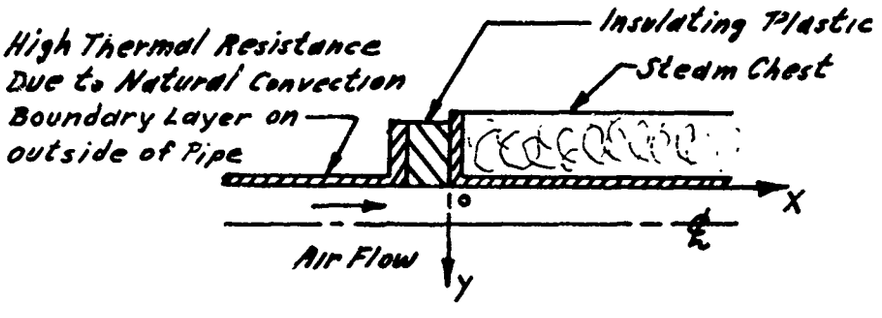

FIGURE 7

In the ideal case with no axial wall conduction, one would expect the wall in the region $x < 0$ but near $x = 0$ to assume a temperature profile lying between $T_w = 0$ and $T_w = T_1$ so that heat removed from the wall

during the positive part of the velocity cycle is compensated for by heat transferred to the wall during the negative part of the velocity cycle when the fluid that was in contact with the heated section of the pipe sweeps back over the section of interest. Assuming that fluid which is in contact with the unheated portion of the pipe during the negative half of the velocity cycle and then sweeps into the leading edge regions of the heated section sees an average wall temperature of $\sim T_w/3$ to $T_w/2$ during its time of contact with the unheated wall, arguments similar to those presented on p. 14 will yield temperature profiles corresponding to Figure 6 which are sketched below (Figure 8)

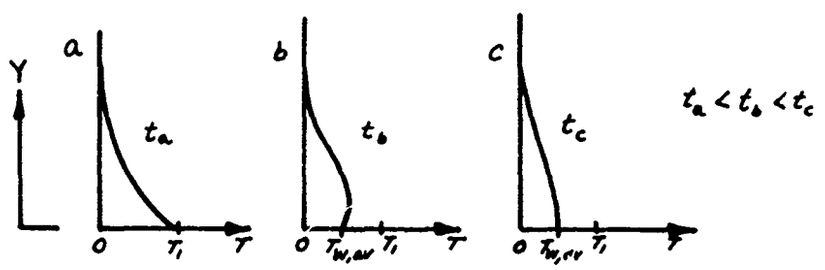

FIGURE 8

Figure 8 (c) corresponds to the moment at which the fluid again sweeps into the heated region. In explaining heat transfer increases in the leading edge regions during the positive velocity part of the cycle by reference to a totally unheated flow (p. 12,13,14), we see that the temperature profile of Figure 8 (c) differs more from the totally unheated case than that of Figure 6 (c). Hence, one would expect the heat transfer increases to be smaller in the case of the more realistic wall conditions of no time-average heat flux for $x < 0$.

We now consider a slightly different problem as sketched in Figure 9 on the next page. In the cases sketched in Figures 9 (a) and 9 (b), when the fluid which was in contact with the leading edge of the heated section

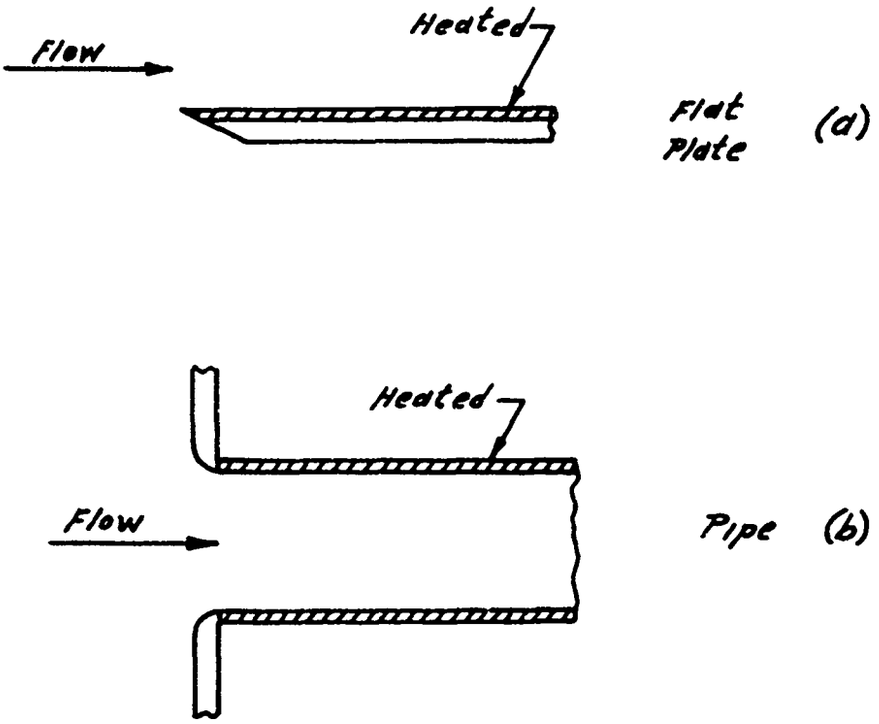

FIGURE 9

is swept back upstream, it will now not be in contact with the wall as in the previously discussed cases but will be in contact with unheated parts of the flow, and hence in this case (assuming laminar flow in this 'wake' region) the temperature profiles corresponding to Figures 6 and 8 will be as sketched on the following page. This case would appear to be superior to the case of Figure 8 but inferior to that of Figure 6 in supplying effectively unheated flow when the fluid in question again flows over the leading edge section. If turbulence is generated or enhanced in the 'wake' region, the diffusion of heat and the production of an essentially unheated temperature profile will be aided considerably. Note that, in this case, the following effect would tend to reduce the heat transfer increases somewhat. The velocity gradients in the steady-state flow are much larger than in the previously discussed cases; hence the effect of the increased velocity gradients due to unsteady flow are smaller. However, the effects due to the

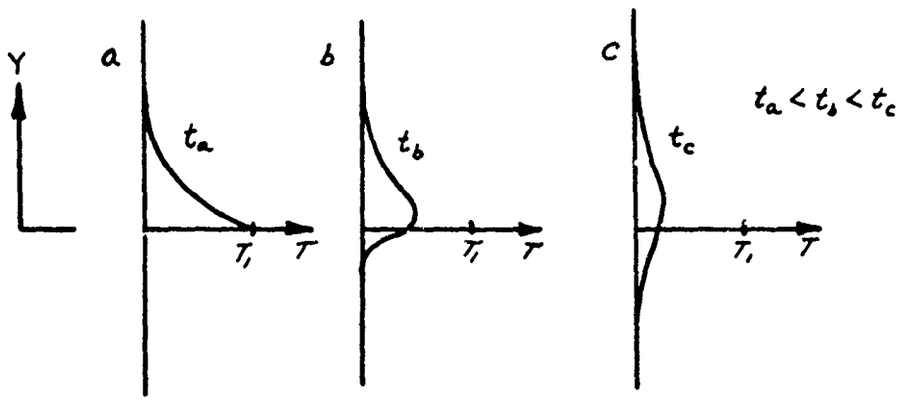

FIGURE 10

instantaneously higher velocity values of the main flow regions in unsteady flow remains.

A case differing from those discussed above and in which the heat transfer increases may be much larger is that where the heated section (here considered to be in a pipe) is of very small extent in the axial direction (Figure 11).

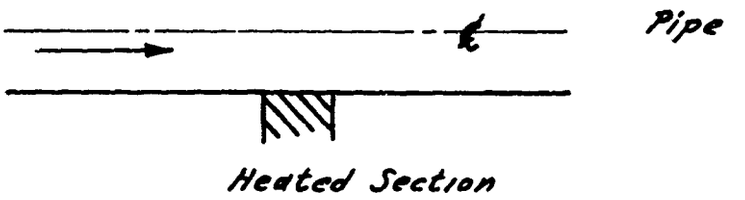

FIGURE 11

Here, arguments as presented previously will produce an increase in heat transfer during the positive part of the velocity cycle. However, if the length of the heated section is short enough, during the negative part of

the velocity cycle also, the flow passing over the heated section will be nearly unheated, and hence this part of the cycle instead of producing a decrease in heat transfer as in all previously discussed cases will also produce an increase in heat transfer. Hence the time-average increase in heat transfer will be greater for this last case.

By analogy with the distance from the leading edge roughly beyond which the heat transfer increases discussed in this section should not occur (p.15), farther upstream than a similar distance from the trailing edge of the heated section, it should be possible to regard the heated section as extending infinitely downstream. That is (Figure 12), if the flow near A has never been in contact with the unheated section,

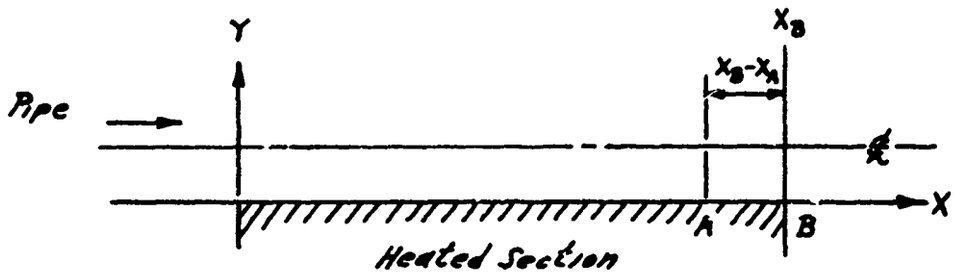

FIGURE 12

$x > x_B$ (which means roughly, $(x_B - x_A) > \hat{x} = \frac{\hat{U}}{\omega}$) we can regard the heated section as extending infinitely far downstream of point A .

We now consider two aspects of the idea that oscillating flow may under certain conditions be regarded as quasi-steady in some aspects. For the first case we consider flow of very low frequency and which does not reverse at any time during the cycle (Figure 13 on the next page). By very low frequency, we mean that $\omega \ll \bar{U}/x_A$, and also that the instantaneous velocity profiles and turbulence levels are very close to the steady values for the instantaneous mean velocities. Under these conditions, the flow can in general travel from $x = 0$ to $x = x_A$ in a time considerably smaller

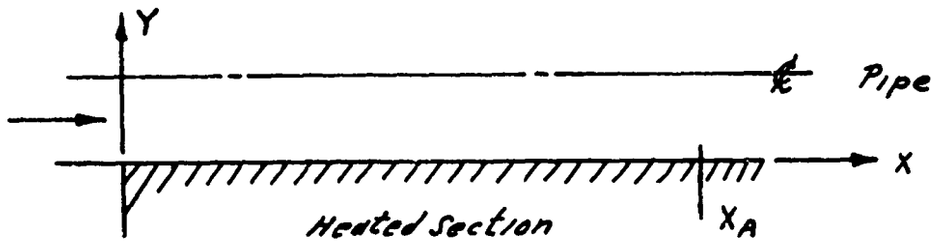

FIGURE 13

than the cycle period, and because of this and the fact that the flow is always unheated at $x = 0$, the heat transfer coefficient at x_A at any time in the cycle is given very closely by the corresponding steady-state value. Hence the time-average ratio of heat transfer coefficient at A under oscillating and steady conditions is given, under turbulent flow conditions, and if the flux is hydrodynamically and thermally developed at x_A by:

$$\frac{Nu}{Nu_o} = \frac{1}{2\pi}\int_o^{2\pi} \left| 1 + \frac{\hat{U}}{2\bar{U}} \sin\theta \right|^{0.8} d\theta \qquad (18)$$

since $Nu \propto Re^{0.8}$ in the turbulent flow regime (assuming a sinusoidal variation of mean velocity). Using Equation (18), the ratio Nu/Nu_o was computed for various values of $\hat{U}/\bar{U}$ and plotted in Figure 14. For the present discussion we are considering only the range $0 \leq \hat{U}/\bar{U} \leq 2$ (no reverse flow). We see from Figure 14 on the next page that in this range, the heat transfer is reduced under the quasi-steady assumption by the application of oscillations.

We now consider the second case. In this case, the frequency is still low enough so that the instantaneous velocity profiles and turbulence levels are close to the steady-state values for the instantaneous mean velocities, but we consider $\hat{U}/\bar{U} > 2$ (reversed flow is allowed). For this discussion, we consider turbulent flow and we also ignore effects of acoustic

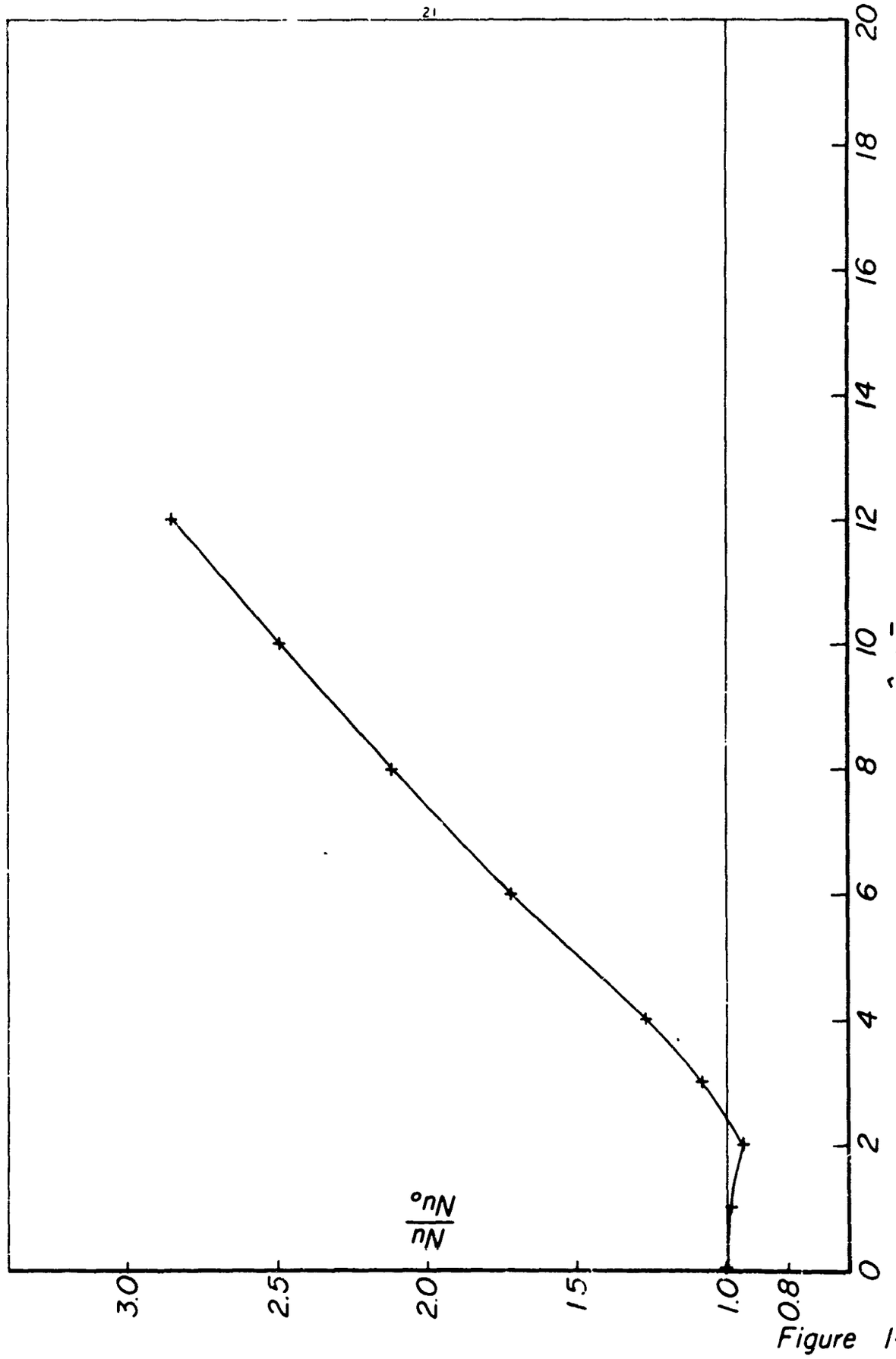

Figure 14

streaming and viscous dissipation discussed in paragraphs (1) and (3) above. Since reversed flow is present, there is ample opportunity for heat transfer increases due to the effects discussed in paragraph (4) to occur, but we consider the region considerably downstream from the entrance to the heated section so that these effects should be unimportant (p. 15). For the further discussion, we consider that at each instant of time, the flow can be regarded as fully developed steady pipe flow at the instantaneous mean velocity. This would, of course require a very low frequency to achieve in practice. Because the time-average absolute velocity in the pipe ($\overline{|U|}$) increases as $\hat{U}/\bar{U}$ rises beyond 2, the time-average absolute turbulence level and the eddy diffusivity in the pipe also rise. Hence, under these conditions, the heat transfer coefficient would be expected to rise above its steady-state value if $\hat{U}/\bar{U}$ is sufficiently large. With the assumptions made above, the ratio of the heat transfer coefficients in oscillating and steady flow may again be calculated from Equation (18), now allowing values computed for $\hat{U}/\bar{U} > 2$ to be considered also (Figure 14). From Figure 14, it can be seen that beyond $\hat{U}/\bar{U} \approx 2.4$, $Nu/Nu_o > 1$ and rises rapidly for further increases in $\hat{U}/\bar{U}$. In very few cases of interest is the frequency of oscillation low enough for one to suppose that the quasi-steady behavior described above applies, but in some cases, experimental data suggests that there is a considerable degree of approach towards the quasi-steady eddy diffusivity values discussed above even for the high frequencies actually employed. This point will be discussed further when the relevant experiments are described (Section 5.5).

2. SURVEY OF THE LITERATURE

In this section, the literature is surveyed using the parameters discussed in Section 1. In order to establish which references may be compared among themselves and with the data of this report, the literature is presented in considerable detail in this section. Further discussion and comparison will be presented in Section 5. Many references read by the author, describing systems very dissimilar to those of interest in this report are omitted in this literature survey. Two examples are those references dealing mainly with natural convection, and references dealing with vibration of the heat transfer surface normal to the flow direction.

In Ref. 8, Havemann investigates heat transfer to air at roughly atmospheric temperature and pressure flowing in a tube of 1 in.I.D. A steam heated heat transfer section 82½ in. long is preceded by a 50 in. long calming section. The overall heat transfer only to the steam heated section is measured. The range of Reynolds numbers is 6,000-25,000 and the frequency range in 5-40 cps. Pulsations are produced by a cam-driven poppet valve just upstream of the calming section. Four different sets of pulsating conditions were generated by using two different cams and either leaving the end of heat transfer tube open to the atmosphere or inserting a ½ in. dia. orifice plate at this point. As a rough approximation, we compute the parameters S and M for the work of this reference using the properties of air at room temperature and pressure. These parameters are given in Table 1.

TABLE 1

	freq,cps	5	20	50
Re	M	S	S	S
5,000	.0087	.267	1.068	2.67
10,000	.0174	.133	.534	1.33
20,000	.0348	.0665	.267	.665

(The reason for presenting these values of Re, M, S, etc. is to allow comparisons between the references to be made. Much of this work is done in Section 5; however, values as in Table 1 are presented here to give a feel for typical ranges of these parameters.)

No data on oscillation amplitude, waveshape or proportions of standing and travelling waves are given. Very different plots of heat transfer versus frequency and Reynolds number were obtained depending on which cam and whether or not the orifice was used. Changes of heat transfer as compared to the appropriate steady flow values range from -40% to +40% depending upon cam, orifice, Reynolds number and frequency. As no information is given on oscillation amplitude or waveshape, it is very difficult and dangerous to make comparisons with the other references or with the experimental work done in connection with the present report.

In Reference 9, Chalitbhan investigated heat transfer to air at roughly room temperature and 90 psia pressure flowing in a .824 in. I.D. tube. Heat transfer was measured in a water-cooled section of the pipe 95.0 in.(= 105.3 dias.) long. Only overall heat transfer to the heat transfer section was measured. Upstream of the heat transfer section was a steam-heated section 50 in.long. This section plus various unheated sections appear (from Fig. 1 in the report) to provide a calming section at least $\sim$ 70 in.(= $\sim$ 85 dias.) long upstream of the heat transfer section. The pulsations in the flow were those directly produced by the compressor operation. The Reynolds number and frequency ranges were 7,000-200,000 and 2-15 cps respectively. Pressure drop across the heat transfer section was measured using a manometer. Time-varying pressures were measured with transducers located about 1.5 ft. up - and downstream of the heat transfer section. However, only a few oscilloscope traces from these transducers are presented in the report; and no scales are given for these, so that effectively there is no information given on oscillation amplitude and waveshape and the proportions of standing and travelling waves present.

The parameters S and M are computed using the properties of

air at 90 psia and room temperature. These values are presented in Table 2.

TABLE 2

	freq.cps	2.66	7.17	15
Re	M	S	S	S
5,000	.00172	.59	1.592	3.332
20,000	.00688	.147	.398	.833
200,000	.0688	.0147	.0398	.0833

(frequencies of 2.66, 4.66, 7.17 and 15 cps were used). The data of this reference always show an increase of heat transfer with pulsating flow. Increases are as high as 80-90% in the Reynolds number range 10,000-50,000, and are around 10-15% in the Reynolds number range 160,000-200,000. The plots of heat transfer vs. Re vary widely depending on frequency. Again, as no amplitude, waveshape, etc., data are given in the reference, it is difficult to compare this data with other references. From the pressure drop measurements, which also showed increases under pulsating conditions, heat transfer coefficients to be expected were calculated using Martinelli's eqn., assuming that the ratio of eddy diffusivity in pulsating and non-pulsating flows is given by ratio of the pressure drops. The agreement between the heat transfer increases so calculated and the measured values is fairly poor (in some cases there being a factor of 2 difference) but an examination of the appropriate figures (Figs. 12-15 in the reference) suggests that there is considerable merit to this approach and that changes in the turbulence exchange properties caused by the pulsations are indeed an important mechanism in explaining the observed changes in heat transfer and pressure drop. Part of the difficulty in getting good agreement between the measured and calculated heat transfer values may be due to the difficulty in making the pressure-drop measurement.

In Reference 10, Lemlich studied heat transfer to water flowing in a ½ in I.D. pipe. Heat transfer was measured in a steam-heated section

of the pipe 3 ft. (72 dias.) long. Pulsations were produced by a solenoid valve located at various distances upstream and downstream of the heat transfer section. Only a rough sketch gives information on the length of the calming section upstream of the heat transfer section. This is simply the distance between the valve and the heat transfer section and thus varies with valve location. Frequency of the pulsation was $\sim$ 1.5 cps and the Reynolds number range was 2,000-20,000. Evaluating the viscosity of water at 70°F in the Reynolds number, we compute Strouhal numbers as presented in Table 3.

TABLE 3

Re	S
2,000	.778
5,000	.3112
20,000	.0778

(In the case of heat transfer to liquids, since the viscosity may vary widely, if the temperature at which the Reynolds number is evaluated is not given, calculations of the mean velocity and Strouhal number from the Reynolds number (as in Table 3) may be quite inaccurate. (In the case of water, the viscosity varies about 6-fold between 32 and 212°F). However, for gas flows, since μ varies relatively weakly with temperature, such calculations should be fairly accurate.)

Again, no information on amplitude or waveshape is given. When the valve was located upstream of the heat transfer section, the heat transfer was always increased under pulsating conditions. Larger increases were observed when the valve was closer to the heat exchanger. At the closest locations, heat transfer increases of $\sim$ 80% were observed at Re=2,000 and $\sim$ 10% at Re=20,000. Lemlich indicates that an important factor in the observed heat transfer increases was cavitation, especially near the heated wall. Locating the solenoid valve downstream of the heat exchanger so that cavitation did not take place produced only a decrease in heat transfer, as would be predicted from the quasi-steady analysis of Section 1.

For several reasons, one should be very careful in comparing results in liquids with those in gases. One is the possible presence of cavitation as mentioned above, which of course, has no analogous phenomena in gas flow. Another is the relatively rapid variation of liquid viscosity with temperature, which means that the parameter T_w/T discussed in Section 1 may become important for values of T_w/T quite near 1, unlike the case for gas flow.(Neglecting viscous dissipation, See Section 1). Another reason is the fact that Pr is no longer nearly constant for all cases (as was assumed in the dimensional analysis of Section 1, which was done for gas flows) and hence must be added to the parameters on the R.H.S of Eqn. (7) for this case of liquid flows. If Pr is considerably different from 1, this means that in general, the thermal and hydrodynamic boundary layers will have different thickness scales.

West and Taylor (11) investigated water flow in a 2 in. schedule 40 pipe (2.067 in. I.D.). Two heat transfer sections were used. The upstream heat transfer section was steam-heated, 18.17 ft. (= 105.4 dias.) long and preceded by a calming section 9 ft. (= 52.2 dias.) long. The downstream heat transfer section was water-cooled, 46 dias. long and preceded by a calming section 4 dias. long. In both heat transfer sections, only the overall heat transfer was measured. Oscillations were produced by a reciprocating pump which fed water to a variable volume air chamber and then to the steam-heated section of pipe. The Reynolds number range was 30,000 - 85,000 (caused chiefly by temperature differences in the water; flow rates varied only from 130 to 148 lbm/min), and the frequency was 1.7 cps. Using a water flow rate of 140 lbm/min, the Strouhal number is computed to be S=1.11. The only indication of the amplitude of the oscillations given in the reference is a "pulsation ratio" defined as the ratio of maximum to minimum air volume in the air chamber over the course of one cycle. Both heat transfer sections show, in general, heat transfer increases under pulsating conditions. Heat transfer increases rise from zero at a pulsation ratio of 1.02(very weak pulsations) to 50-70% at pulsation ratios of $\sim$ 1.4 and then fall to 20-60% at ratios of $\sim$1.55.Again comparisons using this reference are difficult since the "pulsation ratio",the only

amplitude data given cannot be related to the ratio $\frac{\hat{U}}{\bar{U}}$ on the basis of the data given in the reference.

Lemich and Hwu (6) investigated heat transfer to air flowing in a .745 in. I.D. pipe. The air conditions were roughly room temperature and pressure. The heat transfer section was steam-heated, 25 in. (= 33.6 dias.) long, and was preceded by a calming section 65 in. (= 87.3 dias.) long. Only overall heat transfer to the heat transfer section was measured. Oscillations were produced by an electro-magnetic driver located at the upstream end of the calming section. Most of the work was done at frequencies which were resonances of the tube system, allowing large amplitude oscillations to be set up. Hence, the wave system produced was essentially a standing-wave system. The frequencies used were 198, 256 and 322 cps, corresponding to the 3rd, 4th and 5th harmonics of the tube system. The Reynolds number range was 560-5900. Taking air conditions as those corresponding to a speed of sound of 1200 ft/sec (as given in the reference) and atmospheric pressure, M and S were calculated for the case of 256 cps oscillations; these values are presented in Table 4.

TABLE 4

f = 256 cps		
Re	M	S
1000	.001365	60.8
2000	.00546	15.2
5000	.01365	6.08

The only amplitude measurement taken was made as follows: A 1/8 in. O.D. tube lying inside and on the bottom of the heat transfer section, pointing upstream, was connected at its downstream end to an inclined manometer, the other side of which was open to the atmosphere. (Note: a short distance downstream of the heat transfer section, the air flow itself was open to the atmosphere, so that the pressure in the heat transfer section was only of the order of ~ 2 lbf/ft^2 above atmospheric.) The tube was moved axially so that its open end lay at various points along

the heat transfer section length, and the average values of the pressure measurements so obtained minus the corresponding measurement for steady flow was taken as an amplitude measurement for the run in question. This measurement is referred to as $\bar{H}_p$ in the reference. Thus this measurement seems to give some combination of the additional pressure drop between the heated section and the atmosphere caused by the oscillation, plus some kind of average value of the dynamic pressure of the oscillation rather than any quantity simply related to the time-varying pressures or velocities.

In this investigation, the application ot oscillations always caused an increase in the heat transfer coefficient. Increases in heat transfer up to 51% for Re < 2,100 and 27% for Re > 2,100 were observed. Examination of the plots of Nu versus Re and $\bar{H}_p$ (Figures 6, 7 and 8 in the reference) show relatively large increases in the heat transfer for Rc = 1440, 1770, 2030 and abruptly much smaller increases at Re = 2590 and upwards. This tendency leads one to believe that in addition to increasing the rate of turbulence exchange in the nominally turbulent region, the oscillations also can produce turbulence in the nominally laminar range, i.e. promote transition. This point was discussed in further detail by the author of the reference. These conclusions are made somewhat tentative by the uncertainty in the meaning of $\bar{H}_p$, which also make comparisons with this reference difficult.

Zartmann and Churchill (13) studied heat transfer in a premixed propane-air burner. The gas pressure was roughly atmospheric. The apparatus is sketched roughly below (Fig. 15). Local heat transfer coefficients were measured at five points as indicated in the sketch.

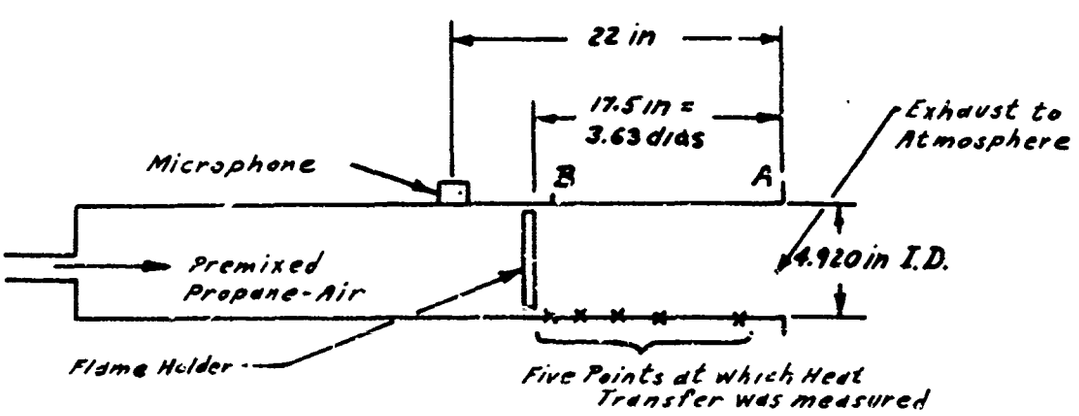

FIGURE 15

Depending upon which flameholder was used and whether or not a water spray muzzle was used downstream of point A, the burner could be made to produce flame-generated transverse or longicudinal oscillations or to burn steadily. For this report, we consider mainly the case of longitudinal oscillations. The frequency of the longitudinal oscillations (fundemental frequency of the chamber acting as an open-closed organ pipe) was $\sim$ 345 cps and the Reynolds number range 35,000 - 48,000. The wave system set up would be expected to be essentially a standing-wave system. Pressure amplitude measurements (in decibels) were taken with a microphone as sketched in Fig. 15. Since this microphone is upstream of the flameholder which blocks off 90.8-98.3% of the pipe area, the pressure amplitude at the microphone would be expected to be much smaller than that,at,say point B in the combustion chamber, which would be truly indicative of the strength of oscillation set up in the chamber. This is borne out by the behaviour of the heat transfer data which will be discussed shortly. We now consider heat transfer data given in the reference for a case with longitudinal oscillations. The Reynolds number of this case is 40,500 and taking the gas properties as those of air at atmospheric pressure and 2,500^{o}F (typical flame temperature given in the reference) and the frequency as given (345 cps) we compute M = .1053 and S = 3.21. Heat transfer increases of $\sim$ 150% were observed at distances of 4 in. from the flame holder falling off to $\sim$ 30% 13 in. from the flame holder. The sound pressure level under oscillating conditions was 155 db. Now, if one takes this sound pressure level to be that at point B (Fig. 15), a velocity node, then the value of $\frac{\hat{U}_A}{\bar{U}}$ in the chamber is roughly .22. Now, from many other references, especially Reference (24), for ranges of M, S, Re and $\frac{x}{D}$ comparable with the values quoted above, heat transfer increases of the order of 100% require $\frac{\hat{U}_A}{\bar{U}}$ values of the order of $\sim$ 6. Hence, the heat transfer data provide additional evidence which strongly suggests that the sound pressure level given in this report is much lower than the actual sound pressure level in the combustion chamber. Hence, this reference also cannot readily be used in comparisons.

The preceding six references (Refs. 6,8-11,13) provided either no amplitude measurements or measurements whose meaning was uncertain. Hence, detailed comparisons and correlations using these references cannot be made. However, some points of interest were obtained from these references as reviewed below: References 9, 11, 6 and 13 indicated that oscillations always raise the heat transfer coefficient, whereas References 8 and 10 indicated either increases or decreases in the heat transfer coefficient depending on conditions. Reference 10 indicated that cavitation may be important where liquids are used, and 6 indicated that oscillations may promote turbulence for flows in the transition region. We now discuss a series of references in which data is given on the oscillation amplitudes.

Linke and Hufschmidt (14) discuss the work of H. F. Klein in their paper. In Klein's investigation air and fuel were burned in a tube with dia. = 18 mm. and length = 1170 mm. (= 65 dias.). Air and fuel are fed in at one end of the tube and the other end is apparently open to the atmosphere. Combustion-driven oscillations cause the tube to resonate at its fundemental frequency (acting as an open-closed organ-pipe). The frequency of the oscillations is 89 cps and the Reynolds number range is 3,500-5,500. Apparently overall heat transfer only to the tube is measured. Under one set of conditions, the variation of the mean velocity with time is given at several points along the tube. These plots were obtained from pressure measurement and a wave diagram. From these plots, values of $\bar{U}$, $\hat{U}_A$ and $\frac{\hat{U}_A}{\bar{U}}$ were taken as follows:

$$\bar{U} = \sim 22 \text{ m/s}$$

$$\hat{U}_A = \sim 130 \text{ m/s}$$

$$\frac{\hat{U}_A}{\bar{U}} = \sim 6$$

Also S was computed to be .46. For oscillating flow in the particular tube in question, a graph is given of heat transfer divided by the appropriate steady flow values versus Reynolds number (Re = 3,500-5,500). We

do not know at what value of Re the given velocity plots were taken, but as the heat transfer curve shows increases of $\sim$ 50% at Re = 3,500 to $\sim$ 70% at Re = 5,500, we assume that the increase under the conditions at which the velocity plots were made is $\sim$ 60%. Computing the speed of sound from the given frequency and tube length, we have $M \approx .052$, under the conditions of the velocity plots. Assembling this calculated data together, we have:

$$\begin{aligned} Re &\doteq 4{,}500 \\ M &\doteq .052 \\ S &\doteq .46 \\ \frac{\hat{U}_A}{\bar{U}} &\doteq 6.0 \\ \frac{L}{D} &= 65 \end{aligned}$$

Overall fractional heat transfer increase $\doteq 0.6$

Shirotsuka (15) studied heat transfer to water flowing in a tube with I.D. 9.5 mm. Heat transfer coefficients were measured in a steam-heated section .6 m (= 63.2 dia.) long. From a sketch in the reference, it appears that the heat transfer section is preceding by a calming section of considerable length (perhaps 50 dias.) but no specific number is given in the text. Pulsations are produced as sketched below.

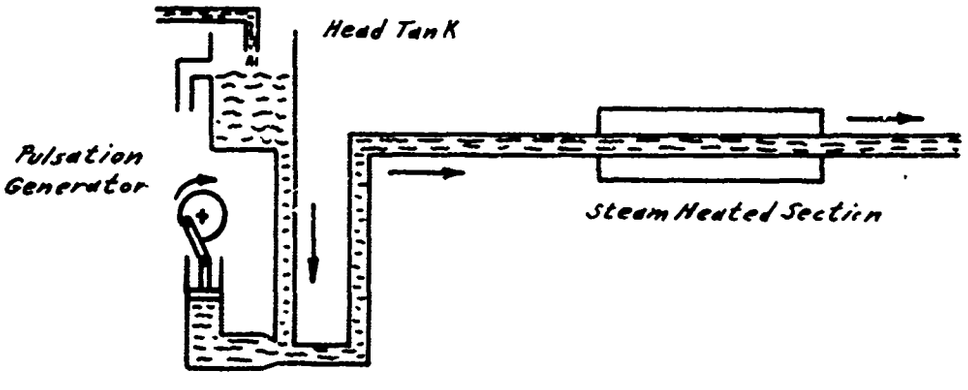

FIGURE 16

The frequency of the oscillations was 3.33 cps and the Reynolds number range 3,000 - 15,000. The displacement amplitude ($\hat{x}$) in the pipe is given as .1114 m. The method of measuring this amplitude is not given. To compute the mean flow velocity, S and $\hat{U}/\bar{U}$ from the given values of the Reynolds number, a value must be taken for the viscosity of water. The reference states that the fluid is water at room temperature; hence presumably the water enters the heat exchanger at room temperature; but the temperature rise across the heat exchanger and the temperature at which the viscosity is evaluated in the Reynolds number are not known. To compute the desired parameters we assume that the viscosity of water is evaluated at 70°F. If the viscosity was actually evaluated at 140°F, the values computed for $\hat{U}/\bar{U}$ and S will be off by a factor of ~ 2. In the reference, a graph is presented of the j-factors for heat transfer versus Reynolds number for both steady flow and oscillating flow with the parameters given above. Using this data, the following table may be constructed.

TABLE 5 (May be in error depending on the value of μ used in Re)

Re	$\bar{U}$ (ft/sec)	$\hat{U}/\bar{U}$	S	Fractional Change in Heat Transfer
3,000	1.011	7.56	.644	1.95
5,000	1.685	4.54	.386	.67
10,000	3.37	2.27	.193	.33
15,000	5.05	1.51	.129	.21

In this investigation, oscillations always produced an increase in the heat transfer. The reference states that in the laminar flow regime, steam bubbles appeared in the water flow inside the heat exchanger, and that hence heat transfer measurements were not taken for laminar flow. This implies that in the data actually taken, cavitation and boiling did not occur and hence this special phenomena does not need to be considered here.

Romie (16) investigated heat transfer to air flowing through a .98 in I. D. tube. Heat transfer measurements were taken in an electrically heated section of the tube 25 dias. long, preceded by a calming section of length 28 dias. The air is roughly at room temperature and pressure. Oscillations were produced using a rotating valve as sketched below.

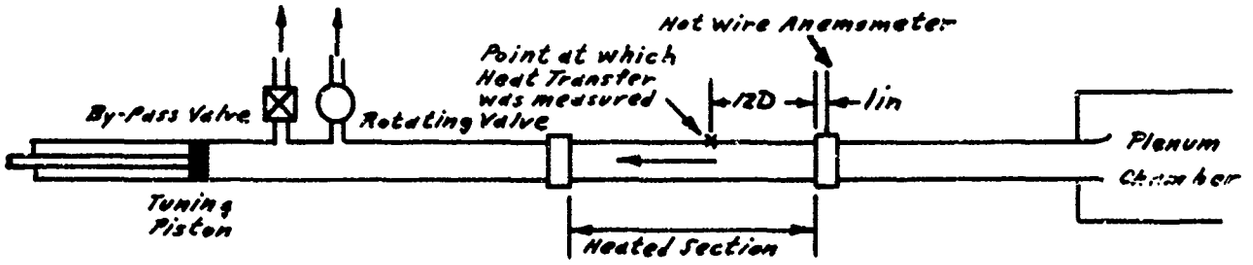

FIGURE 17

Heat transfer data were computed at a point 12 dias. downstream of the heated section entrance. Amplitude of the oscillation was determined using a hot-wire anemometer located on the pipe axis 1 in. upstream from the heated section entrance. The Reynolds number was 5,000 and the frequency range 3.3 - 133 cps. At the frequencies below $\sim$ 20 cps $\frac{\lambda}{4}$ was considerably greater than the duct length and hence the velocities at all points along the duct would be roughly the same at any given time during the cycle. Therefore, oscillation amplitudes measured with the hot-wire would be representative of conditions existing all along the heated section and especially at the point where the heat transfer measurement was taken. At frequencies of 30 and 43 cps (at which data was taken in the reference) the duct may have been tuned to resonance (at the fundemental frequency of an open-closed organ pipe), however $\frac{\lambda}{4}$ is still so long that conditions across the entire heated section do not vary too severely, and still conditions at the hot-wire should be fairly representative of conditions at the heat-transfer point. However, for the two highest

frequencies investigated (75 and 133 cps), the standing wave pattern becomes so short that the hot-wire probe and the heat-transfer point see considerably different environments with respect to local oscillation amplitude. Hence, in the graph presented in the reference which plots the ratio of the Nusselt number under oscillating conditions to that under steady flow conditions versus $\hat{U}/\bar{U}$ (at the hot-wire) and frequency, for points above f = 43 cps, the indicated effect on heat transfer would not be typical for the given value of $\hat{U}/\bar{U}$, if $\hat{U}/\bar{U}$ was interpreted as a local value. Data are presented for $\hat{U}/\bar{U}$ = 1,2,3 and 4. The data for $\hat{U}/\bar{U}$ = 4 are presented in Table 6; for smaller values of $\hat{U}/\bar{U}$, the effects on heat transfer are of similar form but smaller in size. S and M were calculated using air properties at room temperature and pressure.

TABLE 6

f	S	Fractional Change in Heat Transfer
cps		
3.3	.186	.09
10	.533	.22
17	.906	-.02
30	1.60	-.12

Re = 5,000
M = .0087
$\hat{U}/\bar{U}$ = 4.0

For frequencies above 43 cps, the change in heat transfer rises again becoming positive at about 75 cps, but as discussed above, these values are likely not typical if $\hat{U}/\bar{U}$ was interpreted as a local value.

Bayley (5) investigated airflow over a flat plate. The flat plate was electrically heated, 8 in. long by 3 1/8 in. wide and mounted in a center plane of a 4 1/8 in. dia. pipe. Air was drawn into the pipe from the atmosphere through a bell mouth, passed over the plate, then through a rotating valve which generates the oscillations (and a bypass valve) to a blower which discharges to the atmosphere. The frequency range of the rotating valve is 10 - 100 cps. Heat transfer coefficients were measured using five thermo couples mounted in the plate surface at various axial positions; however

all data in the paper are presented in the form of average Nusselt numbers based on the average plate surface temperature and the overall plate length. Time-varying pressures were measured using a transducer mounted in the pipe wall, above the center-point of the plate. It appears that at some frequencies, resonances can occur in the pipe, and hence, in general, the nature of the wave system (proportions of standing and travelling waves) is not known. While some data is given in the report over a fairly wide range of frequencies and Reynolds numbers, the only data sufficiently detailed to allow M, S_L and $\hat{U}/\bar{U}$ to be calculated is given at $Re_L = 1.75 \times 10^5$ and f = 30 and 96 cps. (Re_L and S_L are based on the 8 in. length of the plate). As will be discussed later, transition took place at $Re_x = 1.8 \times 10^4$ or lower, hence the flow was essentially turbulent over the whole length of the plate under both steady flow and oscillating conditions. The pressure amplitudes are given in terms of a parameter which we will call P' defined as:-

$$P' = \frac{\hat{P}}{2} \Big/ \frac{\rho \bar{U}^2}{2} \tag{19}$$

where $\bar{U}$ is the mean flow velocity.

To estimate $\hat{U}/\bar{U}$ we assume that the wave system is one of travelling waves-if an appreciable proportion of standing waves are present, the following equation will likely be significantly in error. From simple wave theory, for travelling waves,

$$\frac{\hat{P}}{\bar{P}} = \frac{\gamma \hat{U}}{c} \tag{20}$$

hence

$$\hat{U}/\bar{U} = P' \frac{\bar{U}}{c} = P' M \tag{21}$$

Using this assumption, the aforementioned data can be reduced to the form shown in Table 7.

TABLE 7

	P'	$\hat{U}/\bar{U}$ *	Fractional Change In Heat Transfer	
f = 30 cps	20	.76	.06	
S_L = 2.93	40	1.52	.24	$Re_L = 1.75 \times 10^5$
	60	2.28	.37	M = .0380
f = 96 cps	30	1.14	.06	
S_L = 9.43	50	1.90	.15	
	70	2.66	.20	

(*$\hat{U}/\bar{U}$ values may be in error if an appreciable proportion of standing waves are present; see text)

In the data of Table 7, as well as in all other data of the reference, oscillations produce only an increase in heat transfer. As noted previously, transition took place at such a low value of Re_x, that the flow was essentially turbulent over the whole plate under all conditions. The reference states that Re_x (transition) $\approx 1.8 \times 10^4$ under steady flow conditions, but that under the severest conditions of oscillation Re_x decreased by about 50%, and decreased by intermediate amounts under less severe conditions of oscillation. Hence, we have evidence the oscillations can promote transition in flat plate flow as well as in pipe flow (see discussion of Reference 6, p. 28, 29).

Evans (18) also investigated air flow over a flat plate. The air flow was at room temperature and pressure. The plate was 4½ in. long by 2½ in. wide and mounted in a tube of diameter 4 in. The air flow was steady and the flat plate was oscillated axially using a jig-saw mechanism. The oscillation frequency range was 1-60 cps. The model was painted black and heated by infrared lamps adjusted to give a nearly constant heat flux over the model surface. Local heat transfer measurements were taken using mainly 14 thin film platinum resistance thermomenters spaced at ½ in. intervals along the centre-line of the model surface. The purpose of Evans' work was mainly to measure the time-varying rates of heat transfer from the

model; but some measurements of time-average heat transfer rates were taken; these latter are of interest in the present context. Hot-wire measurements showed that the boundary layer was laminar over the entire plate up to $\bar{U}$ = 45 ft/sec. and f = 60 cps. The displacement amplitude of the oscillations (simply twice the radius of the crank arm) was $\hat{x}$ = .986 in. In a series of tests at $\bar{U}$ = 5 ft/sec, for f up to 10 cps [$S_x \triangleq 2$, (S_x is based on the distance from the leading edge of the model to the thermometer used in the heat transfer measurement)], no measureable change (< 3%) in the time-average heat transfer was observed. The maximum value of $\hat{U}/\bar{U}$ for these tests (which would have been at f = 10 cps) was calculated to be 1.03. Under these conditions, M = .0044 and Re_L (based on the full length of the plate) = 10,800. Some support for the hypothesis that changes in the turbulence structure are important in explaining the observed heat transfer changes may be had by comparing the above data with the data of Table 7.(Ref. 17). We consider the case of f=10 cps given above. We first note that the Strouhal number in Table 7 (f = 30 cps) is quite close to that given above (the average Strouhal number for the plate of Table 7 is $\frac{1}{2} S_L$ = 1.46). By linear interpolation from Table 7, one could estimate the fractional change in heat transfer for $\hat{U}/\bar{U}$ = 1.03, $\frac{1}{2} S_L$ = 1.46, as .12. Hence, under conditions of $\hat{U}/\bar{U}$ = 1.03, $S_x \approx 2$, we see that heat transfer increases of $\sim$ 12% occur in turbulent flow, but less than 3% in laminar flow. However, the fact that M and Re_x are very dissimilar in the two situations being analyzed, and the fact that in one case, the flow is oscillating and in the other, the plate, make any conclusions somewhat uncertain.

Feiler and Yeager (19) studied airflow over a flat plate. The flat plate was 6 in. long by 4 in. wide and was mounted in an 8 in. diameter duct. Air was drawn from the room through a siren wheel (which produced the oscillations) into the duct. The air passes down the duct over the plate, through an acoustic muffler and flow control valves to an exhaust facility. One surface of the plate was heated electrically by five 0.5 in. x 3 in. nichrome ribbons mounted transversely and spaced .06 in. apart starting 1 in. from the leading edge. Heat transfer was measured using thermocouples welded to the nichrome ribbons. Heat transfer data

given in the paper were taken only from the second and third (from the leading edge) ribbons. The frequency range of the siren was 34-680 cps. Oscillation characteristics are measured using a hot-wire anemometer mounted in the free stream, and a microphone flush mounted in the duct wall, both located at the test section. By moving the microphone axially to other positions along the duct, it was observed that the wave system in general was one of standing plus travelling waves. The proportion of standing wave was higher at lower frequencies; data given in the paper show an s.w.r. of ~ 2.5 at 98 cps but only ~ 1.25 at 680 cps. The amplitude parameter given for each heat transfer run is

$$\frac{\widetilde{\rho U}}{\overline{\rho U}}$$

Since the fractional variations in ρ are much smaller than the fractional variations in U, we have approximately

$$\frac{\tilde{U}}{\bar{U}} \simeq \frac{\widetilde{\rho U}}{\overline{\rho U}} \tag{22}$$

Further assuming the waves to be roughly sinusoidal in shape, we can write

$$\frac{\hat{U}}{\bar{U}} \simeq 2\sqrt{2}\,\frac{\widetilde{\rho U}}{\overline{\rho U}} \tag{23}$$

This allows us to estimate the values of $\hat{U}/\bar{U}$ for the data of this reference. The range of Re_x (based on distance from the leading edge to the center of the relevant heat transfer ribbon) was $2.5 - 11\times10^4$. Typical values of M and $S_{x(3)}$ (S_x for the third ribbon) are given below for various values of f and $Re_{x(3)}$ (Re_x for the third ribbon).

TABLE 8

		f (cps)		
		34	148	680
$Re_{x(3)}$	M	$S_{x(3)}$		
3×10^4	.022	1.52	7.55	33.7
7×10^4	.052	.72	3.14	14.5
11×10^4	.081	.46	2.00	9.21

The maximum amplitu .s used were about $\widetilde{\rho U}/\overline{\rho U} = .60$ ($\hat{U}/\bar{U} \simeq 1.70$). (Amplitudes were varied by changing the gap between the siren rotor and stator). We now discuss the experimental results. In general, little effect of frequency was found. The main effects seemed to be those of Re_x and $\hat{U}/\bar{U}$. For $\hat{U}/\bar{U}$ in the range 1.4 to 1.8 increases in heat transfer of 40-60% were observed at $Re_x = 8\text{-}11 \times 10^4$ decreasing to 10-15% at $Re_x = 2.5\text{-}3.5 \times 10^4$. At smaller values of $\hat{U}/\bar{U}$, the data had a similar trend but the heat transfer increases were smaller. It should be pointed out that the steady-state flow had a very high turbulence intensity ($\widetilde{U}/\bar{U} = .09\text{-}.10$) due to the siren ports acting as turbulence generators. Hence, the above heat transfer increases might have been even larger if the steady state reference flow had a low turbulence level. The range of Re_x, the fact that for the steady flow case, it was observed that $Nu_x \propto Re_x^{.675}$ and the above mentioned behaviour of the heat-transfer increases suggest that the boundary layer flow was in the transition region, and the main effect of the oscillations was to move the transition region upstream. Further investigations were carried out by one of the authors of Reference 19 (Feiler) and published in Reference 4 . This work is now discussed.

The same apparatus used in (19) was used again in (4), with modifications as discussed below. The siren was now located downstream of the test sec. .on, the air passing directly from the room, through a bell-mouth into the duct, then through the acoustic muffler and over the model. This allowed the turbulence intensity of the reference flow to be kept at 3-4%. The test body was a cylinder as sketched below

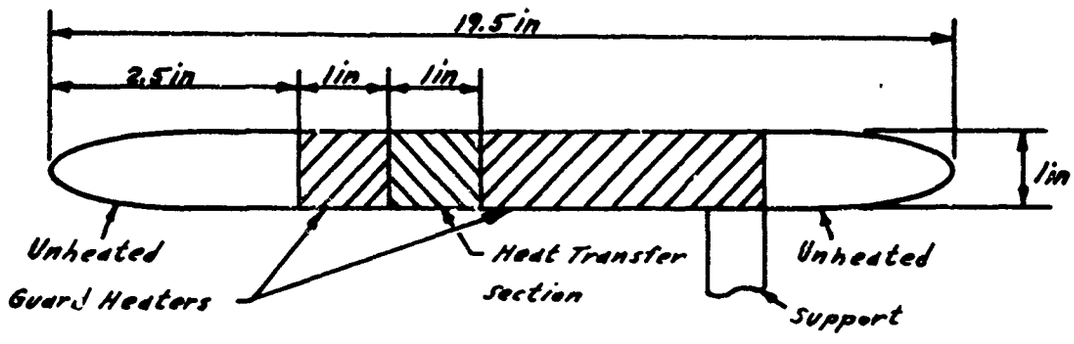

FIGURE 18

Three sections of the cylinder (see Figure 18) were heated electrically. Heat transfer measurements were taken at the center heated section using thermocouples flush with the outer surface. All work was done at a frequency of 100 cps. The oscillation amplitude was again measured at the test section using a hot-wire anemometer; amplitudes were given in terms of $\widetilde{\rho U}/\overline{\rho U}$ as before. All work was done over a relatively narrow range of oscillation amplitudes, $\widetilde{\rho U}/\overline{\rho U}$ = .45 - .65. Essentially, then, there was just one variable, Re_x, which is varied by changing the mean flow velocity. Under steady flow conditions, hot-wire velocity boundary-layer surveys taken at the center of the heat transfer section indicated good agreement with the Blasius profiles for a flat plate if the effective distance from the leading edge was taken as 1.78 in. instead of the actual value of 4 in. This agreement was obtained over a range of Re_x values (based on x = 1.78 in.) of 1.24 - 11.1x10^4. Heat transfer data for steady flow showed good agreement with the laminar flow relation

$$St\left[1-\left(\frac{x_o}{x}\right)^{3/4}\right]^{1/3} = .332\ Pr^{-2/3}\ Re_x^{-1/2} \qquad (24)$$

where x_o = unheated length.

up to $Re_x = 10^5$, beyond which the heat transfer values increased above those predicted by Equation (24). This indicates that the transition took place at $Re_x = 10^5$. Under oscillating conditions, the heat transfer data show a fair agreement with the following turbulent flow relation given in the reference.

$$St\left[1-\left(\frac{x_o}{x}\right)^{39/40}\right]^{7/39} = .0296\ Pr^{-0.4}\ Re_x^{-0.2} \qquad (25)$$

The heat transfer values start falling below the curve of Equation (25) at $Re_x = 2x10^4$ and would appear, if extrapolated, to approach the laminar curve at about $Re_x = 10^4$ indicating that transition starts at about the latter value. The heat transfer values also fall somewhat below the curve of Equation (25) at $Re_x > 5x10^4$, but the data

are much closer to the curve of Equation (25) than to that of Equation (24).

The above data strongly suggests that the effect of the oscillations is to induce earlier transition from laminar to turbulent flow. This is supported by hot-wire boundary layer velocity profiles taken in the reference, which show that the mean velocity profiles under oscillating conditions deviate markedly from those in the laminar portion of the flow under steady conditions and rather resemble profiles taken under steady conditions with trip-induced transition to turbulent flow. We give below the parameters M and S_x (based on x = 1.78 in.) for the Reynolds number range of these experiments.

TABLE 9

Re_x	M	S_x	
10^4	.0098	8.4	
$5x10^4$	.049	1.68	$\frac{\hat{U}}{\bar{U}}$ = 1.27 - 1.84
$20x10^4$	.196	.42	

In a continuing series of investigations at the Georgia Institute of Technology, T. W. Jackson et. al. have investigated air flow in a pipe. While these authors have published many reports, here we discuss only data from those most applicable to the present work These are References 1, 2, 3, 21, 22 and 23.The experimental measurements will be described first. Heat transfer was measured in a steam heated section of tube 3.86 in I.D., and 10 ft. ($\sim$ 31 dias.) long. 21 condensate collection chambers in the steam chest allowed local heat transfer data to be obtained. Air was supplied from a blower to a plenum chamber and then through a bell mouth directly into the heat transfer section. Thus, except for effects of the bell-mouth, thermal and hydrodynamic development of the flow start at the entrance of the heat transfer section. Just downstream of the heat transfer section, the air discharged either into another plenum chamber and then to the atmosphere or directly to the atmosphere. Thus, air conditions in the apparatus were

roughly room temperature and pressure. At the centre of the pipe, just downstream of the heated section a horn (facing upstream), driven by an electromagnetic driver was located. The horn was operated at one of the organ-pipe resonances of the pipe to generate sound pressure levels up to 167 db (at the velocity nodes). To measure the intensity of the oscillations, a microphone mounted on a rod was inserted into the duct from the upstream end. The sound pressure level stated in data presentation is that at the pressure antinode farthest upstream in the duct. Data taken with the apparatus essentially as described above is presented in References 21, 22 and 23. The data of Reference 3 was taken with an unheated section 28.22 ft (≙ 87.7 dias.) inserted between the inlet plenum chamber and the heat-transfer section. Hence, in this case, the flow is hydrodynamically developed at the entrance to the heated section. The data presented in References 3, 21, 22 and 23 were obtained at frequencies and Reynolds number ranges as given below.

TABLE 10

Reference	f (cps)	Re	Remarks
21	221; 356	$\sim$ 2,000	-
22	220	2100;11,600	-
23	222	16,000-200,000	-
3	90	19,800- 64,600	Uses 28.22 ft. Calming Section

Typical heat transfer data from these references are reproduced in Figures 19-22. We have added the computed values (using properties of air at room temperature) of S, M, and $\hat{U}_A/\tilde{U}$ for the case of the highest sound pressure level (SPL) in each figure. (Values of $\hat{U}_A/\tilde{U}$ for the lower sound pressure levels may be computed from the decibel values of SPL given, recalling that 10 db = a factor of $\sqrt{10}$ = 3.16).

We have also added, in some cases, the abbreviation V.A. (velocity antinodes) next to the vertical lines denoting the position of the velocity antinodes. We first discuss the behaviour of data taken at

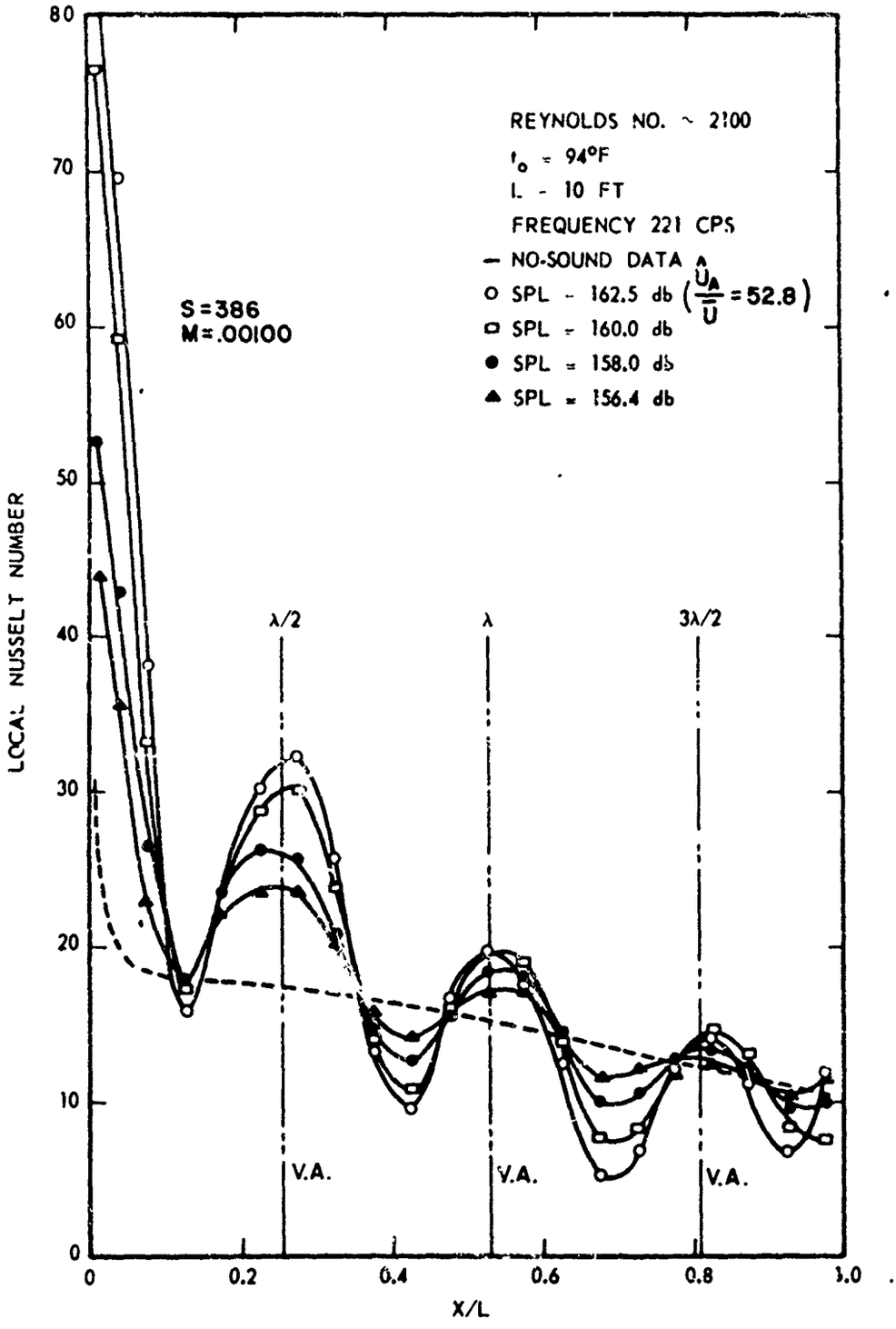

Local Nusselt Numbers Versus x/L for Various Sound Pressure Levels and 221 cps.

FIGURE 19

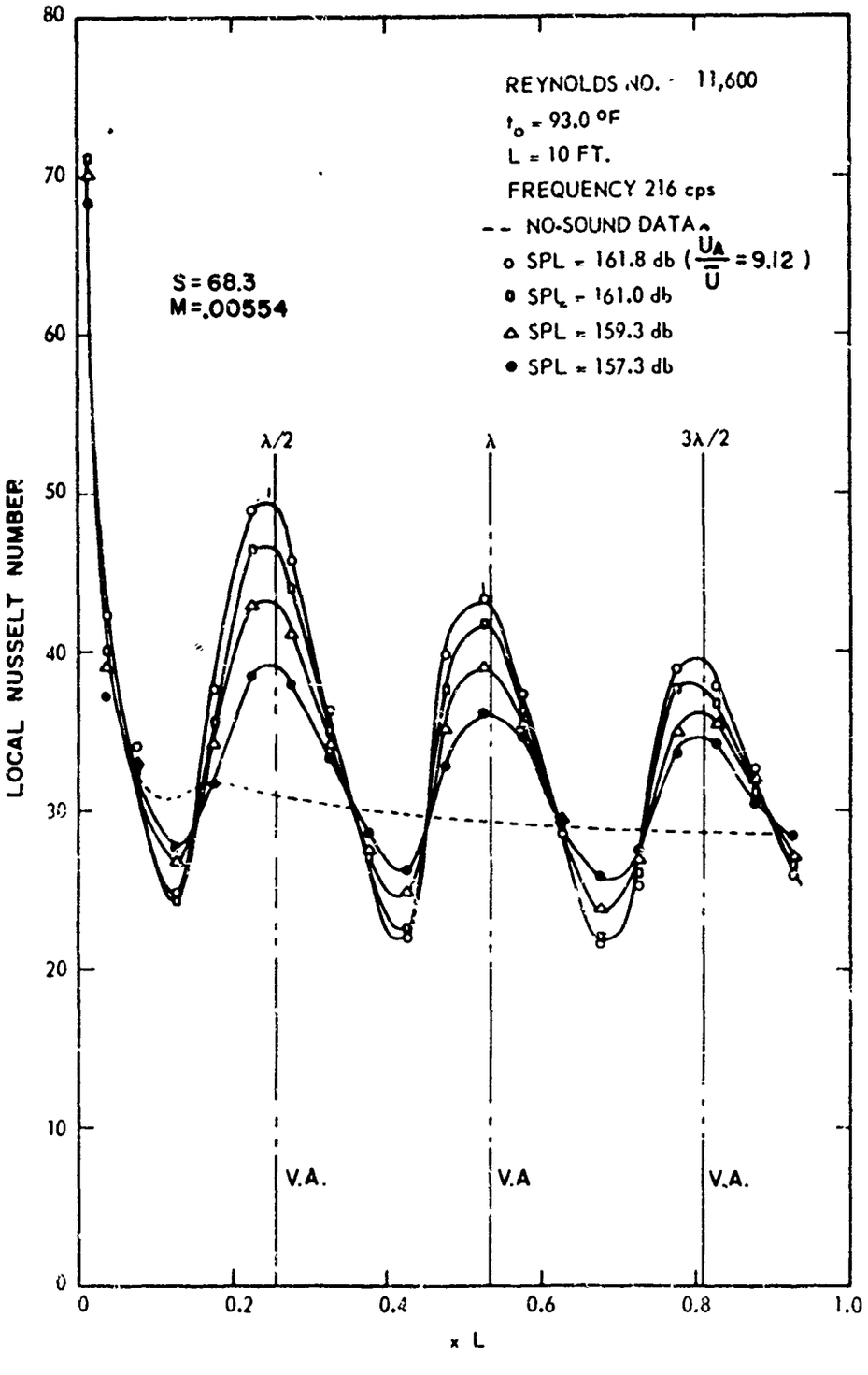

Local Nusselt Number Versus x/L for Various Sound Pressure Levels and 216 cps.

FIGURE 20

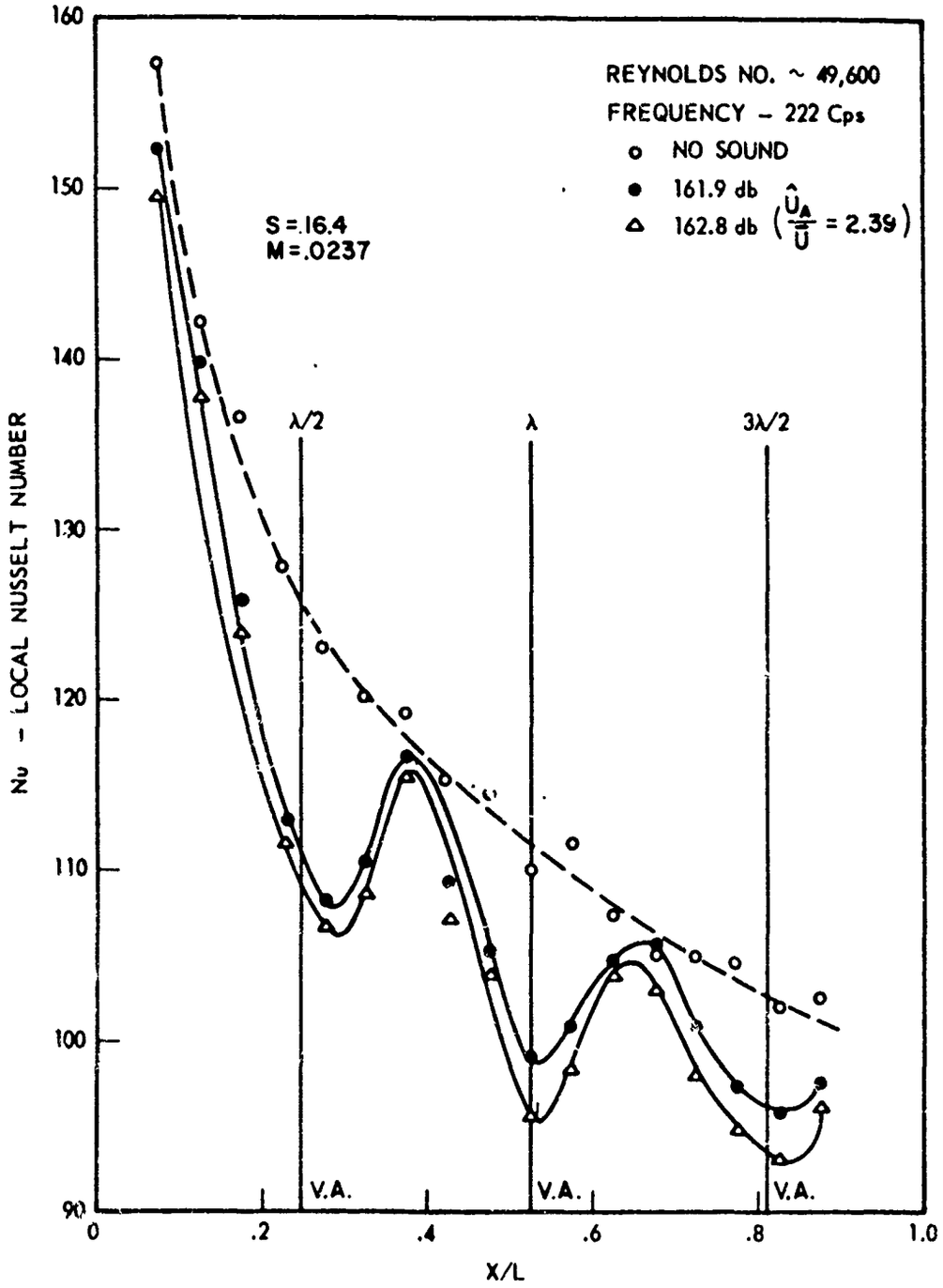

Local Nusselt Number Versus X/L.

FIGURE 21

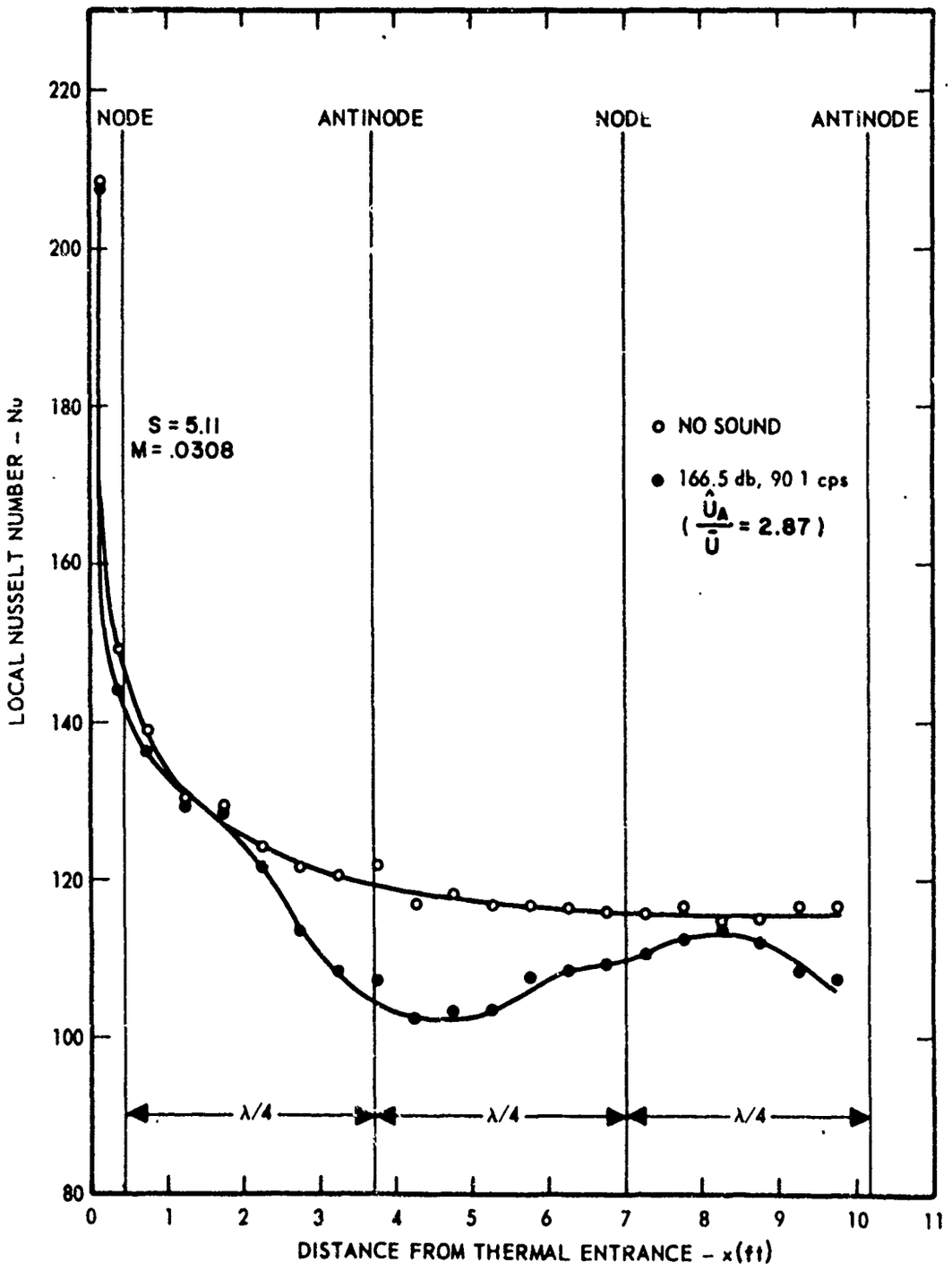

Nu Versus x for Re = 64,600.

FIGURE 22

a frequency of $\sim$ 220 cps (References 21, 22 and 23). At Reynolds numbers of 43,000 and above, the data behaves as exemplified by Figure 21, i.e.,the general effect of oscillations is to reduce the heat transfer rates, the largest reductions appearing near the velocity antinodes, and relatively little effect in the regions of the velocity nodes. As Reynolds number is decreased into the range 22,800 - 33,000 the effects on heat transfer become small and irregular although the sound pressure levels are undiminished. On further decrease of the Reynolds number into the range 11,600 - 16,000, there is again, a strong effect of the oscillation on heat transfer, but the effect is now exemplified by Figure 20, i.e. increases in heat transfer at the velocity antinodes, decreases at the velocity nodes and an overall increase in heat transfer. At still smaller Reynolds numbers (Re $\approx$ 2000, Figure 19) the heat transfer effects still resemble those shown in Figure 20 with respect to the location of the maximum and minima of heat transfer, but the shape of the curve is somewhat changed. The results at Re $\approx$ 2000 may include effects of natural convection as will be discussed below. The measurements at f=356 cps, Re $\approx$ 2000 (Reference 21) are very similar to those shown in Figure 19 (with a closer spacing of velocity antinode lines). The data of Reference 3 (f = 90 cps) show data partially typified by Figure 22. In the Reynolds number range 38,300 - 64,600 there is an overall decrease in heat transfer with the minima of heat transfer being slightly downstream of the velocity antinodes, and the maxima slightly downstream of the velocity nodes. Except for this slight downstream shift of the maxima and minima, this data is quite similar to that discussed above for f $\approx$ 220 cps, Re $\geq$ 43,000. As the Reynolds number is decreased into the range 33,000 - 19,800 the maxima and minima of heat transfer gradually shift further downstream (still with an overall decrease of heat transfer and the maxima of heat transfer closely approaching the steady state values, as in Figure 22) until at Re = 19,800 the maxima of heat transfer appear to occur slightly upstream of the velocity antinodes, and the minima slightly upstream of the velocity nodes. We return now to the free-convection effects discussed above for the case of Re $\approx$ 2000.

The authors of these references have shown that the steady-state (no sound) data at Re $\approx$ 2000 (Figure 19) include strong effects of natural convection. By calculation the Nusselt numbers to be expected for the case of forced convection only, they have shown that except near the heated section entrance, the observed Nusselt numbers are more than double those to be expected from forced convection effects. This implies a strong natural convection effect in these regions. An uncertainty is introduced into the interpretation of the data of Figure 19 as follows. The authors of the references state that the imposed oscillations as well as producing a direct effect on heat transfer, may or may not cause a reduction in natural convection velocities. Now, if the natural convection is unaffected by the oscillations, the proper steady state curve with which to reference the data taken under oscillating conditions is the curve as given in Figure 19. But, if the oscillations should cause a virtual disappearance of natural convection velocities, the proper steady-state reference curve in Figure 19 would be much lower than the one presented, and would be the curve mentioned above, calculated on the basis of forced convection only. Because of this uncertainty, data from these references at Re $\approx$ 2,000 will not be used in later correlation attempts (Section 5.5). The authors of the references state that for fully turbulent flow, natural convection effects should be negligible, even in steady flow. Hence, the authors' data for Re $\geq$ 10,000 should be suitable for the above mentioned correlation attempts and will be so used.

With the restricted range of frequencies (essentially, only f $\approx$ 90 and f $\approx$ 220 cps) and amplitudes (sound pressure levels less than 167db) of the data discussed above, it is not immediately apparent which of the parameters Re, S, M and $\hat{U}_A/\bar{U}$ are most important in determining the nature of the effects of the oscillations on heat transfer, i.e. considering data taken at f $\approx$ 220 cps (Re = 11,600-200,000, ignoring data at Re $\approx$ 2000 for reasons discussed above), as the Reynolds number increases, M $\propto$ Re and S $\propto \frac{1}{Re}$. Hence the change in the nature of the effects of the oscillations on heat transfer as Re varies could be due to the changes in Re, M, S or more than one of these parameters. Some

attempt to separate the effect of S can be made since there is another series of data at f $\approx$ 90 cps. Another point to be considered is the fact that at a given value of sound pressure level (the maximum sound pressure level for each case presented seems to be in the range 161-167 db), $\hat{U}_A/\bar{U} \propto \frac{1}{Re}$. However, some separation of the effects of $\hat{U}_A/\bar{U}$ can be attempted, since in many cases at fixed values of f and Re, runs were made at various sound pressure levels (see Figures 19, 20 and 21). We note that at higher Reynolds numbers, say Re > 40,000, the limitations of the electromagnetic horn driver system prevent values of $\hat{U}_A/\bar{U}$ greater than about 3 from being attained, and hence this data is of limited use in comparison with high-amplitude data taken in rocket motors and in the present author's apparatus. As mentioned above, in Section 5, attempts will be made to correlate heat transfer data from various sources, including the data discussed above.

We now discuss some theoretical results presented in References 1, 2 and 3. References 1 and 2 discuss the velocity fields in laminar channel and pipe flow respectively. We briefly discuss the simplest case, that of Reference 1 (channel flow). The problem is that of a time-average laminar channel flow with a superimposed pressure field which varies sinusoidally with time and with x-dimension (a standing-wave system). Restrictions applied to the range of validity of the solution given are (using our notation):-

$$\frac{2\bar{U}}{\hat{U}_A} = o(\delta) \tag{26}$$

$$\frac{\hat{U}_A}{2c} = o(\delta) \tag{27}$$

$$2\frac{D}{\lambda} = o(\delta) \tag{28}$$

where δ = a small number.
and D = channel width.

The method of solution is as follows: The two momentum equations and the continuity equation are used. A time varying momentum equation

in the x-direction is reduced by an order of magnitude analysis and an assumption of periodicity in time and x-dimension o an ordinary differential equation in one dependent variable. This equation is solved to yield the unsteady component of the U velocity. Using the velocity so obtained, and density obtained using the isentropic relation and the known pressure field, the unsteady component of the V velocity is obtained from the time-varying continuity equation. Using again, order of magnitude reductions, now on a time average momentum equation in the x direction, and using the previously obtained time-varying velocities to aid in the evaluation of terms such as $\overline{UU}_x$, a solution for the time average U-velocity can be obtained. Using the time-average continuity equation a solution for the time average V-velocity is obtained. The nature of the time average velocity fields produced are shown in Figure 23 and 24. These figures show the time-average stream lines, and are taken from Reference 2, which treats the case of pipe flow, rather than channel flow; however, the nature of the secondary flows produced are very similar in the two cases. We have added arrows on some stream lines, the letters V.A. and V.N. at velocity antinodes and nodes, and have altered the parameters to our notation. In addition to the large vortex shown in Figure 23, there are present, two very thin vortices near the walls as shown in Figure 24. (δ_{AC} for most cases is very much smaller than the channel or pipe diameter). It is to be noted (from References 1 and 2) that the flow fields obtained, non-dimensionalized with respect to the mean flow velocity, depend (except for the thin wall vortices) only on the parameter $(\hat{U}_{A}/\bar{U})^{2}_{M}$, and particularly, do not depend on Re.

These secondary flows are an example of the acoustic streaming phenomena. The equations giving the acoustic streaming velocities in Reference 1, will be used in a discussion (See Section 5) of attempts to detect acoustic streaming in the test rig of the present investigations.

In Reference 3, a solution for heat transfer in laminar channel flow is presented. The channel wall conditions are:

$$\text{wall temperature} = T_0, \quad x < 0$$

$$\text{wall temperature} = T_w, \quad x > 0$$

The problem is mathematically, a steady-flow problem; the velocity field used is the time-average velocity field obtained from the solution

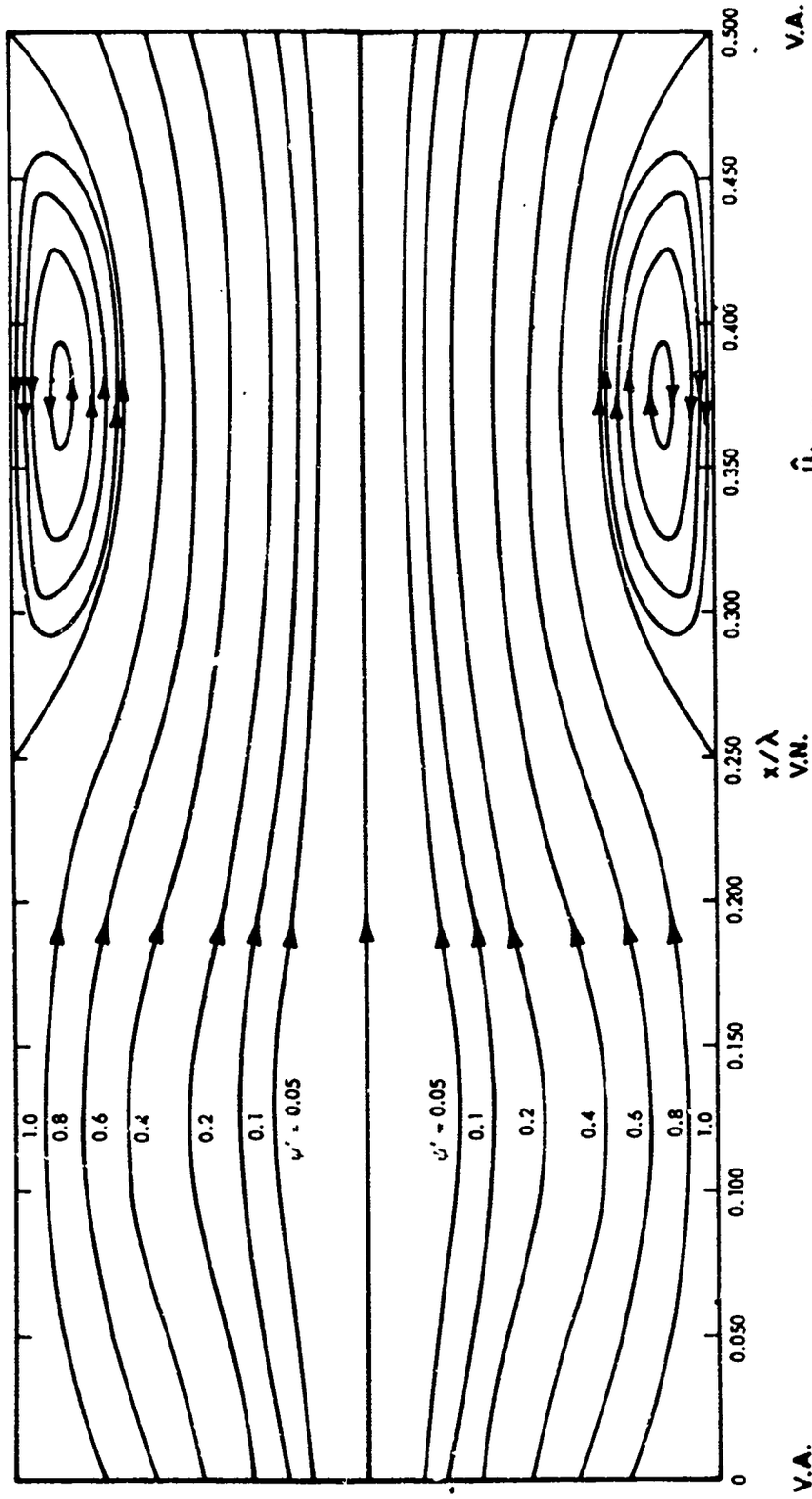

Time-Mean Stream Function for $\left(\frac{\hat{U}_A}{U}\right)^2 M = 13.3$

FIGURE 23

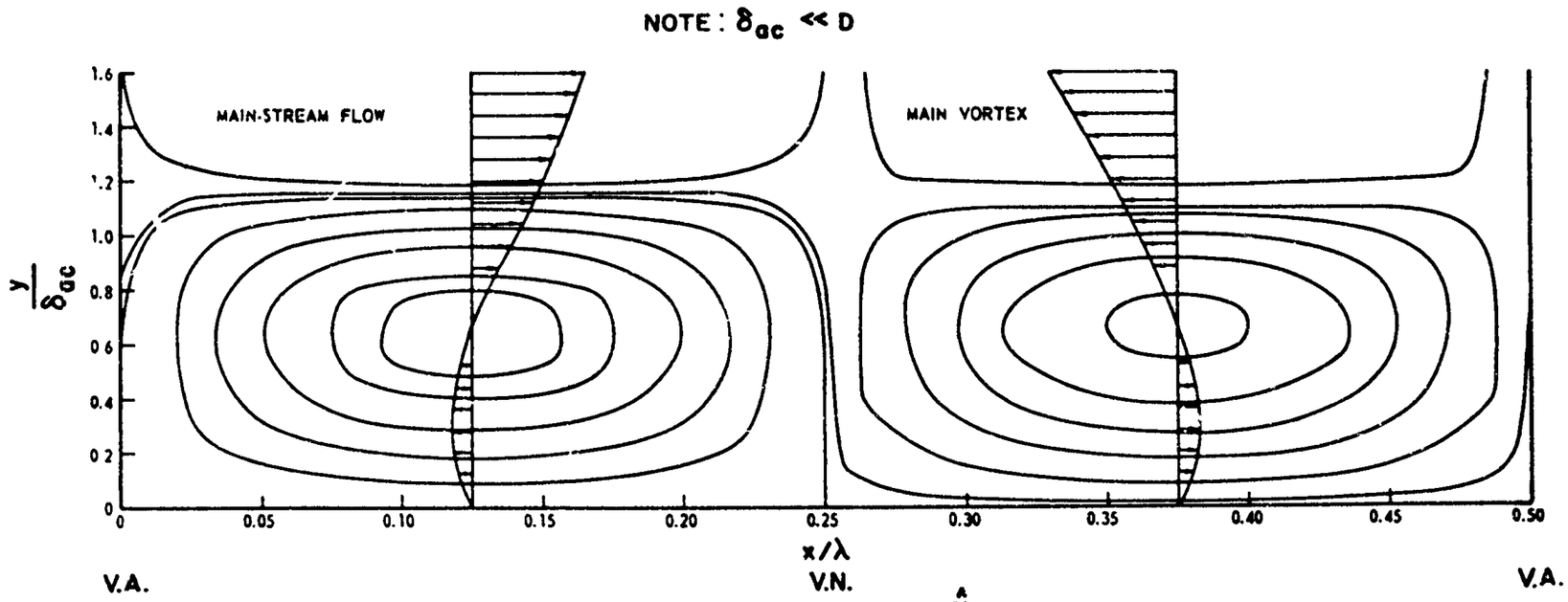

Time-Mean Stream Function for $(\frac{\hat{U}_A}{\bar{U}})^2$ M=13.3 Showing Details of the Wall Vortices.

FIGURE 24

in Reference 1 (discussed above). Thus the time-varying velocities in the actual physical system are not included in this treatment; the changes in heat transfer calculated only include the effect of the oscillation - induced time-average secondary flows. The time-average energy equation is reduced to the form

$$\rho C_p U \frac{\partial T}{\partial x} + \rho C_p V \frac{\partial T}{\partial y} = K \frac{\partial^2 T}{\partial y^2} \qquad (29)$$

(all quantities are time-averaged), and solved by a finite-difference method. The solution was found to be divergent in regions with $U < o$ (reverse flow, in vortices, see Figure 23); the authors avoided this problem by setting $U = o$ in Equation (29) where U was actually negative. This technique appears to have been satisfactory, since the resulting heat transfer curves obtained show no discontinuities and also some of the above finite difference solutions were checked by a relaxation technique which showed no significant errors in heat transfer. The nature of the results so obtained are shown in Figure 25 taken from Reference 3. The time average streamlines are sketched at the top of this figure, and the shaded regions at the bottom of the figure indicate the ranges of x where, for some y-values, the approximation $U = o$ discussed above was used. We observe that the maxima of heat transfer are slightly downstream of the nodes, and that there is little overall change in heat transfer. From their theoretical calculations, the authors have also found the correlation shown in Figure 26 . This correlation shows a linear relationship between the product of the maximum fractional change in heat transfer multiplied by $Re^{-1/3}$ and the parameter

$$\left(\frac{\hat{U}_A}{\bar{U}} \right)^2_M$$

No statement is given in Reference 3 on what value of Pr applies in Figure 26 , but since to obtain the acoustic streaming velocity fields used in the heat transfer analysis, a compressible fluid was used, we shall assume that Figure 26 may be applied to fluids such as air with $Pr \approx 0.7$. Both the nature of the heat transfer changes (Figure 25)

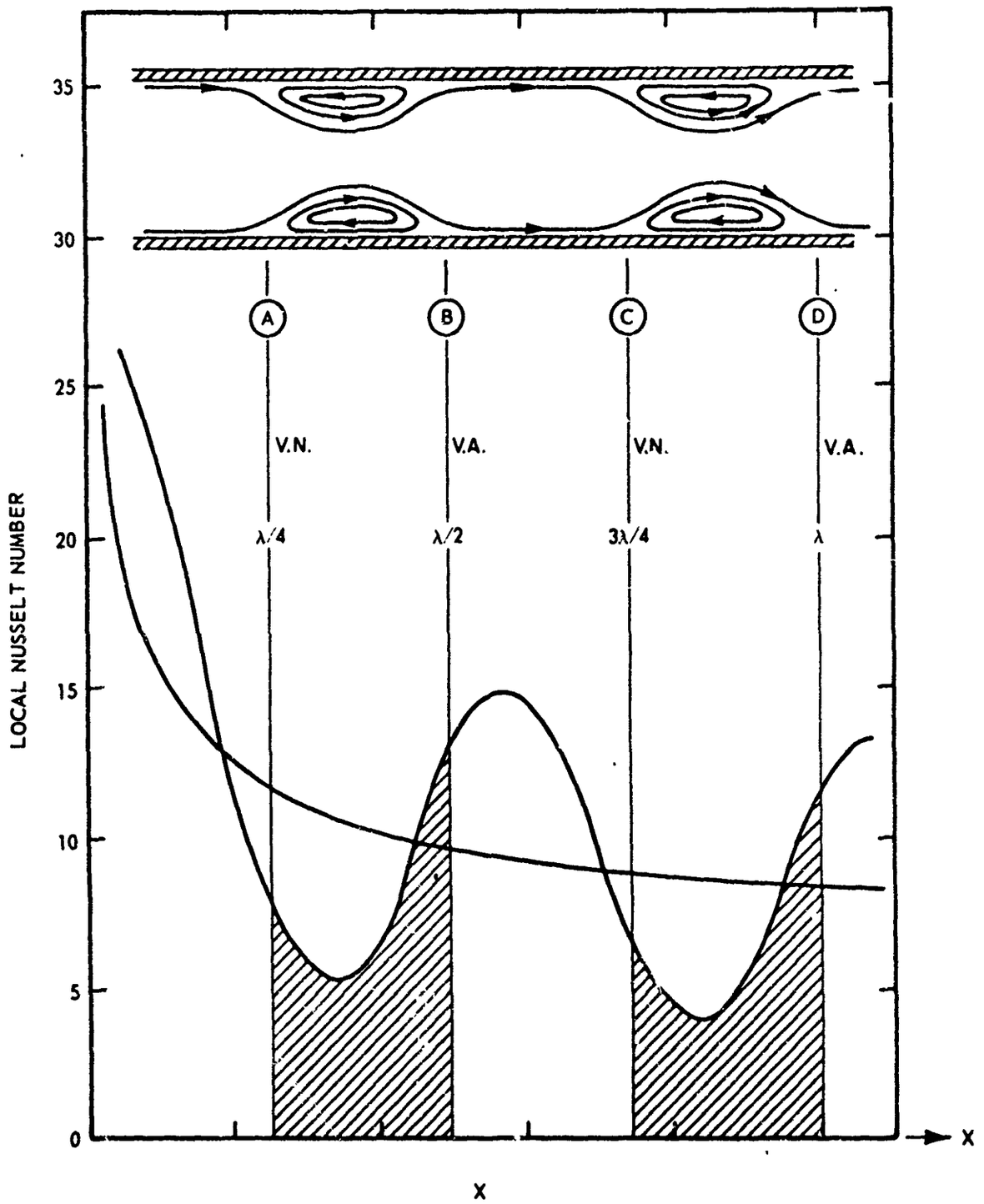

Local Nusselt Number Versus x Showing Relation of Heat Transfer and Velocity Field and Regions of Approximation.

FIGURE 25

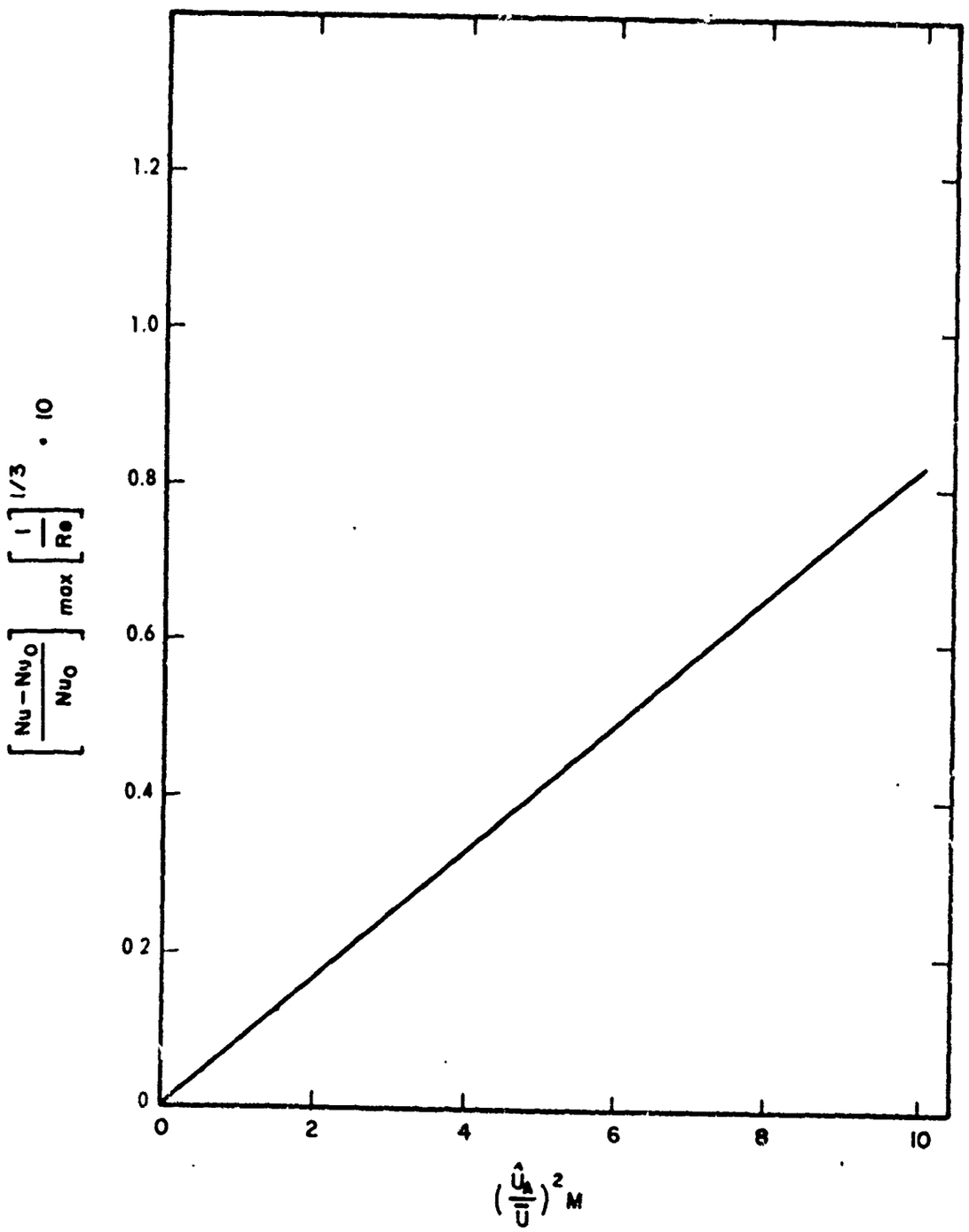

Correlation of Maximum Deviation from No Sound Nusselt Number.

FIGURE 26

and their magnitudes (Figure 26) as predicted by the above theoretical analysis, will be used in Section 5.2 in attempts to estimate the importance of acoustic streaming in explaining changes of heat transfer under oscillating conditions, as observed in various experimental investigations including the present author's.

In Reference 24, heat transfer measurements were taken in a rocket motor 3 in. dia. by 31 in. long. The propellants were O_2 - N_2H_4 at a mixture ratio (mass flow oxidizer/mass flow fuel) of .36, and a chamber pressure ($\bar{P}$) of 300 psia. was used. Throat diameter was .875 in. Heat transfer (and time varying pressure-) measurements were taken using water-cooled 'Dynisco' strain gauge type pressure transducers located at varying axial positions along the chamber wall. The cooling water flows in a spiral channel just underneath the transducer diaphragm and heat transfer is measured using thermocouples to measure the cooling water temperature rise across the transducer. The gas properties are estimated as follows: a typical rocket combustion gas value of γ ($\approx$ 1.22) is assumed. The gas molecular weight is calculated assuming complete conversion to H_2O, N_2 and H_2 ($\approx$ 14.5 lbm/lbm mole). The speed of sound ($\approx$ 4180 ft/sec) is taken from a commercially available table. The gas temperature and density are then estimated from Equations (30) and (31) below respectively:

$$c^2 = \frac{\gamma RT}{m} \tag{30}$$

$$\rho = \frac{P}{RT} \tag{31}$$

From a report by Bartz, an approximate formula for calculating the viscosity of rocket combustion gases is used to estimate μ . From these data, we compute $M \approx .050$, $Re = 161{,}000$. Heat transfer and pressure data were taken both for stable operation and unstable operation at the first longitudinal mode of oscillation (fundemental of a closed-closed organ pipe). Taking $\lambda = 2x31 = 62$ in., the above calculated speed of sound and M values, the Strouhal number is calculated as $S \approx 6.0$. The heat transfer data for stable and unstable operation are shown in

Figure 27 taken from Reference 24 . The value of $\hat{P}_N$ (actually measured $\sim$ 1.5 in. from the injector face) is 145 psi. We note that the fractional heat transfer increases are very large being of the order of 0.6 at the transducer locations near the velocity nodes, increasing to $\sim$ 1.8 at the velocity antinode. Several points should be borne in mind in comparing this data to that of previous references. One point is the fact that the fractional pressure fluctuations ($\hat{P}_N/\bar{p}$) are large enough (unlike those in most of the previously discussed references) to introduce substantial non-linear effects. However, much more serious is the fact that the wave system (as is also shown in Reference 24) is basically one of shock waves, followed by exponential rarefactions, and the effect of these waves upon the turbulence and the boundary layer may be much different than that of smooth waves (even if quite distorted from pure sine waves) of the same amplitude. Other effects of the shock waves as opposed to sinusoidal or near sinusoidal waveforms are the facts that at the 'pressure node' (midway along the chamber) $\hat{P}$ still has a large fraction of its value at the antinodes (in this case about 65%), and that correspondingly, $\hat{U}$ is still a large fraction of $\hat{U}_A$ quite near to the 'velocity nodes', (though $\tilde{U}$ is much smaller than $\tilde{U}_A$ at these points). In view of the above facts, an estimate of $\hat{U}_A$ computed from $\hat{P}_N$ using the simple acoustic formula will be somewhat inaccurate; but it will give some idea of the value of $\hat{U}_A/\bar{U}$ in the rocket engine. The value of $\hat{U}_A/\bar{U}$ so calculated was 7.90.

Another point to be borne in mind is that in the rocket motor, $\frac{T_w}{T} \not\approx 1$, and hence the gas properties vary considerably through the boundary layer. Also, since L/D for the chamber is $\approx$ 10, flow would not be expected to be fully developed thermally and hydrodynamically on the chamber; perhaps rather than comparing the rocket motor data with fully developed pipe flow data, a more profitable comparison might be made with data from a flat plate or from regions of simultaneous thermal and hydrodynamical development in pipe flow. Even the above suggested comparisons may be difficult, since the flow does not start

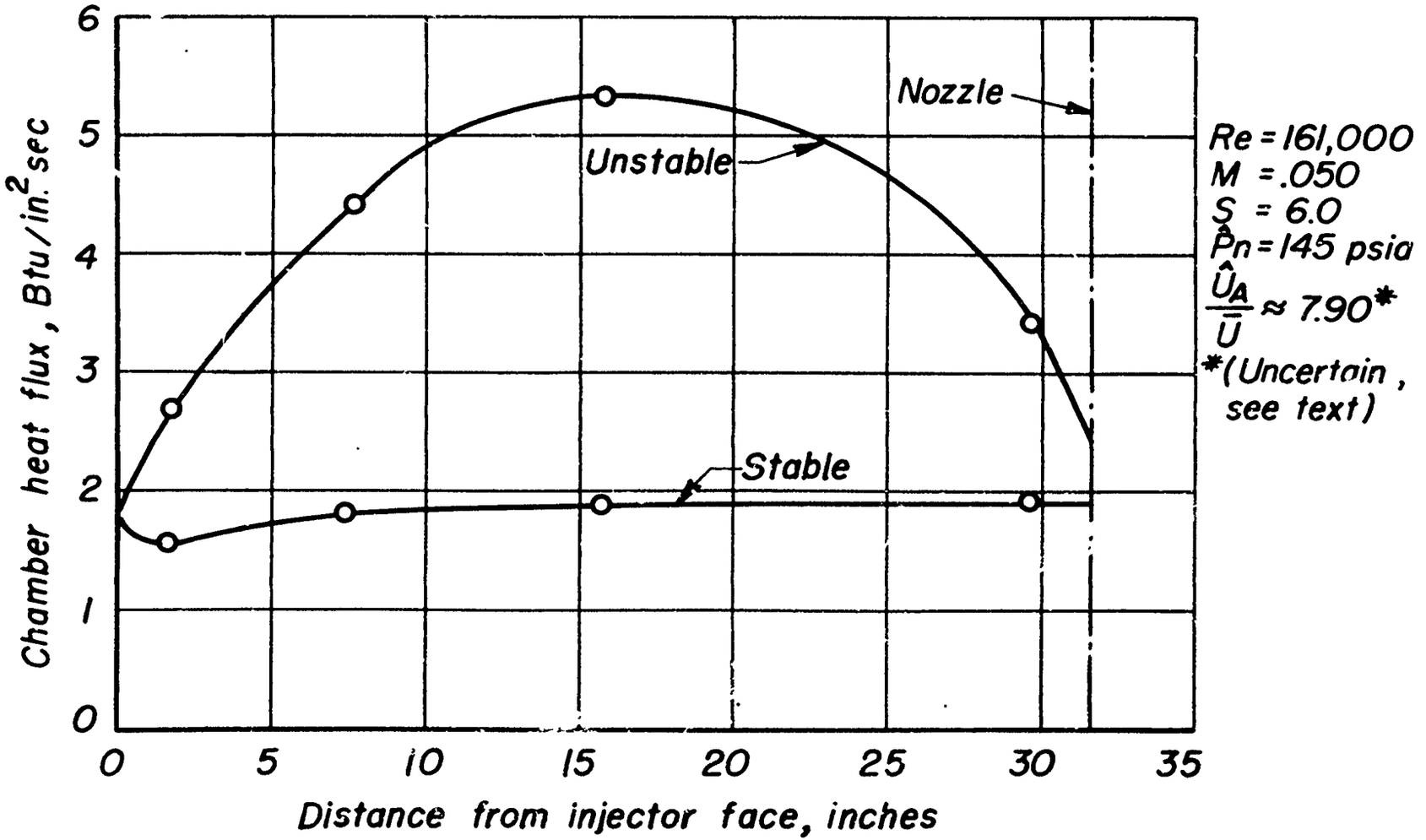

Figure 27

Comparison of stable and unstable operation under similar conditions of length and mixture ratio using showerhead injector, hydrazine-oxygen

at the injector face with essentially the same mean velocity and temperature found further downstream, but rather over the first 10 inches of the chamber, the temperature and gas mass flow increase as the injected liquid propellants are vaporized and burn. The above mentioned points make correlation of the rocket motor heat transfer results with that of the other references difficult, but some attempts will be made, and further discussion is given in Section 5.5 .

Data from another series of runs (also presented in Reference 24) is now discussed briefly. This data was taken in the same motor as that described above, but the addition or subtraction of cylindrical segments of the motor allowed the motor length to be varied. The data discussed here was taken with lengths of 22, 32 and 48 in. The propellants were O_2-N_2H_4 as before, but the mixture ratio is now 1. Chamber pressure was 300 psia and the amplitude of the oscillations (measured about 1.5 in. downstream of the injector face) was 48 psi rms, I.E. $\tilde{P}_N \approx 48$ psi. (The oscillations again occur in the first longitudinal mode). Heat transfer was measured with the same transducers described above, now located in all cases 3 in. upstream of the nozzle. Re, M, S $\hat{U}_A/\bar{U}$ were calculated as previously, and the resulting data is given in Table 11.

TABLE 11

Chamber Length In.	$\frac{x}{D}$* In.	S	Fractional Change in Heat Transfer
22	6.33	8.28	1.44
32	9.57	5.75	1.20
48	15	3.85	.74

Re = 93,700
M = .0503
$\tilde{P}_N$ = 48 psi
$\frac{\hat{U}_A}{\bar{U}}$ = 7.40 (Estimated, See Text).

In this case, the estimate of $\hat{U}_A/\bar{U}$ may be even more inaccurate than in the previously discussed case, since we have assumed that $\hat{P}_N \approx 2\sqrt{2}\,\tilde{P}_N$, as well as the simple acoustic relation between $\hat{P}_N$ and $\hat{U}_A$. However, again, this figure does give some idea of the value of $\hat{U}_A/\bar{U}$.

* x is the distance of the heat transfer measuring transducer downstream of the injector face.

We see from Table 11 that as the chamber becomes longer and the transducer moves closer (relative to λ) to a velocity node, that the heat transfer increase drops, thus showing the same trend as in Figure 27.

In Reference 31, Koshkin investigated heat transfer to air flowing in an electrically heated tube of 9.7 mm inside diameter. Local heat transfer measurements were taken at various points over a heated section 185 diameters long. The Reynolds number range was 10^4 - 10^5. The air was roughly at room temperature and the air pressure range was 5-20 x 10^5 n/m^2 (72-290 psia). Oscillations were generated by a rotating valve upstream of the heated section. From a sketch in Reference 31, there appears to be a calming section of perhaps 10-20 diameters length between the rotating valve and the entrance to the heated section of the duct. Slightly downstream of the heated section is a throttle. The rotating valve is operated at a resonant frequency of the duct, which appears to act as a closed-closed organ-pipe, the valve and the throttle acting as the closed ends. Data was taken at the fundamental and second through fifth harmonic frequencies of the duct (f = 90, 180, 270, 360, 450 cps.). Only data taken at the third harmonic is presented in the paper, however. Much data in this paper suggests that there is considerable attenuation of the wave strength as one moves away from the rotating valve. Hence, although organ-pipe resonances of the duct were used, there may be a significant proportion of travelling waves present in the duct. Koshkin's data for the third harmonic frequency of the duct is reproduced in Figure 28. Here, K is the unsteady flow Nusselt number divided by the Nusselt number in the reference steady flow. We note the following: (1) the overall decline in the heat transfer increases as one moves downstream may be an effect of attenuation of the wave; this is suggested in the text, and (2) the fractional changes in heat transfer are quite large, and therefore this data is of interest to the present author. However, correlation attempts using this data are not possible, since the particular Reynolds number and mean pressure values relevant to each curve of Figure 28 are not given; we are only told that all Re values lie between 10^4 and 10^5 and that all mean pressures are between 5 x 10^5 and 20 x 10^5 n/m^2. Also,

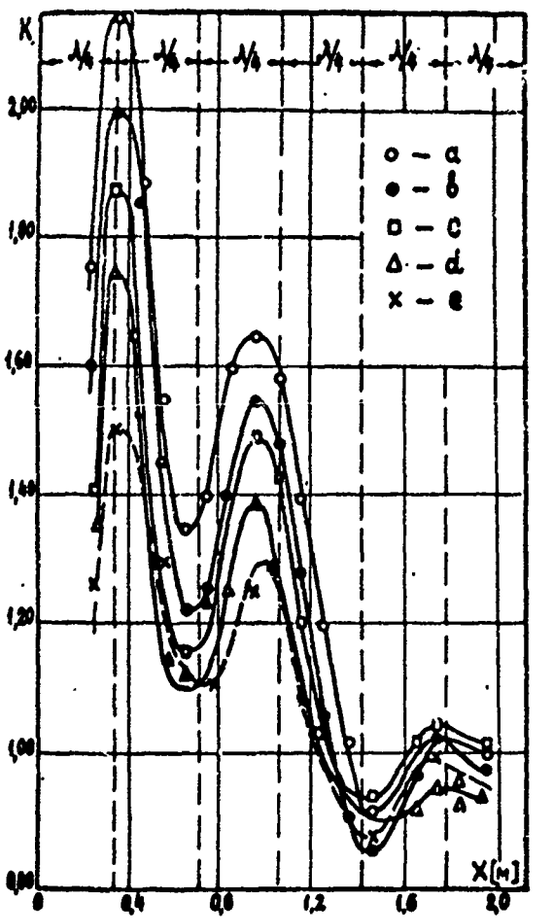

Heat transfer distribution (K) along the experimental tube with n=3 for various values of $(\frac{f}{f})_o$; Re= $10^4 \div 10^5$; a-$(\frac{f}{f})_o$=0.225; b -$(\frac{f}{f})_o$=0.184; c -$(\frac{f}{f})_o$=0.11, d -$(\frac{f}{f})_o$= 0.090, e -$(\frac{f}{f})_o$ = 0.054.

Figure 28

there is some doubt as to whether Koshkin's symbol $(\frac{\Delta p}{\bar{p}})_o$ (see Figure 28) refers to the peak-to-peak pressure at the duct inlet divided by the mean pressure or half this value. For the above reasons, little use can be made of this data. The present author attempted unsuccessfully to communicate by letter with Koshkin to ask for additional information.

3. EXPERIMENTAL HEAT TRANSFER MEASUREMENTS IN AN OSCILLATING FLOW SYSTEM

Experimental heat transfer measurements in an oscillating pipe flow system are now presented. (A discussion of the literature on the problem of heat transfer in oscillating flow is presented in Section 2 .) A brief description of the apparatus is given first.

3.1 General Description of the Apparatus:

An overall sketch of the apparatus is given in Figure 31 . From the high pressure supply ($\sim$ 2000 psig), the air is passed through a coil submerged in a thermostatically controlled water bath (a commercial hot-water heater) in order to feed constant-temperature air to the remainder of the system. The air then passes to a 0-500 psig regulator which feeds the upstream side of a calibrated sonic orifice (5 different orifices are available). Just upstream of the orifice are a copper-constantan thermocouple and a static pressure tap leading to a bourdon-tube guage to enable the mass flow through the orifice to be calculated. The flow then passes inco a plenum chamber (at 40 psig) and from the plenum into the 9 ft length of 1.5 in I.D. pipe in which the oscillations are set up. The average static pressure in the pipe is measured at the upstream end of the pipe using a line leading to a bourdon-tube gauge. A restriction in the line at the pipe enables the guage to take an average pressure reading under oscillating conditions. Just upstream of the steam heated section a copper-constantan thermocouple measures the air temperature. It should be pointed out that the section of pipe upstream of the heated section is uninsulated. However, the setting of the thermostat in the water bath is adjusted so that the air temperature in this section of the pipe is within $30^{\circ}F$ of the ambient (room) temperature. This small temperature difference together with the high thermal resistance of the natural convection boundary layer on the outside of the pipe, reduces heat transfer to the air flow in this section of the pipe to very low values. Hence, as has been experimentally verified, the temperature profile at thermocouple A (Fig.31) is almost perfectly flat, and a single thermocouple reading at the center-line of the pipe gives a very good estimate of the air bulk temperature at this point. Calculated estimates of the heat transfer to the air flow in the upstream unheated section of pipe indicate this to be completely negligible. After passing through the steam-heated

Figure 31

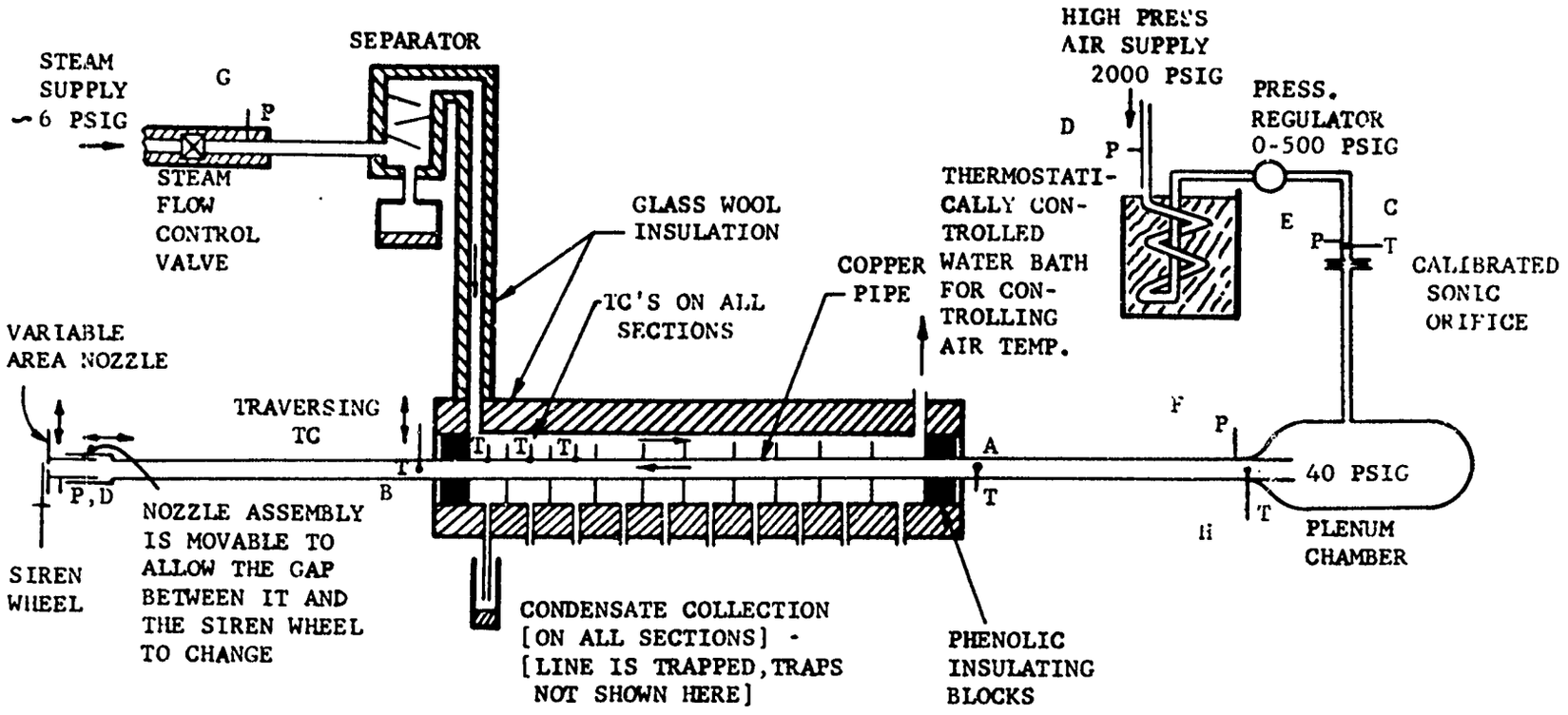

TC = THERMOCOUPLE
T - COPPER-CONSTANTAN THERMOCOUPLES (LINES CONNECTED TO MAIN CONTROL PANEL)
P - TAKE-OFF POINTS FOR LINES LEADING TO BOURDON-TUBE PRESSURE GAUGES
P,D - STRAIN GAUGE TYPE PRESSURE TRANSDUCER TO MEASURE THE STRENGTH OF THE OSCILLATIONS

section, the air flow passes through another unheated section of pipe and exhausts through a variable-area choked nozzle to ambient conditions. A copper-constantan thermocouple is traversed across the airflow just downstream of the heated section in order to determine the air bulk temperature at this point. The average flow conditions are set using the variable area nozzle and the 0-500 psig pressure regulator as follows: the pressure on the upstream side of the calibrated sonic orifice is adjusted to produce the desired mass flow using the 0-500 psig pressure regulator; then the variable area nozzle is adjusted to bring the mean pressure in the pipe and plenum chamber to the desired value (40 psig). The siren wheel is just downstream of the variable area nozzle, and parts of the holes in the siren wheel, together with parts of the nozzle assembly act as the nozzle throat, which thus changes its area as the wheel rotates. This action induces the oscillating component of the flow. In operation the siren wheel is rotated so as to be in resonance with one of the organ-pipe frequencies of the 9 ft length of pipe. The siren wheel is driven through a timing belt system by a 15 HP U.S. Electric Motors 'Vari-drive' Motor (3-phase, 440 volt). This motor consists of an electric motor which can be driven at two different constant speeds, a system of 2 variable-width pulleys and a belt, a gearbox and control equipment. The output speed of the motor is adjusted by operating a small electric speed-change motor which changes the widths of the pulleys. The direct output of the motor gearbox is variable over a speed range of $\sim$ 8 to 1 . The timing belt system provides additional speed reductions of 1:1, 3.43:1, and 11.76:1 . Also siren wheels with 2, 4, and 28 holes are available. The total range of the siren frequency is roughly 5-5000 cps.

The gap between the downstream surface of the variable area nozzle assembly and the siren wheel can be changed to allow the strength of the oscillation (at resonance) to be varied (Fig.31). I.E., when the gap is at its minimum value ($\sim$ .019 in) the strength of the oscillations produced is at its greatest value (other things being equal).

Just upstream of the variable area nozzle is a Norwood strain-guage type pressure transducer which is used to determine the amplitude of the pressure fluctuations in the pipe (P,D - Fig.31).

From a supply of steam at $\sim$ 6 psig, steam flows through a flow control valve, and a separator into the steam chest surrounding the copper

pipe (1.5 in. I.D. x 1/16 in wall) carrying the airflow. The pressure gauge attached just downstream of the flow control valve enables the proper steam flow to be set. The steam heated section of the pipe is 45 7/16 in. (= 30.3 Dias.) long divided into 25 chambers as sketched in Fig. 32. After passing through the steam chest, the steam is exhausted to ambient conditions at the upstream end of the heated section. The steam heated section is insulated on the sides with about 2 in. of glass wool insulation, and on the ends with phenolic plastic blocks 2 in. thick (Figs. 31,32,33). From each of the 25 condensate collection chambers a trapped line leads to a bottle in which the condensate is collected (Figs. 31,34). Midway between the partitions in each chamber on the side of the copper pipe, is a copper-constantan thermocouple used to measure the local pipe temperature (Fig. 31,34). (The copper pipe is used as one wire of the thermocouple; hence, leading out of the steam chest there are 25 constantan wires and 1 copper wire.) Upstream of the heated section is an unheated section 49.05 (= 32.7 Dias.) long. As discussed on p.63 , this upstream section may be regarded as insulated, since a negligible amount of heat transfer to the airflow takes place in this section.

3.2 Instrumentation

3.2.1 Thermocouples

All thermocouples are copper-constantan, referenced to ice cold junctions. Lines from the 25 thermocouples measuring the local pipe wall temperature (Figs.31,34) are brought out through a switching system at the main control panel, and the voltages are measured on a hand balanced potentiometer. The apparatus proper is in an enclosed cell. The control panel and operators are in a separate room; this greatly reduces the sound level to which the operators are subjected. From the airflow thermocouples (Fig.31, TC's A,B,C) lines are run through another switching system to a Leeds and Northrup 'Speedomax' chart recorder where the voltages are recorded on chart paper. For the traversing thermocouple (Fig.31, TC B), the radial position is determined as follows: the thermocouple is moved downward until it touches the bottom of the pipe (this is determined electrically), then readings are taken 0.1 in. above this point and at 0.1 in. intervals (16 readings) as the TC is moved upward across the pipe diameter. The position

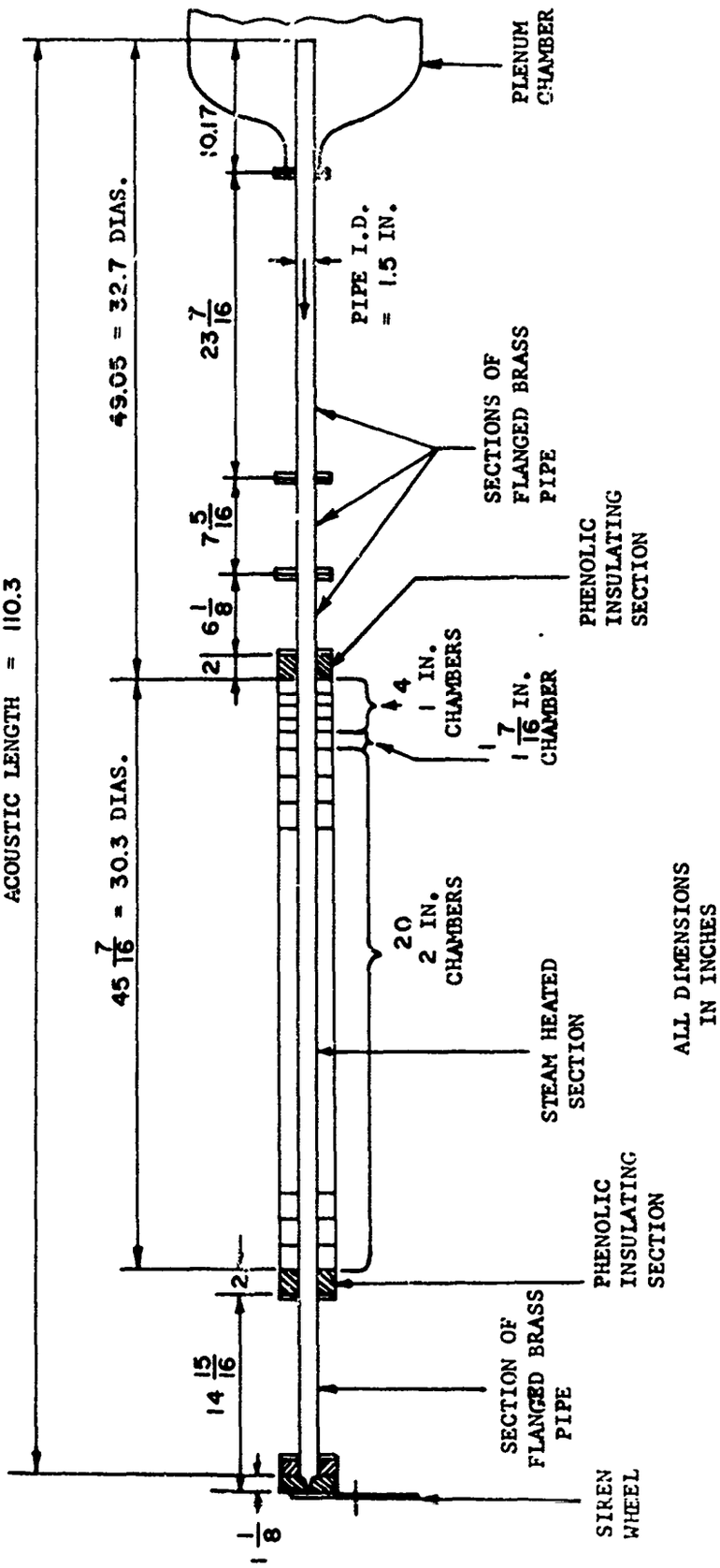

Figure 32

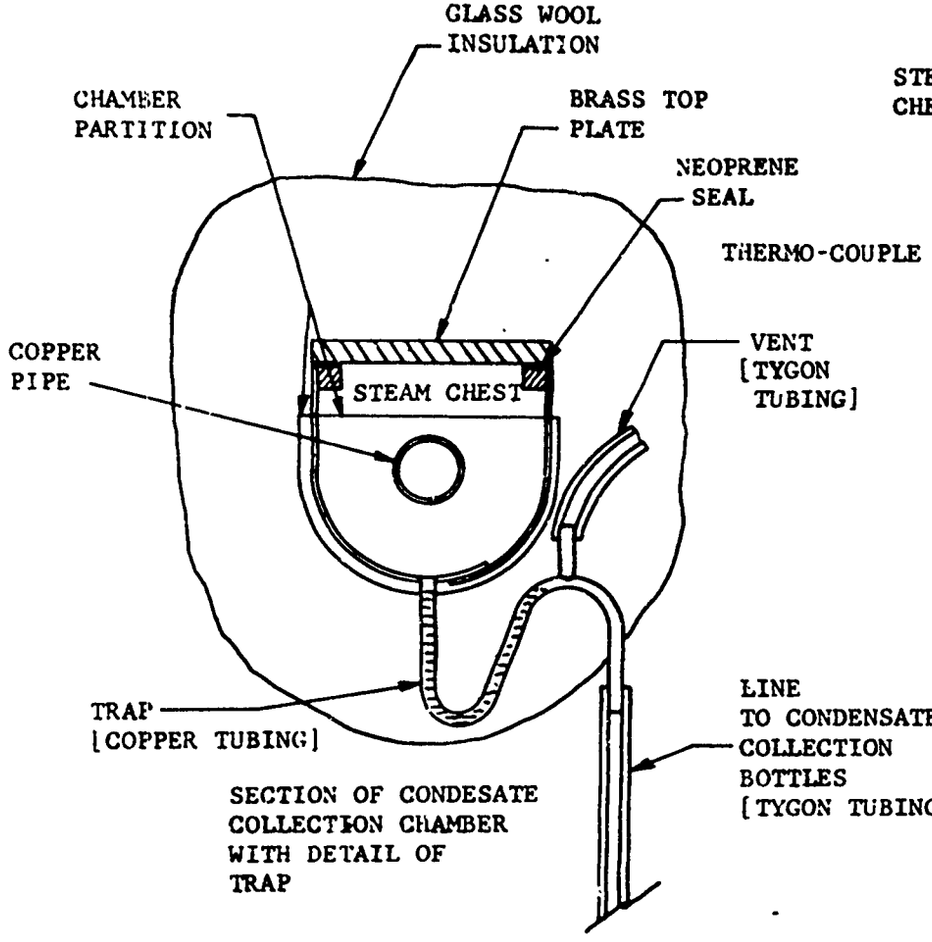

Figure 34

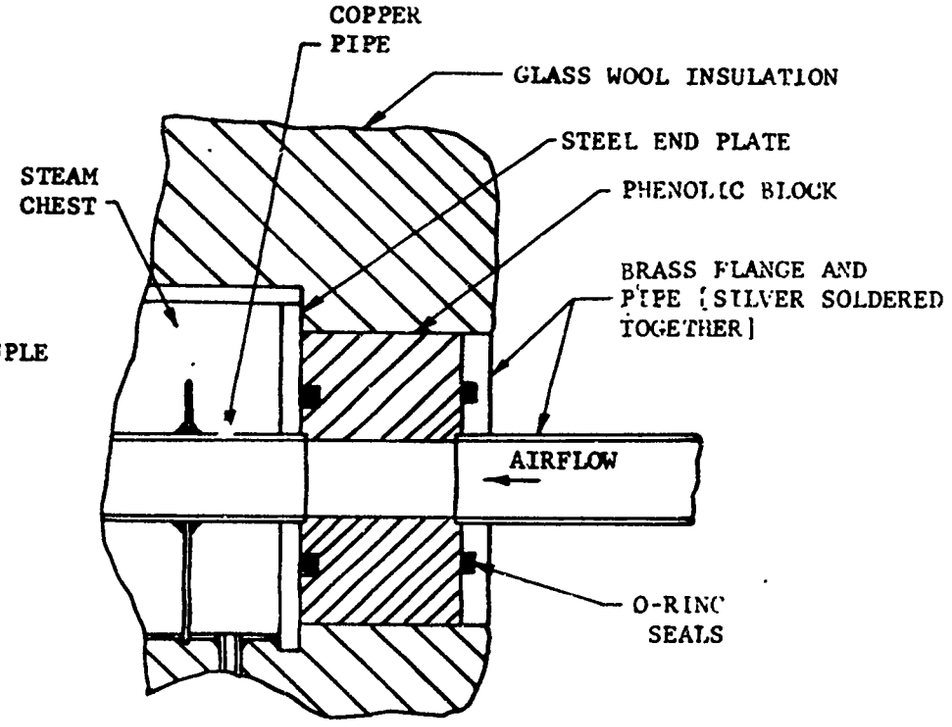

SKETCH OF UPSTREAM PHENOLIC INSULATING BLOCK [DOWNSTREAM BLOCK IS VERY SIMILAR]

Figure 33

of the TC is determined using a scale and a reference mark. The operator traversing this thermocouple, is of course in the test cell during the traverse and wears ear defenders as protection against the high sound level.

3.2.2 Condensate Measurement

The volume of condensate in each bottle is measured by pouring the condensate into a graduated cylinder. The temperature of the condensate ($\sim$ room temperature) in 3 or 4 of the bottles is measured using a mercury thermometer.

3.2.3 Steady Pressure Measurements

Pressure taps D, E, and F (Fig.31) lead to bourdon-tube gauges of ranges 0-3000, 0-1000 and 0-100 psig respectively on the main control panel. Pressure tap G (Fig.31) leads to 0-100 in/H_2O gauge in the test cell.

3.2.4 Dynamic Pressure Measurement

Measurement of the amplitude of the pressure fluctuations is taken just upstream of the siren wheel (P,D - Fig.31) using a Norwood Controls Model 101, 0-500 psig air cooled pressure transducer. This transducer is a 2-arm bridge strain gauge type transducer with the two elements wound circumferentially and axially on a strain tube. The circuit directly associated with the transducer (bridge circuit) is sketched in Fig.35 . B_2 supplies the excitation voltage (45 V.) to the bridge. The bridge current is adjusted to the proper value with R_4 and R_5, referring the voltage drop across R_6 and R_7 to the 1.35 V. mercury cell reference (B_1), using the galvanometer. The bridge is balanced using R_1 and the galvanometer. The output of this circuit is fed to a 4-transistor A.C. amplifier with gain of $\sim$ 1000 . The output of the transistor amplifier is fed to a Ballantine model 320 S/5 true rms meter. The bridge circuit and transducer were calibrated by applying pressures from 0-500 psig to the transducer with a dead weight tester, and recording the output of the bridge circuit on a Leeds and Northrup 'Speedomax' chart recorder. The gain of the transistor amplifier and the loading effect of its first stage on the bridge circuit at the frequency of interest ($\sim$270 cps; this is the frequency of the 9th harmonic of the 9 ft. length of pipe. Most of the heat transfer measurements were taken at this harmonic.) is as follows. Battery B_2 was replaced by an audio oscillator operating at 270 cps,

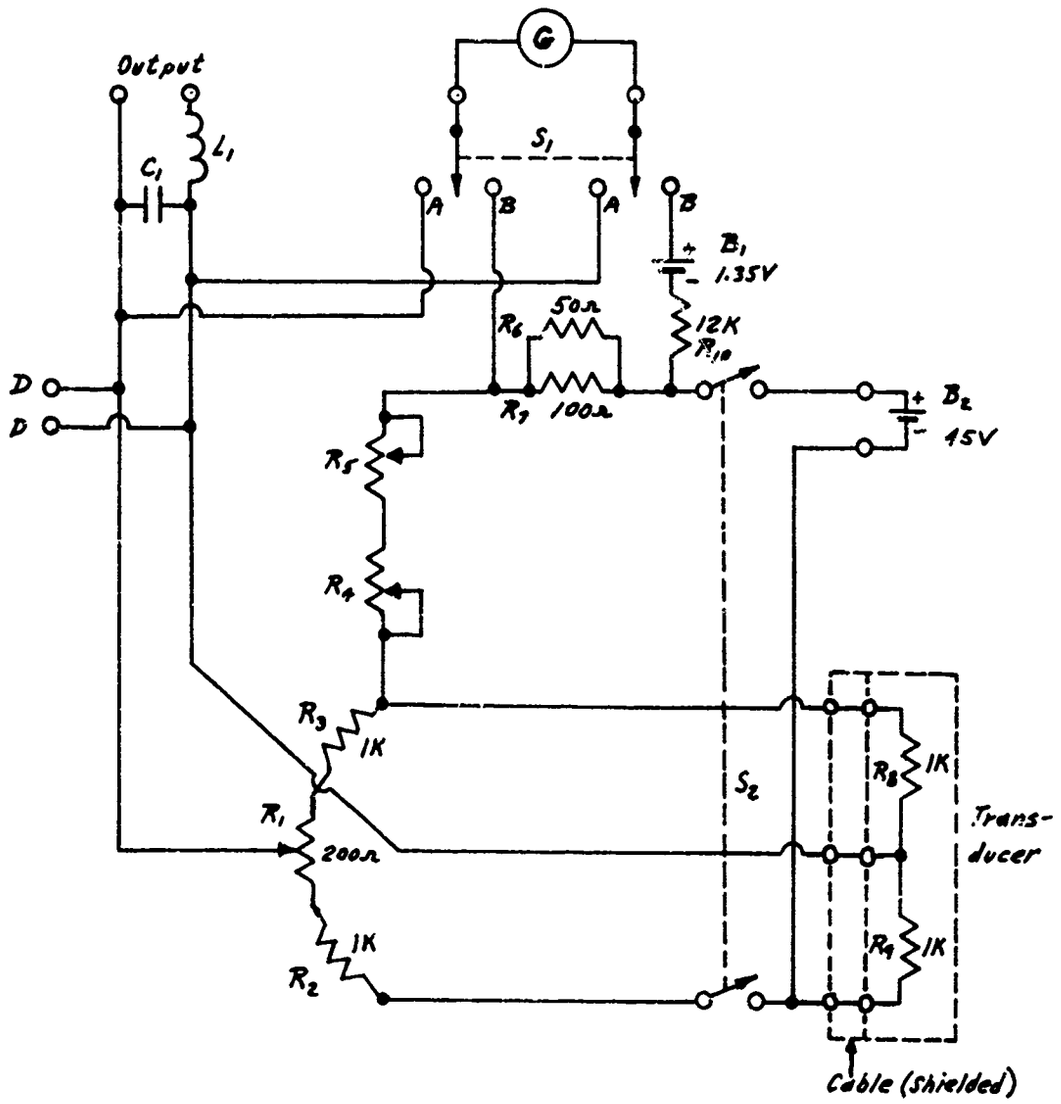
Output
L1
C1
G
S1
A
B
A
B
B1
1.35V
50Ω
R6
12K
R10
D
D
R7 100Ω
B2
45V
R5
R4
R3
1K
R1
200Ω
R2
1K
S2
R8
1K
R9
1K
Trans-
ducer
Cable (shielded)

FIGURE 35

and an amplitude which gave A.C. bridge output voltages similar to those observed under normal conditions (D.C. excitation, oscillating flow in the pipe). The following rms voltage measurements were taken using the Ballantine rms meter:

(1) Voltage at bridge circuit output (points D, Fig.35) with amplifier disconnected.

(2) Same with amplifier connected.

(3) Voltage at amplifier output.

Readings (1) and (2) give the loading effect of the amplifier on the bridge circuit. Readings (2) and (3) give the gain of the amplifier. All signals were checked with an oscilloscope; no noise signals large enough to cause significant errors in the rms readings were observed. All ranges of the Ballantine rms meter used were checked using a thermocouple rms meter and voltage dividers; the maximum error found was $\sim$ 2% and the error was usually less than 1%.

The method of computing the overall sensitivity of transducer + bridge circuit + amplifier is illustrated with values from an actual calibration:

Sensitivity of transducer and bridge circuit (unloaded) measured using dead-weight tester = .0811 MV/psi

Rms voltage readings at 270 cps (see above):

(1) .414 MV rms

(2) .382 MV rms

(3) .381 V rms

Hence the sensitivity of the transducer and bridge circuit (loaded) at 270 cps is:

$$\frac{.0811 \times .382}{.414} = .0749 \text{ MV/psi}$$

Gain of amplifier at 270 cps is:

$$\frac{.381 \times 1000}{.382} = 997$$

Sensitivity of transducer, bridge and amplifier at 270 cps is:

$$.0749 \times 997 = 74.6 \text{ MV/psi}$$

We are here assuming that the sensitivity of the transducer and bridge circuit is the same for D.C. and 270 cps A.C. The dynamic sensitivity (at $\sim$ 270 cps) of these elements has been checked against a Kistler piezoelectric transducer (by mounting the two transducers on the opposite sides of the pipe in which oscillations were set up) and has been found to agree well with the static sensitivity. Hence, the procedure outlined above has been used to calibrate the Norwood pressure transducer system.

3.3 Operation (Ref. to Fig. 31 for pieces of equipment described in this section)

The operating procedure for the apparatus is now briefly described. First the steam flow rate is set to the required value using the steam flow control valve. (Too low a rate cannot supply all the chambers; too high a rate can raise the steam chest pressure high enough to blow the water out of the traps.) The water bath temperature control system and the airflow are next turned on. The mass flow of air is set using the 0-500 psig pressure regulator and the pressure in the pipe is adjusted with the variable nozzle. The following electrical gear is then turned on and allowed to warm up:

(1) A Leeds and Northrup 'Speedomax' chart recorder, used to record the readings of thermocouples A, B, and C (Fig. 31). (See Section 3.2.1).

(2) The transistor amplifier used with the Norwood pressure transducer and bridge circuit. (See Section 3.2.4 , and Fig. 31 , - P,D)

(3) A Ballantine model 320 S/5 rms meter used to measure the rms amplitude of the output of the pressure transducer - bridge circuit-amplifier system (see Section 3.2.4).

The apparatus is then allowed to run for $\sim 1\frac{1}{2}$ hours to come to thermal equilibrium. The siren is then turned on and the average pipe pressure reset with the variable area nozzle. (This is necessary since turning on the siren reduces the average effective area of the variable area nozzle.) The siren speed is then set to the desired resonance by adjusting until the rms reading on the pressure transducer system output is at a maximum. The desired amplitude of oscillation is then obtained by adjusting the gap between the nozzle assembly and the siren wheel. Actually the 3 above mentioned settings, (1) pipe average pressure, (2) siren speed to the resonance, and (3) amplitude

of pressure oscillations at resonance may have to be gone through 2 or 3 times in succession to get all 3 adjusted as desired. These settings are watched closely throughout the run and if slight drifts are noted are readjusted to the desired values. Drifts may be caused by changes in siren speed, changes in temperature or pressure of the supply air, slight changes in the water bath temperature, etc. The traps are then filled and the bottles emptied and replaced under the lines; this latter starts the run proper (the time at which the empty bottles are replaced is noted). The run proper lasts $\sim$2 hrs. During the run settings (1), (2) and (3) (see previous page) are maintained constant as closely as possible; also the pressure on the upstream side of the sonic orifice is maintained nearly constant. About midway through the run the temperatures of the 25 thermocouples on the pipe are measured on a potentiometer and recorded. Also the airflow temperatures at thermocouples A, B, and C (Fig. 31) are recorded on the 'Speedomax' chart recorder. Temperatures from TC's, A and C are single readings; temperatures from TC B form a profile across the airflow in the pipe (see Sections 3.1 and 3.2.1). The average pipe pressure, calibrated sonic orifice supply pressure, and steam pressure during the run proper are recorded. Also, the average rms output voltage of the pressure transducer-bridge circuit-amplifier system is noted. At the end of the run proper, the condensate collection bottles are removed from under the lines and the time is noted. The steam, air, siren and electrical gear are turned off in that order. The condensate volume in each bottle is then measured. Condensate temperatures are measured in 3 or 4 bottles to give a typical value.

3.4 Data Reduction

The data reduction method is now described briefly by going through typical calculations for a run (Run 27).

Temp. on upstream side of calibrated sonic orifice = 518.1°R

Press. " " " " " " " = 168.7 psia

Coefficient of calibrated sonic orifice = $.01612 \frac{\text{lbm } (^{\circ}\text{R})^{\frac{1}{2}}}{\text{sec psia}}$

Mass flow = $.01612 \times \frac{168.7}{\sqrt{518.1}} = .1198$ lbm/sec.

Specific heat of air = .240 BTU/lbm$^{\circ}$R.

Heat capacity of airflow = .1198 x .240 x 3600 =103.5 BTU/hr^{o}R

Typical condensate temperature = 93^{o}F

Density of water at 93^{o}F = 62.1 lbm/ft^{3}

Heat of condensation of water at 1 atm. pressure = 970.3 BTU/lbm

Heat released by 1 cm^{3} of condensate in condensing

$$= \frac{970.3 \times 62.1}{(30.46)^{3}} = 2.13 \text{ BTU/cm}^{3}$$

Run proper duration = 2 hr.

For x cm^{3} of condensate, heat transfer rate for that chamber is

$$= \frac{2.13x}{2} = 1.065x \text{ BTU/hr}$$

Temperature at inlet to heated section = 64.0^{o}F

Heat carried by airflow at inlet to heated section above 0^{o}F is

$$= 64.0 \times 103.5$$
$$= 6{,}630 \text{ BTU/hr}$$

We now refer to the table on p. 75(Table 14) which presents the next steps in the data reduction process. (Results for the first 4 of the 25 chambers are shown.) To allow for heat loss from the chambers through the side and end insulation of the heated section, a 2-hr. run was taken with steam flow only (no airflow). The condensate volumes measured during this 'heat loss run' are entered in column 2. The large condensate volume measured during the heat loss run for Chamber No. 1 (also for Chamber No. 25) is due to the relatively high thermal conductivity of the phenolic insulating blocks used on the ends of the heated section. The condensate volumes measured in run 27 are entered in column 1. By subtracting col. 2 from col. 1, the condensate volume due to heat conduction to the airflow is obtained (col. 3). We then multiply col. 3 by the factor $1.065 \frac{\text{BTU}}{\text{hr cm}^{3}}$ computed above to get the heat transfer rate of the chamber (col. 4). By adding these heat transfer rates successively to the heat carried by the airflow at the entrance to the heated section (6,630 BTU/hr), we get the heat carried by the airflow at points between the chambers (col. 5). We then divide by the heat capacity of the airflow (103.5 BTU/hr^{o}R) to obtain the bulk temperatures of the air at these same points (col. 6). Interpolating between these bulk temperatures, we get the bulk temperatures at the center of each chamber (col. 7). The

PRINCETON UNIVERSITY
Department of Aerospace and Mechanical Sciences
Guggenheim Laboratories for the Aerospace Propulsion Sciences

Form No. G-1 TABLE 14 Date: _____

DATA SHEET RUN 27 By: _____

Research Number _____

	1	2	3	4	5	6	7	8	9
Chamber No.	Condensate Volume	Heat Loss Condensate Volume	Net Cond. Volume = ① - ②	Net Heat Transfer = 1.065 ③	Heat Carried Above °F BTU/hr	Bulk Temp = ⑤ / 98.7 °F	Bulk Temp	Wall Temp	ΔT = ⑧ - ⑦
	CM^3	CM^3	CM^3	BTU/hr			°F	°F	°F
1	248	25.5	222	236	6,630	64.0	65.2	209.4	144.2
2	195	10.7	184	196.0	6,866	66.4	67.4	210.6	143.2
3	125	5.0	120	127.9	7,062	68.3	68.9	211.1	142.2
4	121	4.6	116	123.6	7,189	69.5	70.1	211.3	141.2

	10	11	12	13
Chamber No.	Area	h = ④/⑨/⑩	D/K	Nu_h = 100 ⑪ ⑫
	ft^2	BTU/ft²hr°F	hr ft °F/BTU	
1	.0327	50.0	8.40	420
2	↓	41.9	8.37	351
3		27.5	8.35	229.3
4		26.7	8.33	222

pipe wall temperatures are entered in col. 8. Subtracting col. 7 from col. 8 gives the driving temperature difference for the heat transfer (col. 9). The area for heat transfer of each chamber (based on the pipe I.D.) is entered in col. 10. The heat transfer coefficient (h, BTU/ft^{2}hr$^\circ$F) is computed in col. 11 as h = ④/⑨⑩ . To compute the Nusselt number (based on pipe I.D., and thermal conductivity of air at the bulk temp., K) the factor D/K (hr ft^2 $^\circ$F/BTU) is computed in col. 12. By multiplying col. 11 by col. 12 we would obtain the Nusselt number. Since the heat transfer runs are taken over a slight range of Reynolds numbers ($\sim$3%), the Nusselt numbers are normalized to a reference Reynolds number.

The Reynolds number of the flow is computed (based on pipe I.D., air mass flow and air viscosity at the bulk temperature halfway along the heated section), and the Nusselt numbers are normalized as follows:

$$Nu_n = Nu \left(\frac{Re_r}{Re}\right)^{0.8} , \qquad (38)$$

where Nu = unnormalized Nusselt number (= col. 11 x col. 12 in Table 14)

Nu_n = normalized Nusselt number

Re_r = reference Reynolds number (= 97,500)

Re = run " "

since for steady turbulent pipe flow, $Nu \propto (Re)^{0.8}$. In column 13, Nu_n is calculated as

$$Nu_n = \left(\frac{Re_r}{Re}\right)^{0.8} ⑪⑫ ,$$

$\left(\frac{Re_r}{Re}\right)^{0.8}$ being equal to 1 in this case.

The heat balance calculations using the traversing thermocouple just downstream of the heated section are now presented. Using the temp. profile from the thermocouple, we could compute the bulk temp. at the exit of the heated section ($\bar{T}_b$) :

$$\bar{T}_b = \frac{\int T_b \rho v \, 2\pi r dr}{\int \rho v \, 2\pi r dr} \tag{39}$$

$\bar{T}_b$, T_b in ^oF

Using the equation of state,

$$P = \rho R T_R \tag{40}$$

T_R in ^oR

we get the final equation from which $\bar{T}_b$ is calculated as

$$\bar{T}_b = \frac{\int \frac{T_b}{T_{R,b}} \left(\frac{v}{v_m}\right) r dr}{\int \frac{1}{T_{R,b}} \left(\frac{v}{v_m}\right) r dr} \tag{41}$$

$$T_{R,b} = T_b + 460 \tag{42}$$

v_m = pipe center line velocity.

The velocity profile, $\frac{v}{v_m}(r)$ is taken as that of fully developed pipe flow at $Re \approx 97{,}500$. The fractional error in the heat balance is then computed as:

$$E_{FH} = \frac{\bar{T}_b - \bar{T}_{b,s}}{\bar{T}_{b,s} - \bar{T}_a} \tag{43}$$

where $\bar{T}_{b,s}$ = air bulk temperature at exit of heated section based on $\bar{T}_a$ and total steam condensate due to heat transfer to airflow (= last entry in col. 6, Table 14).

$\bar{T}_a$ = air bulk temperature at entrance of heated section (= first entry in col. 6, Table 14).

The fractional heat balance errors for the runs discussed in this report are given on the next page (Table 15).

TABLE 15

RUN NO.	FRACTIONAL HEAT BALANCE ERROR
16	.080
17	.078
18	.062
20	.050
21	.062
22	.040
23	.070
26	.045
27	.045

We note that the fractional heat balance errors range from .04 to .08. The author believes that the average fractional heat balance error of $\sim$ .06 is caused by conduction effects in the traversing thermocouple used to measure the temperature profile from which $\overline{T}_b$ is calculated. A typical temperature profile (from Run 27) together with a sketch of the thermocouple is shown in Figure 35 A. For data reduction, the profile was arbitrarily shifted until it became symmetrical and values of T_b used in Equation (41) were read off the shifted profile. The asymmetry in the temperature profile gives evidence of a significant conduction effect. Heat is likely conducted down the sheath and wires of the thermocouple from the hotter airflow in region B and also from section A of the thermocouple, where the sheath is in close contact with the pipe wall which is essentially at T_A. Conduction errors may be especially large when the junction is in region B and the distance between the hot wall and the junction is small. Errors in the regions near the wall are more important because of the r factor in Equation (41). It should be pointed out that a lowering of $\overline{T}_b$ by 2.5° F would be sufficient to reduce the average

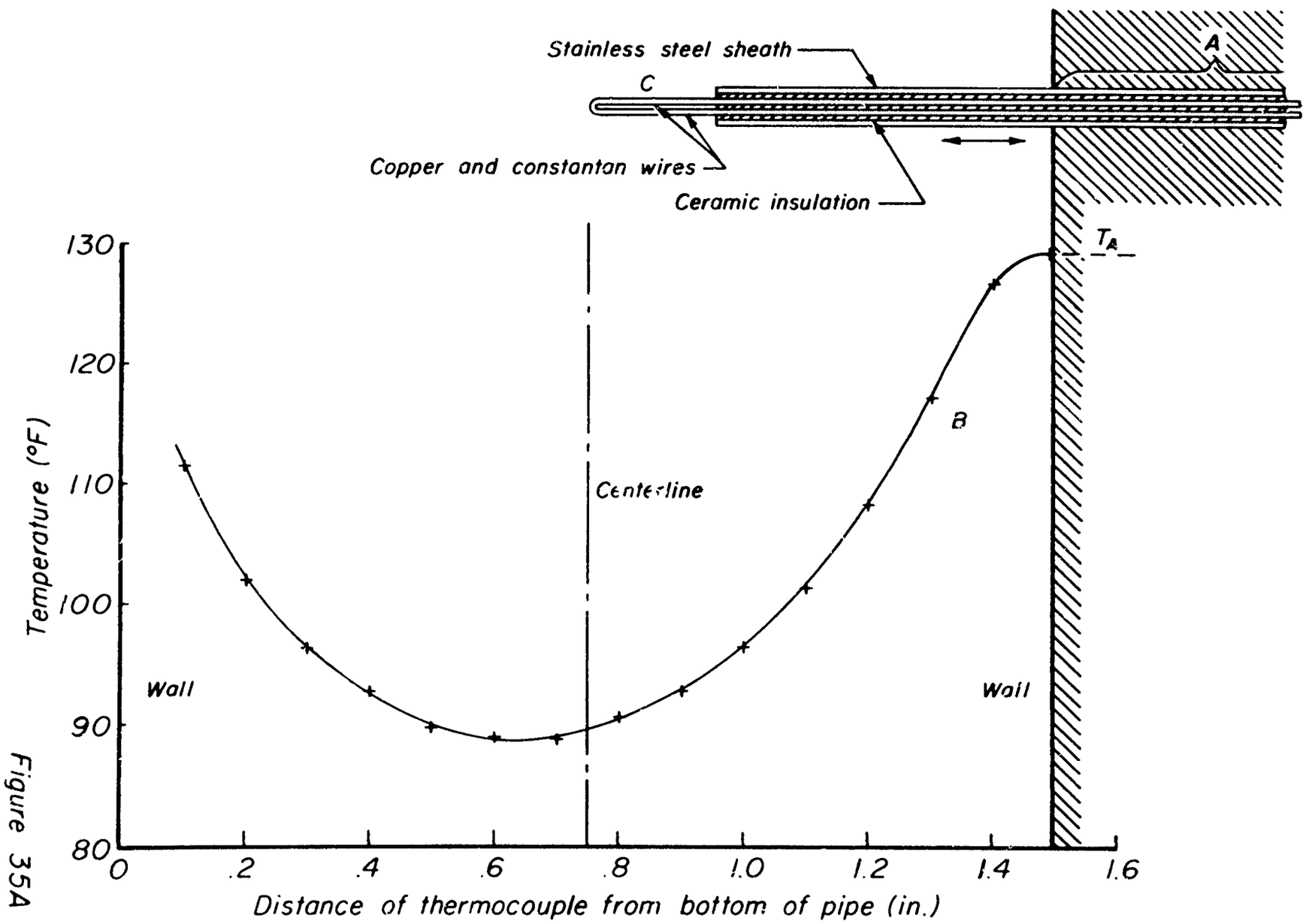
Stainless steel sheath
A
C
Copper and constantan wires
Ceramic insulation
T_A
130
120
110
100
90
80
Temperature (°F)
B
Centerline
Wall
Wall
0
.2
.4
.6
.8
1.0
1.2
1.4
1.6
Distance of thermocouple from bottom of pipe (in.)

Figure 35A

fractional heat balance error to ~ 0. From the degree of asymmetry of the profile in Figure 35 A, a conduction effect of this magnitude seems quite possible. If this is the correct explanation for the average fractional heat balance error, removal of this error would yield fractional heat balance errors of $\pm$ .02 instead of .04 - .08. That is, the author suspects that $\sim$ .06 of the fractional heat balance error is due to conduction effects, while the true random scatter is $\pm$.02.

We now discuss the calculation of M_a, S_a, and Re_a (based on conditions upstream of the heated section) and $\tilde{P}_N/\bar{P}$ and $\tilde{U}_A/\bar{U}$ [based on pressure fluctuations measured just upstream of the variable area sonic orifice (P,D, Figure 31)]. From the mean pressure and temperature measurements in the pipe upstream of the heated section (thermocouple 'A', pressure tap 'F', Figure 31) the density and sound speed are computed. Then, using the known mass flow rate (see p. 73) and the pipe cross sectional area, the mean flow velocity is calculated. Also, the air viscosity is determined from tables. From the above quantities, the Mach Number (M_a) and Reynolds number (Re_a) upstream of the heated section are determined. The frequency of oscillation is determined from the sound speed computed above and the known acoustic length of the pipe (allowing for the change of speed of sound through the heated section). With the frequency known, the Strouhal number ($S_a = \omega D/\bar{U}_a$) is computed.

The average rms output voltage of the pressure-transducer-bridge circuit-amplifier system (p. 69 , Section 3.2.4) when multiplied by the sensitivity of this system (also see Section 3.2.4) gives the rms pressure just upstream of the variable area nozzle ($\tilde{P}_N$). Dividing by the mean pressure ($\bar{P}$ = 54.7 psia) gives the parameter ($\tilde{P}_N/\bar{P}$). Rms pressure measurements were chosen because accurate rms electronic voltmeters are readily available, and also, because rms measurements give a measure of the energy in the wave for any waveshape. $\tilde{U}_A/\bar{U}$ was computed from the simple wave formula

$$\frac{\tilde{P}_N}{\bar{P}} = \frac{\gamma \tilde{U}_A}{c} \tag{44}$$

$$\frac{\tilde{U}_A}{\bar{U}} = \frac{\tilde{P}_N}{\bar{P}} \Big/ \frac{\gamma \bar{U}_b}{c_b} = \frac{\tilde{P}_N}{\bar{P}} \Big/ \gamma M_b \tag{45}$$

The Mach number in the denominator of Equation (45) (M_b) is the Mach number downstream of the heated section. Since M_b can be written as

$$M_b = \left(\frac{\bar{T}_{b,s}}{\bar{T}_a} \right)^{\frac{1}{2}} M_a \tag{46}$$

using the continuity equation, Equations (45), (46) the values of $\tilde{P}_N/\bar{P}$ and M_a, computed above, and the values of $\bar{T}_a$ and $\bar{T}_{b,s}$ computed in Table 14 allow $\tilde{U}_A/\bar{U}$ as defined above to be calculated.

3.5 Experimental Results

The experimental results for 7 runs at the 9th harmonic and 1 run at the 13th harmonic are presented in Figures 36-43. For each run, the parameters discussed in Section 3.4 (M_a, S_a, Re_a, $\tilde{P}_N/\bar{P}$ and $\tilde{U}_A/\bar{U}$) as well as other information are presented. The shapes of the pressure waves were observed to be roughly sinusoidal, and hence, a fairly accurate estimate of $\hat{U}_A/\bar{U}$ for these runs is

$$\frac{\hat{U}_A}{\bar{U}} \approx 2\sqrt{2}\ \frac{\tilde{U}_A}{\bar{U}} \approx 2.83\ \frac{\tilde{U}_A}{\bar{U}} \tag{47}$$

Points designated ⊕ instead of + are likely to be in error. The probable causes of error of such points are now discussed briefly. The error in chamber 1, Figure 37, is probably caused by a small air leak from the high-pressure (40 psig) air in the pipe into the steam chest, thereby

Figure 36

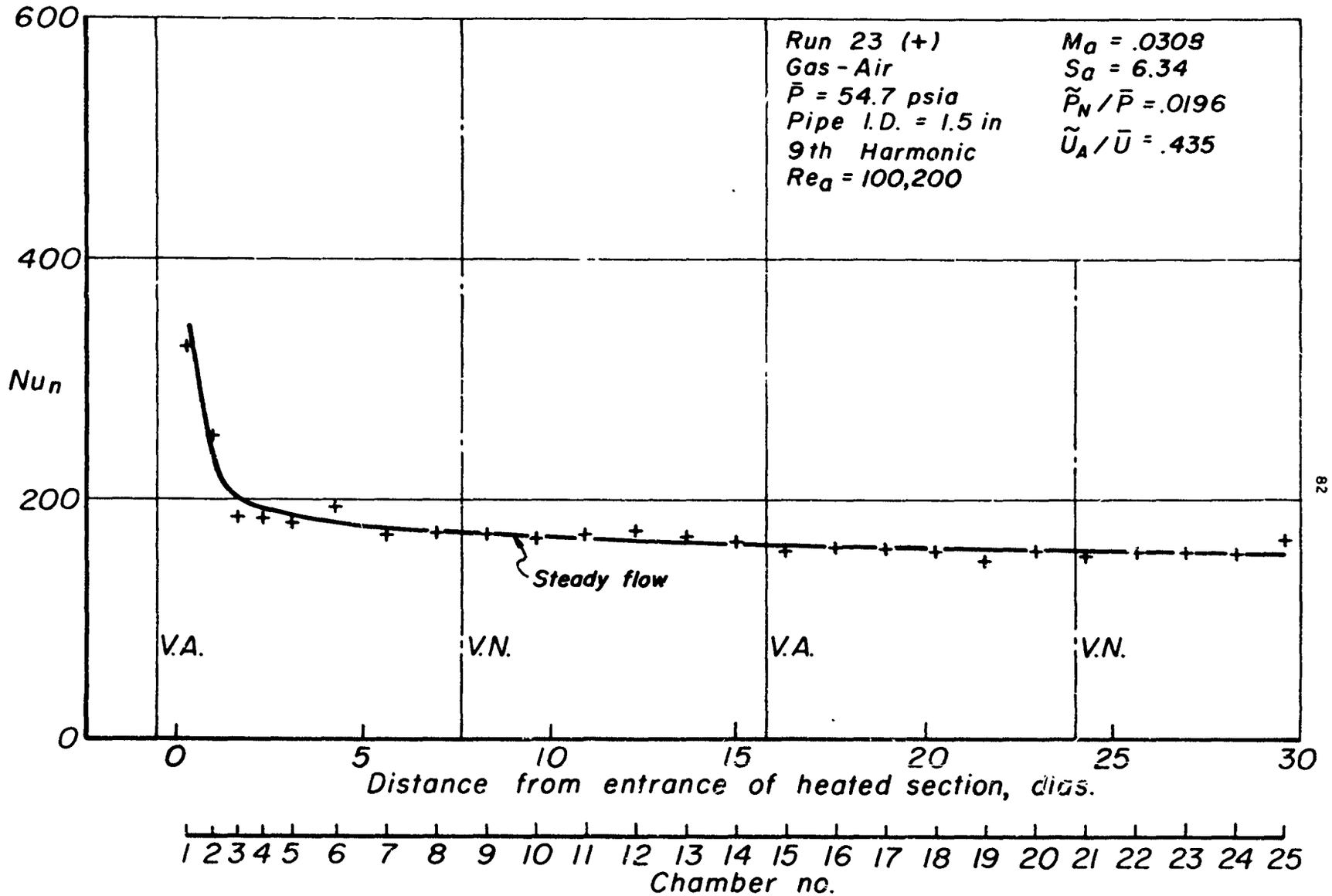
Run 23 (+)
Gas - Air
$\bar{P}$ = 54.7 psia
Pipe I.D. = 1.5 in
9th Harmonic
Re_a = 100,200
M_a = .0308
S_a = 6.34
$\tilde{P}_N / \bar{P}$ = .0196
$\tilde{U}_A / \bar{U}$ = .435
600
400
200
0
Nu_n
Steady flow
V.A.
V.N.
V.A.
V.N.
0
5
10
15
20
25
30
Distance from entrance of heated section, dias.
1 2 3 4 5 6 7 8 9 10 11 12 13 14 15 16 17 18 19 20 21 22 23 24 25
Chamber no.

JP 17 R 4005 67

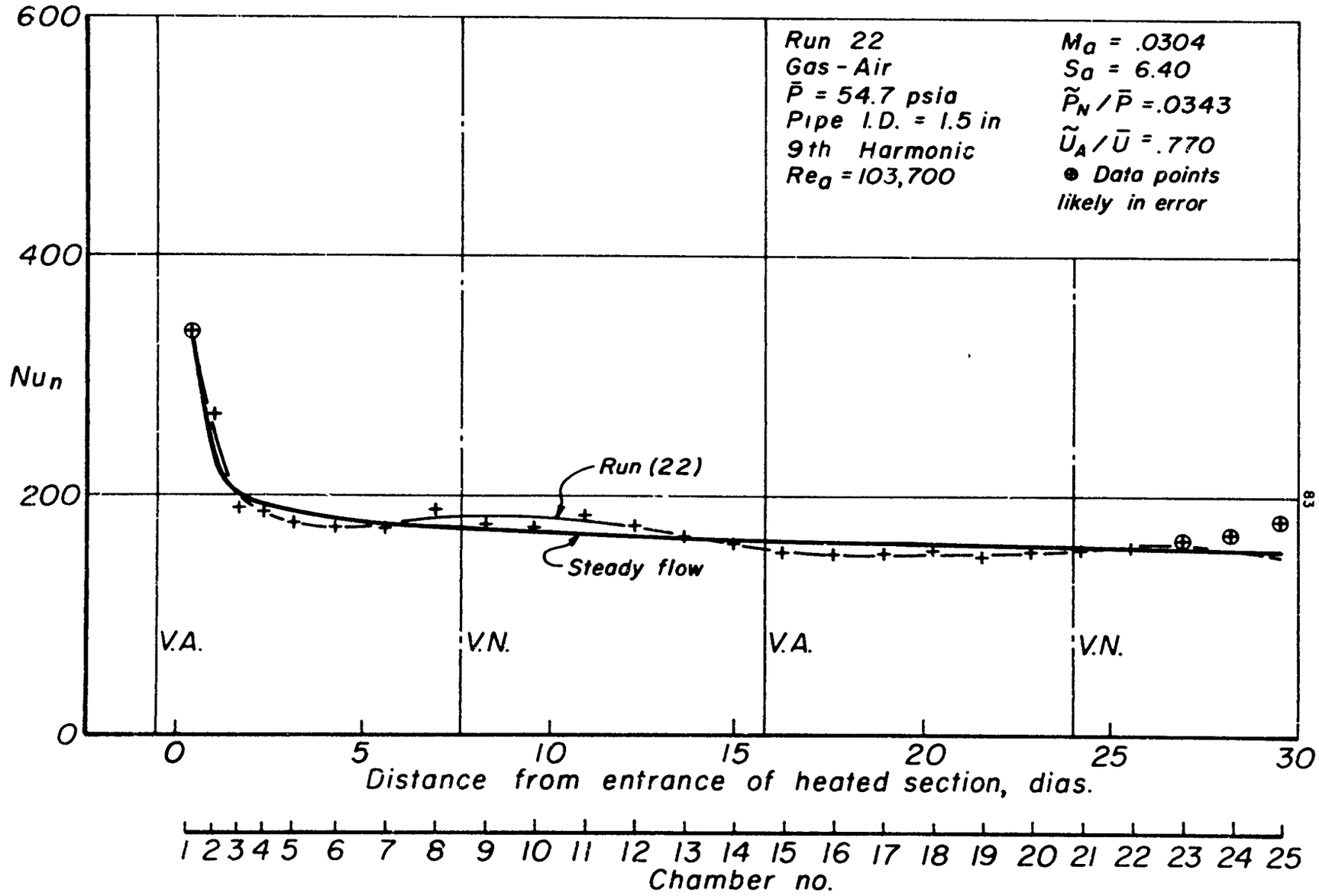

Figure 37

Figure 38

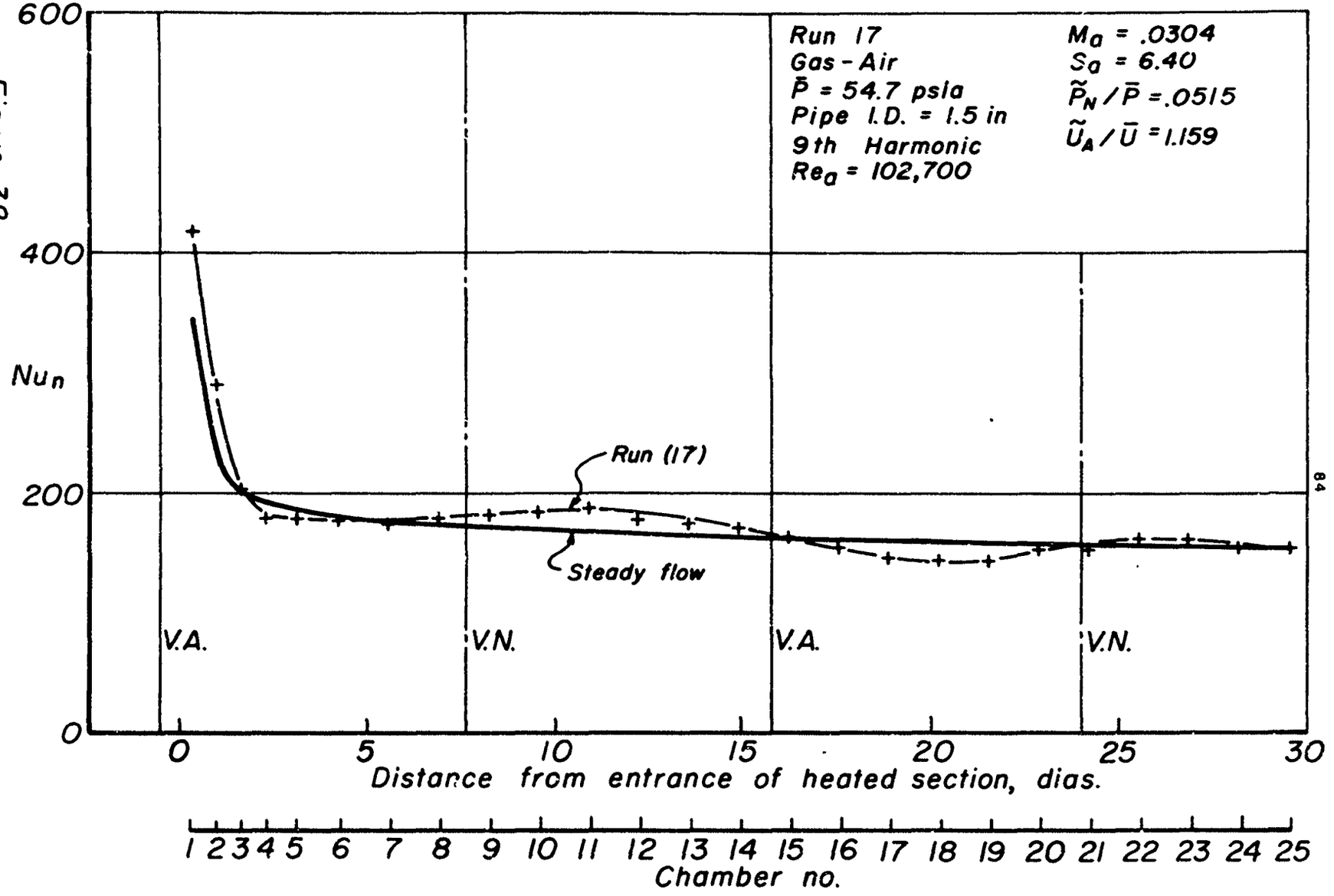
Run 17
Gas - Air
$\bar{P}$ = 54.7 psia
Pipe I.D. = 1.5 in
9th Harmonic
Re_a = 102,700
M_a = .0304
S_a = 6.40
$\tilde{P}_N / \bar{P}$ = .0515
$\tilde{U}_A / \bar{U}$ = 1.159
Run (17)
Steady flow
V.A.
V.N.
V.A.
V.N.
Nu n
600
400
200
0
0 5 10 15 20 25 30
Distance from entrance of heated section, dias.
1 2 3 4 5 6 7 8 9 10 11 12 13 14 15 16 17 18 19 20 21 22 23 24 25
Chamber no.

JPL e 4008 67

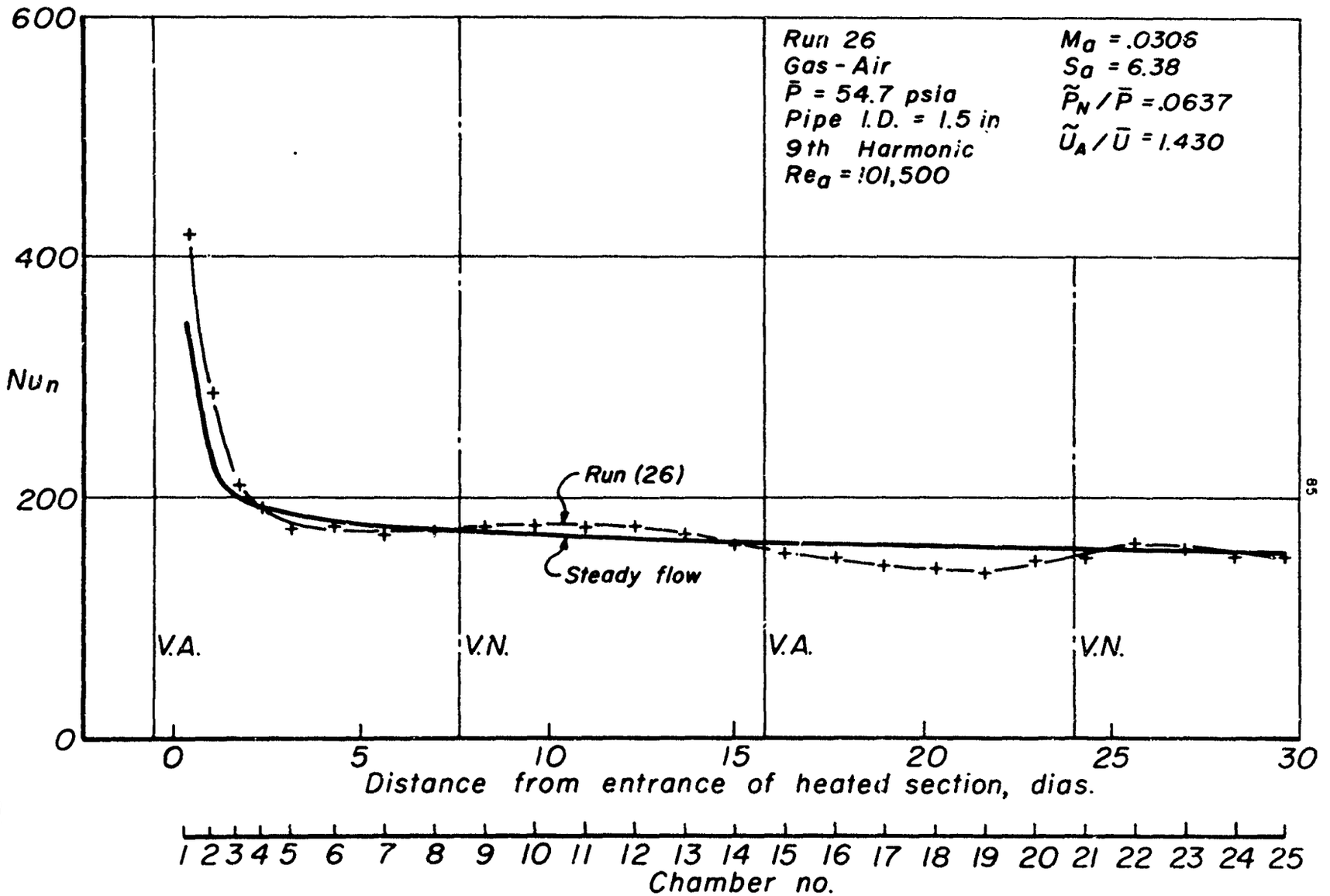

Figure 39

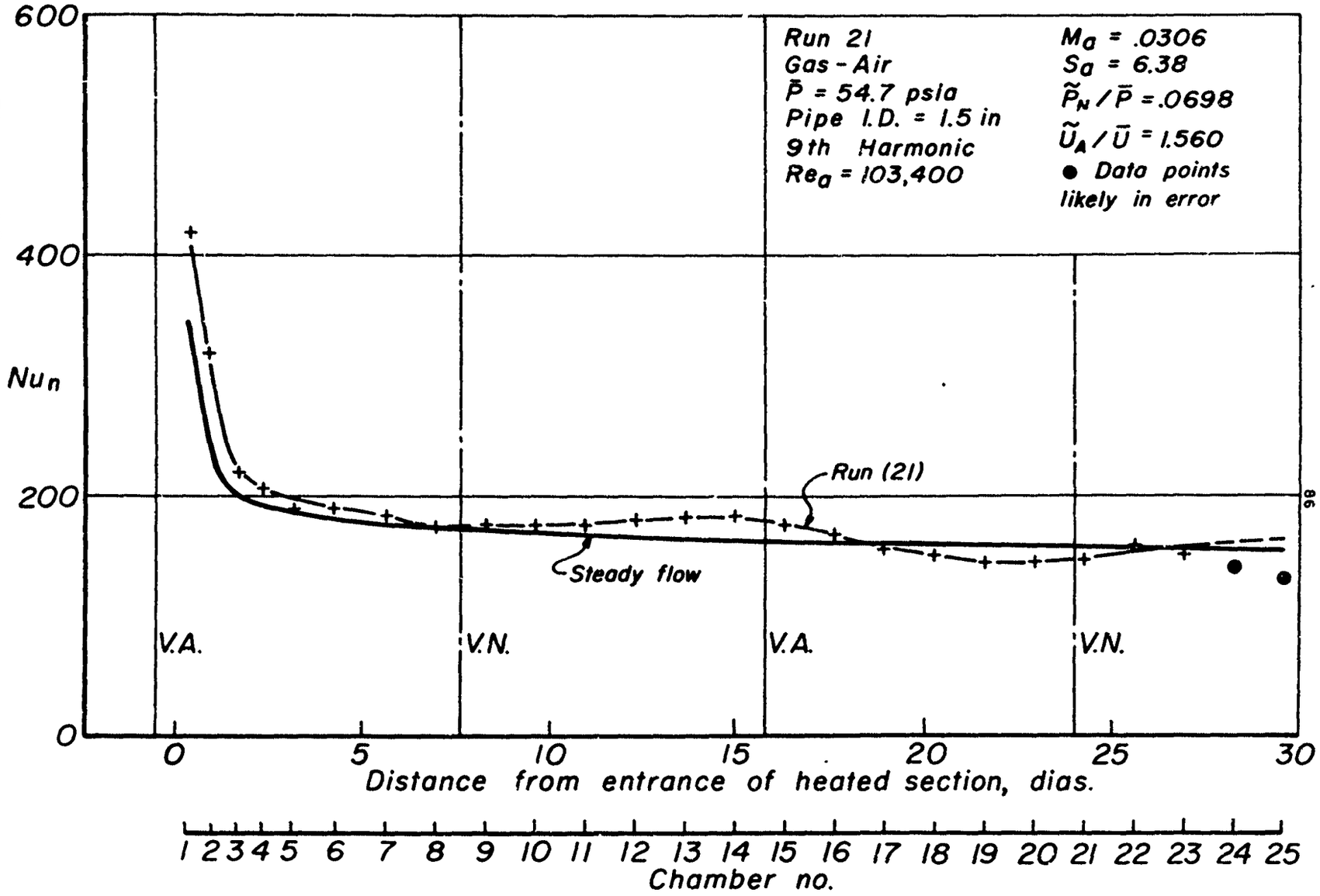
Run 21
Gas - Air
$\bar{P}$ = 54.7 psia
Pipe I.D. = 1.5 in
9th Harmonic
Re_a = 103,400
M_a = .0306
S_a = 6.38
$\tilde{P}_N / \bar{P}$ = .0698
$\tilde{U}_A / \bar{U}$ = 1.560
● Data points likely in error
Run (21)
Steady flow
Nun
600
400
200
0
V.A.
V.N.
V.A.
V.N.
0
5
10
15
20
25
30
Distance from entrance of heated section, dias.
1 2 3 4 5 6 7 8 9 10 11 12 13 14 15 16 17 18 19 20 21 22 23 24 25
Chamber no.

Figure 40

JP 17 R 4010 67

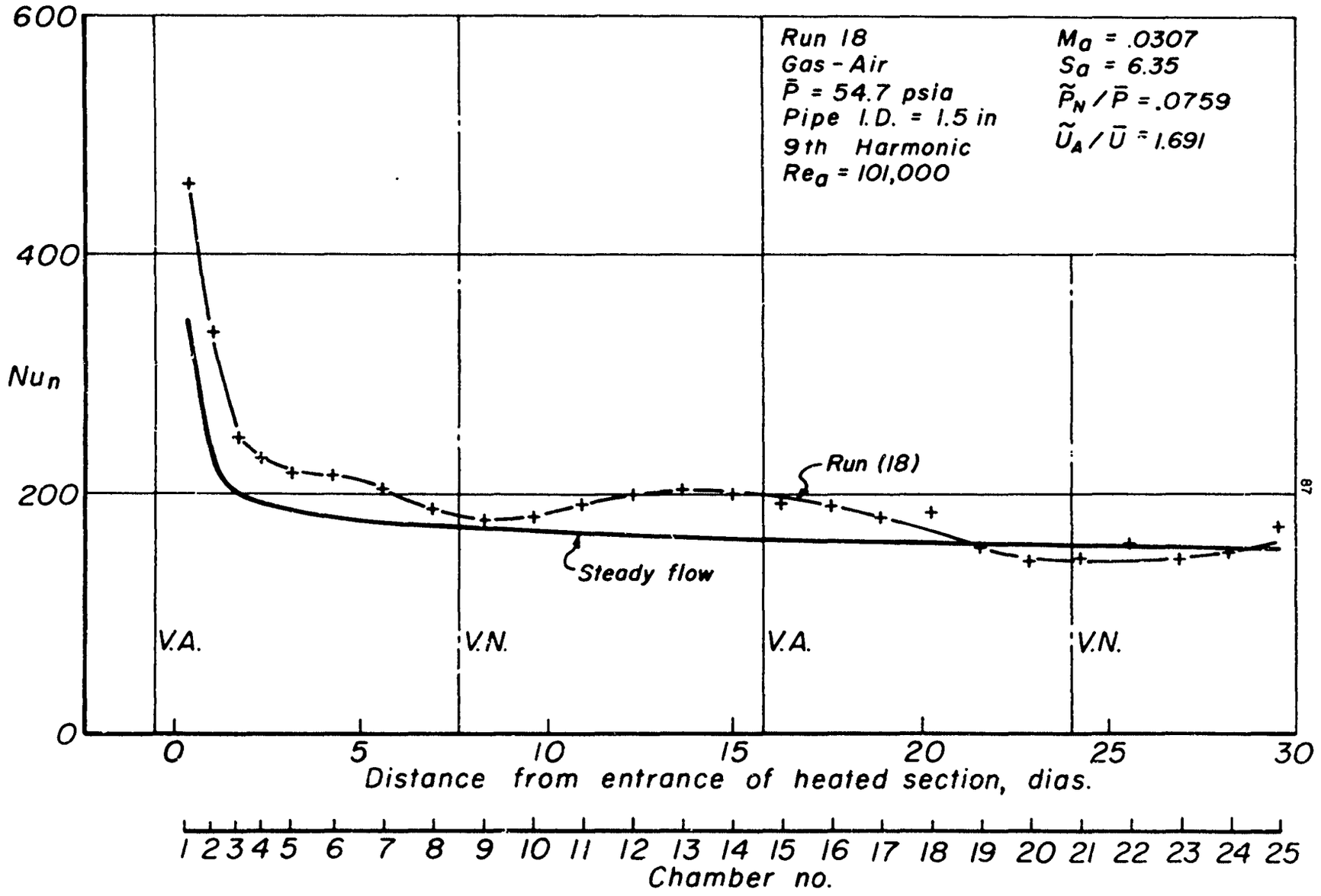

Figure 41

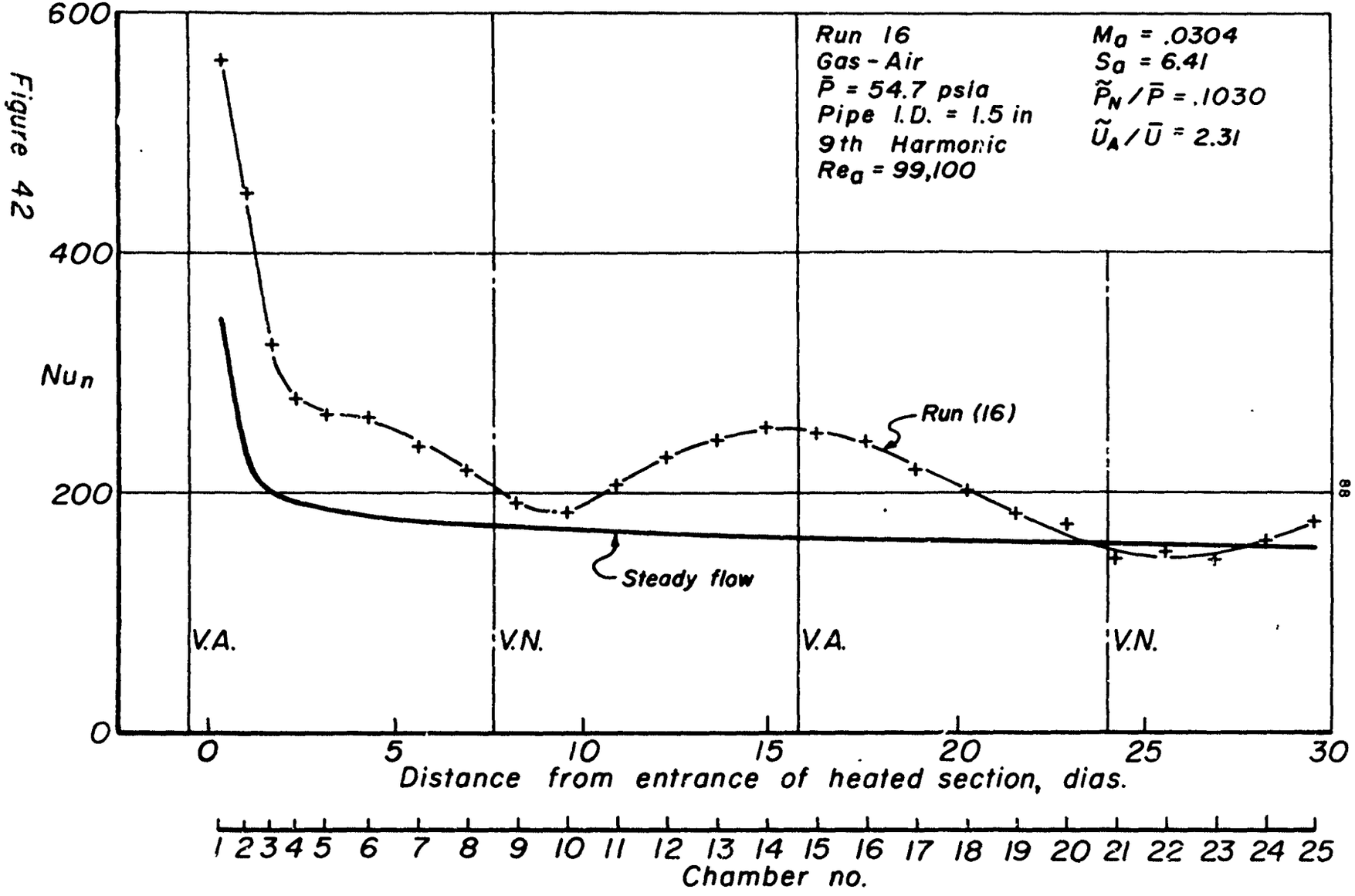
Run 16
Gas - Air
$\bar{P}$ = 54.7 psia
Pipe I.D. = 1.5 in
9th Harmonic
Re_a = 99,100
M_a = .0304
S_a = 6.41
$\tilde{P}_N / \bar{P}$ = .1030
$\tilde{U}_A / \bar{U}$ = 2.31
Run (16)
Steady flow
V.A.
V.N.
V.A.
V.N.
Nu$_n$
600
400
200
0
0
5
10
15
20
25
30
Distance from entrance of heated section, dias.
1 2 3 4 5 6 7 8 9 10 11 12 13 14 15 16 17 18 19 20 21 22 23 24 25
Chamber no.

Figure 42

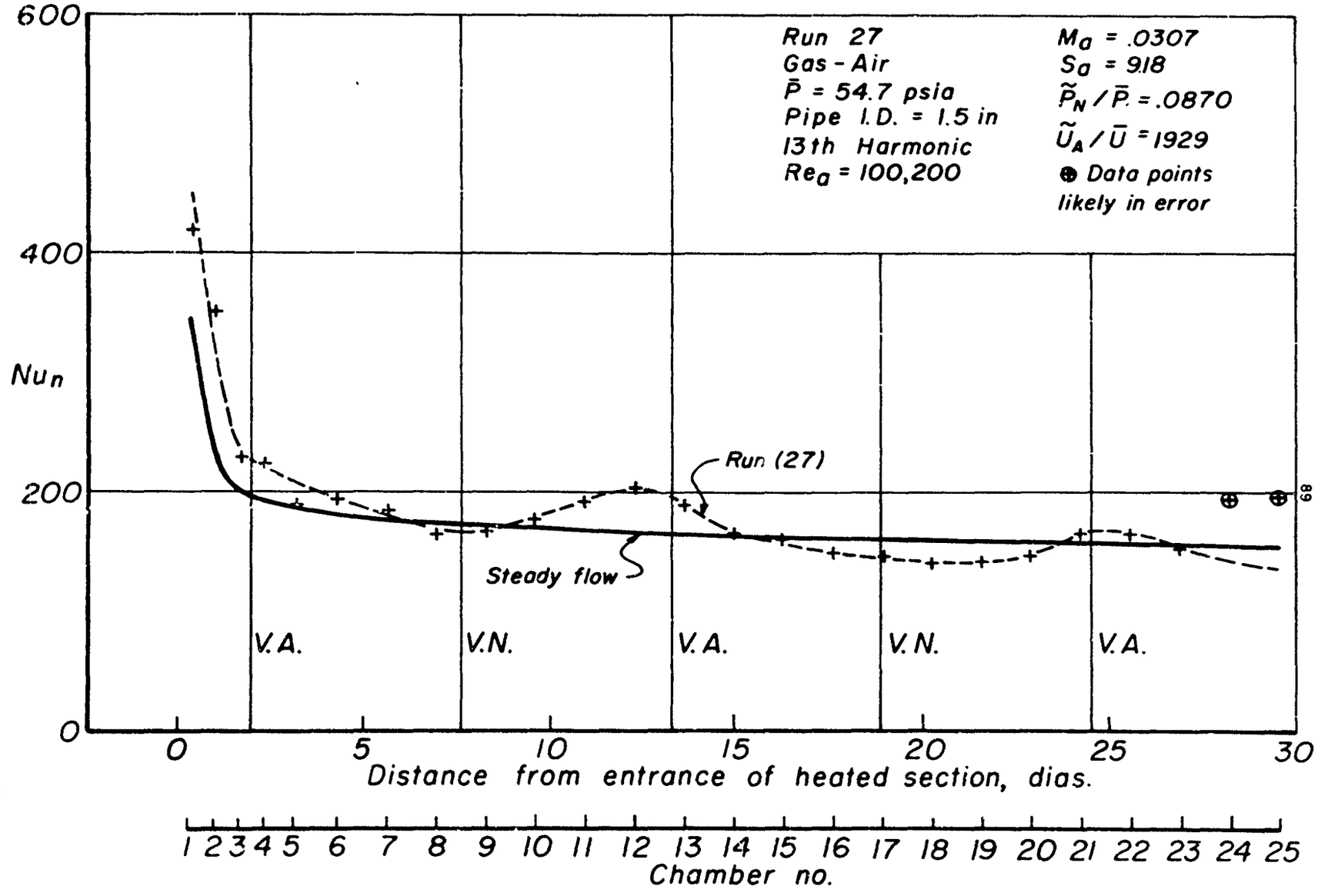

Figure 43

cooling the condensation chamber slightly and reducing the condensate volume. Errors in chambers 23, 24 and 25, Figure 37 and chambers 24 and 25, Figure 43 may be due to slight carry-overs of moisture from the separator, or possibly to temporary blow-outs of the water in the traps, allowing direct steam flow into the condensate collection bottle. These errors are positive. Chambers at this end of the steam chest are immediately below the steam inlet from the separator, and also would show the highest steam pressure. The errors in chambers 24 and 25, Figure 40, which are negative, are likely due to leakage of condensate at the junction of the condensate collection chamber and the trap (see Figure 34). Leaks at this junction have been observed (and repaired) in earlier checkout runs. In any event, since the number of readings likely to be considerably in error is $\sim$ 8 and the total number of data points is 8 x 25 = 200, these errors degrade the quality of the data very little.

We now briefly discuss the nature of the data. For all runs, $Re_a \approx 97{,}000$ and $M_a \approx .030$. For all 9th harmonic runs, $S_a \approx 6.40$, and for the 13th harmonic run, $S_a = 9.18$. From Figure 36, we see that oscillations have little effect on heat transfer at $\tilde{U}_A/\bar{U} \approx .4$. At $\tilde{U}_A/\bar{U} \approx .8$ (Figure 37), the oscillations produce a noticeable effect on the heat transfer, with sinusoidal variations of the latter being produced. The maxima of heat transfer are $\sim \frac{\lambda}{12}$ downstream of the velocity nodes, the minima $\sim \frac{\lambda}{12}$ downstream of the antinodes and there is little overall change of heat transfer. As the oscillating amplitude increases (Figures 38 - 40 , $\tilde{U}_A/\bar{U} \approx 1.2, 1.4, 1.56$), the amplitude of the variation of heat transfer increases, the maxima and minima move downstream, but the overall heat transfer changes remain small. Increasing the oscillation amplitude still further (Figures 41 and 42, $\tilde{U}_A/\bar{U} \approx 1.7, 2.3$) moves the maxima and minima still further downstream (in Figure 42, the maxima is near the velocity antinode, and the minima are slightly downstream of velocity nodes), increases the amplitude of the heat transfer fluctuations, and produces substantial overall increases in heat transfer (especially for $\tilde{U}_A/\bar{U} \approx 2.3$, Figure 42). The one test taken at the 13th harmonic (Figure 43), shows fluctuations of heat transfer whose maxima and minima are located similarly to those at the 9th harmonic for comparable $\tilde{U}_A/\bar{U}$ values (Figures 41 and 42) ($\tilde{U}_A/\bar{U} \approx 1.90$ for Figure 43), but a considerably smaller overall increases in heat transfer.

Possible explanations for this behavior, and correlation of this data with that of some of the references, will be discussed in detail in Section 5.

4. HOT-WIRE ANEMOMETER MEASUREMENTS

4.1 Introduction

To investigate the flow pattern set up under oscillating conditions, it was decided to take velocity profiles (both instantaneous and time-average) across the pipe at various x dimensions along the pipe. This work was done by replacing the steam-heated test section described in Section 3.1 (Figures 31-34) with an unheated test section which mounted a hot-wire anemometer probe and a wall-mounted pressure transducer. This test section will be described in more detail in Sections 4.2, 4.4 and 4.5. The tests were taken under approximately the same conditions as the maximum oscillation amplitude heat transfer run at the 9th harmonic (Run 16, Figure 42, Section 3.5). The purpose of these tests was to attempt to search for distortions of the velocity profiles due to acoustic streaming effects (See Section 1, p. 10 , and Section 2, pp. 50-56) and to variations in eddy diffusivity values (see Section 1, pp. 10,11).

4.2 General Description of Hot-Wire Test Section

Referring to Figure 31 (which shows the apparatus set up for heat transfer measurements), for the velocity profile measurements, the steam heated section of the pipe is removed and replaced the hot-wire test section shown in Figure 44. The rest of the apparatus remains essentially as sketched in Figure 31. The pressure transducer and hot-wire are mounted in a block of brass, as sketched in Figure 44. Flanged pipes (1.46 in. I. D., $\sim$ 1.50 in. O. D.) mounted flush with either side of the block (Figure 44) using o-ring seals, telescope into flanged sections of 1.50 in. I. D. pipe, which mate with fixed lengths of pipe making up the remainder of the resonant duct. (O-rings are also used on the seals between the telescoping pipes.) The test section is traversed back and forth using a 'Zeromax' variable speed motor which drives a length of screw mounted parallel to the duct through a flexible coupling. This screw engages a nut mounted on an aluminum frame bolted to the brass block of the test section. The Aluminum frame, together with the test

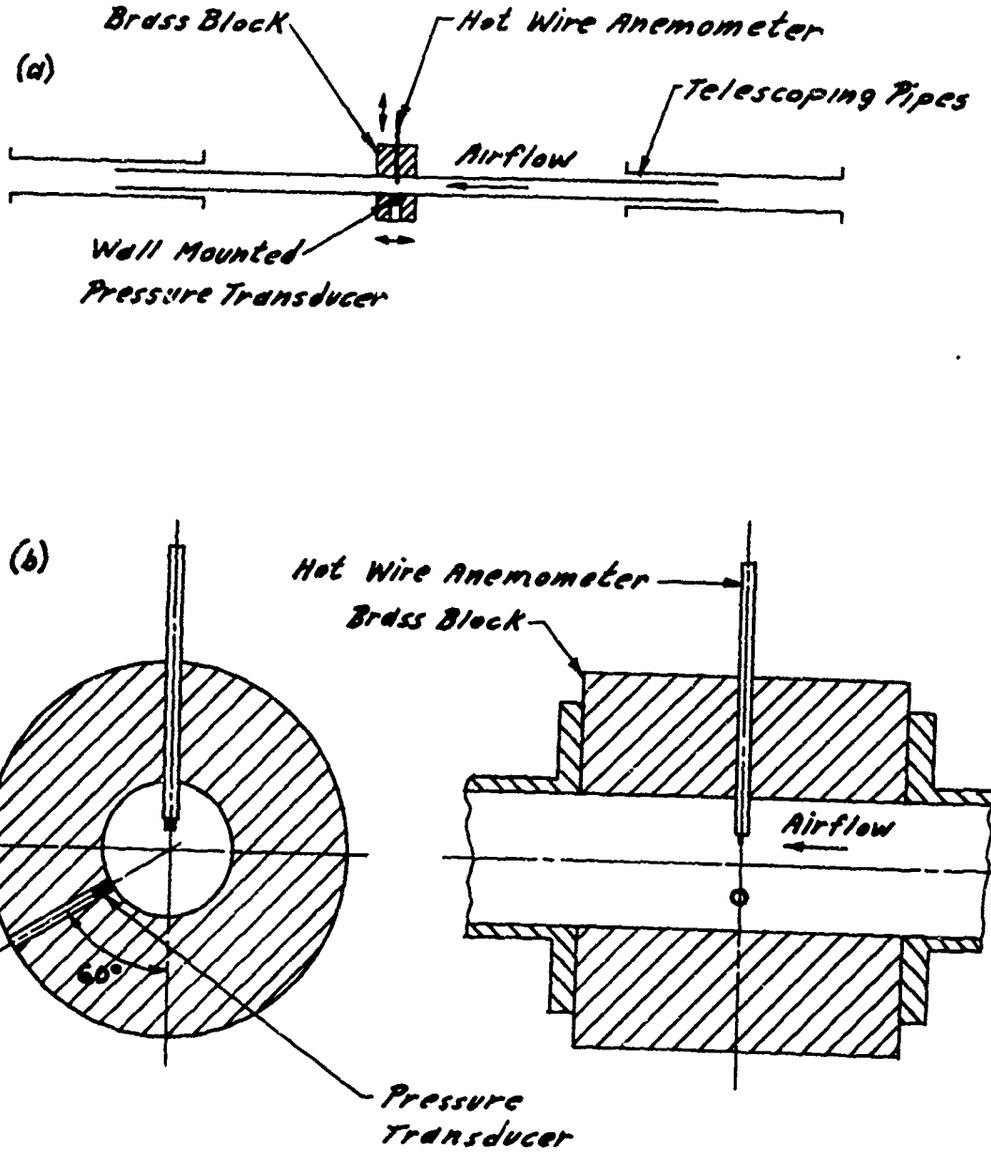
(a)
Brass Block
Hot Wire Anemometer
Telescoping Pipes
Airflow
Wall Mounted
Pressure Transducer
(b)
Hot Wire Anemometer
Brass Block
Airflow
60°
Pressure
Transducer

FIGURE 44

section assembly, moves (on sliding bearings) on two rods mounted parallel to the duct. The 'Zeromax' motor is operated from the main control panel through a relay system. The range of x-positions accessible is ~17 in. This is somewhat smaller than desirable for the case of operation at the 9th harmonic, since the flow pattern should be repeated only every 24.5 in. (= $\lambda/2$), however much useful information was obtained in spite of this fact. The x-position of the test section is presented at the control panel on a 0-100μa meter. Two potentiometers mounted on the control panel allow the extreme up and downstream positions of the test section to be set to 100 and 0μa respectively on the meter. Limit switches prevent the test section from running into the flanged tubes on the upstream and downstream sides. The hot-wire probe was mounted vertically in the central plane in the top of the brass block (Figure 44) and could be traversed across the pipe radius (this traversing gear will be described further in Section 4.5). The body of the hot-wire probe is .125 in. in diameter. The pressure transducer was flush-mounted at an angle of 120^{o} (Figure 44) from and in the same plane as the hot-wire probe entry hole. (The pressure transducer system will be described further in Section 4.4.)

4.3 'Dynisco' Pressure Transducer System

A slight digression must be made at this point, since the Norwood pressure transducer mounted just upstream of the variable area nozzle (Section 3.1, Figure 31, Section 3.2.4), used to measure oscillation amplitudes in the heat transfer tests was replaced by a Dynisco pressure transducer for the velocity profile runs. This replacement was made since the calibration curves of the Norwood transducers showed slight non-linearities and, at one point, a Norwood transducer was observed to change its sensitivity substantially (10-15%). These errors should not effect the amplitude measurements taken with the heat transfer work, since the non-linearity of the calibration curve was outside the range of pressures being measured (beyond 100 psi) and the sensitivity change took place after the heat transfer runs were completed. However, on principle, it was

decided to replace the Norwood transducer with the Dynisco, which had shown much better linearity and stability in previous service on other test rigs. The transducer used was a Dynisco Model PT 76-1M, 0-1000 psig. This transducer is of the strain-guage type, four-arm bridge, with two windings wound circumferentially and two windings wound axially on a strain tube mounted between the diaphragm and the backing plate. The bridge was excited with a Video Instruments Model SR-200-EHM D. C. power supply, set to 10 V. The output of the bridge was fed to a Dana Model 2200 operational amplifier, set to a gain of 1000; the amplifier output was fed to the same Ballantine rms meter (see Section 3.2.4) used in the heat transfer runs to obtain an rms voltage reading for the oscillation amplitude. The sensitivity of the power supply + transducer part of the system was determined using a dead-weight tester to load the transducer over the pressure range 0-500 psig, while the output of the transducer bridge was recorded on Bristol chart recorders on ranges of 5.5-8.5 and 5-20 millivolts. The sensitivity of the power supply + transducer part of the system was .0284 MV/PSI over the range 0~100 psig. The gain of the Dana amplifier was checked by using a hand-balanced potentiometer to supply D. C. input signals at the millivolt level and a digital voltmeter to measure the amplifier output. The gain of the amplifier was found to be within 0.2% of the nominal figure of 1000. Under oscillating conditions, the rms amplitude of the output of the power supply + transducer + amplifier system was about .150 volts. With no airfl w, the noise level (chiefly amplifier noise) was about .006 volts rms; hence, since these are rms measurements, the noise should cause negligible errors in the amplitude measurements. The frequency response of the transducer and amplifier (roll-off at about 20 KC for both pieces of equipment) is far beyond that necessary for accurate rms measurement of the 270 cps waveforms. All the equipment mentioned above except the transducer itself and part of the transducer cable are in the room containing the control panel rather than in the test cell. (See Section 3.2.1.)

4.4 Kistler Transducer System

The pressure transducer mounted in the test section (Figure 44) and mentioned in Sections 4.1 and 4.2 will now be discussed in more

detail. The transducer is a Kistler Model 601A and has a diameter of 1/4 in. This is a quartz piezoelectric type of transducer. The transducer is mounted flush with the inside surface of the brass block. The transducer output is fed to a Kistler Model 504 charge amplifier, which is operated at a potentiometer setting of 1.00 turn and a rotary switch setting of 200. For the velocity profile measurements the output of the charge amplifier is applied to one beam of a two-beam oscilloscope, (the other beam carries the hot-wire signal) and Polaroid pictures of the traces are taken (see Section 4.10). Again, all components of the system except the transducer and some cabling are located in the room containing the control panel. The Kistler transducer was not calibrated using the dead-weight tester as were the Norwood and Dynisco transducers (Sections 3.2.4 and 4.3) but rather, because of zero drift, using the gas pressure system sketched in Figure 45.

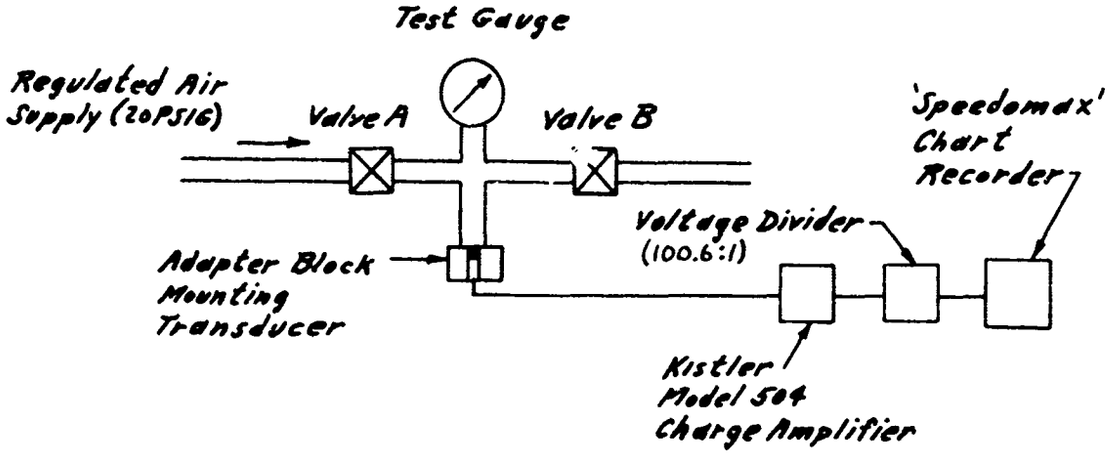

FIGURE 45

For calibration, the output of the amplifier is fed through a 100.6:1 voltage divider to a 'Speedomax' chart recorder (range 0-3 MV). Calibration is as follows: after all electrical gear is warmed up, valve b is closed (valve A has been closed from the beginning of the calibration procedure) and the chart recorder started. The pressure on the test

gauge is then noted (this is not quite zero, since the zero of the gauge was slightly off). Valve A is opened and closed quickly, bringing the transducer pressure up to $\sim$20 psig in about one second. The test gauge reading is again noted, and about three seconds later, valve B is opened returning the transducer pressure to atmospheric. Again the test gauge reading is noted. The three test gauge readings, together with the corresponding millivolt reading obtained from the chart recorder trace, and the voltage divider ratio allow the sensitivity of the transducer to be calculated. The difference between the final and initial voltage readings was only about 1% of the difference between the 0 and $\sim$20 psig readings, so the zero drift problem was almost eliminated using this method of calibration. The sensitivity of the transducer + change amplifier system was measured as 163.1 psi/volt or 6.13 MV/psi.

4.5 Mechanical Details of Hot-Wire Traversing System

The essential details of the hot-wire traversing device are presented in Figure 46 (the hot-wire probe itself is described in Section 4.6). Many details such as o-ring seals are omitted. By rotating the handwheel, through the system of four gears lying on top of the frame, the two threaded rods are rotated in opposite directions. The threaded rods engage tapped holes in the travelling block which is thus moved up and down. The travelling block is rigidly connected to the hot-wire probe below and to the pin of the dial indicator above. The travelling block moves up and down in slots in the frame. Two springs are kept heavily loaded in compression between the frame and the travelling block to lessen the danger of the block moving spontaneously due to the vibration of the test rig. The spring restraining rods are fastened to the travelling block with set screws. The position of the hot-wire is measured using both the dial guage readings and the number of turns (whole + fractional) of gear A (Figure 46). Turns of gear A are measured down to 1/16 part (the gear has 16 teeth). The position of the hot-wire is set as follows: the screws fastening the downstream telescoping tube to the brass block (Figures 44 and 46) are removed, and the tube is drawn back into its telescoping mate, allowing a microscope to be positioned as shown in Figure 46.

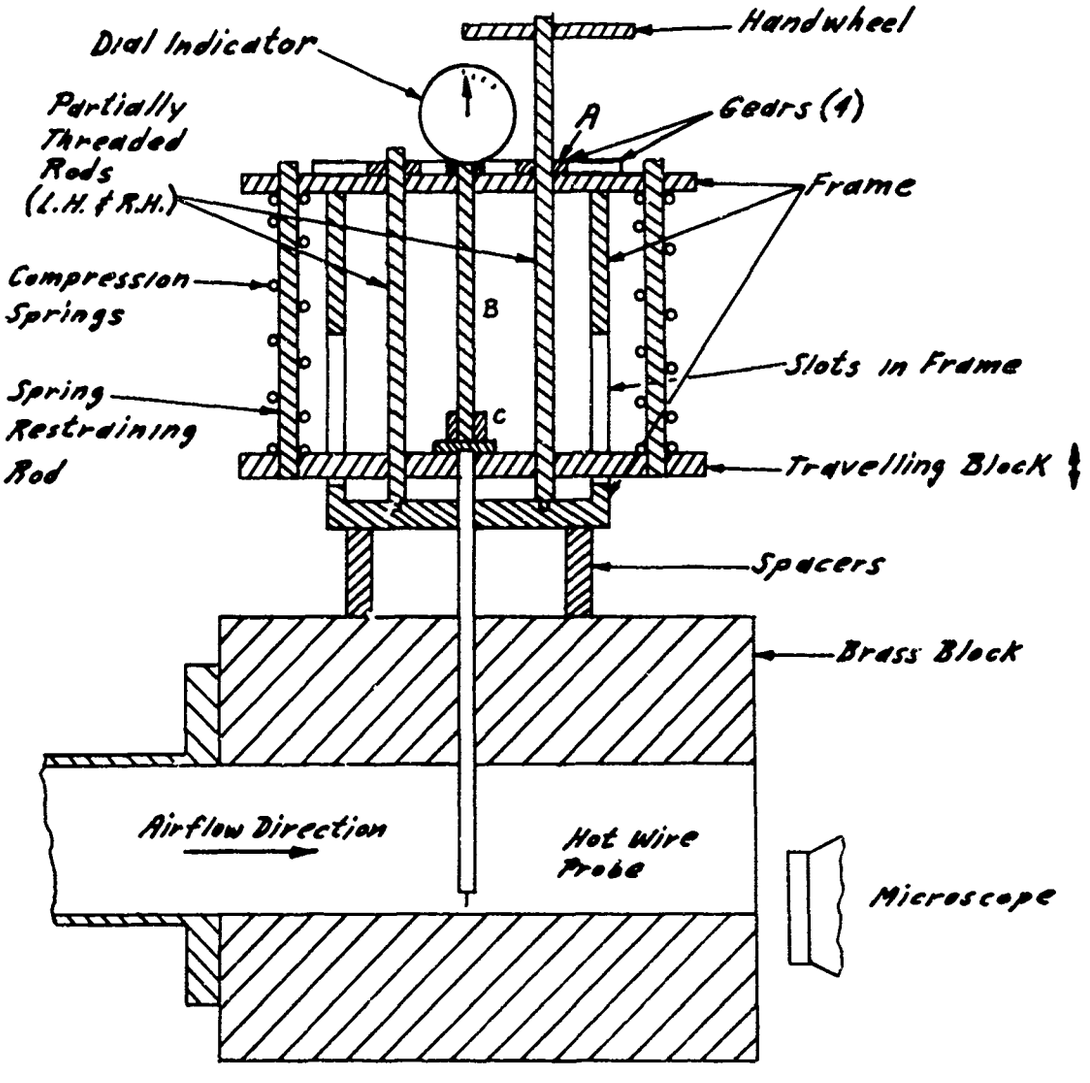
Dial Indicator
Handwheel
Partially Threaded Rods (L.H. & R.H.)
A
Gears (4)
Frame
Compression Springs
B
Slots in Frame
Spring Restraining Rod
C
Travelling Block
Spacers
Brass Block
Airflow Direction
Hot Wire Probe
Microscope

FIGURE 46

A list of desired positions is prepared (usually 20 positions starting at $\sim$ .001 in. from the wall and progressing to a distance of .73 in. from the wall - the pipe center-line), and the closest position to the wall is set using the (40 - power) microscope equipped with a 50 division calibrated reticle in the focal plane of the eye piece. The reticle was calibrated using a 1 mm slide mounted scale with smallest division = .01 mm. The wire was somewhat slack for reasons discussed in Section 4.6, and the distance measured was one-half the minimum distance between the wire and its reflection (Figure 47).

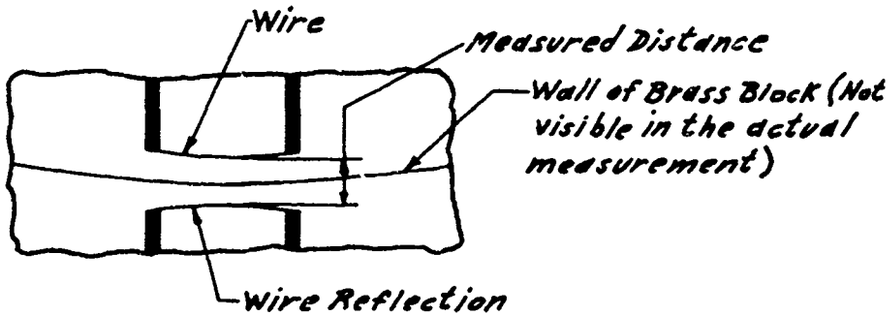

FIGURE 47

The wire was illuminated from behind by breaking the resonant duct open several feet upstream of the test section and hanging a 100-watt bulb in front of the duct opening. (The duct is composed of a number of flanged brass sections.) The setting of the closest position to the wall was done while the travelling block was moving upwards, a further precaution taken to avoid backlash and spontaneous movement of the travelling block. The setting could be made to an accuracy of better than $\pm$ .0001 in. Once this setting is made, we now have related one dial guage reading and one turns count on gear A (Figure 46) to an absolute distance of the hot-wire from the wall. At this point, the dial gauge readings and gear turns counts for all other desired hot-wire positions are calculated. The settings are made using the handwheel (Figure 46). It should be noted, that although there is considerable slop in the gear system, this should not cause any errors in dial gauge readings, since the dial gauge is rigidly connected to the hot-wire probe. Also, since there was no steam heating in these series of experiments, temperature changes in the

traversing apparatus are limited to $\sim 10^{\circ}F$ at most (due to the airflow in the duct being at a somewhat different temperature than the test cell) and dimensional changes due to thermal expansion effects should cause negligible errors in the setting of the hot-wire position. Since the range of the dial indicator was .250 in., hot-wire position settings up to .150 in. from the wall were made using the dial guage. These settings were checked before and after the Polaroid picture of the hot-wire data was taken. No differences larger than .00003 in. were observed between the two dial gauge readings taken at each position. For hot-wire distances greater than .150 in. from the wall, the dial guage and shaft B (Figure 46, were removed by loosening set screws holding the shaft in cup C (Figure 46) and other set screws fastening the dial gauge to the top of the frame. Positions of the hot-wire greater than .150 in. from the wall were measured only by counting the turns of gear A which yielded an estimated error of $\pm$ .002 in. hot-wire position. This error is not serious for measuring the velocity profile beyond .150 in. from the wall. Because of the necessity to remove the dial gauge as discussed above, the reading of the gauge if the hot-wire was returned to the closest position to the wall after the profiles were taken (as determined by the microscope) could not be checked against the original value of this reading, in the usual tests made. However, in one case, a large number of measurements were taken within .100 in. of the wall [with normal conditions of vibration, airflow, run duration ($\sim$ 2 hr.)] and in this case, the above-mentioned test could be made. It was found that the difference of the final and initial conditions as observed in the microscope for the same dial gauge setting was smaller than .0001 in. The estimated error in hot-wire position, for distances $\leq$ .150 in. from the wall, based on thermal expansion effects and the error figure in the previous sentence is $\pm$ .0001 in.

After the setting of the wire position closest to the wall was made, the telescoping section which was moved was drawn back up and refastened to the brass block, and the section of the duct removed to allow illumination of the wire was replaced.

4.6 Mechanical Details of Hot-Wire Probe

Parts of the hot-wire probe are shown in Figure 48. These parts were obtained from Thermo-Systems, Inc., Minneapolis, Minnesota, except as described below. In ordinary use the sensor holder Figure 48b, mounting the hot-wire between the needle tips, is plugged into the probe Figure 48a, electrical contact being made by the two stainless steel pins on part (b) fitting into miniature jacks in part (a). Wires inside part (a) complete the circuit to the BNC connector on (a). In practice, the plug joint between (a) and (b) was found to have an erratically varying contact resistance, and hence a soldered joint unit, Figures 48 (c) and (d) was made up. (d) is a sensor holder from Thermo-Systems Inc., (identical to part (b), except for the shape of the hot-wire support needles), and (c) is a hollow tube of outer dimensions similar to that of (a) and mounting a BNC connector as shown. Wires were threaded through the tube and soldered to the pins of the sensor holder [(d)]. The sensor holder was then slipped into the tube, glued with epoxy cement, and the other ends of the wires connected to the BNC connector. No contact resistance problems occured using this probe system. In the normal system, when (a) and (b) are used, the locking sleeve [Figure 48 (e)] is slipped over (a) and (b) until the shoulder of (b) butts against a lip at the end of (e). The screw or the locking sleeve is then tightened to hold the sleeve to the probe (a) and prevent the sensor holder (b) from coming loose. Since our hot-wire system was originally designed to work using (a) and (b), we continue to use the locking sleeve with (c) and (d), although it no longer fulfills its intended function. An o-ring seal in the block on (e) prevents air leakage between (c) and (e) when these parts are joined. A second o-ring seal between the tube of (e) and the brass block of the test section (Figure 46) prevents leakage at this point. Note that details of the hot-wire probe are omitted from Figure 46. The block of the locking sleeve (Figure 48e) is tightly clamped to the travelling block (Figure 46) of the traversing mechanism. The dimensions of the hot-wire support needles and the wire proper are shown in Figure 49. The needles are stainless steel, .025 in. in diameter and tapering towards the ends as shown. The wires were supplied by Flow Corporation, Cambridge, Massachusetts, (manufacturers filament code no. W1), and

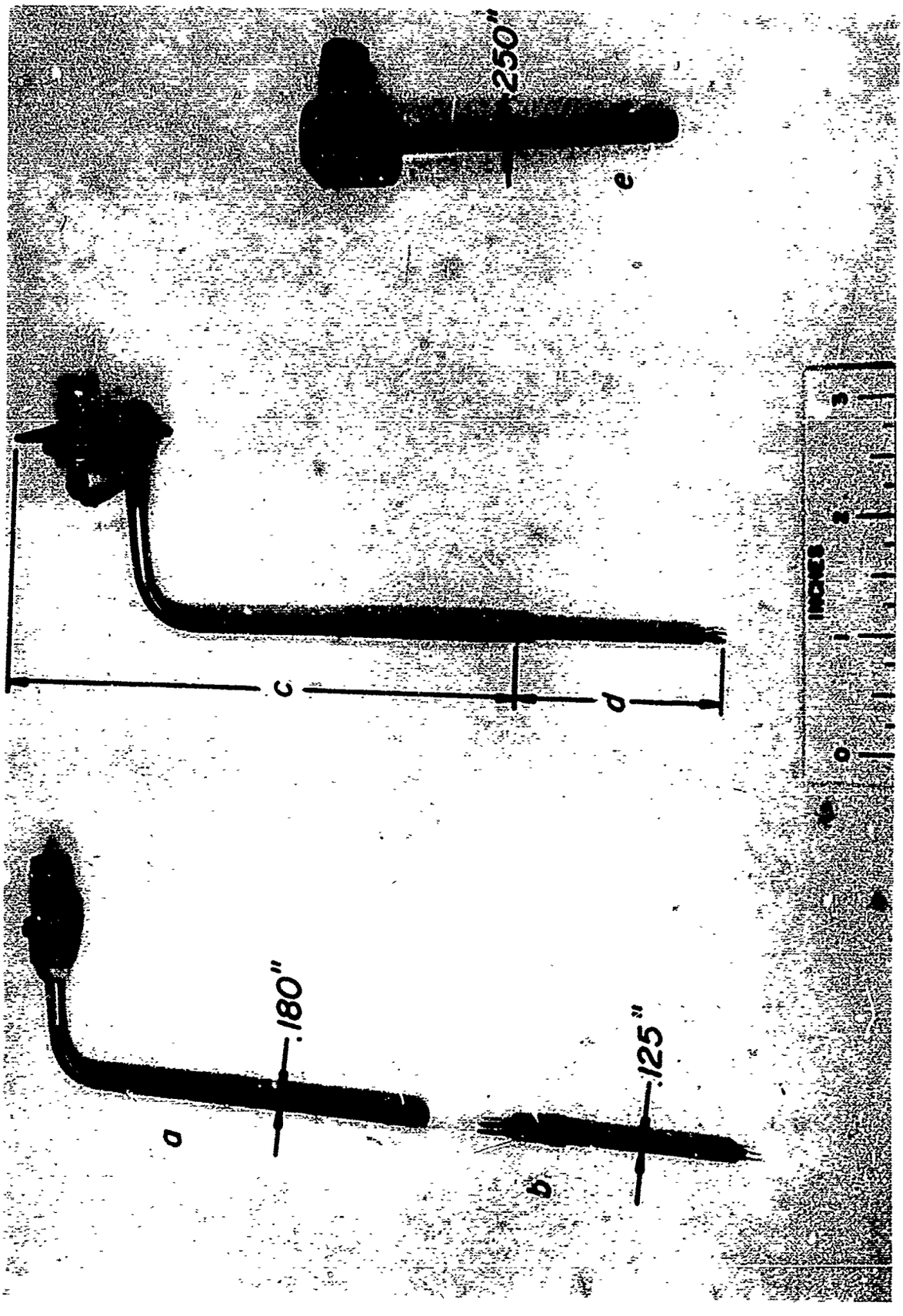

JP 17 P-3 G7

Figure 48

are tungsten, ~.00015 in. in diameter.

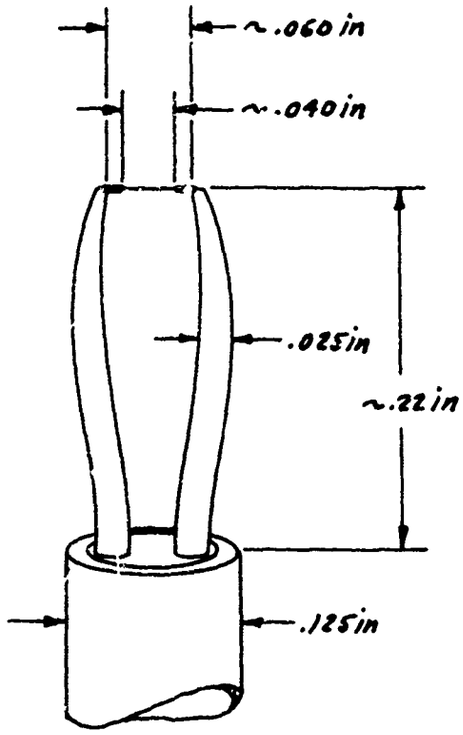

FIGURE 49

As supplied the wires are spool mounted, and copper plated and tinned over their entire length except for a bare section ~.040 in. long. The wires are soldered to the sensor holder under a 30x binocular microscope with the wire probe, soldering iron and the spool-mounted wire held in 3-direction micrometer movements. The tip of the soldering iron (25 w) is extended with a short length of no. 22 (~.025 in.) wire which is actually used for the soldering operation. All-state

no. 430 silver solder and no. 430 flux are used. To reduce deposition of flux on the wire, the latter was moved away when the needles were tinned. After allowing a short time for burning off excess flux, the spool mounted wire was moved up until the tinned sections of the wire rested lightly in the needles, with the bare section of the wire roughly centered in between the needles. For reason described later the wire was mounted with some slack present, rather than taut. The tip of the wire attached to the soldering iron was then brought up below the joint to be made until the solder melted, making the joint. The soldering iron wire did not have to be brought into contact with the needle; heat conduction through the air was sufficient to melt the solder. In fact, touching the needle with the iron usually caused the wire to slip off the needles. After the solder joints were made, the excess length of wire was broken off by bending back and forth using a razor blade. Despite the precautions taken, some condensation of vaporized flux on the wire was usually observed on the wire after the latter was mounted. Also thin filaments of the glue used to mount the wire on the spool were frequently found stuck to the needle mounted wire. To clean the wire, it was dipped in a solution of concentrated sulfuric acid saturated with potassium dichromate for about one minute. To remove the excess crystals of this solution, the wire was then dipped in water, also for about one minute. Finally, the wire was dipped in ethyl alcohol to remove the excess water. After such cleaning, the wire appeared to be free of all attached glue filaments, and crystals, and the diameter of the wire appeared to be uniform indicating comparative freedom from deposits, when viewed under a magnification of $\sim$1000.

We now discuss the reason why the wire is slackly mounted (as mentioned previously). When a taut wire was used, oscillations at $\sim$20 KC (and sometimes at $\sim$40 KC) were observed on the output of the hot-wire amplifier. These oscillations could not be removed by adjusting the amplifier (this type of adjustment attempted is discussed in Section 4.7), but were observed to be almost entirely eliminated by the use of a slack wire. Also, the fundamental resonant frequency of the wire support needles, treated as vibrating free-clamped

beams was computed to be $\sim$ 16 KC. These facts lead the author to suspect that the observed oscillations were caused by the wire acting like a strain gauge when the needles vibrated (Figure 50). There is ample opportunity for excitation of such vibrations since not only is the airflow oscillating, but severe vibration of the whole test rig occurs due to the operation of the siren wheel drive system.

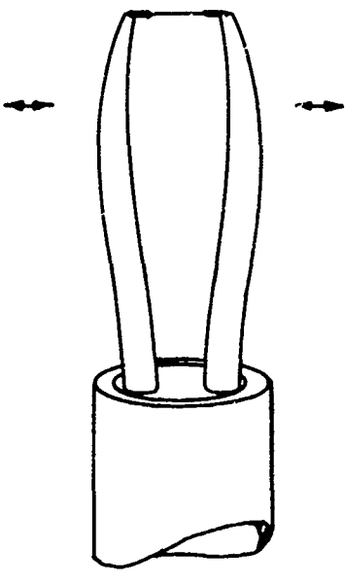

FIGURE 50

There is, of course, no conclusive proof that such strain gauge effects in fact do cause the oscillations observed on the hot-wire amplifier output; but nevertheless, the slack wires seemed to almost entirely eliminate the oscillation problems and were used for all measurements described herein.

4.7 Electrical Details of Hot-Wire System

The hot-wire amplifier is a Thermo-Systems, Inc., Model 1000A constant temperature unit. The basic circuit of the amplifier is sketched in Figure 51. A stabilized differential voltage amplifier of

gain $\sim$ 1000 (Amp. 1, Figure 51) and a current amplifier of gain $\sim$.93 (Amp. 2, Figure 51) are used in the feedback path. Ideally, such a system should be stable no matter how high the gain, but in practice unavoidable phase shifts in the bridge and amplifiers can cause instabilities at high gains.

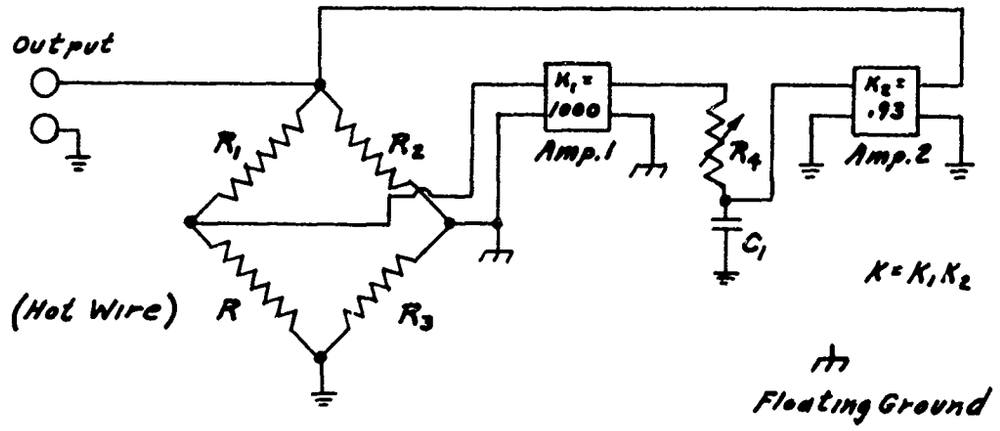

FIGURE 51

Phase shifts in the bridge circuit are kept to acceptably low values by (1) compensating for inductance and capacitance introduced by the cable leading to the hot-wire probe (in series with R, Figure 51) by another cable inserted in series with R_3 and (2) by providing variable capacitors in parallel with R_1 and R_2 which may be adjusted to reduce phase shifts to a minimum. The destabilizing effects of phase shifts in the bridge circuit and amplifiers may also be reduced by adjusting potentiometer R_4 which (with capacitor C_1) produces a variable phase lag between the amplifiers. The effective gain of the feedback amplifier system may be altered by changing the reference voltage in the differential amplifier (Amp. 1, Figure 51) so that the bridge normally operates unbalanced, and hence some fraction of the output voltage of Amp. 2 appears directly on the input of Amp. 1, in addition to those voltages caused by resistance changes of the hot-wire due to the changing

current. Depending upon in which direction the bridge is unbalanced, the wire current change produced by a given wire resistance change will be larger or smaller than the corresponding value with the bridge balanced, and hence, the effective amplifier gain is altered. This method of controlling the effective gain of the feedback amplifier system was not used because of the slight bridge unbalance so produced; rather the differential amplifier reference voltage was adjusted so that the bridge was balanced as observed on the bridge galvanometer in the unit. Under oscillating conditions, this means that the bridge was operated at conditions of time average (not instantaneous) balance. In operation, the phase shifts of the system were minimized as follows: resistance R_4 was decreased until pronounced ringing appeared on the hot-wire amplifier output; then the capacitors in parallel with R_1 and R_2 were adjusted to minimize the ringing and finally R_4 was increased until the ringing just disappeared. R_4 was thus adjusted to produce the smallest possible phase-shift that would eliminate ringing.

The methods of calculating and measuring the wire frequency response are now briefly discussed. We use simple hot-wire theory, neglecting end effects and considering small perturbations. Calculations indicate that taking a typical hot-wire (dia. $\approx$ .00015 in., length $\approx$ .040 in.) and typical air conditions (P = 54.7 psia, T = 530° R) the fraction of the heat lost out the ends of the wire varies from $\sim$ .33 at 5 ft./sec. to $\sim$ .18 at 150 ft./sec. Also, of course, under the experimental conditions encountered, the fractional velocity fluctuations are not small. Despite these two facts, the simple frequency response calculation discussed above should give a rough estimate of the frequency capability of the wire system. The frequency response was calculated at a velocity of 45 ft./sec., which is near the average velocity in the duct under steady flow conditions ($\sim$ 36 ft./sec.). We first calculate the natural frequency of the wire alone, which would determine the frequency response of the wire if operated in a constant-current system. Under the simplifying assumptions made above (no end effects, small perturbations), the wire behaves a a simple first-order system with a frequency response as sketched on the next page.

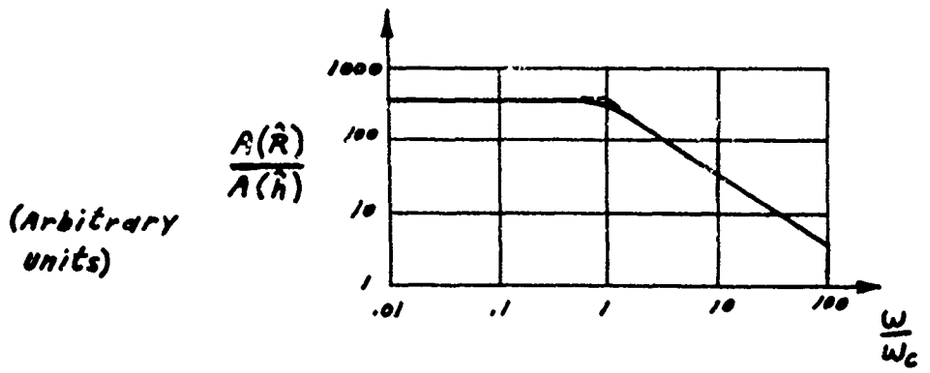

FIGURE 52

$A(\hat{R})$ = amplitude of wire resistance fluctuation

$A(\hat{h})$ = amplitude of heat transfer coefficient fluctuation

ω = frequency of heat transfer coefficient fluctuation

ω_c = critical frequency of wire

The critical frequency is given by

$$\omega_c = \frac{4\bar{h}}{R'\rho C_p D} \cdot \tag{48}$$

where $\bar{h}$ = average heat transfer coefficient of wire

ρ = density of wire

C_p = specific heat of wire

D = wire diameter

R' = wire resistance ratio = average operating resistance of wire (electrically heated) divided by resistance of unheated wire.

For the case discussed above, $f_c = \omega_c/2\pi = 576$ cps. When the hot-wire is used in a constant temperature system, (Figure 51), neglecting all phase shifts (other than those produced by the wire) in the bridge

circuit and feedback amplifier, considering small perturbations and the case where the total gain of the feedback amplifier is >> 1, and the bridge is operated at balance, the wire amplifier system behaves as a simple first-order system, but the critical frequency is now much higher than that of the wire alone when operated in the constant current system. The ratio of the critical frequency of the wire-amplifier (constant temperature) system, to that of the wire alone (constant- current operation) may readily be shown to be:

$$R_f = \frac{\omega_c'}{\omega_c} = 1 + 2K \frac{\left(\frac{\bar{R}}{R_1}\right)}{\left(1 + \frac{\bar{R}}{R_1}\right)^2} (R' - 1) \qquad (49)$$

where: ω_c' = critical frequency of wire-amplifier system

$\bar{R}$ = average value of R, see Figure 51

R_1, K - refer to Figure 51

For the Thermo-Systems, Inc. unit used in this work, K = 930 (Figure 51) and $R_1 = 56\,\Omega$. All our experiments were done with $R' = 1.3$, and a value of $\bar{R}$ for a typical wire under typical conditions was $8.51\,\Omega$. Under these conditions, $R_f = 64.9$. It should be noted that the improvement in frequency response is by a considerably smaller factor than the electrical gain of the feedback amplifier. This is partially due to voltage division across the bridge in the ratio $\bar{R}/(R_1 + \bar{R})$. The critical frequency of the wire-amplifier system was calculated to be

$$\omega_c' = R_f \omega_c = 37{,}400 \text{ cps.}$$

The critical frequency of the wire was measured by applying a 5 v, 1000 cps square wave to the wire through a 10 K resistor as sketched on the following page. Air conditions were: pressure ≈ 54.7 psia, temperature ≈ 530° R, velocity ≈ 36 ft./sec. A typical hot-wire operated with $R' = 1.3$, resistance R_4 (Figure 51) set to zero (no phase shift between the amplifiers) and the bridge balanced was used. The output of the hot wire system was as sketched also on the following page

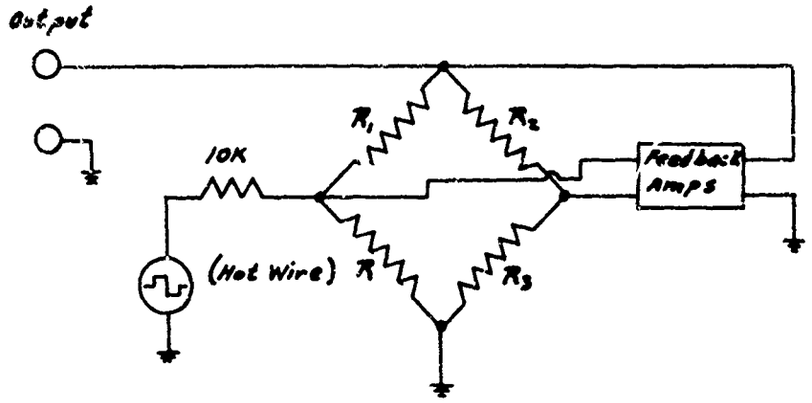

FIGURE 53

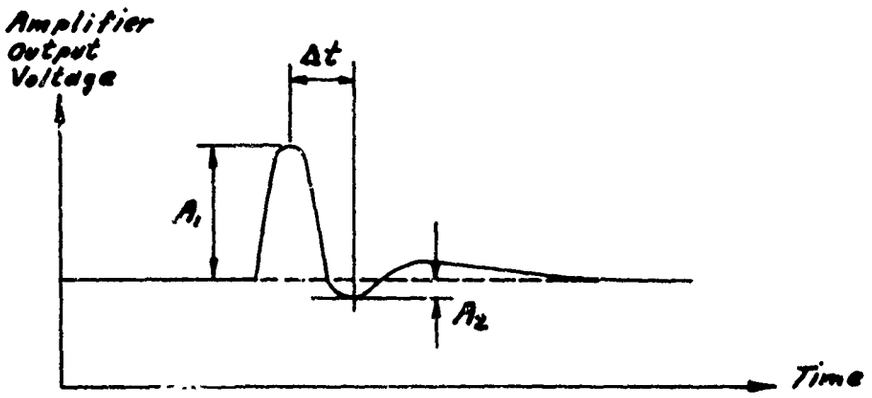

FIGURE 54

(Figure 54, slight ringing present). (It was noted that the rise time of the input square wave pulse was much smaller than Δt, so that the wave shape of Figure 54 is very closely representative of the response of the hot-wire system to an ideal square wave.) The critical frequency is estimated as

$$\frac{A_2}{A_1} = e^{-\omega_c' \Delta t} \tag{50}$$

The value obtained thus experimentally was $\omega_c' = 23{,}900$ cps, in moderately good agreement with the theoretically calculated value given previously. Since the fundamental frequencies of the oscillations in the airflow studied were 270 and 390 cps, and the hot-wire in general should be able to follow frequencies as high as 2-3000 cps with only slight phase shifts and amplitude losses, the output of the hot-wire system should very closely be interpretable directly in times of a steady-state calibration curve. There is one situation in which the hot-wire is unable to follow the variations of the gas velocity. Since, in our studies, the airflow often reverses, there is a short time period in each oscillation cycle during which the flow velocity is near zero. When the velocity is near zero, $\bar{h}$ in Equation (48) is much smaller than for the case calculated previously (vel. $\approx$ 45 ft./sec.) and consequently ω_c is much reduced (we assume here, that the airflow field around the wire remains quasi-steady; this assumption too, may break down at $v \approx 0$). Under there conditions, the wire cannot follow the velocity fluctuations. The wire output under conditions of reversed flow is typically as sketched in Figure 55. It is always observed that E_{m1} and E_{m2} are substantially greater than E_0. However, the errors only become important at velocities less than 5 - 10 ft./sec. and then only during a small fraction of the cycle. Since the peak-to-peak velocity is typically 100 - 200 ft./sec. the above phenomena should cause negligible errors in the time average velocity profiles, and will cause substantial errors in the instantaneous velocity profiles only where the velocity is $<$ 10 ft./sec. which is in a very small number of the latter profiles.

We discuss briefly certain aspects of the (steady-flow) wire calibration procedure. This consists basically of measuring the current drawn by the wire under various conditions of air velocity, pressure and temperature. (In our calibrations, pressure and temperature are held almost constant and only the velocity was varied). The wire bridge circuit, now shown in somewhat more detail is given in Figure 56.

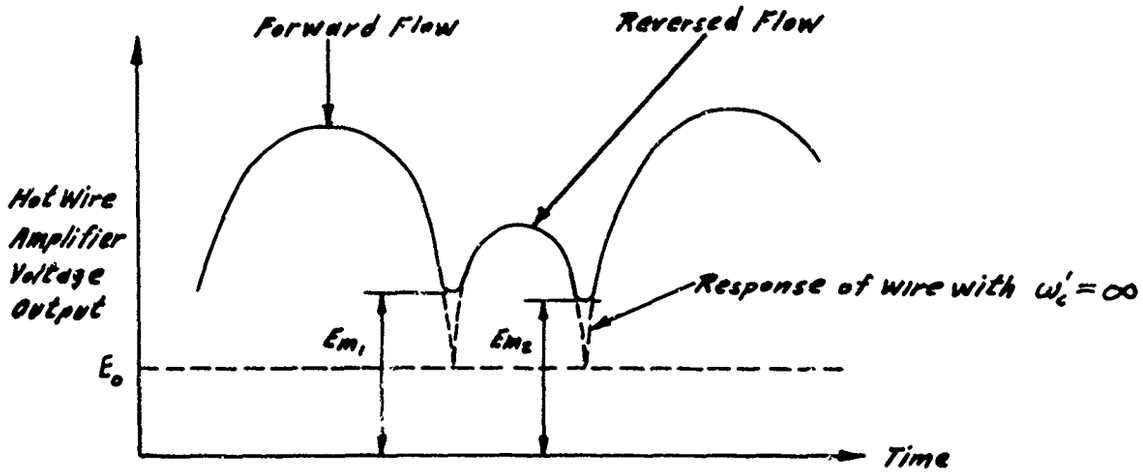

FIGURE 55

E_0 = voltage level to be expected for vel. = 0 from steady-state calibration.

The bridge output voltage is measured using a 1000:1 voltage divider and a hand balanced potentiometer. R_w is the resistance of the wire itself, while R_c is the resistance of the cable, wire support needles, etc. as determined by replacing the hot-wire with a piece of no. 22 copper wire and measuring the resistance of the cable, needles, etc. on a Wheatstone bridge. R_3 in the hot-wire amplifier unit is actually variable (3 decade resistors) and is now so shown. R_3 is used to set the value of R' as follows: the feedback amplifier is removed from the circuit by breaking at point E, and a low D. C. voltage (too small to heat the wire significantly) is applied intermittently to the bridge (between points A and C). The R_3 is adjusted until no voltage change is observed at point F when the D. C. voltage is applied to the bridge. This means that the bridge is balanced. From the known valued of R_1, R_3, R_2, and R_c, R_w (cold)

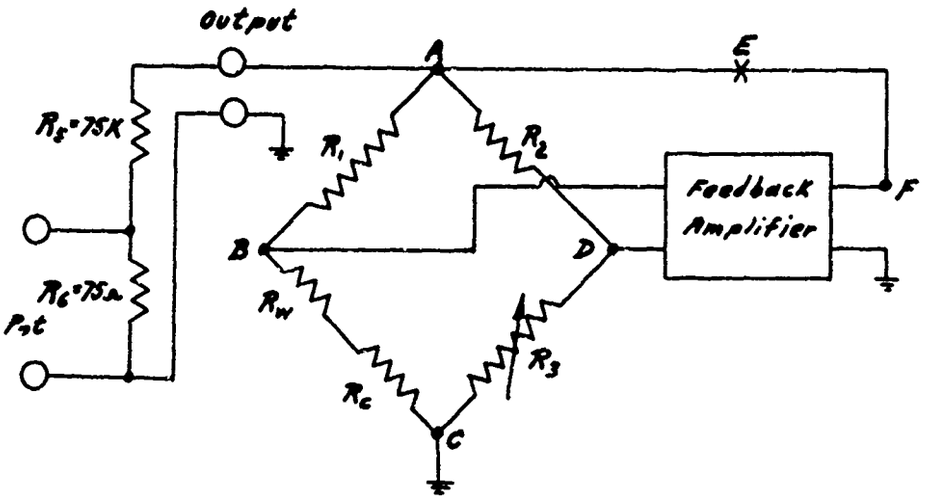

FIGURE 56

is determined. Then the low D. C. voltage is removed from the bridge, R_3 is set so that at balance $1.3 = R' = R_w$ (hot)$/R_w$ (cold) = $R_{w,h}/R_{w,c}$, and the feedback loop is closed. Then, by observing the bridge unbalance on a galvanometer inserted between B and D, the reference voltage of the differential amplifier (see pp.103-105) is adjusted until the bridge is in balance. Under oscillating conditions, the same procedure is followed; in this case, the bridge is in a time-average balance only. For the calibration, the voltage across A and C is measured using the potentiometer, and the wire current (I_1) calculated as

$$I_1 = \frac{\text{(voltage across A C)}}{R_1 + R_{w,h} + R_c} \qquad (51)$$

Slight errors in these methods of resistance and current measurements were observed as follows. By inserting precision resistors in place

of $R_w + R_c$ and measuring their resistance (point E open, Figure 56) on the bridge it was found that the resistance indicated by the bridge was about .07 Ω high over the range 4 - 10 Ω (which range included all hot-wires used). This error was taken account of in all velocity measurements made. Also the wire current determined from Equation (51) was found to differ from that computed taking the voltage BC (Figure 50) measured with a digital voltmeter, and the known value of $R_{w,h} + R_c$ (allowing for the previously discussed error in resistance measurement) by about .7%. The latter current measurement was considered as correct ('standard') In practice, currents had to be computed from Equation (51); however these were corrected to the equivalent 'standard' values using the correction factor .9928 determied from a small number of current measurements made in both ways.

4.8 Measurement of Parameters of the Wires

The measurement of the diameter, length, temperature coefficient of resistance, and thermal conductivity of the wires are now briefly discussed. These parameters will be used in the wire calibration procedure (Section 4.9) and in the data reduction (Section 4.12). The wire length (bare length of wire between the copper coated and tinned sections) was measured using a microscope of about 30x magnification with a calibrated reticle in the focal plane of the eye piece. The reticle was calibrated using a slide mounted 1mm scale with least division = .01 mm. From the reproducibility of the measurement, it was judged to be accurate to within $\pm$ 0.5%. The diameter of the wire was measured in exactly the same way using a magnification of $\sim$ 1000x, and taking the average of measurements at 6 - 8 different points along the wire length. The nominal wire diameter was .00015 in. Taking the wavelength of white light as $\sim$ 5500 Å $\approx$ .0000216 in., we see that the wire has a diameter of $\sim$ 7 wavelengths. Hence, it would be expected and is observed that the wire would appear considerably blurred under the microscope. On account of this, the above measurement is relatively inaccurate and estimated error limits are $\pm$ 4%. It was noted that the wires tended to be somewhat thicker than the nominal size, one wire for example being measured as .00016 $\pm$ .000006 in. in diameter.

The temperature coefficient of resistance of the wire was determined by measuring the resistances of the wire plus support needles plus cable etc., under the following two sets of conditions. The probe assembly [Figure 48, (c) and (d)] was immersed successively in Dewar flasks filled with ethyl alcohol at two different temperatures, room temperature and near the boiling point ($\sim 170^{\circ}$ F). The alcohol temperatures in the two cases were measured using mercury thermometers. These resistances were measured using the bridge of the hot-wire amplifier unit, allowing for the error of this bridge described in Section 4.7. Allowance was made, of course, for the cable resistance, the resistance of the stainless steel needles supporting the wire and the resistance of the copper wires joining the stainless steel needles to the BNC connector, (see Section 4.6). The resistances of the cable and the copper wires were essential identical for the measurements at both temperatures, but the resistance of the stainless steel needles was somewhat different at the two temperatures. A separate test, likewise in alcohol baths at two temperatures, with the hot-wire replaced by a piece of no. 22 copper wire, allowed the resistance and temperature coefficient of resistance of the needles to be determined. This made it possible to allow properly for the effect of the needles in the measurement of the temperature coefficient of resistance of the hot-wire. A list of the temperature coefficients of various wires measured as described above is given in Table 16. The reference temperature for the coefficients is 68° F. The wires are identified by the date they were mounted on the probe. In two cases, the coefficient of the same wire was determined twice. Three facts may be noted from Table 16. One is the fact that the coefficients are very different from the handbook value of .0025 $(^{\circ}R)^{-1}$ for tungsten. Secondly, the coefficients vary as much as 10% from wire to wire. Finally, in the cases where there are two determinations of the temperature coefficient of one wire, the two results agree within 2%. From the last point, we estimate the error in determining the temperature coefficient as $\pm$ 1%. The thermal conductivity of the wire is estimated using data from the wire calibration as discussed in Section 4.9.

TABLE 16

WIRE	CALIBRATION DATE	TEMPERATURE COEFFICIENT OF RESISTANCE $(^{\circ}R)^{-1}$
15 Jul. '66	same	.001805
10 Aug. '66	same	.002042
14 Sept.'66	same	.002040
31 Jan. '67	same	.001963
31 Jan. '67	25 Apr. '67	.001926
2 May '67	same	.001981
2 May '67	8 May '67	.002004

4.9 Calibration of the Hot-Wire

Calibrations are made in the same apparatus used for all the velocity profile measurements. (The apparatus is as sketched in Figure 31, with the steam-heated test section replaced by the hot-wire test section shown in Figure 44.) The wires are calibrated at 19 points over the range of velocities 0 - 180 ft./sec. The gas pressures and temperatures are 40 psig, and $\sim 70^{\circ}$ F, respectively. We first outline the method of determining the gas velocity at the various calibration points. Calibrations were taken with the hot-wire located at the center of the duct, and with the travelling test section (Figure 44) mounting the hot-wire in the extreme downstream position, so that the hot-wire is located about 49 diameters from the inlet of the duct. In order to cover the range of mass flows required, four different calibrated sonic orifices are used (see Figure 31), of diameters .0465, .1023, .200 and .292 in. (The .200 in. orifice is used in all test runs under oscillating and steady flow conditions.) The range of the variable area orifice (Figure 31) just upstream of the siren wheel, is insufficient to accommodate the necessary mass flows at a duct pressure of 40 psig.

Hence, about a foot upstream of the siren wheel, there is a fitting on the duct to which a piping network leading to three hand valves can be attached for calibration purposes. (This fitting is simply plugged when tests are being run.) The largest of these valves together with the variable area orifice, can pass sufficient mass flow at a duct pressure of 40 psig, to allow the air velocity at the wire of ~180 ft./sec. to be achieved. For the very low velocities, also, the range of the variable area nozzle is insufficient. In this case, a plate sealing on a sheet of rubber is used to block off the variable area orifice and the largest of the three hand valves is closed; under these conditions, the two smaller hand valves can be adjusted to pass the necessary mass flow at 40 psig duct pressure. For calibration, a list has been made up giving for each of 19 nominal air velocities at the wire, the orifice to be used and the pressure required on the upstream side of the orifice. To set the gas flow for a particular calibration point, the proper orifice is installed, the pressure on the upstream side of the orifice is brought to the proper value using the 0 - 500 psig pressure regulator (Figure 31), and finally the duct pressure is set to 40 psig using the variable area orifice (Figure 31) or the valves discussed above. Conditions are allowed to stabilize for 2 - 10 minutes, and than the following airflow measurements are taken (together with various hot-wire measurements, which will be discussed later).

1. Static pressure just upstream of calibrated sonic orifice - pressure tap 'E', Figure 31
2. Air temperature just upstream of calibrated sonic orifice - thermocouple 'C' Figure 31
3. Static pressure in duct - pressure tap 'F', Figure 31
4. Air temperature in duct - thermocouple 'H', Figure 31

From measurements (1) and (2) and the orifice coefficient, the mass flow can be determined. From measurements (3) and (4) the air density in the duct is computed. From the mass flow, the density of air in the duct and the duct area, the mean air velocity in the duct is computed. To check the ratio of the mean air velocity in the duct to the velocity at the duct centerline (the location of the hot-wire), a pitot probe, described below, was used. A photograph of the pitot probe, together

with the assembled hot-wire probe (see Figure 48, pieces c, d, and e are now put together) is shown in Figure 57. The smallest section of tube making up the probe tip is .021 in. O. D. by .005 in. wall, and the length of the section of the tip parallel to the flow is $\sim$.300 in. The pitot probe was designed to be similar to the hot-wire probe and was used through the same hole in the brass block and with the same traversing mechanism (Figure 46). The similarity between the probes is apparent from Figure 57. From the pitot probe and from a static hole in the brass block essentially in the same plane as the pitot tube entrance, lines were run to either of two oil manometers, depending on the velocity range being studied. The two manometers were a 36 in. vertical manometer and an 18 in. inclined manometer with a ratio of 7.2 to 1. The oil used was Dow Corning '200' Fluid, the specific gravity of which was measured, using a hydrometer, as .937. A first attempt to use colored water as the fluid led to the observation that with water, if the manometer fluid was displaced, and then allowed to seek its own level under conditions of zero differential pressure, pressure differences of as much as 1 in./H_2O (inclined) [$= \frac{1}{7.2}$ in./H_2O] would be indicated. Under similar conditions using the oil, the manometer returned to zero to within .02 in./oil (inclined). A number of determinations of the ratio of $\bar{v}$ (average air velocity) to v_m (air velocity at duct center-line) were made using the calibrated sonic orifice (see Figure 31) to determine $\bar{v}$ as outlined earlier in this section and the pitot tube to determine v_m. The Reynolds number range covered was about $3 \times 10^4 \longrightarrow 4.5 \times 10^5$ (corresponding to a $\bar{v}$ range of 11 - 162 ft./sec.). Below Re $\approx 5 \times 10^4$ the (inclined) manometer deflections were too small to allow accurate values of $\bar{v}/v_m$ to be measured. In the range Re = 5×10^4 - 4.5×10^5, the curve of $\bar{v}/v_m$ vs. Re experimentally obtained ran about 1% higher than that given in McAdams, (Reference 25) p. 155. In the range mentioned above, the curve obtained experimentally was used for all calculations. For the range Re $< 5 \times 10^4$, the experimentally obtained curve was faired into McAdams' curve, and the resulting curve used for calculations. Using the $\bar{v}/v_m$ curves obtained as described above, the air velocity at the hot-wire (v_m) was computed from the value of $\bar{v}$ known from the mass flow measurement.

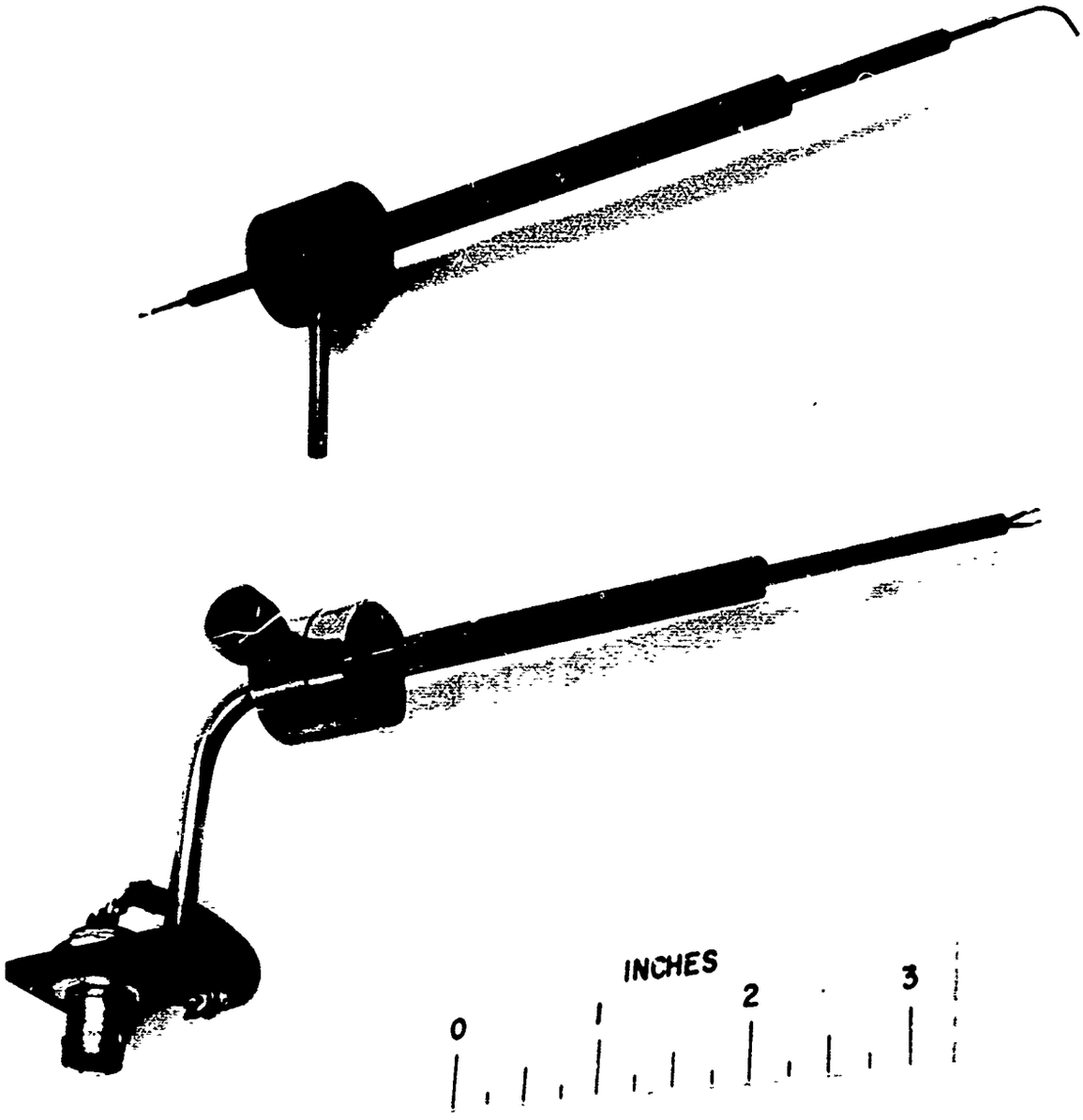

JP 17 P-4 67

Figure 57

Since there was some variation of gas temperature and pressure among the various calibrations points, it was decided to reduce all points to a standard temperature and pressure. To do this use is made of the following experimental correlation between Nusselt number and Reynolds number for hot-wires, obtained by Collis and Williams (Reference 26).

$$\frac{h_1 D}{K_F} = \left(\frac{T_F}{T_E}\right)^{.17} \left[.24 + .56 \left(\frac{\rho_F v D}{\mu_F}\right)^{.45}\right] \qquad (52)$$

where:

D = wire diameter

h_1 = heat transfer coefficient at wire surface

T_E = free stream temperature

T_F = film temperature = 1/2 (free stream temperature + wire temperature)

v = air velocity

μ_F = air viscosity

K_F = air thermal conductivity

ρ_F = air density

*evaluated at film conditions (T_F and the free stream static pressure near the wire).

It can readily be shown (Reference 27, pp. 7-11) that, for a given hot-wire, operated at fixed resistance ratio (R'), the wire current I depends only on h_1. Hence, a calibration point taken at given values of pressure and temperature can be reduced to an equivalent hypothetical calibration point at the standard pressure and temperature merely by requiring that the values of h_1 in the two cases be the same. This yields (using subscript C to denote standard conditions, and S to denote the conditions under which the measurement was actually made):

$$h_{1C} = h_{1S} \qquad (53)$$

$$K_{FC}\left(\frac{T_{FC}}{T_{EC}}\right)^{.17}\left[.24 + .56\left(\frac{\rho_{FC}v_C D}{\mu_{FC}}\right)^{.45}\right]$$

$$= K_{FS}\left(\frac{T_{FS}}{T_{ES}}\right)^{.17}\left[.24 + .56\left(\frac{\rho_{FS}v_S D}{\mu_{FS}}\right)^{.45}\right] \qquad (54)$$

Using the values of v_C obtained from Equation (54) (using a computer program) the calibration curve under the hypothetical standard conditions was constructed. Two points should be noted here. According to Reference 26, for $\frac{\rho_F v D}{\mu_F} > 44$, Equation (52) no longer applies and should be replaced by the equation:

$$\frac{h_1 D}{K_F} = \left(\frac{T_F}{T_E}\right)^{.17} \times .48\left(\frac{\rho_F v D}{\mu_F}\right)^{.45} \qquad (55)$$

In some cases, the highest calibration point taken had

$$\left(\frac{\rho_F v D}{\mu_F}\right) > 44.$$

In these cases, the transformation of the calibration point to standard conditions was done in a similar manner to that described above, but now using Equation (55). Since $\rho_F vD/\mu_F$ was fairly close to 44 in these cases, the difference caused by using Equation (55) instead of Equation (52) to compute the calibration point at standard conditions was quite small. For the point taken at zero velocity, the test rig was at atmospheric pressure instead of 40 psig. However, in one case, the wire was inserted into a special closed chamber which could be maintained at either 0 or 40 psig. For those two pressures, and at the same gas temperature, it was found that the wire current drawn at 40 psig

was $\sim$ 1.018 that drawn at 0 psig. In all subsequent wire calibrations in the test rig at zero velocity, this factor was used to convert the current measured at 0 psig to that expected at 40 psig. For the zero velocity calibration point, no attempt was made to correct for the difference of the gas temperature at which the point was taken from the standard conditions; rather the point was used directly on the calibration curve (after the above mentioned transformation from 0 to 40 psig was made). Slight errors in the calibration curve at standard conditions caused by this fact should be of little importance, especially since the wire never indicated velocities less than $\sim$ 5 ft./sec. under oscillating conditions (see Section 4.7, Figure 55, p. 109). The difference of the actual air conditions at the calibration points from the standard conditions were less than .2 psi and 20° F for almost all points.

The calibration curve was constructed as a plot of air velocity versus wire current at the standard values of free stream pressure (P_C) free stream temperature (T_{EC}), and wire resistance ratio (R'). The wire current was measured as discussed at the end of Section 4.7.

We now discuss the determination of the thermal conductivity of the wire and certain related points. To do this, we used the previously mentioned relation between h_1, I and R' obtained from Reference 27. This is given below.

$$(R' - 1) = \frac{1}{P^2} \left(1 - \frac{2}{PQ} \tanh \frac{PQ}{2}\right) \tag{56}$$

$$P^2 = \frac{\pi D h_1 L}{I^2 \alpha R_o} - 1 \tag{57}$$

$$Q^2 = \frac{L I^2 \alpha R_o}{K_w a} \tag{58}$$

$$a = \frac{\pi D^2}{4} \tag{59}$$

where I = wire current

L = wire length

α = temperature coefficient of resistance of wire at $68^{\circ}F$

R_o = resistance of wire at $68^{\circ}F$

K_w = thermal conductivity of wire

other symbols have been defined previously: all symbols are in the nomenclature.

For each calibration point (excepting the zero velocity point), from the airflow conditions (pressure, temperature and velocity) and the resistance ratio, R'(used to determine the wire temperature and from this the film temperature) a value of h_1 is calculated from Equation (52) [or Equation (55) if $\rho_F vD/\mu_F > 44$] using a computer. We call this value of h_1, h_{1F}. Also for each calibration point, as described at the end of Section 4.7, the cold resistance of the wire ($R_{w,c}$) and the current drawn by the wire (I) when operated at a set resistance ratio (R') are known. From the known values of α and $R_{w,c}$, R_o may be calculated. Hence, in Equations (56) - (59) R', I and R_o are known. From the measurements of the wire parameters (Section 4.8), D, L and α in Equations (56) - (59) are known. Hence, for each calibration point a value of h_1 may be computed from Equations (56) - (59) if a value of K_w is assumed. This value of h_1 is called h_{1w}, and is again calculated on a computer. For the determination of K_w, we proceed as follows: h_{1F} is calculated for all calibration points. Then assuming successive values of K_w, for each K_w value, values of h_{1w} are computed for all calibration points. Then, for all calibration points the fractional error $E_{Fh1} = (h_{1w}-h_{1F})/h_{1F}$ is computed for all values of K_w. The values of E_{Fh1} plotted versus air velocity with K_w as a parameter for the 31 January 1967 wire are shown in Figure 58. The values of K_w used were 50, 60, 70 and 75 BTU/ft-hr $^{\circ}R$. (Only 13 points were taken in this calibration.) At first we ignore the points plotted thus: □ . We see that the curve indicated by the points has the best shape (that is, is closest to being parallel to the $E_{Fh1} = 0$ line) for $K_w = 75$ BTU/ft-hr $^{\circ}R$. The handbook value for the thermal conductivity of tungsten at $\sim 150^{\circ}F$ (a typical value for the average of the free stream and wire temperatures) is $\sim$ 93 BTU/ft-hr $^{\circ}R$. The difference may be due to cold-working in the wire drawing process. From Figure 58, it can be seen that even when K_w is chosen to yield the best shape (K_w = 75 BTU/ft-hr $^{\circ}R$)

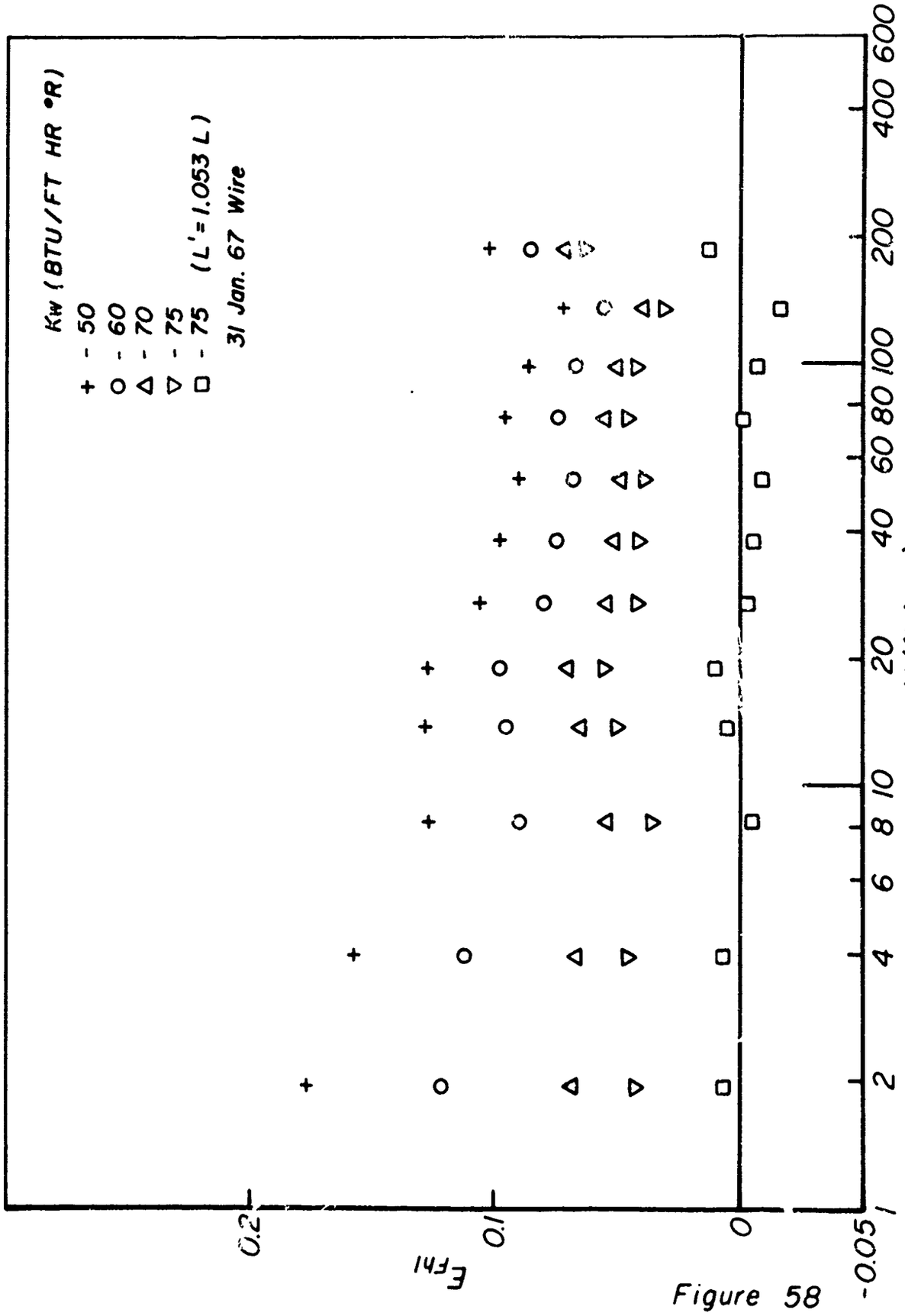

Figure 58

there is residual roughly constant value of E_{Fh1} at all velocities of $\sim$.045. In three other wire calibration, this residual value was $\sim$.02, $\sim$.00 and $\sim$.09. These residual errors may be due to errors in the measured values of α, L and D (see Section 4.8), especially the last, since as pointed out in Section 4.8, the estimated errors limits in the measurement of D are $\pm$ 4%. In order to bring the values of h_{1F} and h_{1w} into closer agreement, it was decided to arbitrarily change the value of the wire length from the measured value until the best agreement was obtained. This is a pure 'fudge'. By choosing K_w = 75 BTU/ft. hr. ^{o}R and L' = 1.053L (L' = 'fudged' value of L), the set of points marked $\square$ in Figure 58 is obtained. Here the absolute value of E_{Fh1} is less than .017 for all points and less than .009 for all but three points. By substituting these values of L and K_w into Equations (56) - (59) along with the measured values of α and D, we have an approximate relationship among R', h, and I for the given wire. This relationship is quite closely but not exactly (due to the 'fudging') based upon the true theoretical analysis. This relationship is used in the data reduction as described in Section 4.11.

4.10 Taking of Data

Velocity profiles were taken approximately under the conditions of Figure 42, Section 3.5. That is, oscillations at the 9th harmonic and with $\tilde{U}_A/\bar{U} \approx 2.4$ (roughly the maximum amplitude of oscillation which the test rig could produce). Profiles were taken at or very close to:

1. a velocity antinode
2. $\lambda/8$ downstream of a velocity antinode
3. a velocity node
4. $\lambda/8$ downstream of a velocity node

Each profile consisted of measurements taken at the following distances from the duct wall (in inches).

.001	.007	.05	.3	
.0015	.01	.07	.4	
.002	.014	.1	.5	
.003	.02	.15	.6	
.005	.032	.2	.73	(center-line)

We now describe how the data from the wall mounted Kistler pressure transducer (see Sections 4.1, 4.2 and 4.4) and the hot-wire, for a particular set of x - and y - positions of the hot-wire are recorded. (The details of the complete run procedure are given later.) The output of the Kistler charge amplifier (see Section 4.4) and the hot-wire amplifier (see Section 4.7) are fed to a Tektronix Model 551 dual beam oscilloscope. We assume that the desired oscillating conditions have been set, and that the wire is operating at the proper value of R' (feedback loop closed). The two oscilloscope traces are recorded on type 47 Polaroid 3000 speed film. Since there was considerable variation of the traces from cycle to cycle, an 'ensemble-averaged' cycle was obtained by 'synching' the 'scope on one of the two traces (whichever was more convenient), letting the 'scope free-run (instead of using single sweep) and opening the camera shutter for five seconds. (The averaging procedure will be discussed in more detail in Section 4.12.) Under the synched conditions about 1 1/2 cycles were visible on the 'scope face. The ensemble average obtained included every second cycle over a period of five seconds. The gains of both 'scope channels were set (after at least one hour's warm-up time) using the 1000 cycle square wave calibration signal from the scope, which was itself checked against the Ballantine Model 320 S/5 rms meter. To minimize parallax errors, when the above gain settings were made, the 'scope face was viewed from roughly the position of the camera lens, when the latter was in place. It was observed that the gain figures fell of slightly ($\sim$ 3%) for the top and bottom-most centimeters of the 6-cm high 'scope graticle, but the signals were positioned to minimize errors due to this fact. The data was read off the pictures by superimposing on the picture a 10 x 6 cm graticle with lines every .2 cm , which matched the photographed image of the 'scope screen graticle. The data reading is discussed in Section 4.11. In general, because of slight differences in the position of the 'scope camera for every run, the data reduction graticle did not automatically match the photographed image of the 'scope graticle. Hence, before every run, the 'scope camera position was adjusted until the above match was achieved. After this adjustment was

made, photographs were taken of the two square wave calibration signals mentioned above; this is the final check that, say, 100 mv on the 'scope input corresponds to 2 cm on the data-reduction graticle. (The 'scope gain settings always used were 500 mv/cm for the hot-wire signal and 50 mv/cm for the Kistler pressure transducer signal.) The camera was always set at 5 sec exposure and f/11; brightness of the photographed image of the trace was adjusted using the 'scope beam intensity control. To record the data, the camera shutter was opened for 5 sec, recording the (properly synched) traces of the Kistler transducer and hot-wire under oscillation conditions. Then a switch was thrown, removing the oscillation signals, and providing D. C. reference voltages on the two 'scope inputs. Finally, the camera shutter was opened for another 5 sec thus photographing the D. C. reference voltage traces superimposed on the oscillation traces. The switching circuit used to supply the reference voltages is sketched (somewhat simplified) in Figure 59. The oscilloscope channel taking the Kistler pressure transducer signal is A. C. coupled, and when S_1 is in the reference voltage position (position 2), the input to this channel is merely shorted, providing a zero input trace on the photograph. The oscilloscope channel taking the hot-wire signal is D. C. coupled and when S_1 is in the reference voltage position, a known D. C. voltage ($\sim$ 2.7 V) is applied to the 'scope input, thus providing a way to determine the D. C. voltage level of the hot-wire signal. The hot-wire reference voltage is measured before and after the test run using the voltage divider shown in Figure 59 and a hand balanced potentiometer. Mercury batteries are used for B_1 (Figure 59), and the voltage change during a 2 hr run is typically $\sim$ .002 volts. The 1 megohm resistor connected to S_1, sections 2 and 3, keeps the load on the battery the same whether S_1 is in the 1 or 2 position, since the input impedance of the 'scope is 1 megohm. Hence, the battery voltage measured on the potentiometer (S_1 in the 1 position) should be the same as that presented to the 'scope when the reference voltage traces are being taken (S_1 in the 2 position). We now discuss checks made on the drift of the 'scope amplifiers between the times of the photographing of the oscillation traces and the

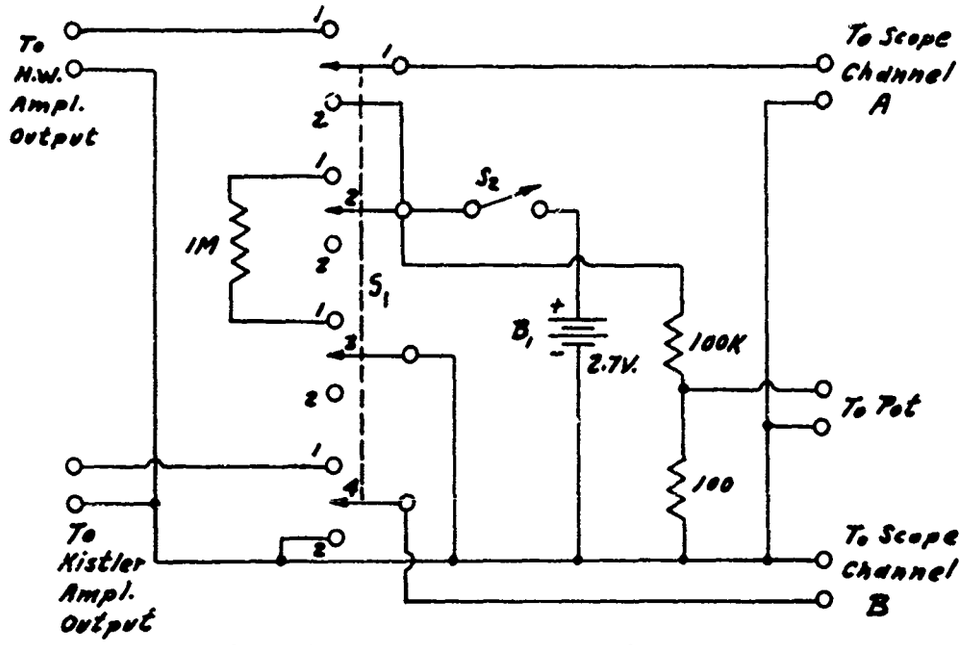

Channel A: D.C. coupled in 'scope
Channel B: A.C. coupled in 'scope

FIGURE 59

reference voltage traces. For this test on the A 'scope channel, the circuit sketched below was used (Figure 60). The audio oscillator frequency and amplitude were adjusted so that the combined output of the oscillator and battery was quite similar to the output of the hot-wire amplifier under oscillating flow conditions. Photographs were taken as described previously for an actual test run, with the oscillation signal being simulated by placing S_1 (Figure 60) in the 1 position, and the reference voltage signal simulated by placing S_1 in the 2 position. On the four photographs taken for this test, it was observed that the

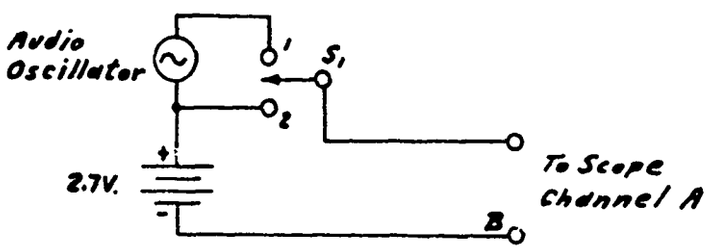

FIGURE 60

'reference voltage' trace was centered on the 'oscillation' trace (sine wave) perfectly, as far as could be determined using the deflection measuring technique that was employed to read actual data (see Section 4.11). Hence, errors due to 'scope amplifier drift in the 5 - 10 sec between the two exposures appear to be negligible. The same type of test was made on 'scope channel B (in this case, the battery B_1, Figure 60, was eliminated and points A and B connected together directly) with the same results.

We now briefly outline the run procedure. A run involves one axial setting of the hot-wire (x - position) and a traverse through all 20 radial positions of the hot-wire listed on p.123. The first step in the run procedure is to set the gap between the siren wheel and the downstream surface of the variable area nozzle assembly (see Figure 31). In the steam runs, this was adjusted after the airflow and oscillations were established to produce a desired strength of oscillation. For the velocity profile tests, all runs were made at the minimum gap (maximum strength of oscillation) setting of .019 in. The closest radial (y-) position of the hot-wire to the wall is then set using the microscope (see Section 4.5). The test section is then set in the desired axial (x-) position (see Section 4.2). The following electrical gear is then turned on:

1. Video Instruments power supply, Dana amplifier and Ballantine rms meter, - this gear is associated with the Dynisco pressure transducer system, (Section 4.3).
2. Kistler charge amplifier - this piece of equipment is associated with the Kistler pressure transducer system, (Section 4.4).
3. Thermo-Systems hot-wire amplifier and Tektronix oscilloscope - gear used with hot-wire probe (Sections 4.7 and 4.10).

Also the following gear is used: a hand balanced potentiometer to read thermocouples and an oscilloscope camera for taking the photographs. Then the thermostatically controlled water bath (Section 3.1, Figure 31) which regulates the temperature of the air supplied to the regulator is

turned on and the desired mass flow and duct pressure set (Sections 3.1 and 3.3). At this point, there is a wait of about one hour to allow the electrical equipment to warm up, and to allow the water bath and airflow to come to thermal equilibrium. The next step is the setting of the 'scope amplifier gains and camera position as discussed earlier in this section. Then the siren wheel is turned on, the average duct pressure returned to 40 psig and the siren speed set to resonance as described in Section 3.3. The hot-wire reference voltage is then measured using the potentiometer (this is described earlier in this section). The distance of the hot-wire from the wall is checked on the dial guage (Section 4.5) and noted down. This step is not done, of course, for those points farther from the wall than .150 in. (when the dial guage is disconnected as described in Section 4.5). We now begin the series of operations which are repeated 20 times [once for each radial (y-) position] during the course of the run. The hot-wire is brought into operation using the procedure described at the end of Section 4.7 (for calibration purposes, in that section), and the measured value of $R_{w,c} + R_c$ and the set value of $R_{w,h} + R_c$ recorded. Next the photograph is taken as described earlier in this section. After the photograph is taken, the hot-wire amplifier system is returned to a 'standby' mode by opening the feedback loop (Section 4.7), for safety purposes. At this point the air temperatures on the upstream side of the calibrated sonic orifice and in the duct are measured using the potentiometer and recorded (TC'S C and H, Figure 31). Also, the average duct pressure and the pressure on the upstream side of the calibrated orifice are noted on bourdon-tube gauges at the control panel and recorded (pressure taps F and E, Figure 31). The time and the rms voltage output of the Dynisco pressure transducer - Dana amplifier system (Section 4.3) are noted down. The latter is observed on the Ballantine rms meter. As in the case of the steam heat transfer runs, throughout the run, the mass flow (determined by the pressure reading on the upstream side of the calibrated orifice), the average duct pressure and the rms amplitude of the oscillation as measured by the Dynisco pressure transducer system are kept as constant as possible. After the above measurements are taken, the y- position of the hot-wire is rechecked on the dial guage and again recorded. Then the hot-wire is moved to the next desired

position, and the corresponding dial guage reading also noted down. For y- positions greater than .150 in., when the dial guage is not used (Section 4.5) and the y- position is determined by counting the turns on gear 'A' (Figure 46), the turns count on the gear is set at the required value before each picture is taken and is checked afterwards. This procedure takes the place of reading the dial guage for these cases. After the hot-wire is set to the next desired position the procedure described above is repeated. After all twenty y- positions have been surveyed, the hot-wire reference voltage is checked and recorded again using the potentiometer, and the airflow, siren, water bath and electrical gear are turned off in that order.

4.11 Reading of Data off Photograph

A typical oscilloscope photograph is shown in Figure 61. Time runs from left to right, the hot-wire amplifier output trace is at the top and the Kistler amplifier output trace is at the bottom. Hot wire voltages greater than the reference voltage appear below the hot-wire reference voltage trace while positive pressure fluctuations appear above the pressure reference voltage trace. The 'scope graticle appears faintly in the background. The vertical lines are scribed on the film with a knife and will be discussed below. The graticle and cross lines used to read off the data are shown in Figures 62 and 63. the vertical lines scribed on the film are located to pass through some sharp feature of the hot-wire trace and are scribed one cycle apart as nearly as possible. These lines are drawn perpendicular to the hot-wire reference voltage trace. The photograph is then taped to the surface of a desk. The graticle is positioned on top of the photograph so that one of its heavy horizontal lines (every fifth line, in both directions is cut heavier) lies on top of the hot-wire reference voltage trace, and one of its heavy vertical lines corresponds to the left hand vertical line scribed on the photograph. Weights are placed on the graticle to keep it in position. During the above alignment procedure and the following data taking procedure, the photograph is illuminated with red light, and the graticle lines with yellow light to allow the latter to readily be

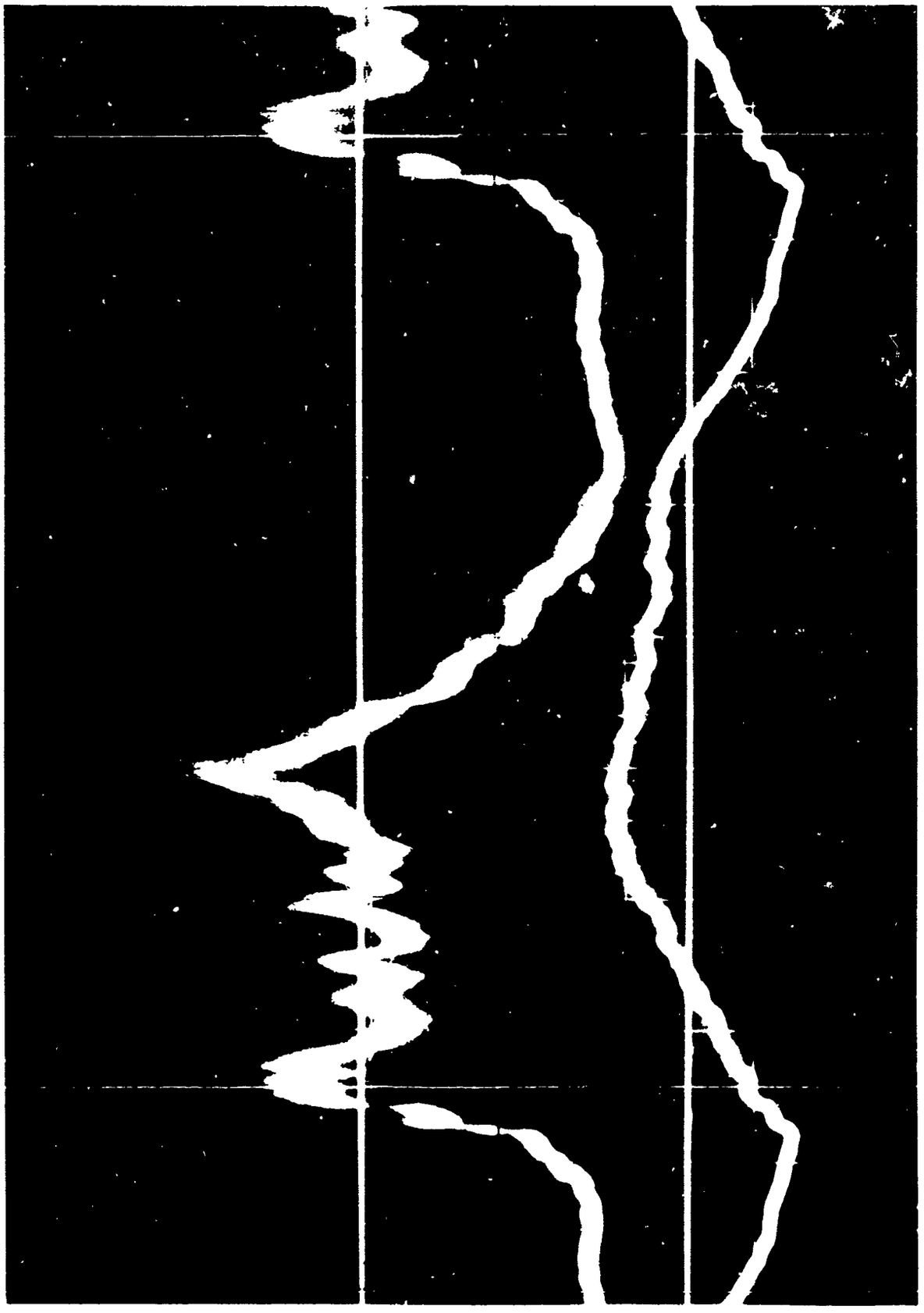

Figure 61

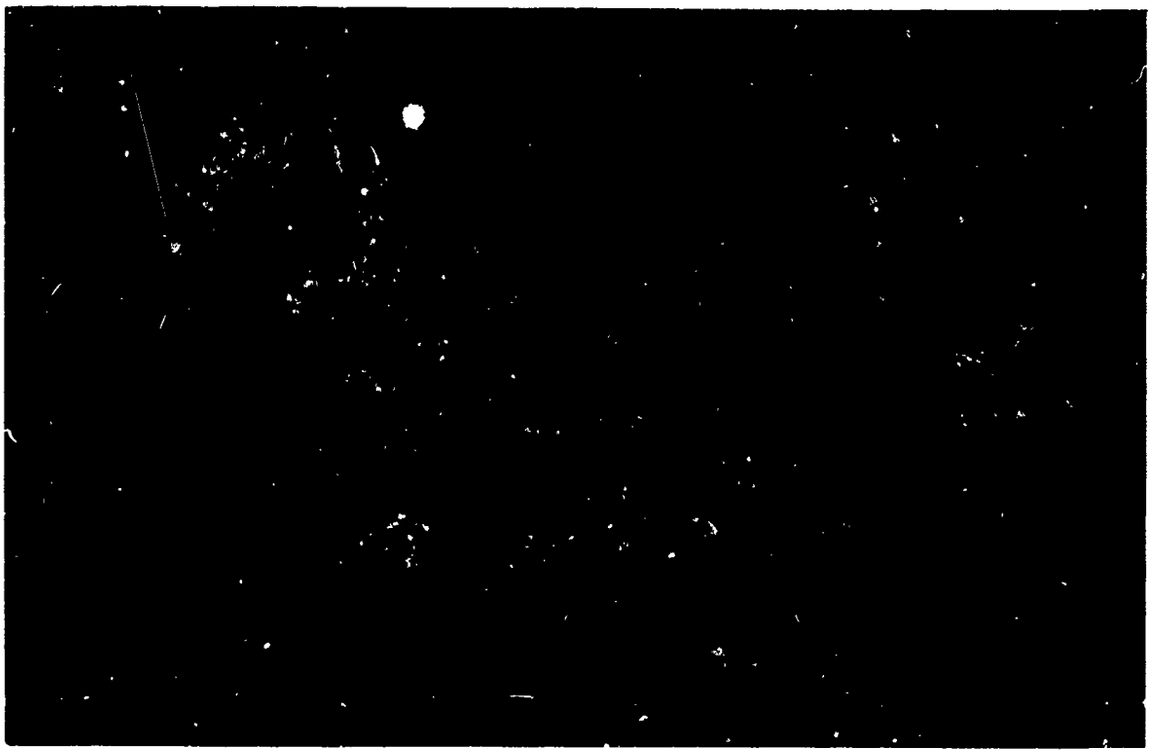

Figure 62

Figure 63

distinguished. At every vertical graticle line between and including the lines scribed on the photograph, the mean deflection of the hot-wire oscillation trace from reference voltage trace is estimated as sketched below (Figure 64). The horizontal cross line (dotted in Figure 64) is adjusted until it appears to bisect the oscillation trace (which is fairly broad, due to the averaging technique used, as discussed in Section 4.10). Then the deflection is read out and recorded.

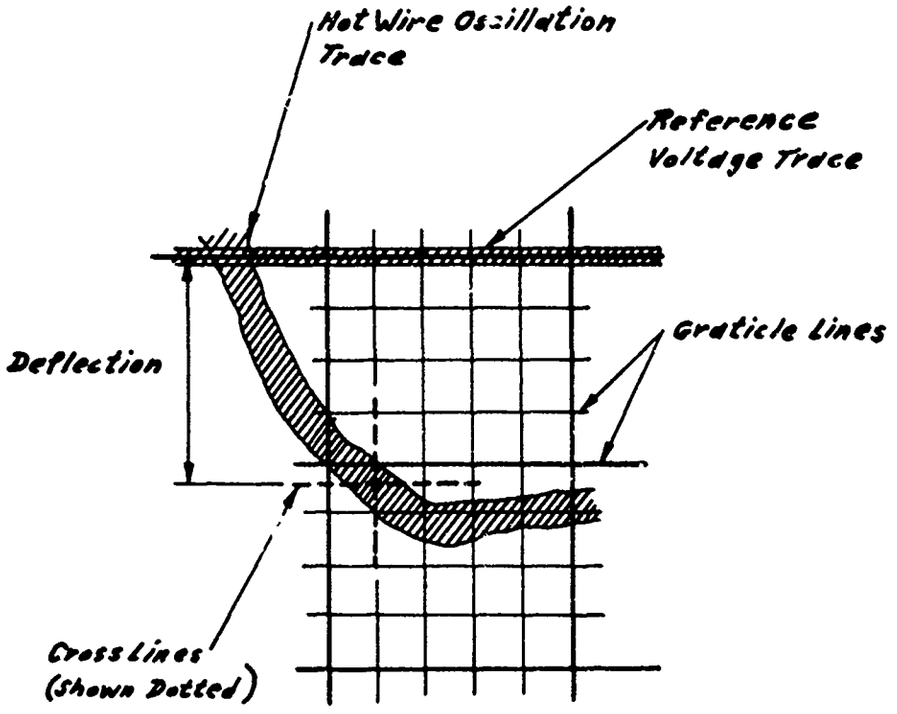

FIGURE 64

By comparing the results of reading out the data from the same picture twice (readings completely independent of each other), the error in this method of read-out was estimated to be less than $\pm$ .02 cm for most of the trace. At a few points in the cycle, the error could be somewhat larger, but these points were always at a low absolute gas velocities so that the error so produced was unimportant. Usually about 40 points were taken over the period of one cycle. The last data point read off the trace came at the location of the right hand line scribed on the film rather than at a graticle line. Thus the last interval between points read off the trace is smaller than all the preceding (equal) intervals. The fractional size of this interval was noted down. After the reading out of points was completed for the hot-wire trace, the graticle was shifted until one of its heavy horizontal lines lay on top of the Kistler reference voltage trace, and one of its heavy vertical lines lay on top of the left hand scribed line as before. Then the same read-out procedure was followed for the Kistler trace. The method of recording the data is shown in Figure 65. The data given is for the picture shown in Figure 61. The column headed DHW gives the deflections of the hot-wire oscillation trace from the reference voltage trace in cm. The column headed DK gives the same data for the Kistler trace. The sweep number is the identification number of of the picture, ZN is the total number of deflections read off the hot-wire trace and ZM is the fractional size of the interval between the last two points read off the hot-wire trace as discussed above. The column headed ZJ indicates whether, in the opinion of the person reading the data off the hot-wire trace, the flow velocity is in the forward (ZJ = +1) or reverse (ZJ = -1) direction, at the point in question. This data reading procedure was usually done by two men, one using the graticle and cross lines to read and call out the trace deflections, and the other writing down these values. To read the data off one picture took $\sim$ 1/4 hour, thus to complete reading for one run (20 pictures) required $\sim$ 20 x 1/4 = 5 hours.

PRINCETON UNIVERSITY
Department of Aerospace and Mechanical Sciences
Guggenheim Laboratories for the Aerospace Propulsion Sciences

Form No. G-1

FIGURE 65

Date: _____

By: _____

DATA SHEET

Research Number _____

DK	DHW	ZJ
CM	CM	—
SWEEP 2520		
ZN = 38		
ZM = 0.2		
- .46	- .46	+ 1
- .34	- .42	- 1
- .24	.24	
- .12	.18	
.0	.28	
.10	- .04	
.18	.30	
.34	- .28	
.44	- .02	
.52	.16	
.58	- .18	
.54	- .42	
.58	- .98	+ 1
.52	- .38	
.42	.0	

4.12 Reduction of Data

To start the data reduction procedure we construct an approximate relation between v, I, R', T_E, and P_E (free stream gas pressure) for the hot-wire of interest using material presented in Section 4.9. The experimental correlation given by Collis and Williams (Reference 26), [Equation (52)], provides a relation between h_1, T_E, P_E, v and R' for a given wire. (R' is needed to determine the wire temperature, T_w; from T_w and T_E, T_F is determined and thence, μ_F, K_F and ρ_F). The theoretical relationship, Equations (56) - (59), slightly modified as described in last part of Section 4.9, is used to relate h_1, I and R' for the given wire. Combining these two sets of equations to eliminate h_1, we obtain an approximate relation between T_E, P_E, v, R' and I for the wire in question. We note at this point that almost all the calculations described herein are done on a computer program. We consider the calculation of the flow velocity at one point in the cycle, i.e. at one of the points read off the hot-wire trace as described in Section 4.11. From the noted value of the deflections of the hot-wire oscillation trace from the reference voltage trace (as in Figure 65) and the known value of the 'scope gain, the difference of the instantaneous hot-wire amplifier output voltage from the reference voltage can be obtained. Adding to this the value of the hot-wire reference voltage obtained as described in Section 4.10 gives the absolute instantaneous value of the hot-wire amplifier output voltage. From the recorded value of $R_{w,h} + R_c$ (Section 4.10) using the correction procedure described at the end of Section 4.7, the wire current, I, is computed. From the deflection of the Kistler oscillation trace from the Kistler reference voltage trace (at the same time as the hot-wire deflection used above, of course), the gain of the 'scope and the sensitivity of Kistler transducer-charge amplifier system (Section 4.4), the difference of the instantaneous duct pressure from the average duct pressure can be obtained. Adding this to the recorded value of the mean duct pressure (taken as discussed in Section 4.10) gives the instantaneous free-stream gas pressure in the duct (P_E). From the known values of the instantaneous duct pressure, the time-average duct pressure, the time-average gas temperature in the duct (also taken as discussed in Section 4.10), and the isentropic relationship, the gas temperature in the duct at the instant of interest is calculated (T_E). From the recorded value of $R_{w,h} + R_c$ (Section 4.10) the hot resistance of the wire

was calculated allowing for the errors in the hot-wire amplifier bridge discussed in Section 4.7. Similarly, from the recorded value of $R_{w,c} + R_c$, the cold resistance of the wire was calculated. Then from the cold resistance of the wire (which is the resistance of the wire at the average gas temperature in the duct), the average gas temperature in the duct, T_E, and the wire temperature coefficient of resistance (α), the resistance of the wire at temperature T_E is calculated. The resistance ratio (R') is then calculated as the ratio of the hot resistance of the wire, to the wire resistance at temperature T_E. Now, in the above-mentioned approximate relationship among T_E, P_E, v, R' and I, we can compute v. This value of v we designate as v_2. Next, we use this approximate relationship, the value of I as determined above, and the values of T_E, P_E and R' appropriate for the standard calibration curve (see Section 4.9) to compute another value of velocity, v_1. v_1 is the velocity necessary to produce the observed wire current, I, if the wire were operated with the standard (calibration) values of T_E, P_E and R' and the approximate relationships between T_E, P_E, v, R' and I were strictly time. Finally a value of v, is interpolated directly from the standard calibration curve (the actual calibration points) of v versus I at the standard values of T_E, P_E and R' (as produced in Section 4.9). This value of v, we call v_5. The value actually taken for the gas velocity is

$$v_4 = (ZJ)\, v_5 \frac{(v_2)}{(v_1)} \tag{60}$$

where ZJ = +1 or -1 according as the flow is in the forward or reverse direction, respectively, (see Section 4.11). The philosophy behind the calculation of Equation (60) will be discussed referring to Figure 66. We consider the approximate relationship $v = f(I, R', T_E \text{ and } P_E)$ discussed previously. To reduce the problem to one which can be visualized in three dimensions, we consider T_E and P_E to be constants throughout the following discussion and hence we deal with a relationship of the form $v = f(I, R')$. In Figure 66, the surface $v = f(I, R')$ is surface ABCD. We also picture in Figure 66 the exact relationship (unknown) between

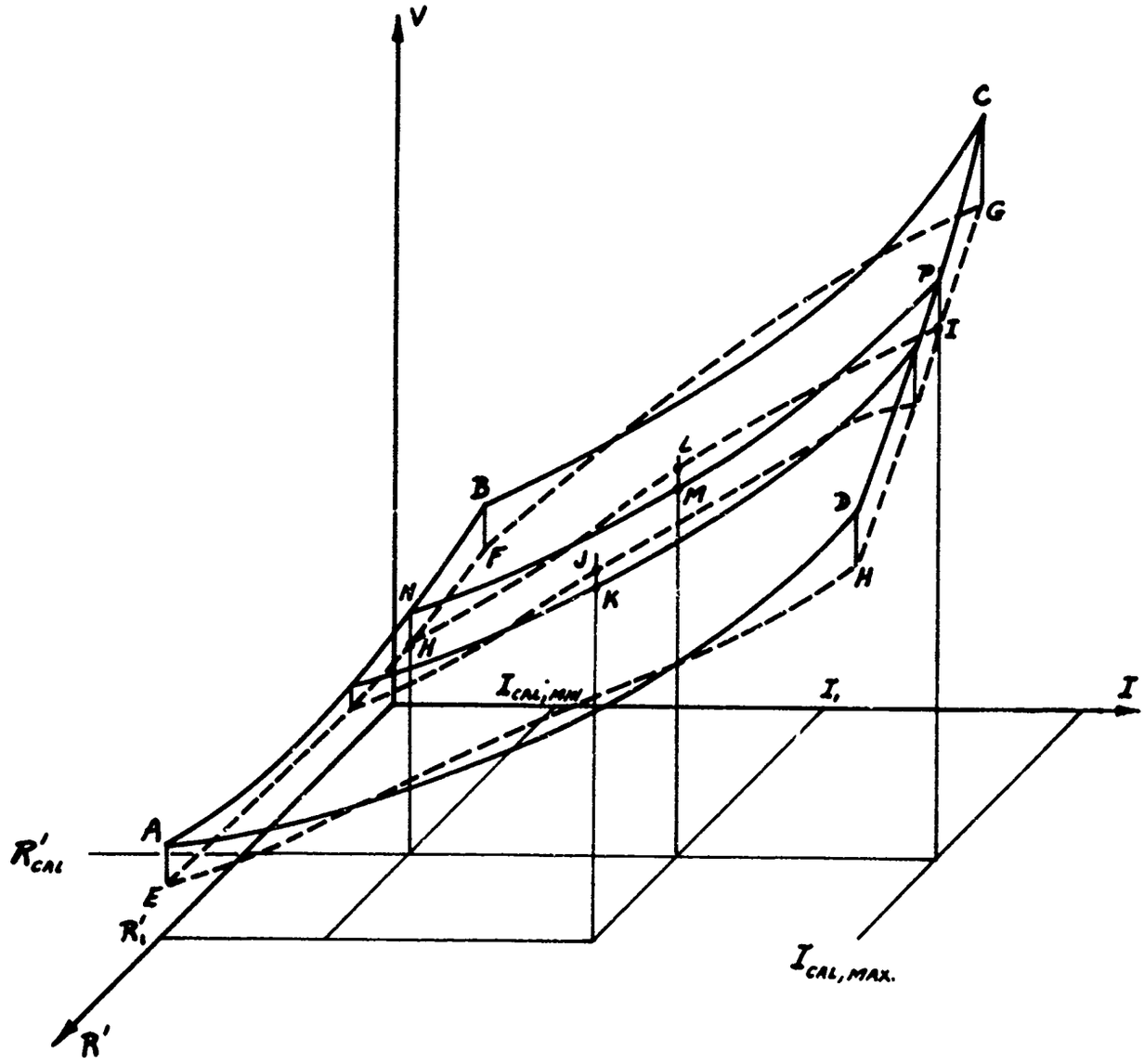

FIGURE 66

v, I, R' [v = g(I, R')] as surface EFGH. The line of intersection of v = g(I, R') and the plane $R' = R'_{cal}$ (the value of R' at which the calibration curve was taken) is known to within experimental error from the calibration procedure. This curve is curve HI in Figure 66. Let us consider a measurement yielding values of R' and I, R'_1 and I_1 respectively ($R'_1 \neq R'_{cal}$). Now, the v value corresponding to the measured values R'_1 and I_1 as computed by the approximate relation v = f(I, R') would be the co-ordinate v_K (Figure 66). (This corresponds to v_2 mentioned earlier.) The v value corresponding to the measured value I_1, and the calibration standard value R'_{cal}, is the co-ordinate v_M (corresponds to v_1). The v value taken directly from the calibration curve (for the measured value, I_1; the calibration being done at $R' = R'_{cal}$) is co-ordinate v_L (corresponds to v_5). The true value of the velocity at the measured conditions, R'_1 and I_1, is v_J. Now v_K and v_M are calculated from the known form of the approximate relation v = f(I, R') (surface ABCD) and v_L is taken from the known calibration curve (line HI). Assuming that the two surfaces, ABCD and EFGH are quite smooth and lie quite close to each other, we may estimate v_J as

$$v_J = v_L \frac{v_K}{v_M} \tag{61}$$

This, of course, exactly corresponds (except for the sign of ZJ) to Equation (60). (Note: from this point on, we allow P_E and T_E to vary again.) In actual fact, the surfaces corresponding to ABCD and EFGH would be the four dimensional surfaces $v = f(I, R', T_E, P_E)$ and $v = g(I, R', T_E, P_E)$ (in a five dimensional space) but the same method of computation of v_J (or v_4) applies. The fact that the two dimensional sections of the four dimensional surfaces $v = f(I, R', T_E, P_E)$ and $v = g(I, R', T_E, P_E)$ taken at $R' = R'_{cal}$, $T_E = T_{E,\,cal}$ and $P_E = P_{E,\,cal}$ corresponding to lines HI and NP in Figure 66) lie quite close to each other is shown by the following list of v_1 (corresponds to v_M) and v_5 (corresponds to v_L) values as computed for picture 2620. These values represent pairs of v co-ordinates taken along

the sections of $v = f(I, R', T_E, P_E)$ and $v = g(I, R', T_E, P_E)$ at various I values.

POINT	v_1	v_5	POINT	v_1	v_5
1	5.19	5.11	21	96.55	96.14
2	16.05	15.70	22	100.86	100.41
3	33.67	33.55	23	108.36	109.04
4	49.36	49.26	24	114.66	116.30
5	58.47	58.31	25	122.91	125.90
6	68.78	68.78	26	137.03	141.85
7	72.12	72.18	27	144.53	150.10
8	68.78	68.78	28	146.45	152.16
9	64.51	64.37	29	146.45	152.16
10	42.86	42.91	30	142.62	148.04
11	28.21	27.58	31	131.60	135.79
12	18.43	17.80	32	100.86	100.41
13	6.48	6.44	33	59.45	59.32
14	18.43	17.80	34	44.42	44.44
15	29.37	28.90	35	20.15	19.51
16	46.02	45.96	36	33.03	32.85
17	56.56	56.29	37	5.72	5.68
18	69.88	69.91			
19	77.96	77.96			
20	84.45	84.04			

Picture 2020 (v_i and v_5 in ft/sec)

The largest fractional deviation of v_1 from v_5 is $\sim 4\%$ at the highest velocities. The amount of disagreement of v_1 and v_5 above, of course, a reflection of the values of E_{Fh1} presented in Figure 58 (Section 4.9) for the curve marked ⊠ (Note here, that the data for v_1 and v_5 given above is not for the same hot-wire as the data given in Figure 58.)

For each point read off the hot-wire trace as described in Section 4.11, the air velocity (v_4) is calculated as described above. For each photograph, all of these v_4 values (about 40) are printed out on the computer output. Also, for each photograph an average air velocity over the cycle is computed as

$$\overline{v'} = \frac{\overline{\rho' v}}{\overline{\rho}} \tag{62}$$

and printed out in the computer output. The peak-to-peak velocity for each photograph is computed merely by hand scanning the computer output for the greatest and least values of v_4, and subtracting these numbers.

Two important points with reference to the averaging procedures used to compute the air velocities must now be discussed. The form of the wire calibration curve (obtained as discussed in Section 4.9) is sketched below (Figure 67).

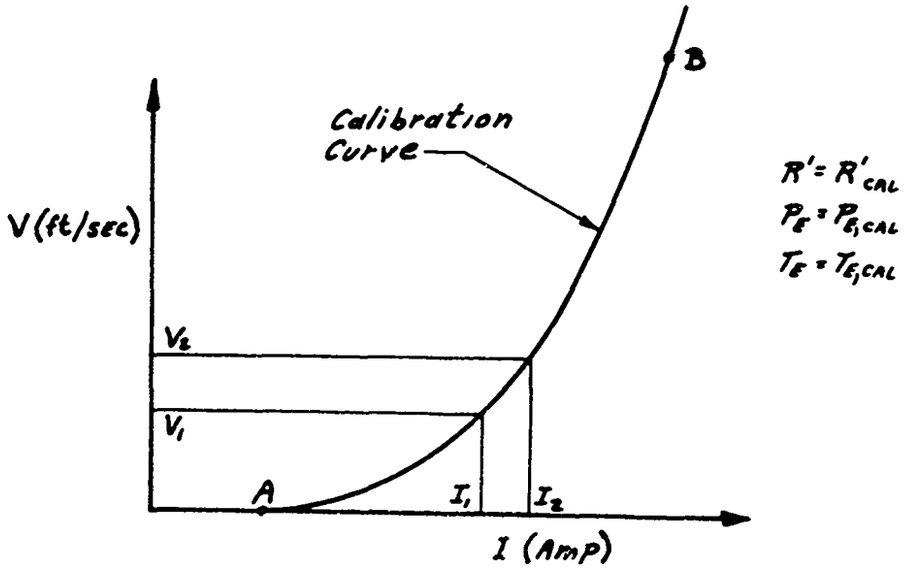

FIGURE 67

Now, estimating the center of the hot-wire amplifier out 'scope trace photograph (see Section 4.11, and Figure 64), at the instant in question, is roughly equivalent to estimating the average of a range of I values, say, I_1 to I_2. (The trace is fairly broad, since it is made up of many hundred cycles as discussed in Section 4.10). Because of the curvature of the calibration curve, the value of v obtained by averaging the I values and then transforming to v (through the curve AB, Figure 67) is different from the value obtained by transforming all the I values through curve AB and then averaging the v values so obtained. However, for almost all points taken off the hot-wire trace, the width of the trace (corresponding to range of I values I_1 - I_2) is small enough so that the portion of the calibration curve between I_1 and I_2 may almost be regarded as a straight line, and the averaging procedures described above are then almost equivalent. In this case, negligible errors are introduced by reading off what is essentially the average I values as is actually done in the data reduction process. This conclusion was reached by taking nine separate single sweep photographs of the hot-wire amplifier output, with the test rig operating under typical maximum amplitude oscillating conditions with the hot-wire located $\lambda/8$ downstream from a velocity mode and .2 in. from the duct wall. About forty deflections were read off each hot-wire trace over the period of one cycle, as described in Section 4.11. At corresponding points in the nine photographs the maximum variations of trace deflection was noted. This value gives, then, an estimate of the width of the band of I values over which an average would have to be taken when the usual data taking procedure (free-running oscilloscope) is used. (This width corresponds to the width of I values I_1 - I_2 in Figure 67.) From these estimates of the band widths, and the known curvature of the calibration curve, the errors caused by the averaging procedure actually used can be estimated. Out of 38 data points spread over one cycle, all except nine data points had errors from this cause estimated at 0.4 ft/sec or less. All except three data points had errors estimated at 0.8 ft/sec or less and the maximum estimated error was 2.8 ft/sec. The points with the largest estimated error values were at low velocities where the curvature of the calibration curve is greatest. Since typical instantaneous velocities

are 50 - 100 ft/sec, errors due to this cause should be unimportant except in a few low velocity points.

The second point involves the length of averaging time ('scope camera exposure) used. Figures 68, 69, and 70 show hot-wire velocity profiles taken under very similar conditions. In all cases conditions of time-average air mass flow and velocity were very similar. All data were taken at resonance at the 9th harmonic of the duct and with the gap between the siren wheel and the downstream surface of the variable area orifice (see Figure 31) set at .019 in., so that the amplitude of the oscillations set up are approximately equal for all three cases. In additions, data for all three figures was taken at an axial position $\lambda/8$ downstream of a velocity mode (this is denoted by the note x = 35 % on the Figures). In the earlier tests (Figures 68 and 69), fewer data points were taken for each velocity profile. We see that when single sweep oscilloscope photographs of one cycle were used (Figure 68), the scatter of the points on the velocity profiles is up to $\pm$ 3 ft/sec, making the data quite useless for analysis. When the photographs are taken of the free-running oscilloscope traces, thus yielding a cycle ensemble average over a period of 0.1 sec (Figure 69), the scatter of points is considerably reduced. Finally, when the ensemble averaging time is taken as 5 sec, (Figure 70) as was done for all data presented in this report (excepting Figures 68 and 69) the scatter of the data points was reduced to $\pm$ 0.7 ft/sec for the extreme cases, and in fact most points in Figure 70 appear to show scatter values less than $\pm$ 0.5 ft/sec. Profiles similar in scatter to Figure 70 were used in the analysis (see Sections 4.13 and 5). Part of the scatter observed in Figure 68 is likely due to turbulence in the flow. The scatter remaining in Figure 69 would imply eddy sizes of greater than 40 x 0.1 = 4 ft if attributed to turbulence. Since the duct has a diameter of 1.5 in., it appears that a considerable amount of scatter is due not to turbulence, but to relatively low frequency flow fluctuations due to some other cause. From Figure 70, it seems that these fluctuations are satisfactorily averaged out using a camera exposure time of 5 sec.

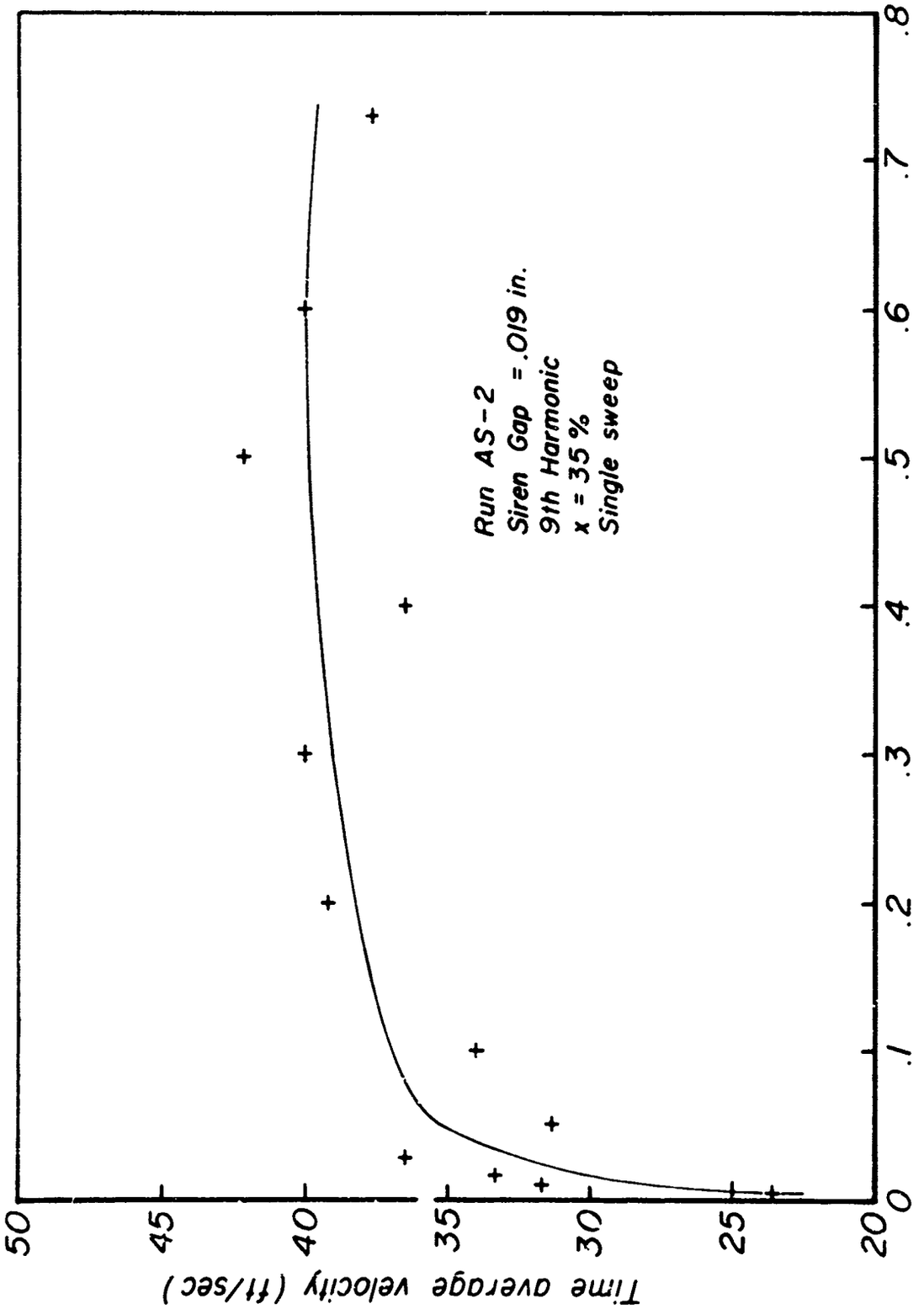

Figure 68

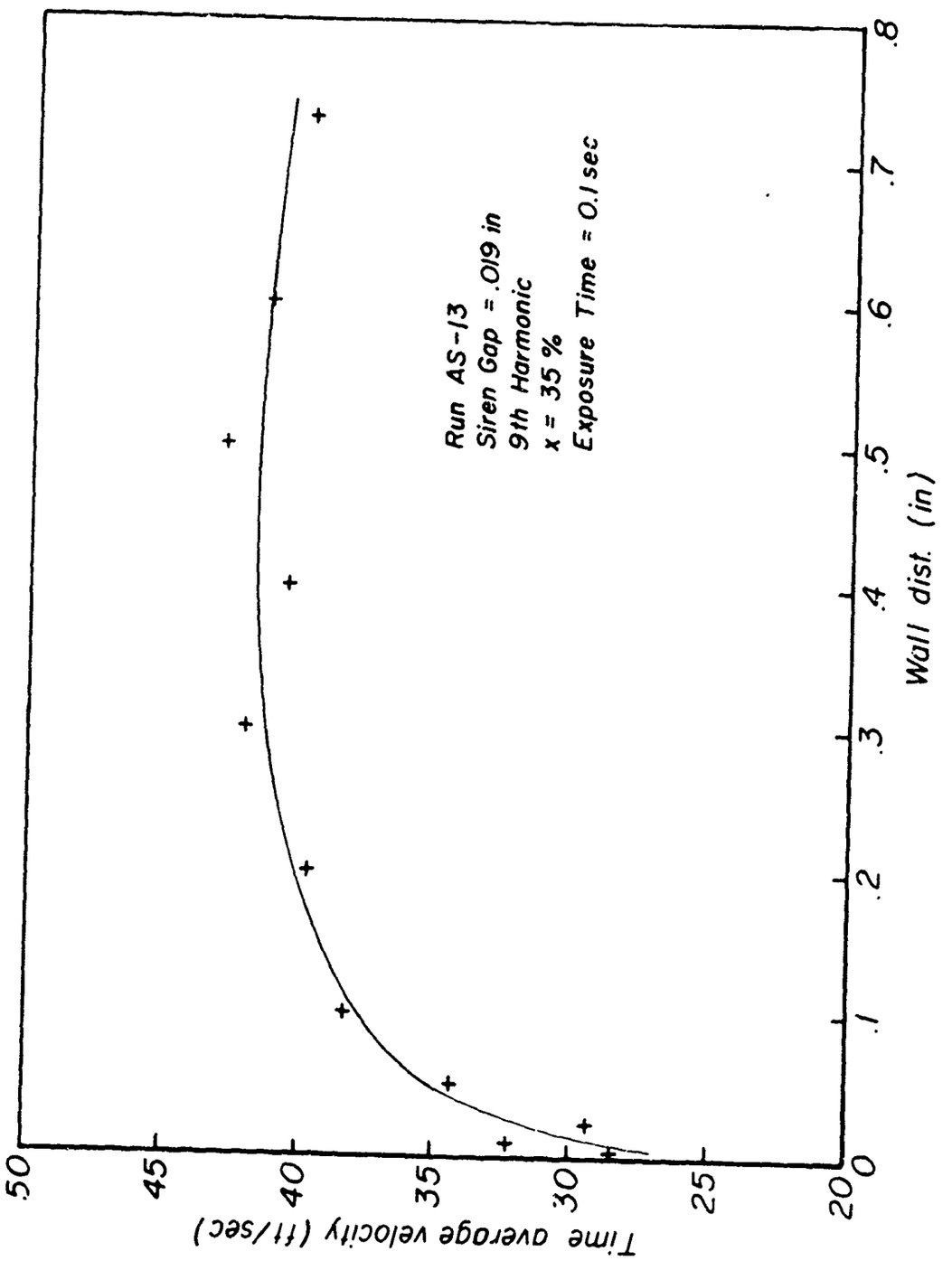
Run AS-13
Siren Gap = .019 in
9th Harmonic
x = 35 %
Exposure Time = 0.1 sec
Time average velocity (ft/sec)
Wall dist. (in)
50
45
40
35
30
25
20
0
.1
.2
.3
.4
.5
.6
.7
.8

Figure 69

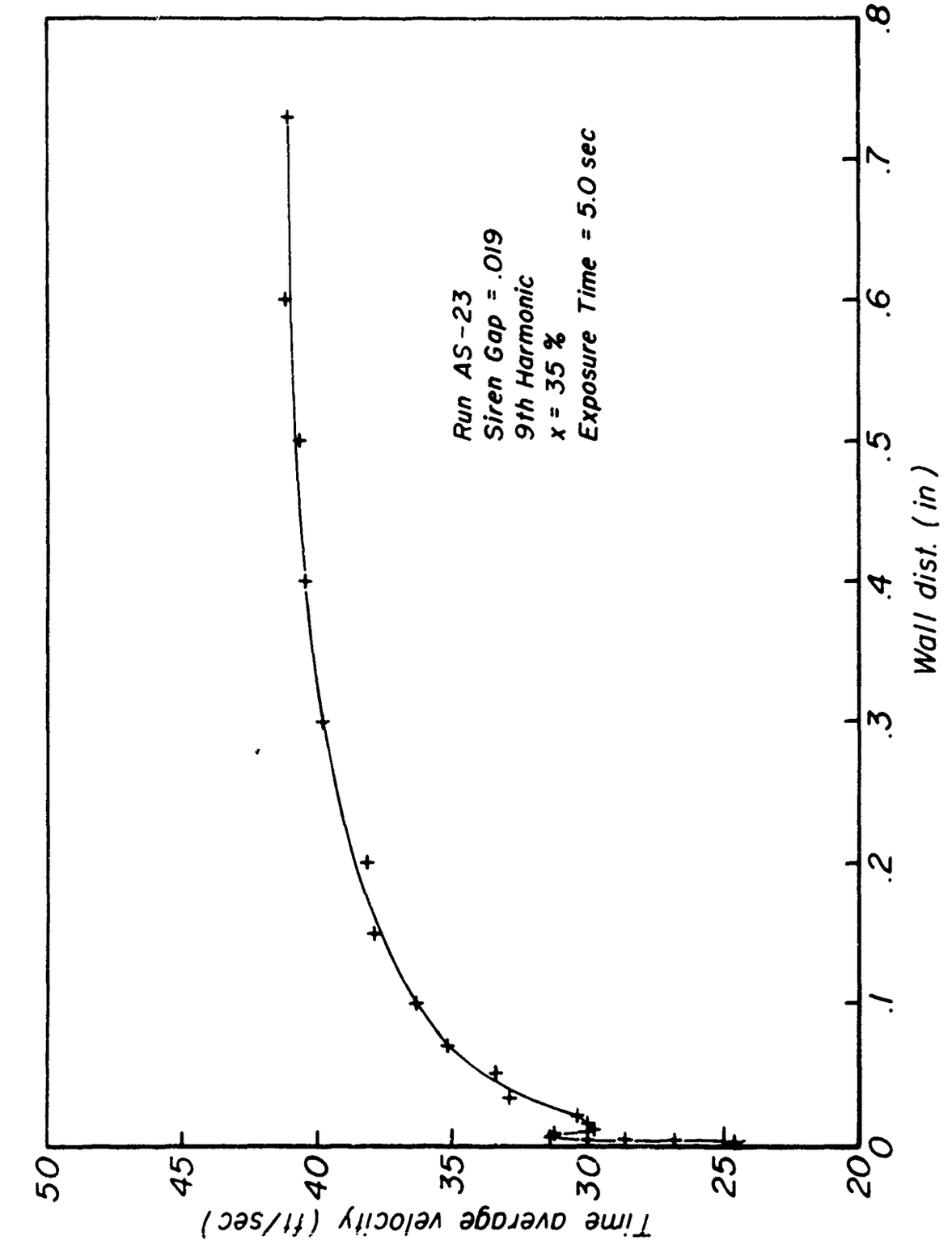
Run AS-23
Siren Gap = .019
9th Harmonic
x = 35 %
Exposure Time = 5.0 sec
Time average velocity (ft/sec)
Wall dist. (in)
50
45
40
35
30
25
20
0
.1
.2
.3
.4
.5
.6
.7
.8

Figure 70

4.13 Experimental Results

Experimental velocity profiles of

$$\bar{v}' = \frac{\int_0^T \rho v \, dt}{\int_0^T \rho \, dt} \qquad (T = \text{period of the oscillation}),$$

$$\bar{v} = \frac{1}{T} \int_0^T v \, dt \, ,$$

and

$\hat{v}$ = peak-to-peak velocity, computed as discussed in Section 4.12 are presented in Figures 71-92. Each of these profiles was taken at one of 4 axial positions along the duct. The relation of these locations to the node-antinode system in the duct is given in Table 17 [the x-position in % represents percentage deflection of the traversing test section (see Section 4.2); i.e. 100% (0%) represents the maximum upstream (downstream) excursion of the Section].

TABLE 17

Desired Location		Nearest Attainable Location
Description	x-position, %	x-position, %
$\frac{\lambda}{8}$ downstream of velocity antinode	107	100
velocity node	71	71
$\frac{\lambda}{8}$ downstream of velocity node	35	35
velocity antinode	- 2	0

downstream ↓

The wall distance given as the abscissae of all the graphs is the minimum distance of the hot-wire from the wall (see Section 4.5). We now briefly go through the data written on each figure. The run number identifies the

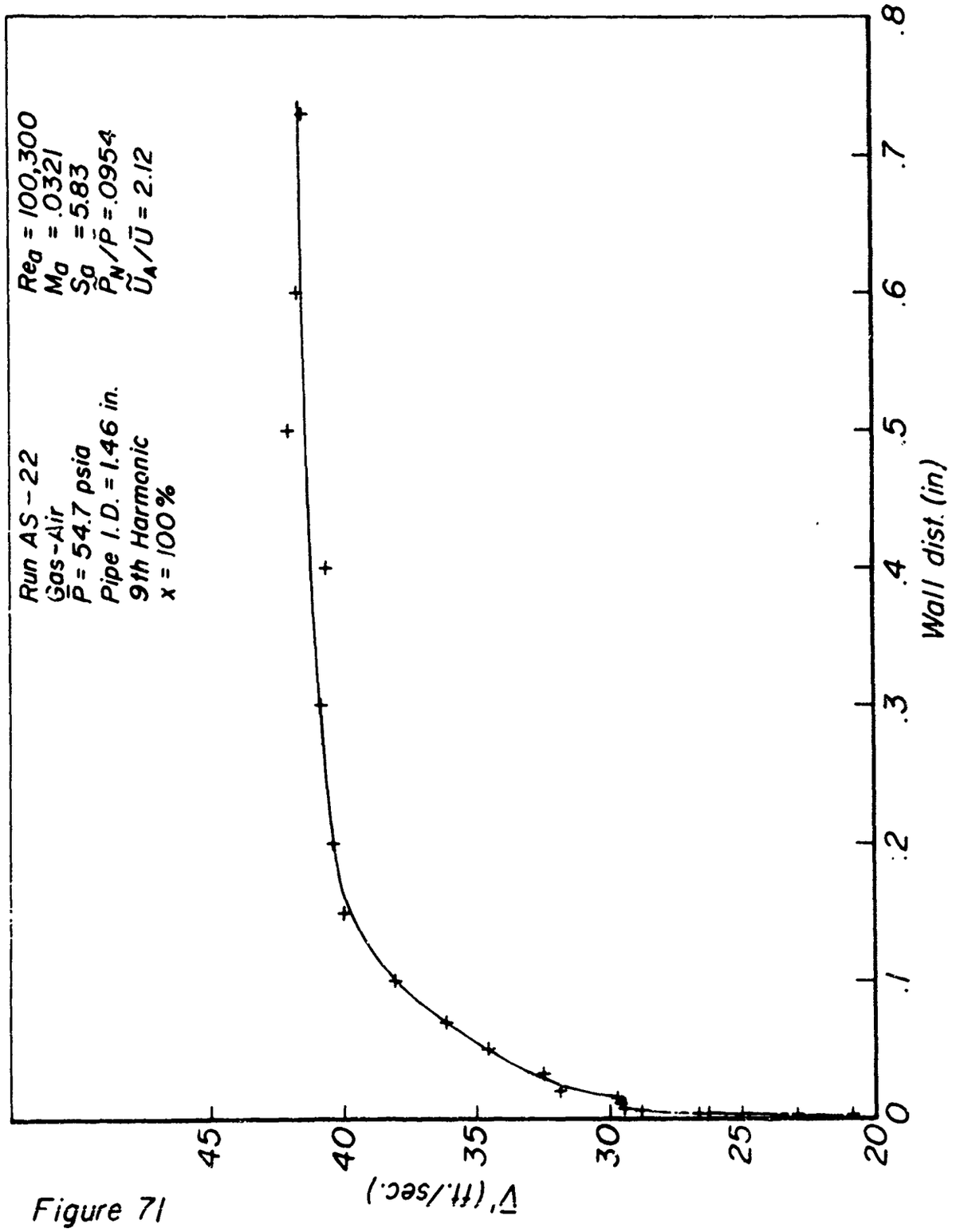
Run AS-22
Gas-Air
$\bar{P}$ = 54.7 psia
Pipe I.D. = 1.46 in.
9th Harmonic
x = 100%
Re_a = 100,300
M_a = .0321
S_a = 5.83
$\tilde{P}_N/\bar{P}$ = .0954
$\tilde{U}_A/\bar{U}$ = 2.12
$\bar{V}$ (ft./sec.)
Wall dist. (in)
45
40
35
30
25
20
0
.1
.2
.3
.4
.5
.6
.7
.8

Figure 71

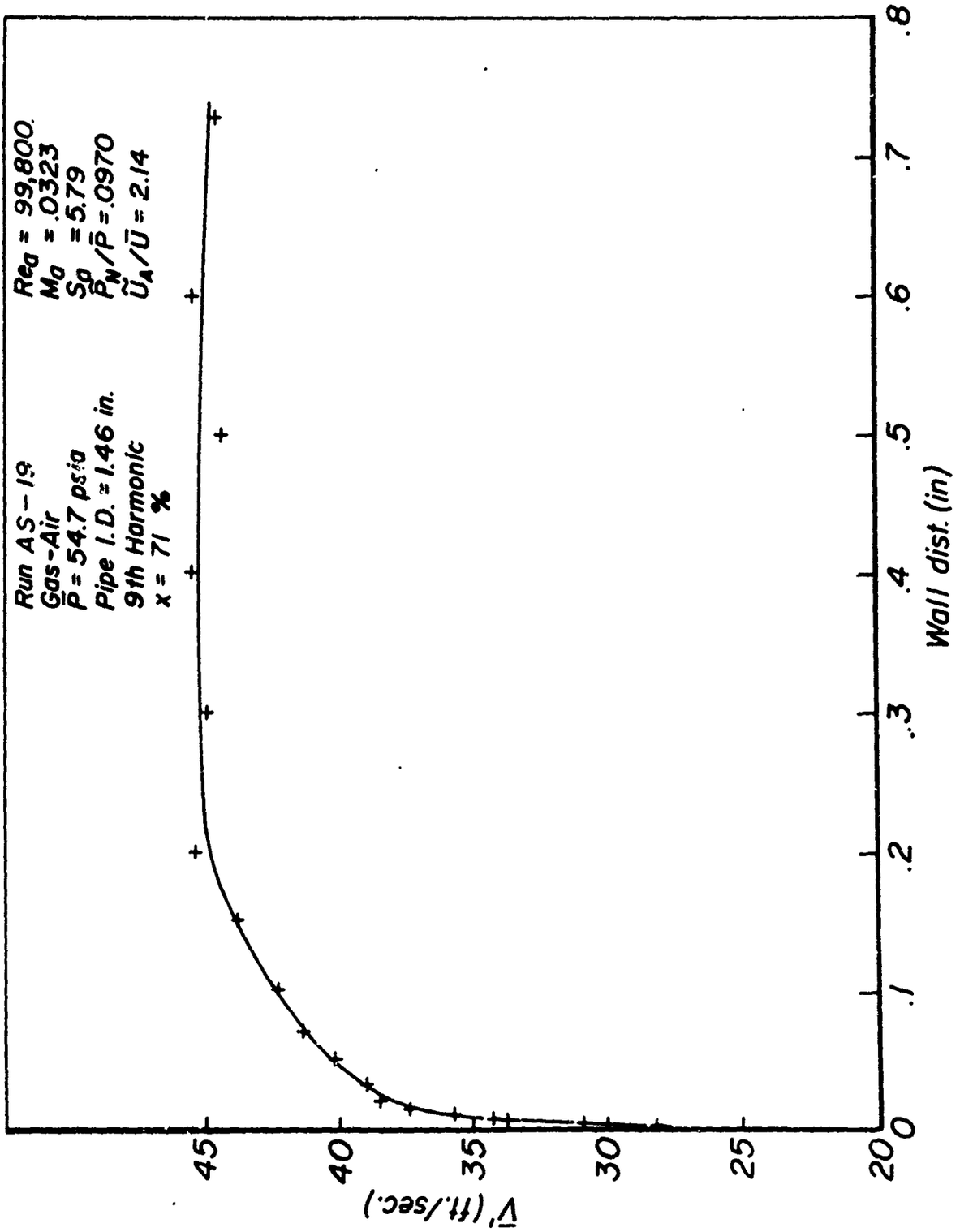

Figure 72

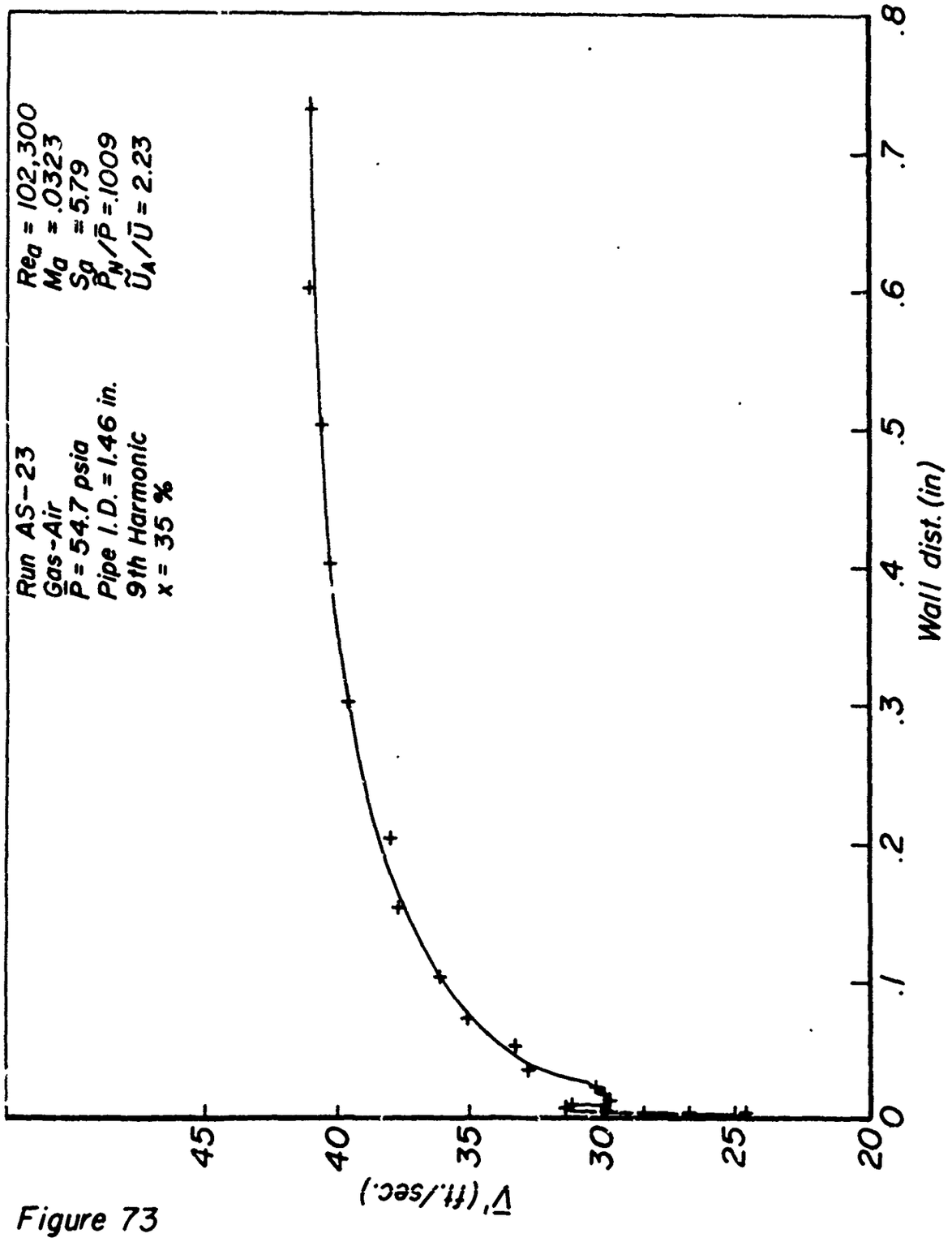
Run AS-23
Gas-Air
$\bar{P}$ = 54.7 psia
Pipe I.D. = 1.46 in.
9th Harmonic
x = 35 %
Re_a = 102,300
M_a = .0323
Sa = 5.79
$\tilde{P}_N/\bar{P}$ = .1009
$\tilde{U}_A/\bar{U}$ = 2.23
$\bar{V}$ (ft./sec.)
45
40
35
30
25
20
0
.1
.2
.3
.4
.5
.6
.7
.8
Wall dist. (in)

Figure 73

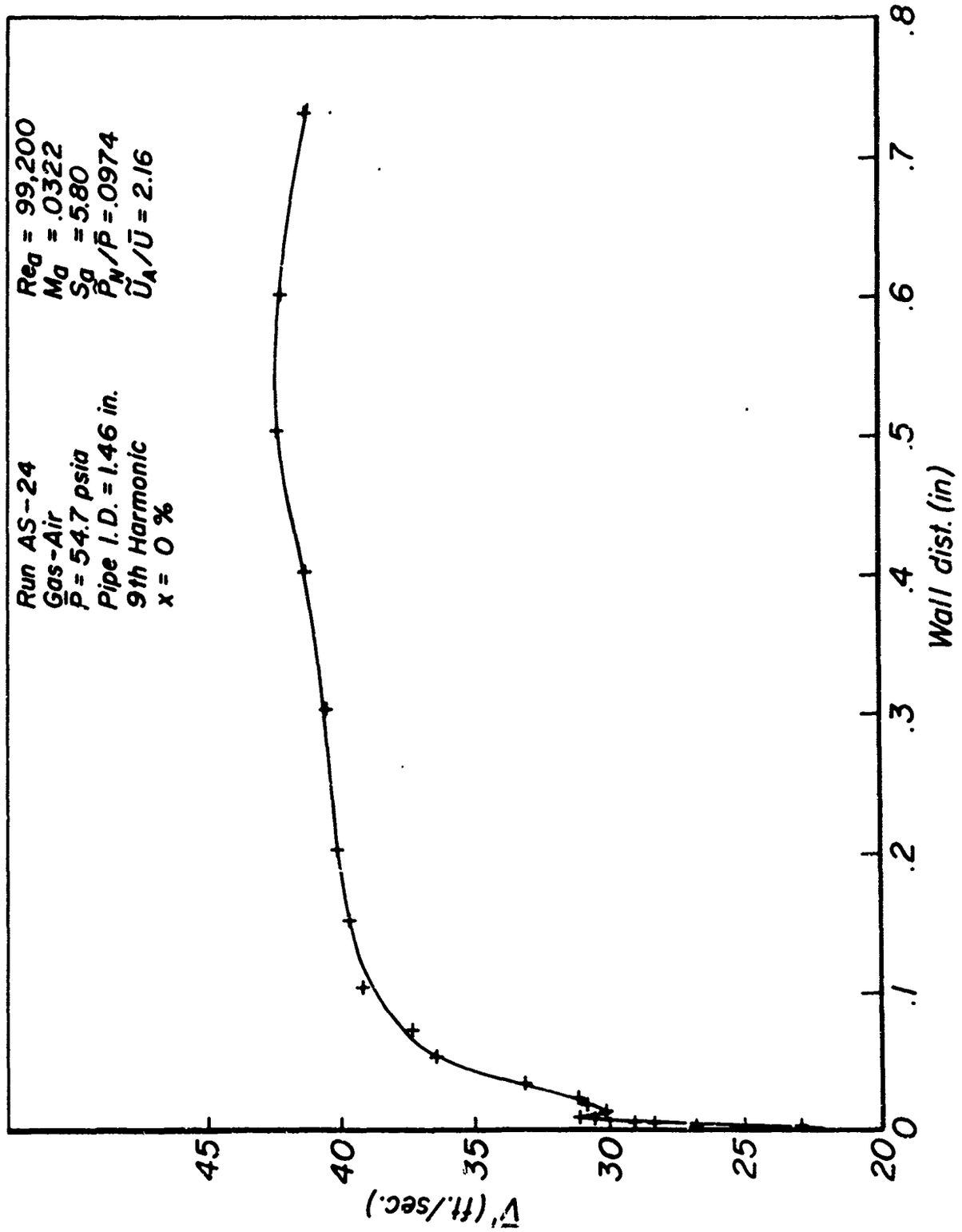

Figure 74

Figure 75

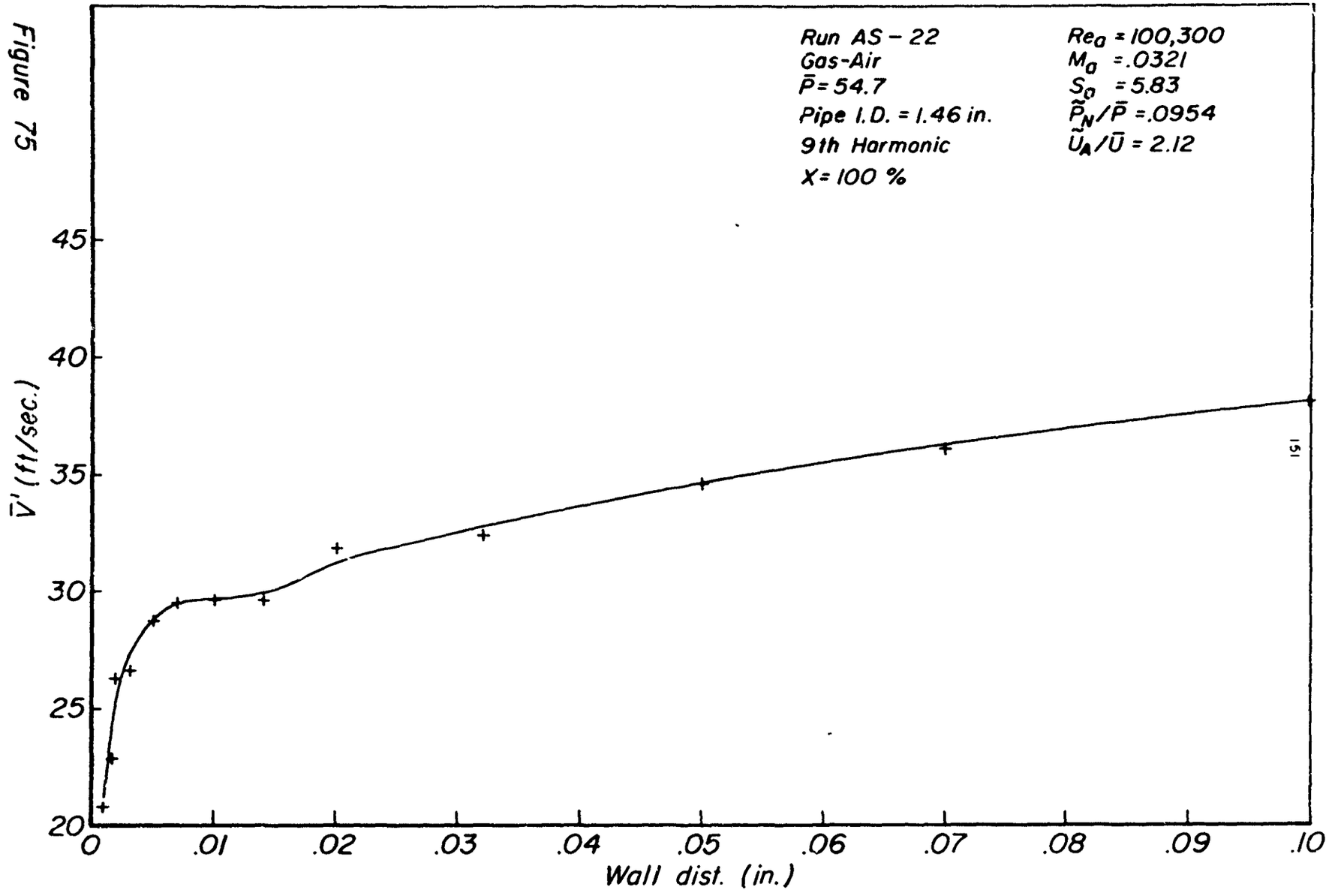

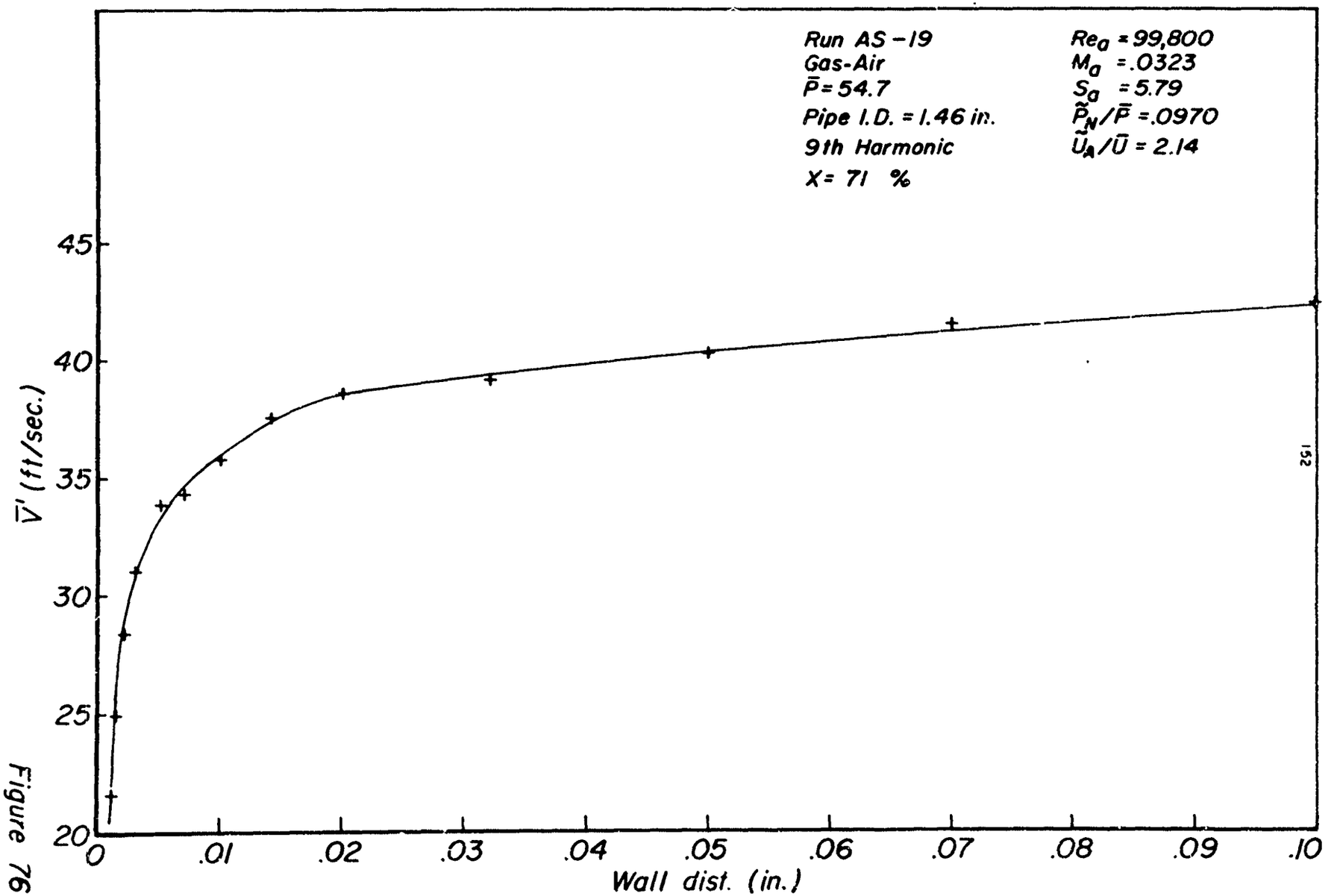
Run AS-19
Gas-Air
$\bar{P}$ = 54.7
Pipe I.D. = 1.46 in.
9th Harmonic
X = 71 %
Re_a = 99,800
M_a = .0323
S_a = 5.79
$\tilde{P}_N/\bar{P}$ = .0970
$\tilde{U}_A/\bar{U}$ = 2.14
$\bar{V}'$ (ft/sec.)
45
40
35
30
25
20
0
.01
.02
.03
.04
.05
.06
.07
.08
.09
.10
Wall dist. (in.)
152

Figure 76

Figure 77

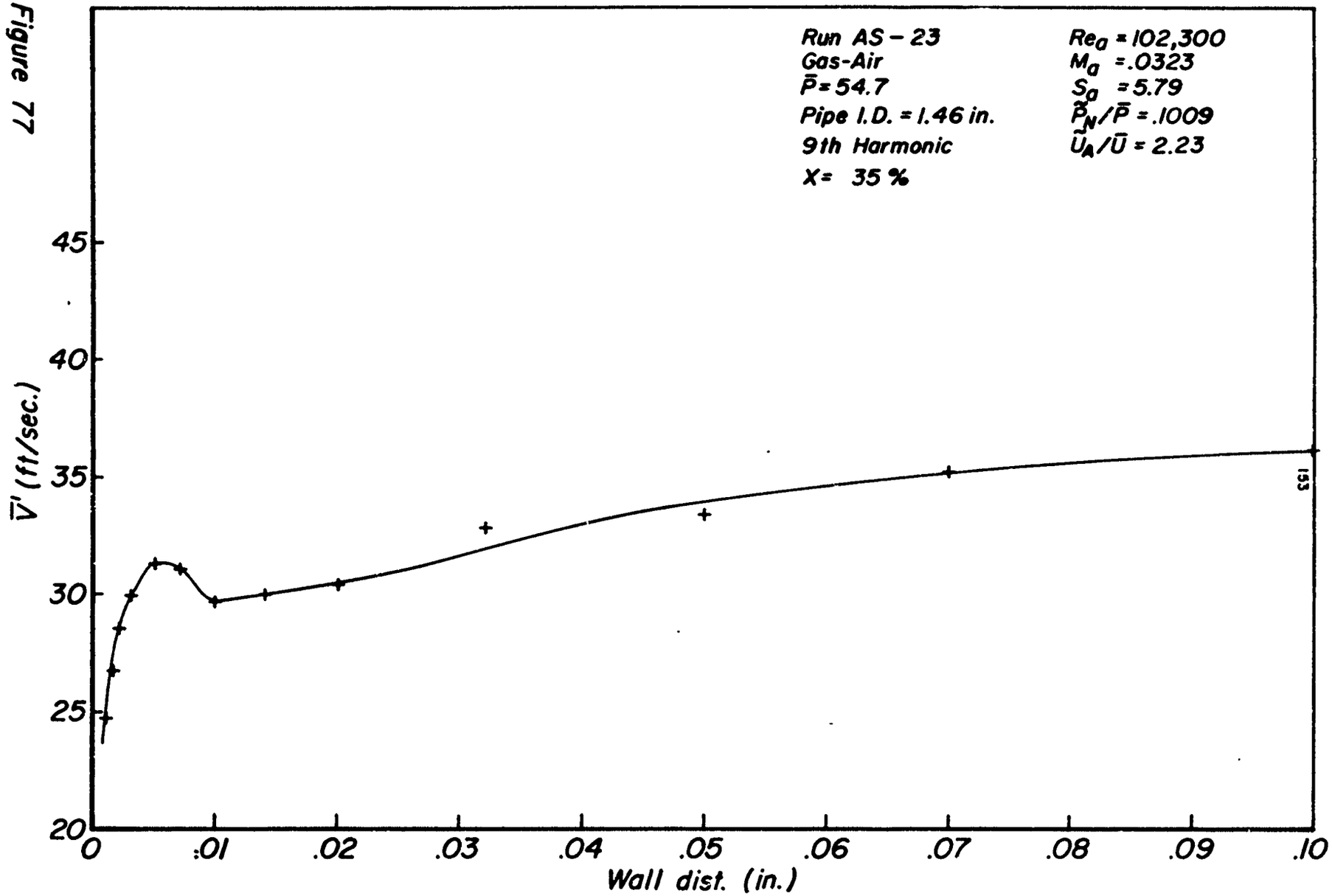

JP 17 4024 67

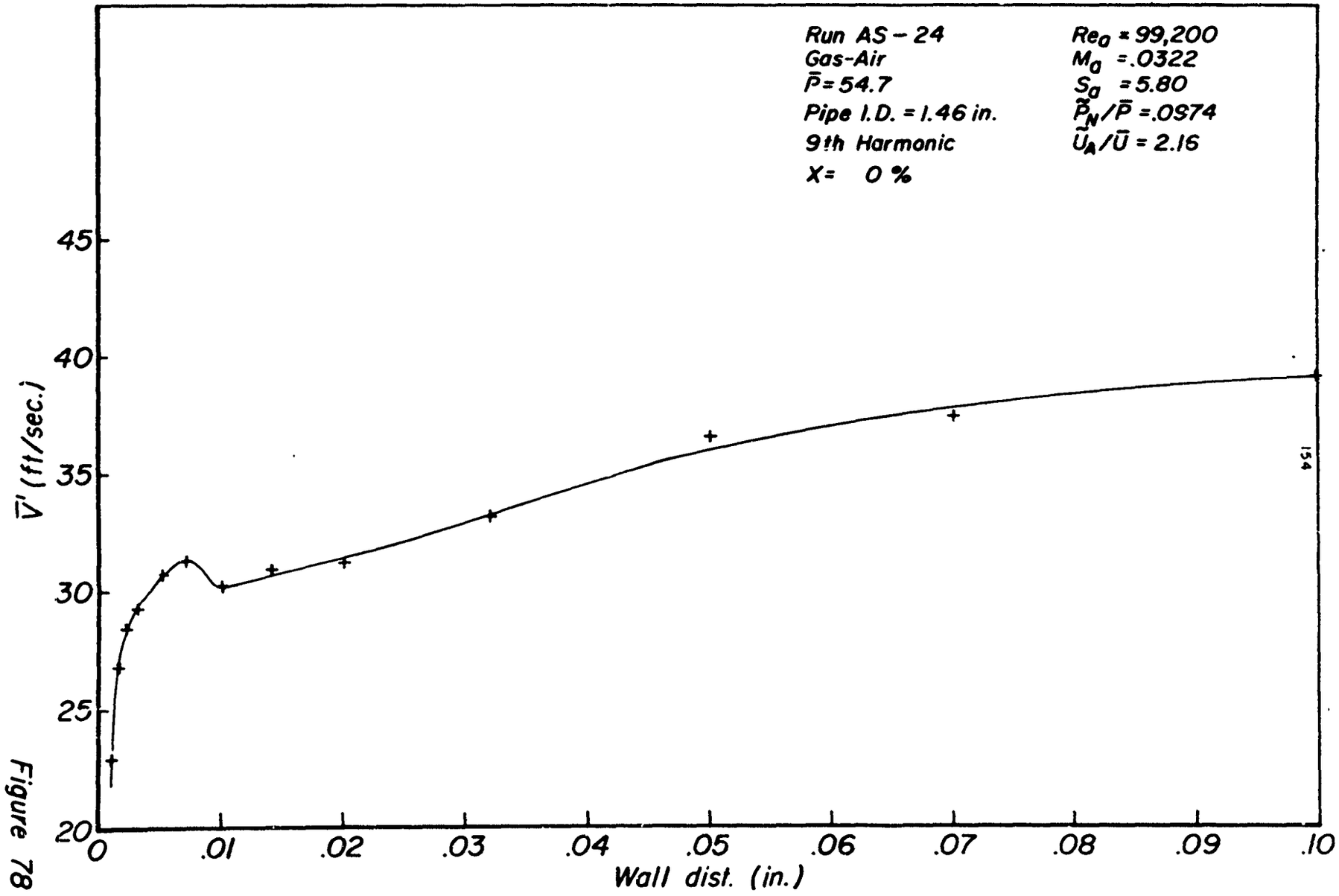

Figure 78

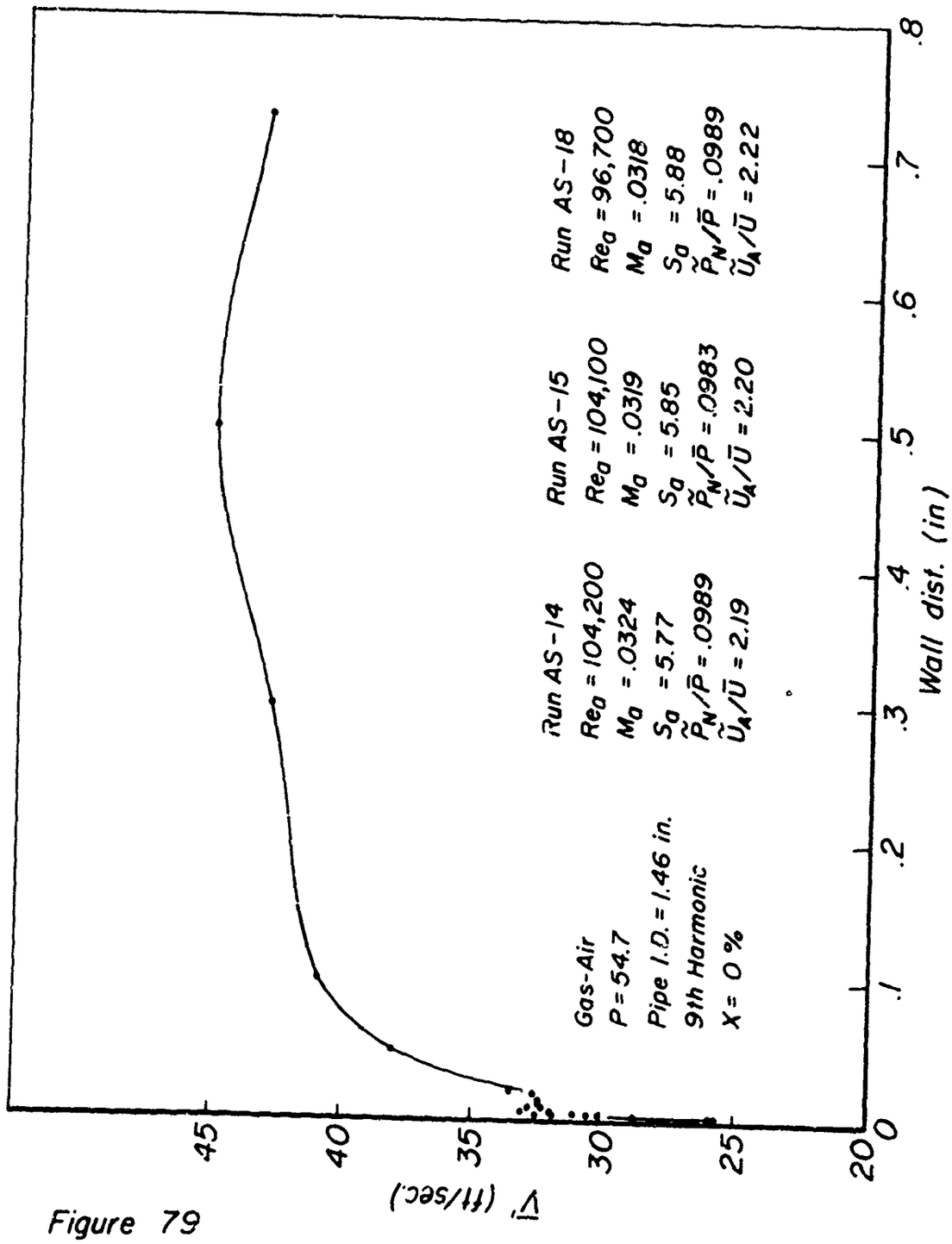

Figure 79

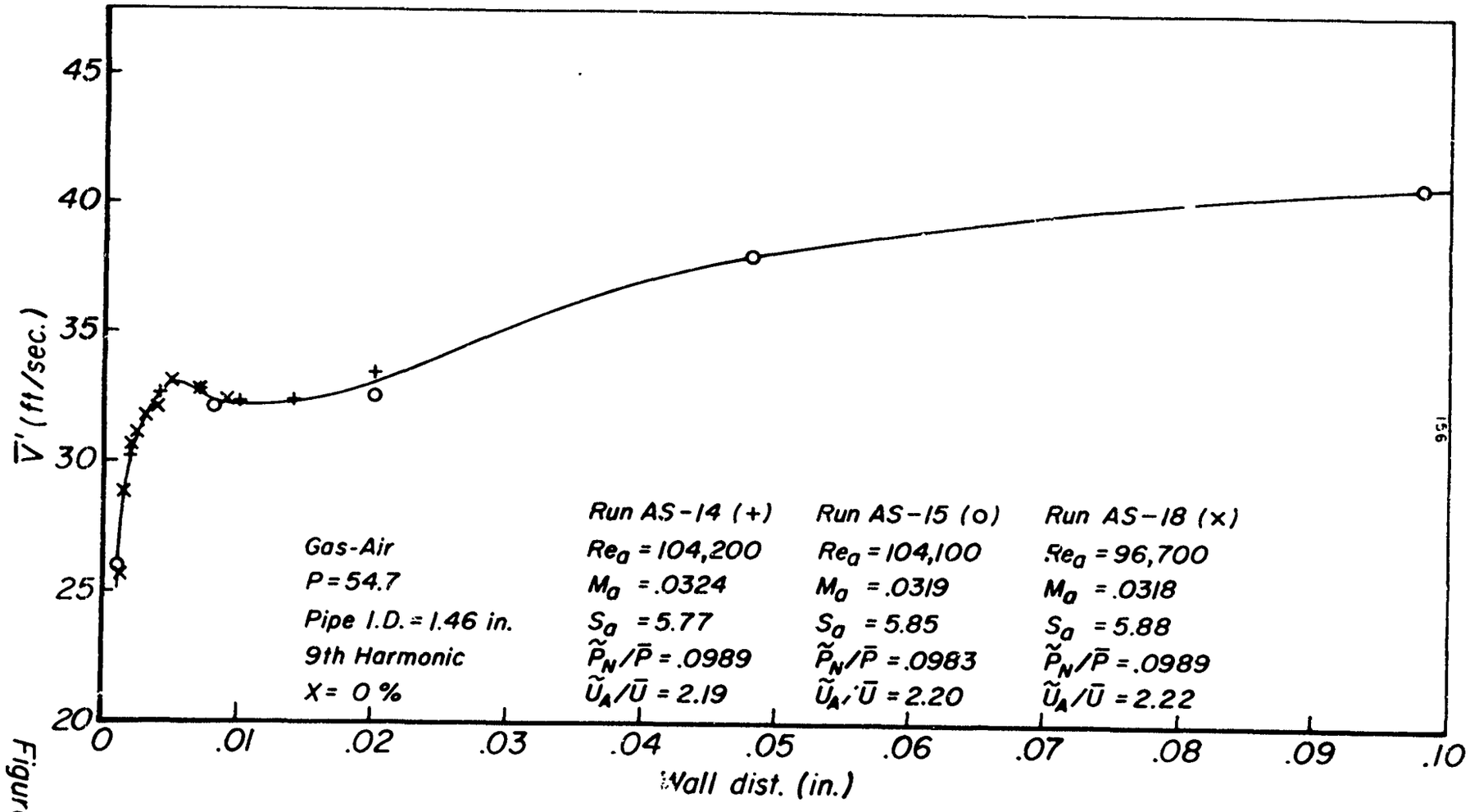

Figure 80

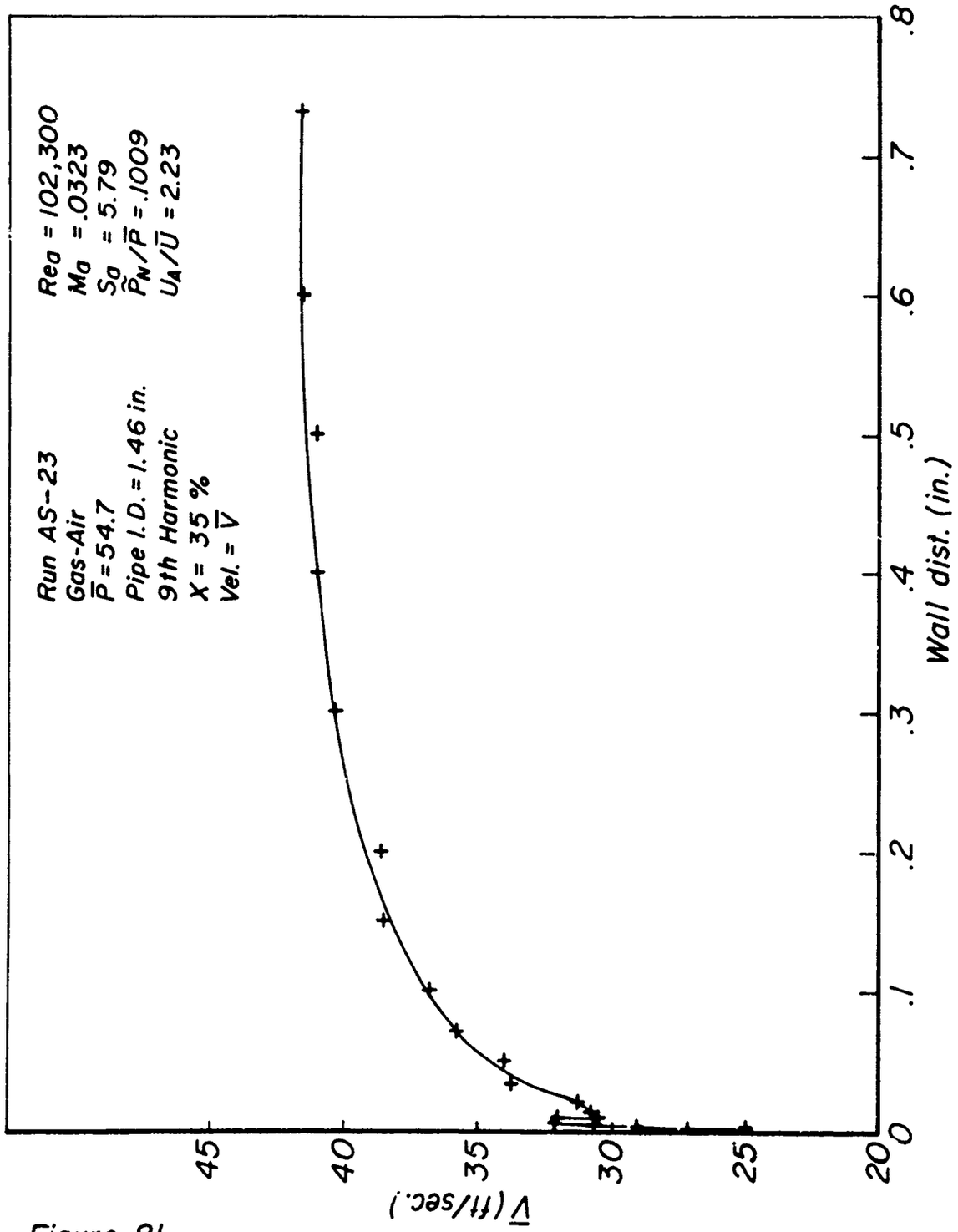
Run AS-23
Gas-Air
$\bar{P}$ = 54.7
Pipe I.D. = 1.46 in.
9th Harmonic
X = 35 %
Vel. = $\bar{V}$
Re_a = 102,300
M_a = .0323
S_a = 5.79
$\tilde{P}_N/\bar{P}$ = .1009
$U_A/\bar{U}$ = 2.23
$\bar{V}$ (ft/sec.)
Wall dist. (in.)
0
.1
.2
.3
.4
.5
.6
.7
.8
20
25
30
35
40
45

Figure 81

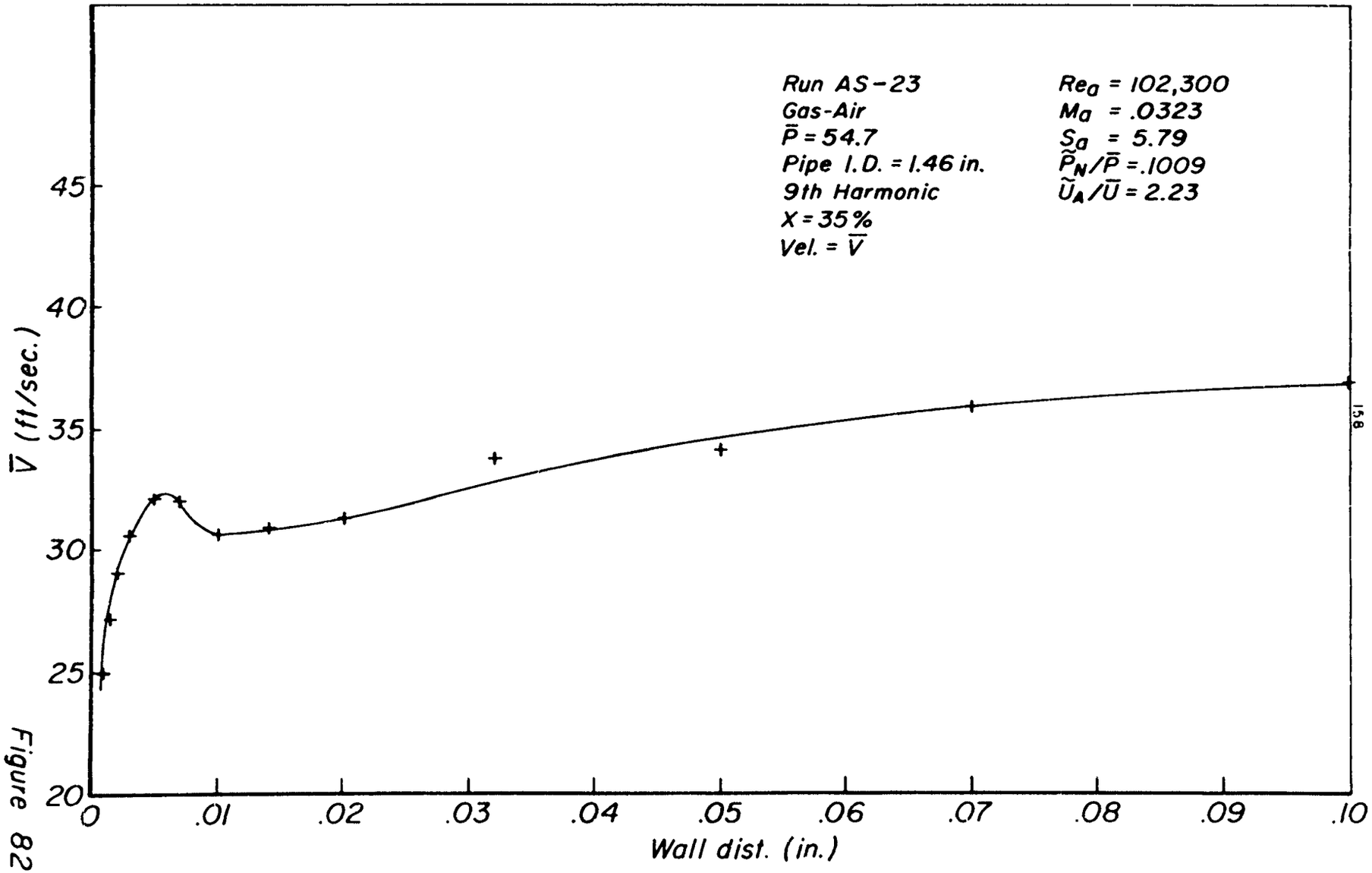
Run AS-23
Gas-Air
$\bar{P}$ = 54.7
Pipe I.D. = 1.46 in.
9th Harmonic
X = 35%
Vel. = $\bar{V}$
Re_a = 102,300
M_a = .0323
S_a = 5.79
$\tilde{P}_N/\bar{P}$ = .1009
$\tilde{U}_A/\bar{U}$ = 2.23
$\bar{V}$ (ft/sec.)
45
40
35
30
25
20
0
.01
.02
.03
.04
.05
.06
.07
.08
.09
.10
Wall dist. (in.)
153

Figure 82

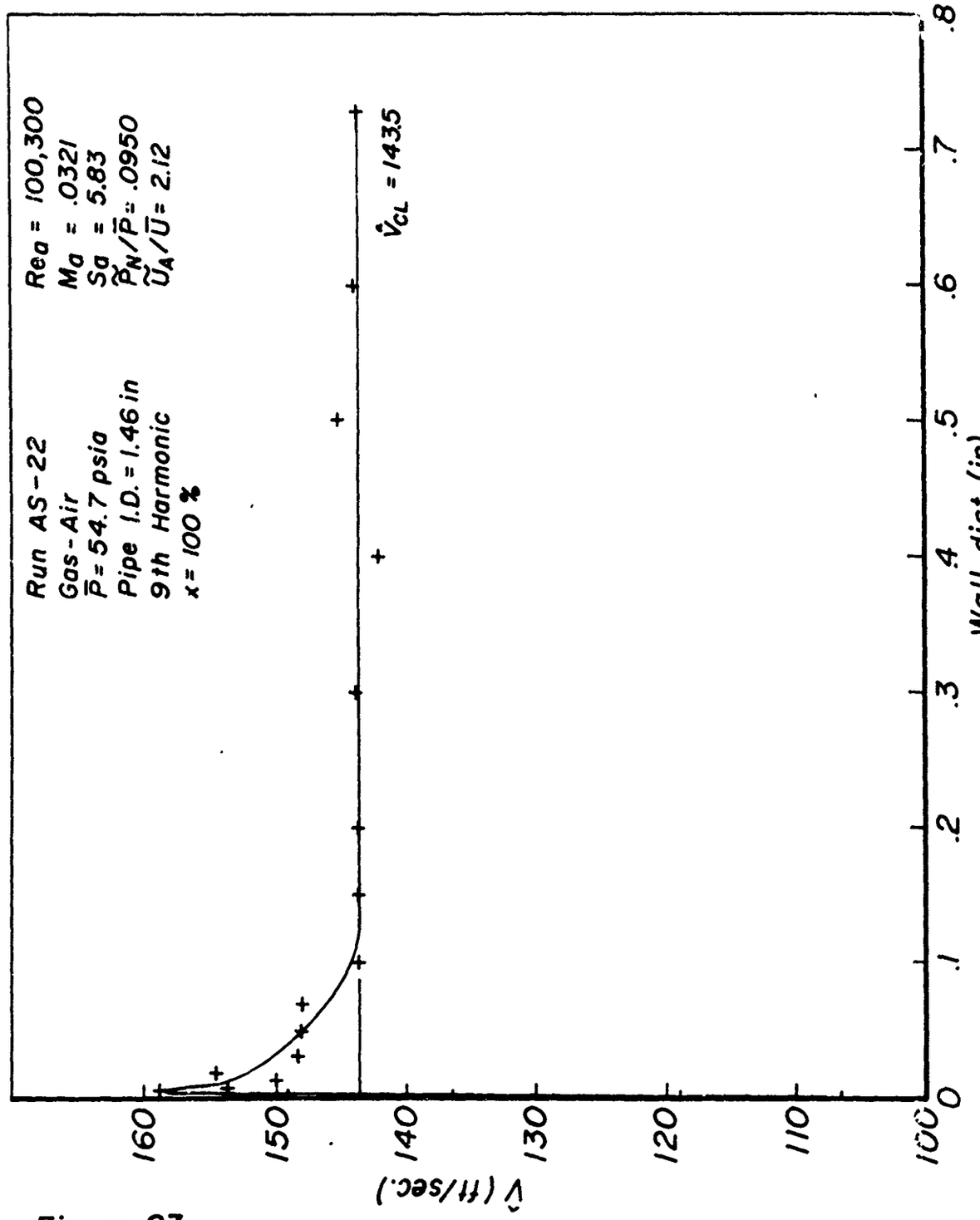

Figure 83

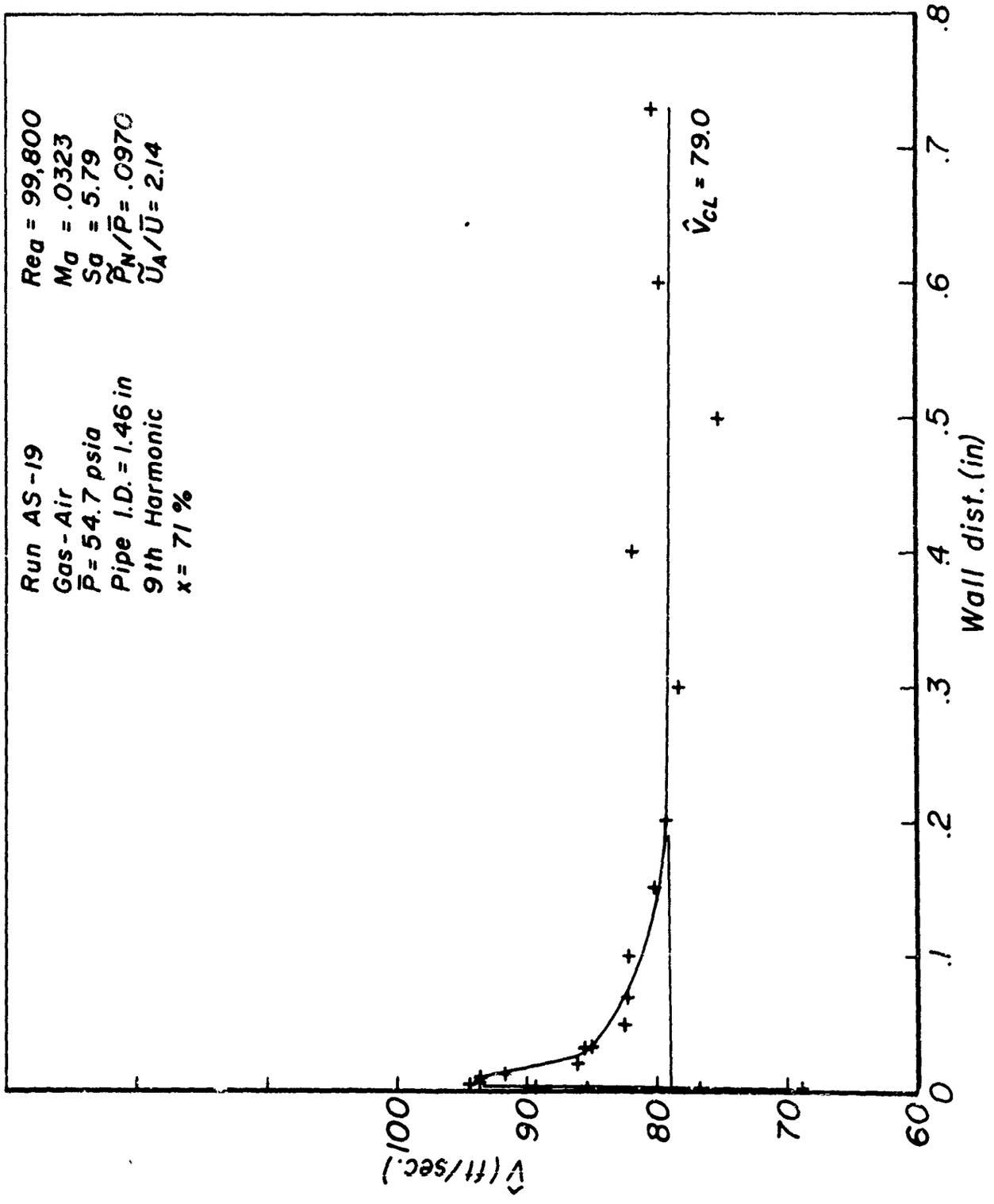
Run AS-19
Gas-Air
$\bar{P}$ = 54.7 psia
Pipe I.D. = 1.46 in
9th Harmonic
x = 71 %
Re$_a$ = 99,800
M_a = .0323
Sa = 5.79
$\tilde{P}_N/\bar{P}$ = .0970
$\tilde{U}_A/\bar{U}$ = 2.14
$\hat{V}_{CL}$ = 79.0
$\hat{V}$ (ft/sec.)
100
90
80
70
60
0
.1
.2
.3
.4
.5
.6
.7
.8
Wall dist. (in)

Figure 84

Figure 85

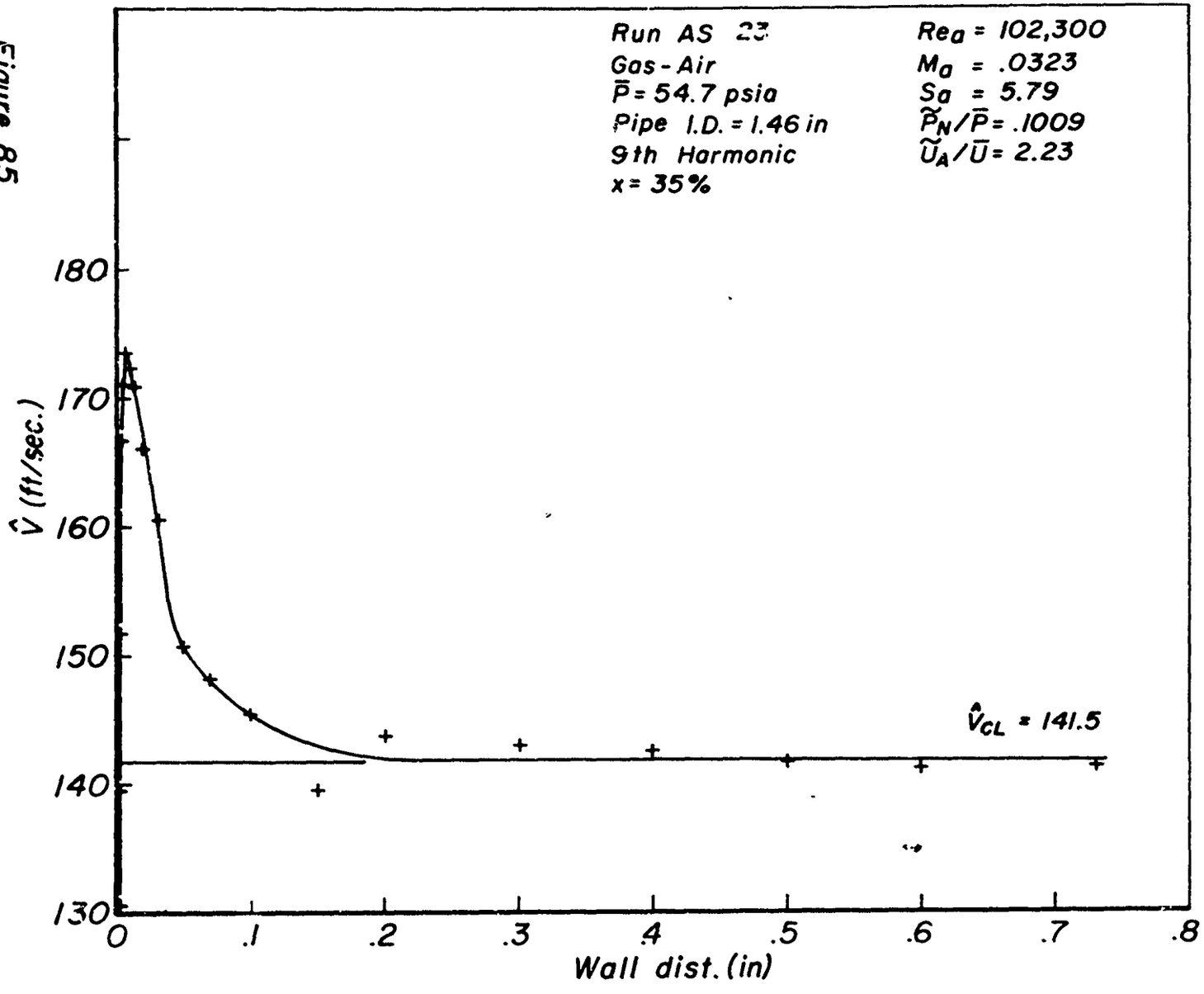
Run AS 23
Gas-Air
$\bar{P}$ = 54.7 psia
Pipe I.D. = 1.46 in
9th Harmonic
x = 35%
Re_a = 102,300
M_a = .0323
S_a = 5.79
$\tilde{P}_N/\bar{P}$ = .1009
$\tilde{U}_A/\bar{U}$ = 2.23
$\hat{V}_{CL}$ = 141.5
$\hat{V}$ (ft/sec.)
180
170
160
150
140
130
0
.1
.2
.3
.4
.5
.6
.7
.8
Wall dist. (in)

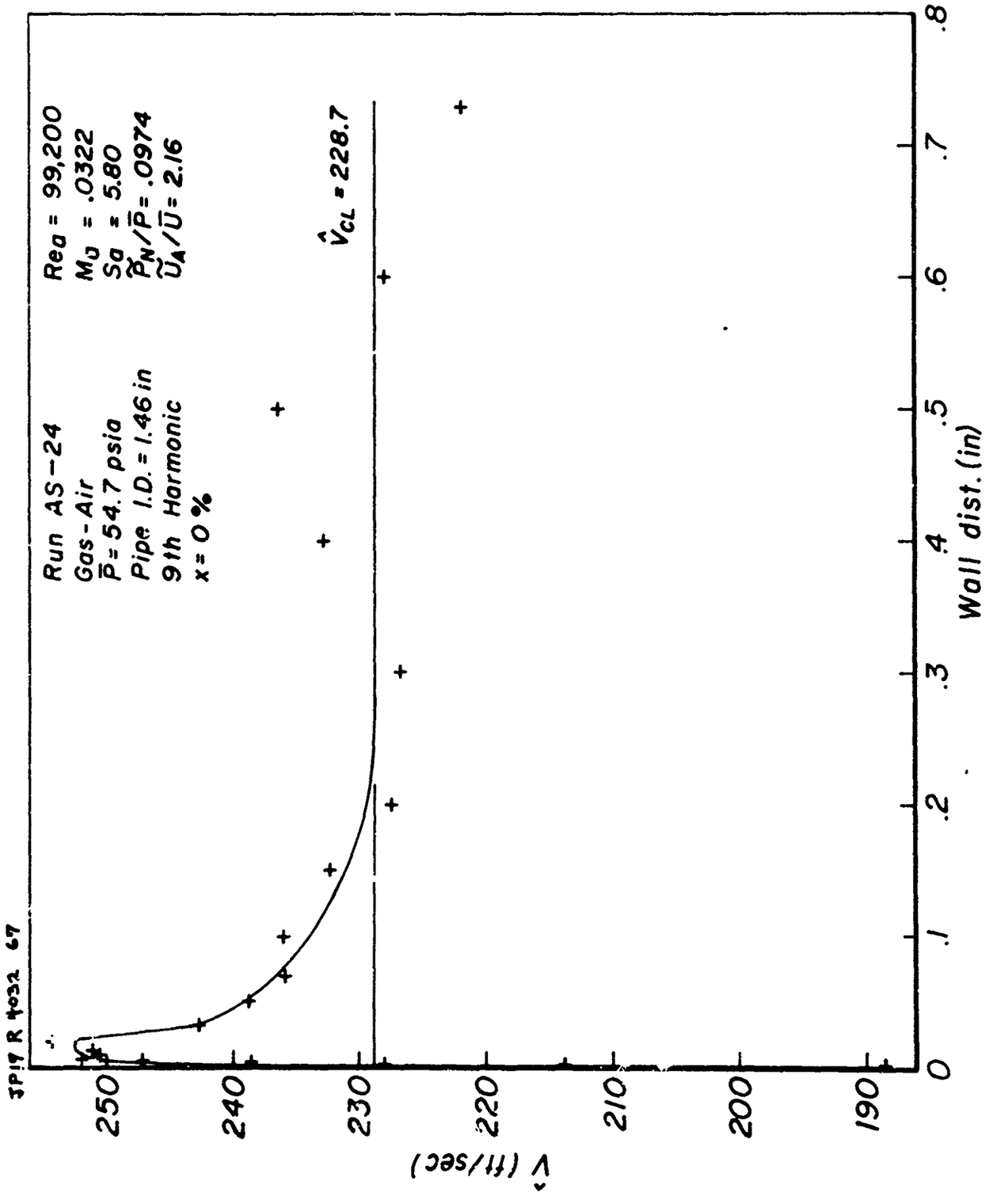
Run AS-24
Gas-Air
$\bar{P}$ = 54.7 psia
Pipe I.D. = 1.46 in
9th Harmonic
x = 0 %
Re$_d$ = 99,200
M_J = .0322
Sa = 5.80
$\tilde{P}_N/\bar{P}$ = .0974
$\tilde{U}_A/\bar{U}$ = 2.16
$\hat{V}_{CL}$ = 228.7
V (ft/sec)
Wall dist. (in)
250
240
230
220
210
200
190
0
.1
.2
.3
.4
.5
.6
.7
.8

Figure 86

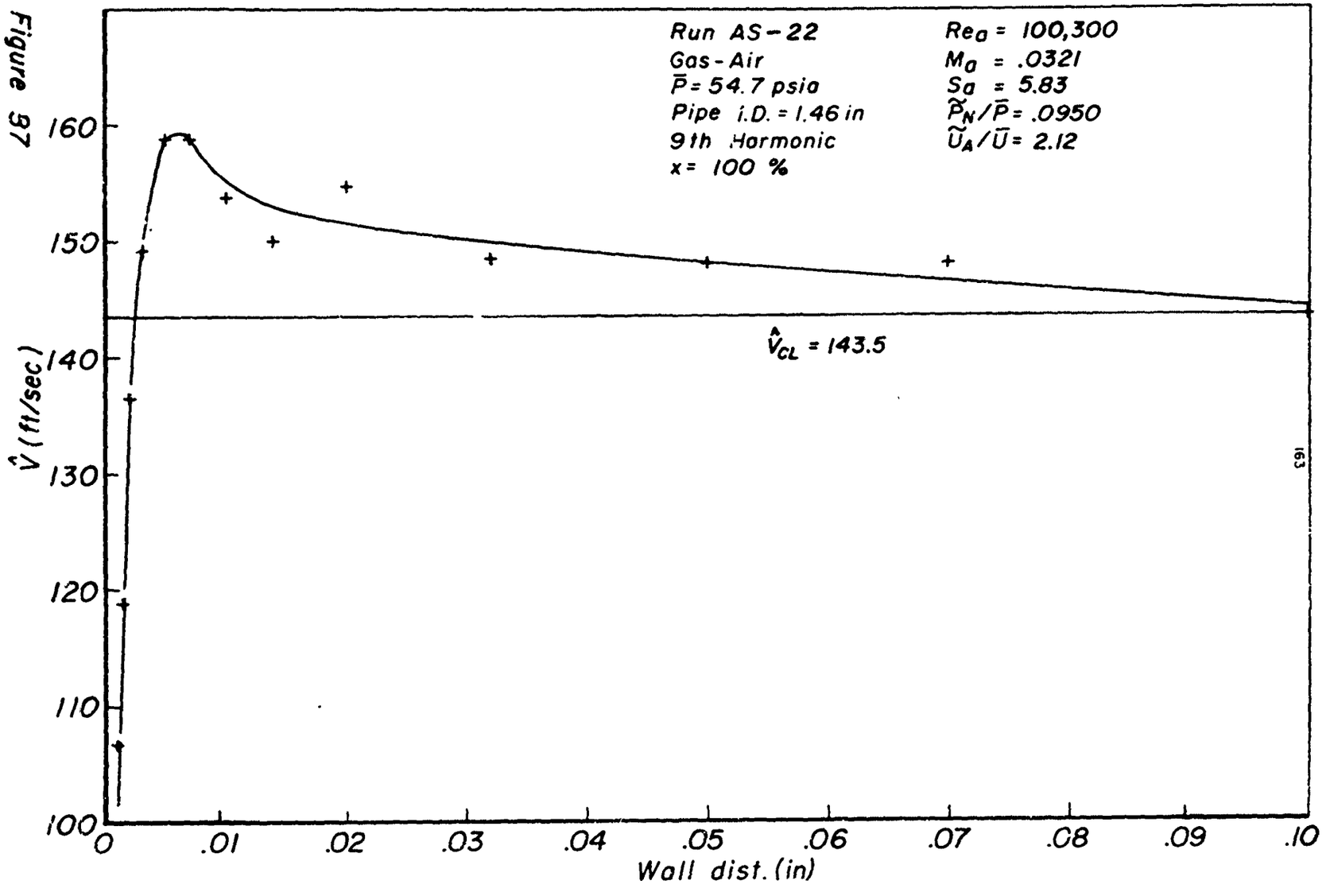
Run AS-22
Gas-Air
$\bar{P}$ = 54.7 psia
Pipe i.D. = 1.46 in
9th Harmonic
x = 100 %
Re_a = 100,300
M_a = .0321
S_a = 5.83
$\tilde{P}_N/\bar{P}$ = .0950
$\tilde{U}_A/\bar{U}$ = 2.12
$\hat{V}_{CL}$ = 143.5
$\hat{V}$ (ft/sec)
160
150
140
130
120
110
100
0
.01
.02
.03
.04
.05
.06
.07
.08
.09
.10
Wall dist. (in)

Figure 37

JPL TR 4034 67

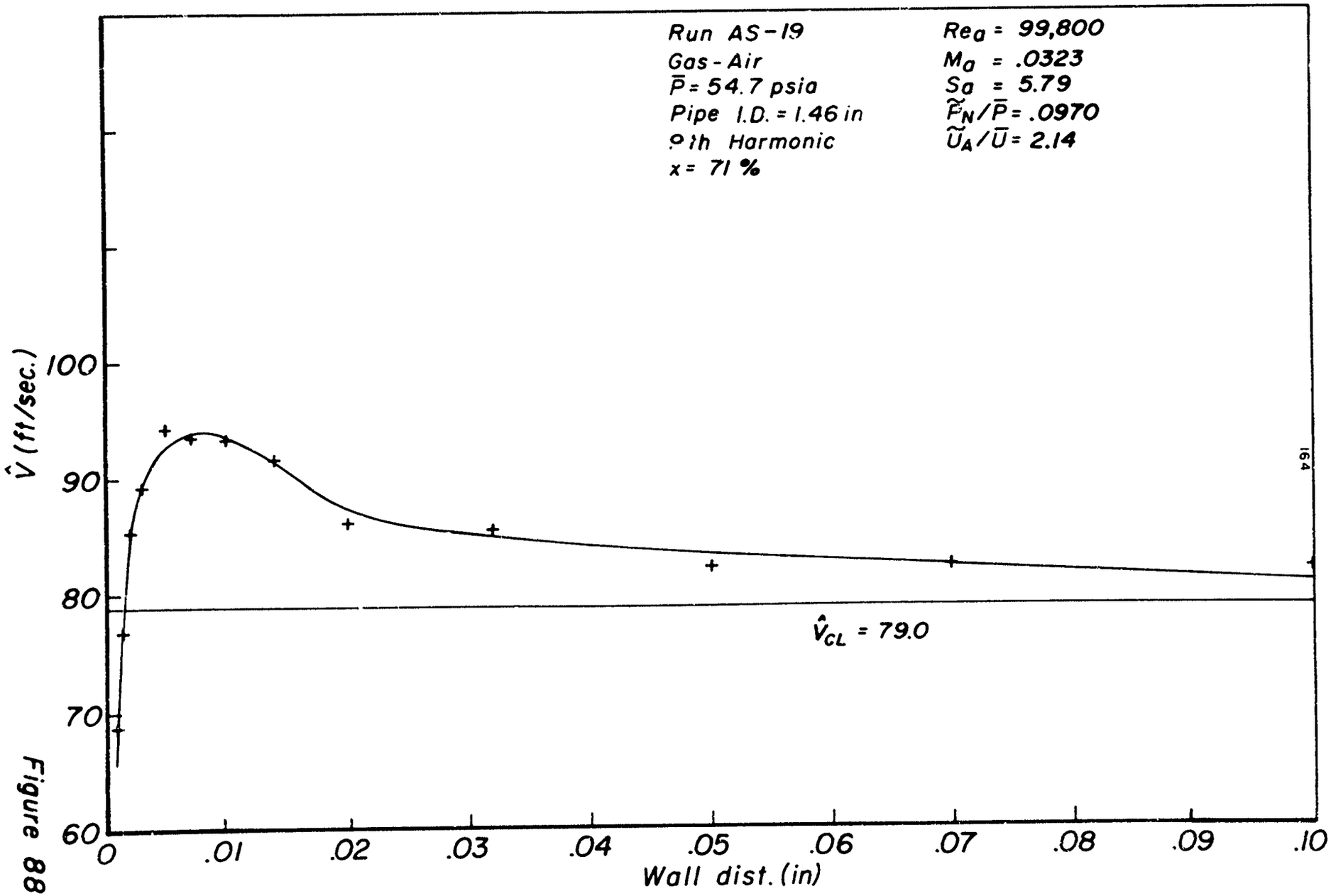

Figure 88

Figure 89

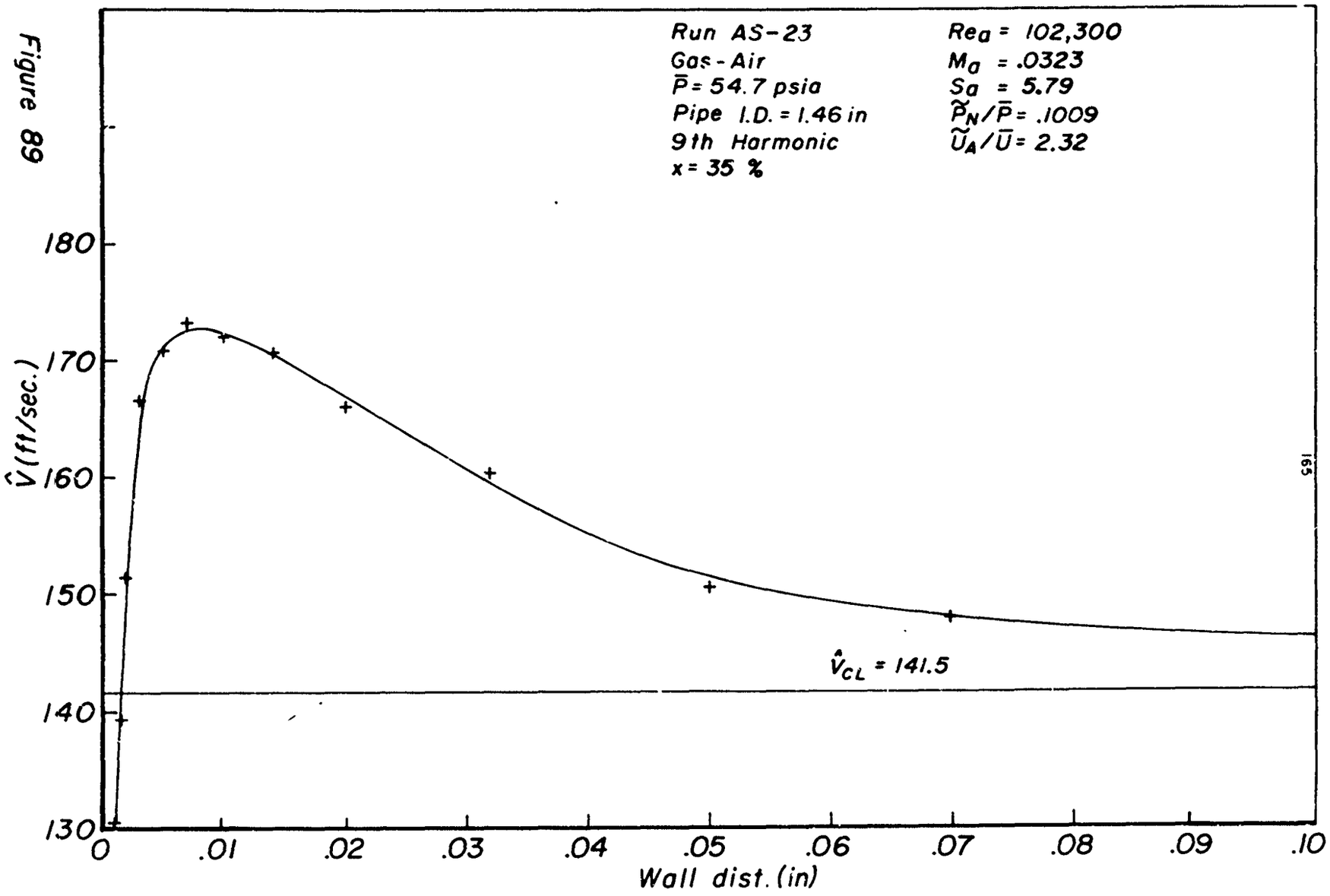

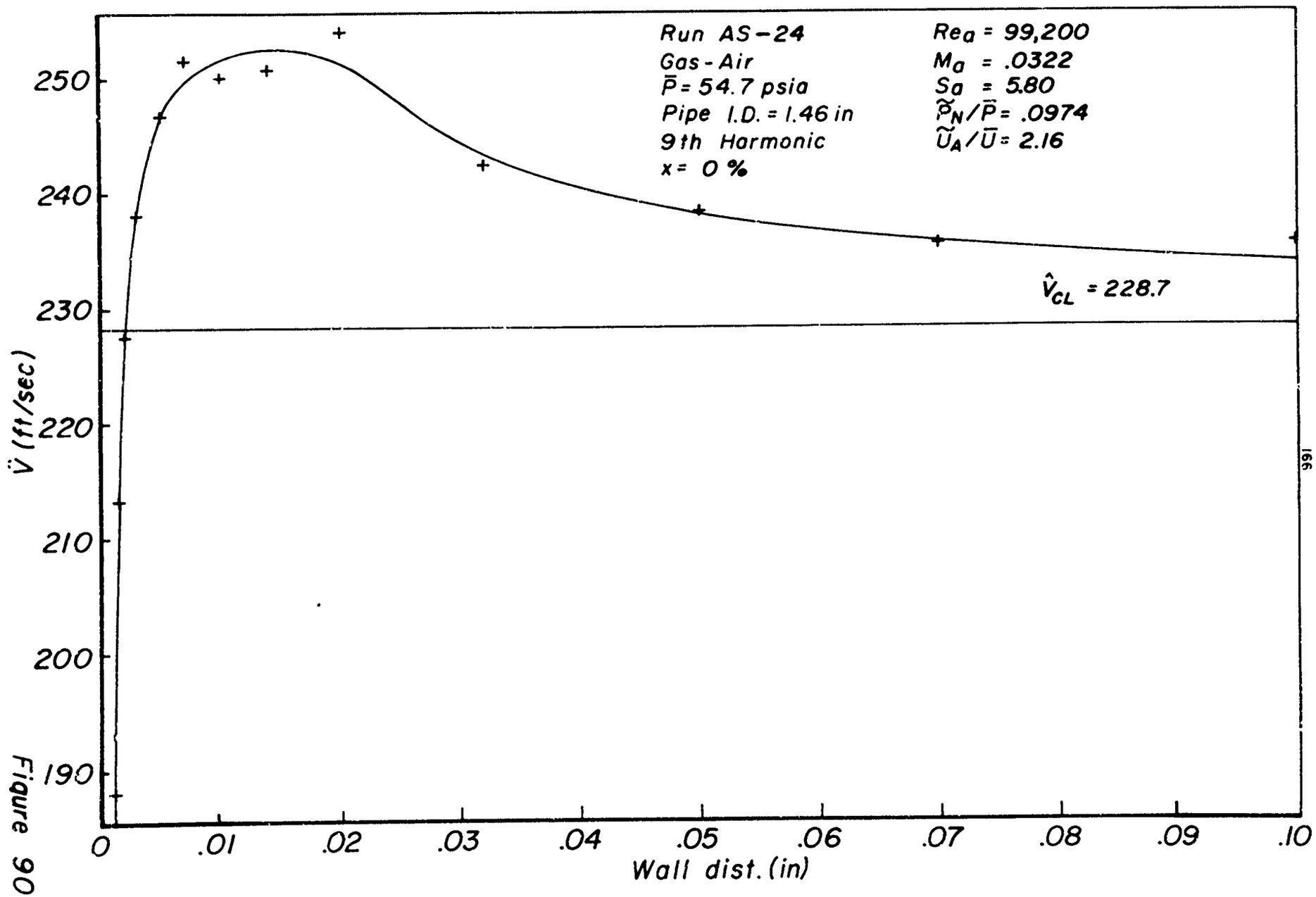
Run AS-24
Gas-Air
$\bar{P}$ = 54.7 psia
Pipe I.D. = 1.46 in
9th Harmonic
x = 0 %
Re_a = 99,200
M_a = .0322
Sa = 5.80
$\tilde{P}_N/\bar{P}$ = .0974
$\tilde{U}_A/\bar{U}$ = 2.16
$\hat{V}_{CL}$ = 228.7
250
240
230
220
210
200
190
$\ddot{V}$ (ft/sec)
0
.01
.02
.03
.04
.05
.06
.07
.08
.09
.10
Wall dist. (in)

Figure 90

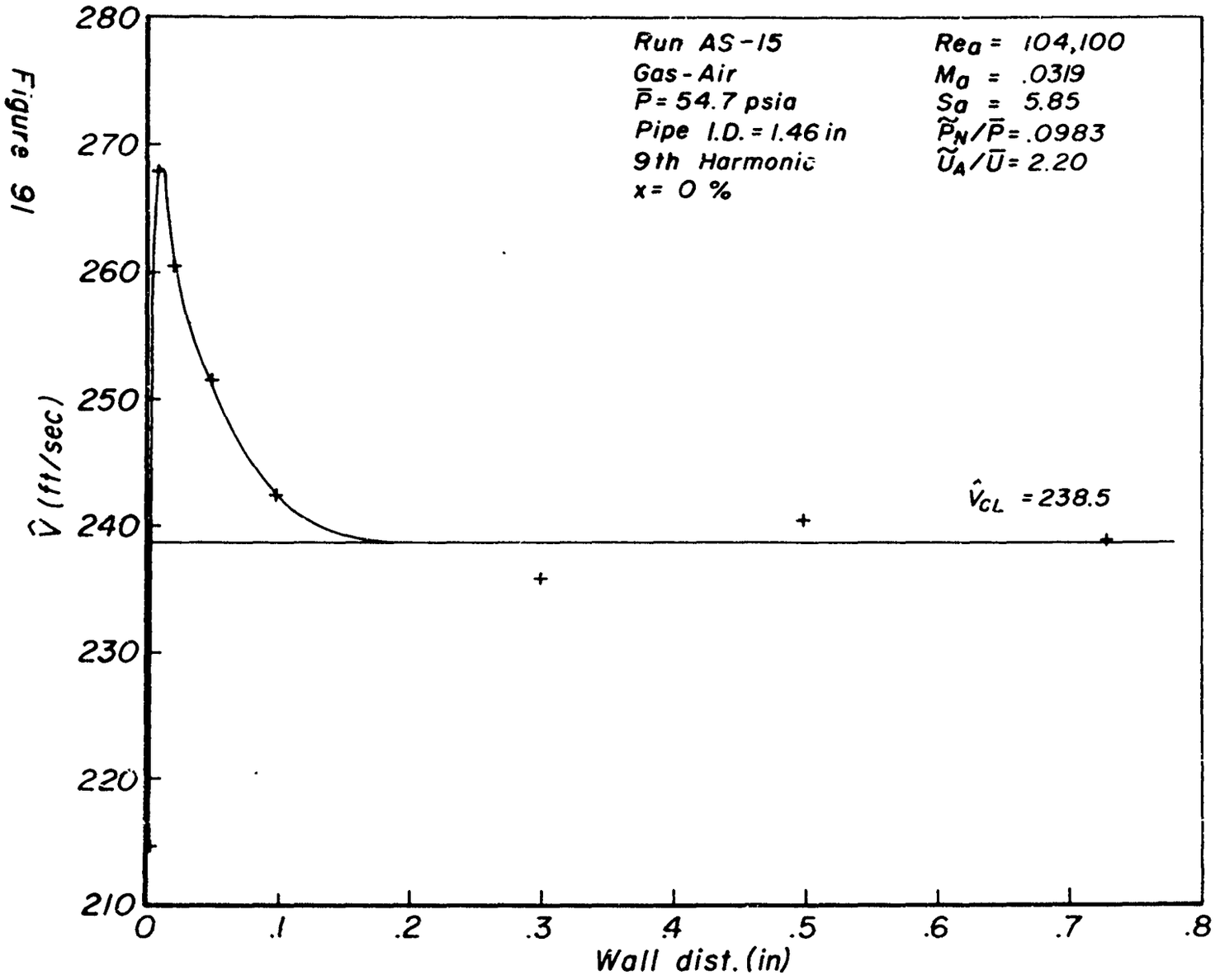
Run AS-15
Gas-Air
$\bar{P}$ = 54.7 psia
Pipe I.D. = 1.46 in
9th Harmonic
x = 0 %
Re_a = 104,100
M_a = .0319
S_a = 5.85
$\tilde{P}_N/\bar{P}$ = .0983
$\tilde{U}_A/\bar{U}$ = 2.20
$\hat{V}_{CL}$ = 238.5
$\hat{V}$ (ft/sec)
Wall dist. (in)
280
270
260
250
240
230
220
210
0
.1
.2
.3
.4
.5
.6
.7
.8

Figure 91

JP 17 4038 G7

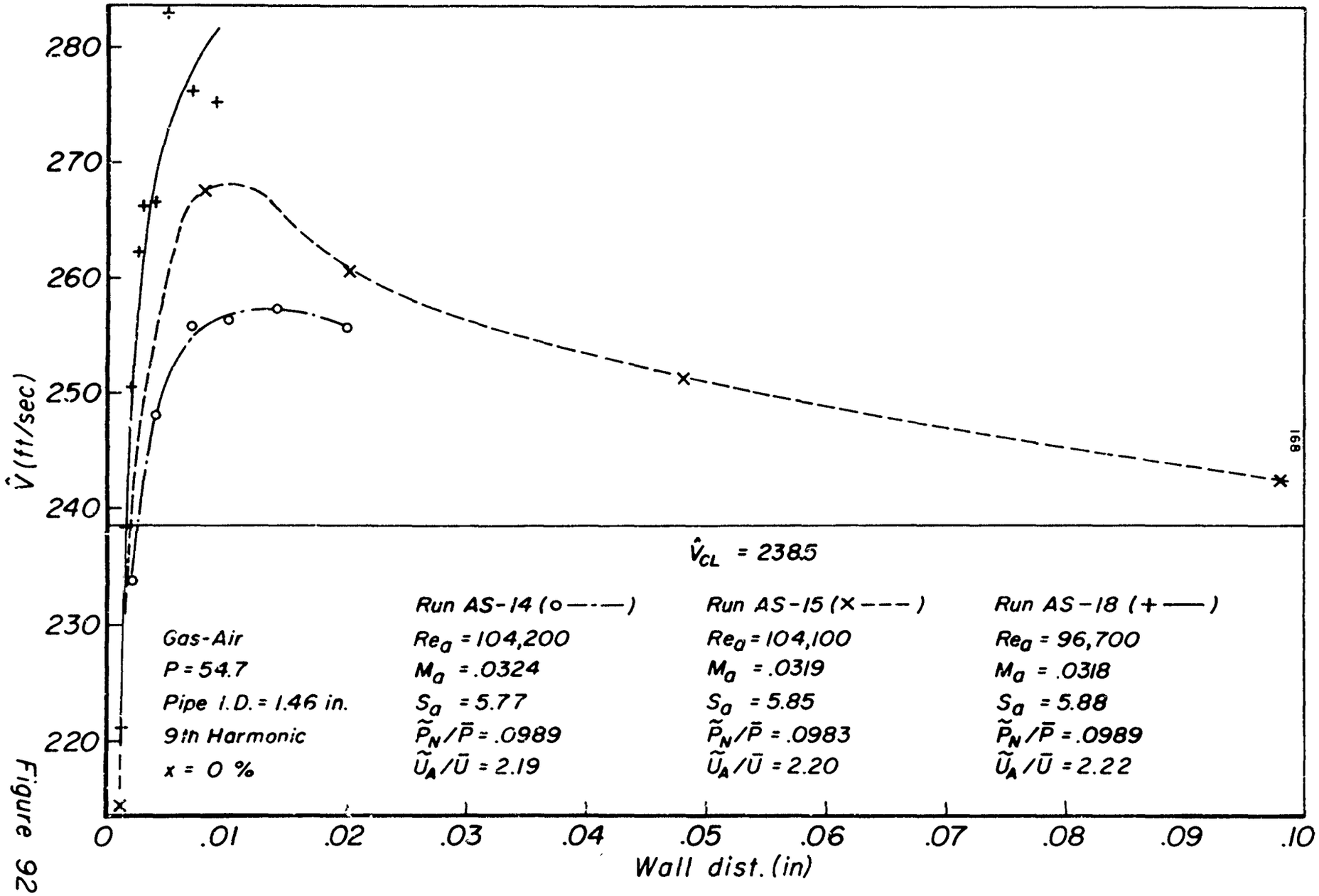

Figure 92

profiles; the gas flowing in the duct is always air. The average air pressure in the duct ($\bar{P}$) is always very close to 40 psig (= 54.7 psia). The pipe (duct) I.D. is 1.46 in. instead of 1.50 in. as in the case of the heat transfer data (Figures 36-43, Section 3.5) since the pipes attached to the movable test section (see Section 4.2) slide inside the 1.50 in. I.D. pipes making up the rest of the duct. All these profiles were taken at the 9th harmonic frequency of the duct. The values of x refer to the axial position of the test section as discussed above. The parameters Re_a, M_a, S_a, $\tilde{P}_N/\bar{P}$ and $\tilde{U}_A/\bar{U}$ are calculated in ways very similar to those discussed in Section 3.4, for the calculation of these same parameters for the heat transfer runs. Hence, only a few remarks will be made about these parameters. The parameters Re_a, M_a and S_a were evaluated for flow in the 1.46 in. I.D. travelling test section. $\tilde{P}_N/\bar{P}$ was computed by first calculating the rms pressure as measured by the Dynisco pressure transducer (Section 4.3) and dividing by the mean duct pressure. This gave the value of $\tilde{P}_N/\bar{P}$ evaluated in the 1.50 in. I.D. section of the duct. By assuming that the wave power propagated through the 1.46 in. I.D. section of the duct equals that propagated through the 1.50 in. I.D. sections, we can estimate

$$\frac{\tilde{P}_N}{\bar{P}} = \left(\frac{\tilde{P}_N}{\bar{P}}\right)_{1.46 \text{ in. I.D.}} = \frac{1.50}{1.46} \left(\frac{\tilde{P}_N}{\bar{P}}\right)_{1.50 \text{ in I.D.}} \quad (63)$$

From this value of $\tilde{P}_N/\bar{P}$, $\tilde{U}_A/\bar{U}$ is calculated using the simple wave formula; i.e.,

$$\frac{\tilde{U}_A}{\bar{U}} = \frac{\tilde{P}_N}{\bar{P}} \Big/ \gamma M_a \quad (64)$$

Figures 71-74 show the $\bar{v}'$ average velocity profiles at x-positions of 100, 71, 35 and 0% (a wall distance of .73 inches places the hot-wire probe at the center of the duct). Figures 75-78 show details of the profiles Figures 71-74 close to the wall on a 10 times smaller radial scale. Figures 79 and 80 show data taken at similar conditions to those of Figures 74 and 78, but from different test runs. These two test runs were taken in an attempt to establish reproducibility of the data. Figures 81 and 82 show the results of taking the data of Run AS-23 (which yielded $\bar{v}'$ profiles Figures 73 and 77)

and computing $\bar{v}$ profiles instead of $\bar{v}'$ profiles. Figures 83-92 show peak-to-peak ($\hat{v}$) velocity profiles taken from the same runs that yielded the $\bar{v}'$ profiles Figures 71-80. As in the case of the $\bar{v}'$ profiles, five of the figures (Figures 83-86, 91) present the complete velocity profiles and the remaining figures (87-90, 92) show detail of the 0.1 in. closest to the wall.

Examining Figures 71-74, it can be seen that these profiles are very different than that of fully developed pipe flow (at $Re \approx 100{,}000$), which would be the profile to be expected for steady flow in the duct. (We are here referring mainly to the general shape of the profile, not to the peculiar details near the wall.) It was suspected that the shape of these profiles was in part due to a blockage of the flow by the hot-wire probe. From Figure 48, Section 4.6, it can be seen that the $\sim \frac{1}{8}$ in. diameter body of the probe is quite close to the wire and hence could cause considerable interference to the flow field around the wire especially when the probe is near the wall and the airflow is somewhat restricted as it passes over the wire by the presence of the probe body. To test the blockage effect of the hot-wire probe, hot-wire and pitot-tube traverses of the duct were taken under steady flow conditions at an x-position of 30%. The pitot tube and manometer system used were those described in Section 4.9. The pitot tube is shown in Figure 57. The results of the pitot and hot-wire traverses are shown in Figure 93 along with a curve for fully developed turbulent pipe flow at $Re = 110{,}000$ taken from Schlicting, Reference 28, p. 505. The level of this last profile was established from the known mass flow in the duct for the case of the pitot tube traverse. The pitot and hot-wire profiles were taken under slightly different flow conditions. We see from Figure 93 that there is a considerable difference between the shapes of the hot-wire and pitot profiles especially near the wall. This is evidence of blockage by the hot-wire probe body as discussed above. The close agreement between the pitot profile and the fully developed profile taken from Reference 28 lend weight to the assumption that the pitot profile is close to the true profile in the duct and can be considered as the standard against which the hot-wire profile can be compared. Hence, when examining the hot-wire profiles taken under oscillating flow conditions (Figures 71-92), the blockage effect of the hot-wire probe must be borne in mind.

Figure 93

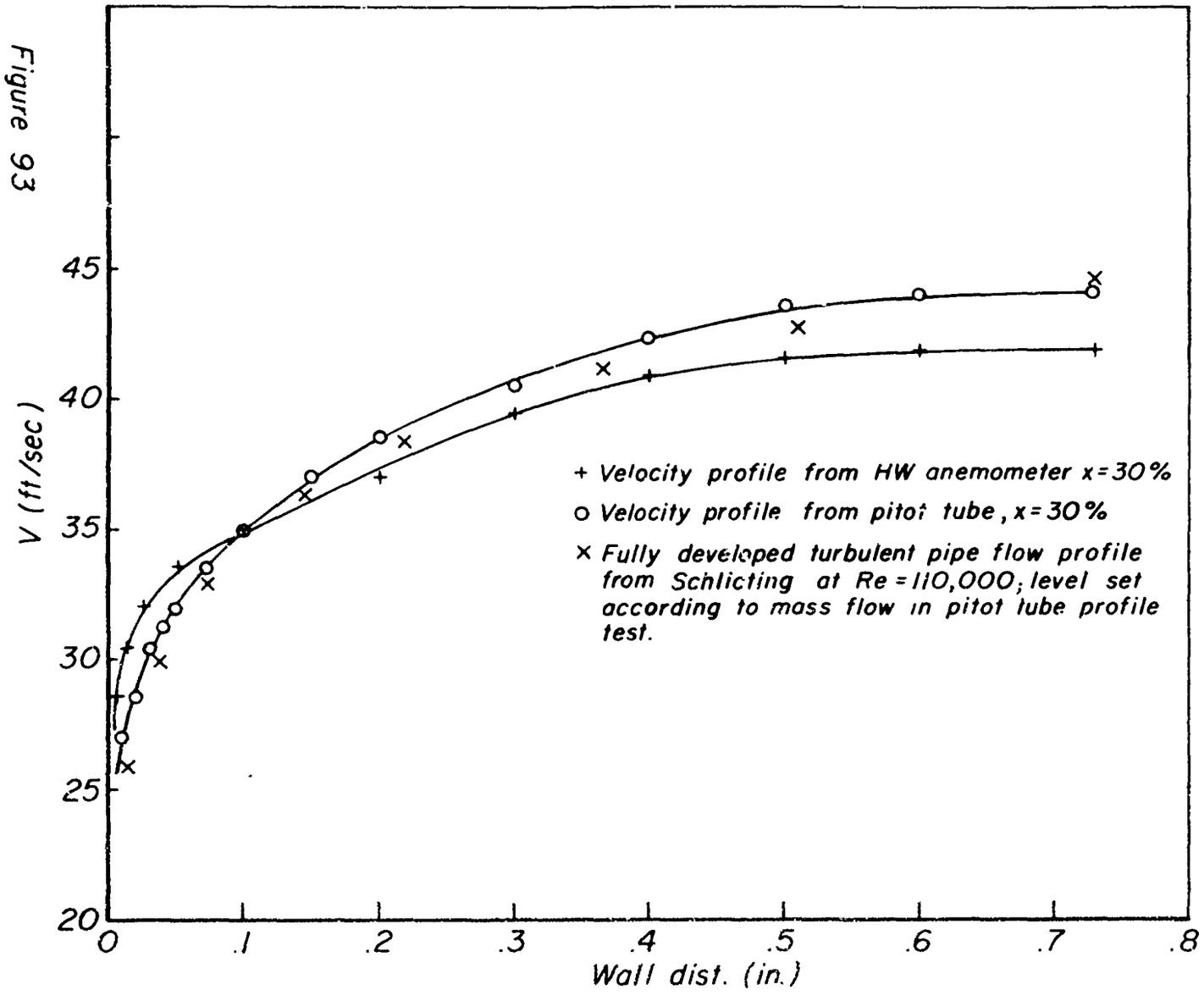
V (ft/sec)
45
40
35
30
25
20
0
.1
.2
.3
.4
.5
.6
.7
.8
Wall dist. (in.)
+ Velocity profile from HW anemometer x=30%
o Velocity profile from pitot tube, x=30%
× Fully developed turbulent pipe flow profile from Schlicting at Re=110,000; level set according to mass flow in pitot tube profile test.

We now consider the general levels of the $\bar{v}'$ profiles (see Figures 71-74 and 79 taken at x-positions of 100, 71, 35, 0 and 0% respectively). It will be noted the general level of the three profiles of Figures 71, 73 and 74 are in quite close agreement. However the general levels of the profiles of Figures 72 and 79 run about 4 and 3 ft/sec higher respectively. While there is some variation in the average velocity in the duct as computed from mass flow and density calculations, this is only about 1 ft/sec and is insufficient to explain the level differences discussed above. About a month was spent investigating these levels shifts. The parameters (Section 4.8) and calibration (Section 4.9) of the hot-wires involved were carefully checked and no significant errors were found. The cause for the level shifts, must, of course lie somewhere in the hot-wire system, but after the month's investigation referred to above could not be found. At this point, due to time limitations, it was decided to proceed with the taking of hot-wire velocity profiles in the hope that useful information could be gained from the shape of the profiles, although, as discussed above, the absolute levels of the profile appeared to show variations for unknown reasons and could not be regarded as correct except as a rough approximation.

The fact that the shapes of the velocity profiles are accurate, except for probe blockage effects as discussed above is supported by the following two facts. The first is the fact that for all profiles (Figures 71-80), the data points lie within $\pm$ 1 ft/sec of a smooth curve, and most points lie within $\pm$ 0.5 ft/sec of the curve. The second point is that in the one case where profiles were taken twice at the same x-position (Figures 74, 78 and 79, 80), despite the fact that there is a level shift as discussed above, the shapes of the profiles, though not simple, are almost identical in the two cases. (This can be seen by comparing Figures 74 and 79 and Figures 78 and 80.) Note, here, also that the data points shown in Figures 79 and 80 represent the data of three separate test runs. Thus, for an x-position of 0%, at least, the reproducibility of the shape of the velocity profile is established. On the basis of the above arguments, the shapes of the $\bar{v}'$ profiles will tentatively be regarded as correct except for effects of probe blockage.

Some investigations were made on the relationship between the two types of velocity profiles,

$$\bar{v}' = \frac{\int_0^T \rho v dt}{\int_0^T \rho dt} ,$$

and

$$\bar{v} = \frac{1}{T} \int_0^T v dt .$$

By examining the oscilloscope photographs taken at each x-position (see Sections 4.10 and 4.11) it was observed that the phase between the pressure and velocity traces changed very little from the center-line of the duct up to the tube wall. Also, the shape of the hot-wire trace remained very roughly the same over the whole range of radial positions. From these two facts it would appear that the velocity profile $\bar{v}$ should be almost identical in shape to the profile $\bar{v}'$ computed from the same data. To check the fact, the computer program used to reduce the data (see Section 4.12) was altered to allow $\bar{v}$ to be computed for each picture instead of $\bar{v}'$. The data of run AS-23 (which yielded $\bar{v}'$ profiles Figures 73 and 77) was run through the modified program to yield $\bar{v}$ profiles Figures 81 and 82. By comparing Figures 73 and 81 and Figures 77 and 82, it can be seen that the shapes of the $\bar{v}$ profiles are in fact almost identical to those of the $\bar{v}'$ profiles. On the basis of the above comparison for data taken at $x = 35\%$ (Run 23) it will be assumed that the $\bar{v}$ profiles are in general, very similar in shape to the $\bar{v}'$ profiles.

The $\bar{v}'$ and $\bar{v}$ velocity profiles will be discussed at considerable length in Section 5.

We now discuss some aspects of the $\hat{v}$ profiles (Figures 83-92). Because of the scales used, there appears to be much more scatter from a smooth curve in the $\hat{v}$ profiles than in the $\bar{v}'$ profiles. However, when the fractional scatter values of the $\hat{v}$ profiles are computed and compared with similar values for the $\bar{v}'$ profiles (Table 18), it is seen that on a fractional basis, the scatter of the $\hat{v}$ profiles is not much poorer than that of the $\bar{v}'$ profiles. Arguments for the accuracy and validity of $\hat{v}$ profiles, except for effects of probe blockage, are similar to those presented earlier for the

TABLE 18

TYPE OF PROFILE	FIGURE NOS.	RUN NO.	x-POSITION	MAXIMUM ABSOLUTE SCATTER	TYPICAL VELOCITY VALUE	MAXIMUM FRACTIONAL SCATTER
			%	FT/SEC	FT/SEC	
$\hat{v}$	83,87	AS-22	100	$\pm$ 3	140	$\pm$ .021
↓	84,88	AS-19	71	$\pm$ 3	80	$\pm$ .037
↓	85,89	AS-23	35	$\pm$ 3	140	$\pm$ .021
↓	86,90	AS-24	0	$\pm$ 7	230	$\pm$ .030
↓	91,92	AS-15	0	$\pm$ 3	240	$\pm$ .012
$\bar{v}'$	71-81	Various	Various	$\pm$ 1	40	$\pm$ .025

$\bar{v}'$ profiles. The first is the relatively small fractional scatter of the data points from a smooth curve. For the $\hat{v}$ profiles, this can be checked most easily in the sections of the profiles between wall distances of .2 and .73 in. (Figures 83-86, 91) where the curve should be a horizontal line. The second point, as before, is reproducibility of the data established in the one case where several separate profiles were taken at the same location. Runs AS-24 (Figures 86 and 90) and Runs AS-14, 15 and 18 (Figures 91 and 92) were all taken at x = 0%. The data of Run AS-15 given in Figure 91 show a profile whose shape agrees fairly well with the data of Run AS-24 presented in Figure 86. The peak of the profile in Figure 91 is somewhat higher than the peak in Figure 86, but is specified by only one point in the former case, and this point is only about 7 ft/sec too high to match the shape of profile Figure 86. Hence, the apparent high peak in Figure 91 is likely due to scatter of that one point. It should be pointed out that the level differences of profiles Figures 86 and 91 need not be due entirely to the unknown cause mentioned earlier with respect to the $\bar{v}'$ profiles, but rather, may partly be due to slight differences in the intensity of the oscillations set up in the different runs.* We now compare $\hat{v}$ profiles obtained from Runs AS-14, 15 and 18 and Run AS-24 in the region close to the wall (Figures 92 and 90). The fair agreement of Run AS-15 with Run AS-24 discussed above may also be noted from Figures 92 and 90. The limited portion of the $\hat{v}$ profile obtained from Run AS-18, (Figure 92) shows fairly good agreement in shape with the profile of Run AS-24. A most important confirmation of the shape of the $\hat{v}$ profile of Run AS-24 (Figure 90) comes from the profile of Run AS-14 (Figure 92) which supplies several points in the region of the profile peak (as opposed to the data of profile of Run AS-15). The shape of the $\hat{v}$ profile peak obtained in Run AS-24 is strongly supported by the data of Run AS-14, as far as the latter goes.

On the basis of the above discussion, the shapes of the $\hat{v}$ profiles will be regarded as accurate to within the scatter values given in Table 18, except for the effects of probe blockage. Despite the fact that the fractional scatter in the $\hat{v}$ profiles is not much worse than that of the $\bar{v}'$ profiles, the former are more difficult to compare among themselves than the latter for the following reason. The fractional changes in shape among the various $\hat{v}$

---

* See note, page 175A.

The follcwing is the note indicated at the bottom of page 175.

The level differences of the $\hat{v}$ data shown in Figures 90 and 92 are likely due to the two causes mentioned in the asterisked sentence on page 175 (there with respect to other data), and also to the fact that the data of runs AS-14, 15, 18 and 24 was likely taken at various frequencies slightly off resonance, and since the velocity waveshape varies relatively rapidly with frequency near resonance, variations in $\hat{v}$ can thus occur even if $\tilde{U}_A$ is unchanged from run to run.

profiles are much smaller than those among the $\hat{v}'$ profiles and hence are more easily submerged in the fractional scatter which is about the same size in the two cases.

In the cases where $\hat{v}$ data was taken out the center of the duct and near a velocity antinode (x = 0%, Figures 86, 91), it is possible to compare the value of $\hat{U}_A/\bar{U}$ measured using the hot-wire with that computed from the rms pressure reading obtained from the Dynisco pressure transducer (see Sections 3.4, 4.3, and early part of the present section). For this comparison we define the following quantities. $\hat{U}_{A1}$ is the value of $\hat{v}$ which the $\hat{v}$ profile (taken at x = 0%, near a velocity antinode) indicates at large distances from the wall. $\bar{U}_1$ is the average flow velocity obtained from mass flow measurements. $\left(\tilde{U}_A/\bar{U}\right)_2$ is the value of $\tilde{U}_A/\bar{U}$ calculated from the rms pressure measurement of the Dynisco transducer. Also, we set

$$\left(\frac{\hat{U}_A}{\bar{U}}\right)_1 = \frac{\hat{U}_{A1}}{\bar{U}_1} \quad , \tag{65}$$

and

$$\left(\frac{\hat{U}_A}{\bar{U}}\right)_2 = 2\sqrt{2}\left(\frac{\tilde{U}_A}{\bar{U}}\right)_2 \tag{66}$$

We make the comparison for the two cases in which it is possible (Table 19)

TABLE 19

RUN NO.	$\hat{U}_{A1}$	$\bar{U}_1$	$(\hat{U}_A/\bar{U})_1$	$(\tilde{U}_A/\bar{U})_2$	$(\hat{U}_A/\bar{U})_2$
	ft/sec	ft/sec			
AS-24	228.7	36.4	6.28	2.16	6.11
AS-15	238.5	35.3	6.76	2.20	6.22

From Table 19, it can be seen that the differences between the values of

$\hat{U}_A/\bar{U}$ as calculated by the two methods are about 3% and 8% in the two cases. This degree of agreement was judged to be quite satisfactory by the author, since the velocity does not time-vary exactly sinusoidally as is assumed in Equation (66). The time-variation of the velocity at the center of the duct in Run AS-15 (x = 0%) is shown in Figure 94. This curve was obtained simply by plotting up the instantaneous velocities (v_4 values) calculated on the computer program for the photograph of interest (see Section 4.12). It can be seen from Figure 94, that the time variation of the velocity is only roughly sinusoidal and shows a relatively sharp peak at the maximum and then falls off more rapidly than the sine curve would. This sharp peak is likely responsible for the fact the $\left(\hat{U}_A/\bar{U}\right)_1$ is more than $2\sqrt{2}$ times $\left(\tilde{U}_A/\bar{U}\right)_2$ (Table 19). The data of Table 19 basically constitutes a rough check on one aspect of the overall consistancy of the time-varying pressure and velocity measurements.

The $\hat{v}$ profiles, like the $\bar{v}'$ and $\bar{v}$ profiles, will be discussed further in Section 5.

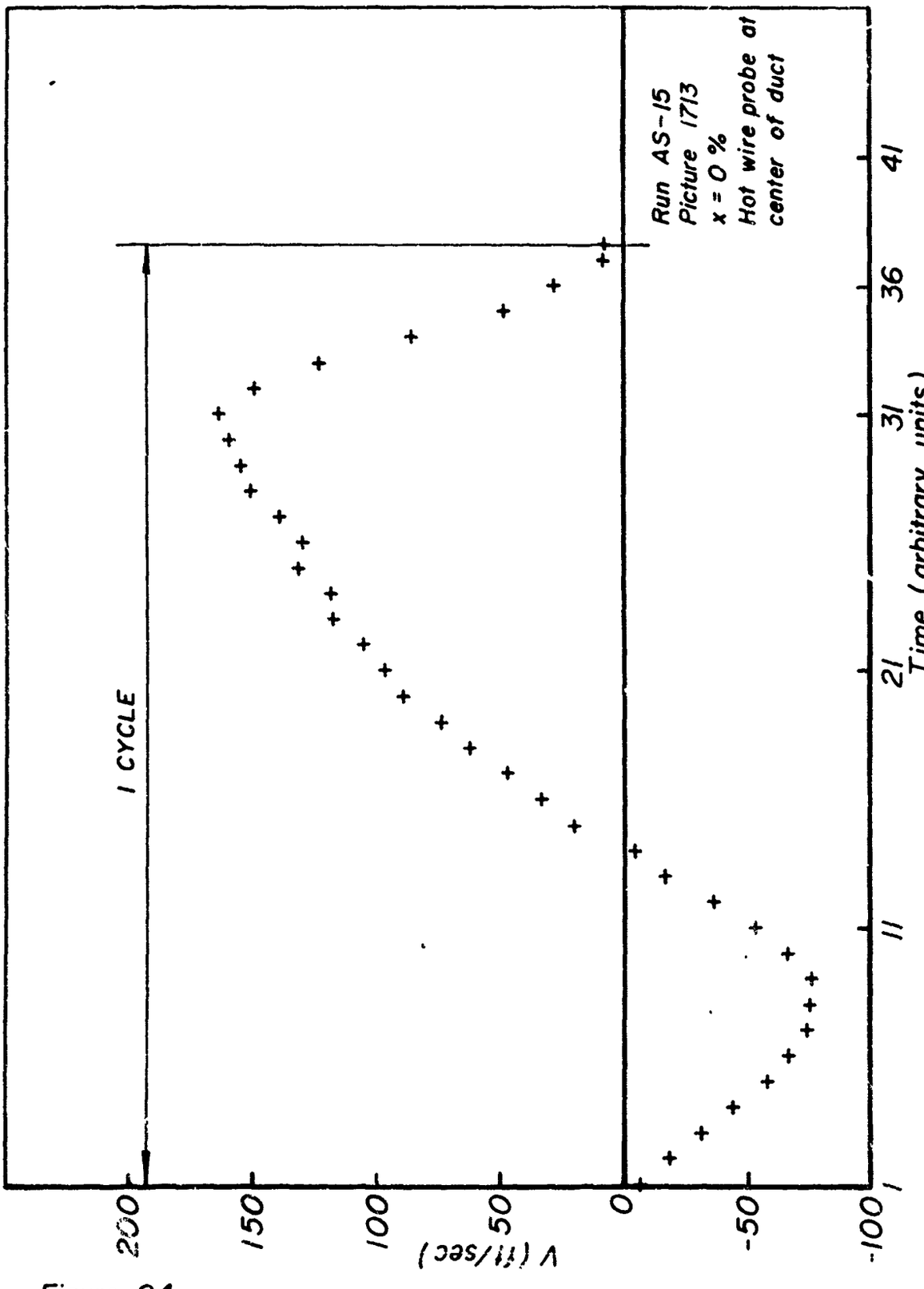
Run AS-15
Picture 1713
x = 0 %
Hot wire probe at
center of duct
1 CYCLE
V (ft/sec)
200
150
100
50
0
-50
-100
1
11
21
31
36
41
Time (arbitrary units)

Figure 94

5. DISCUSSION

5.1 Viscous Dissipation

We consider three examples of heat transfer measurements made in pipe flow with superimposed oscillations. The three cases discussed are taken from References 23 and 24 (see Section 2) and Section 3 of the present report and all give local heat transfer data at many points along the pipe wall. We shall make use of Equation (16) from Section 1 which gives the viscous dissipation to be expected in laminar flow when the local peak-to-peak velocity in the center of the pipe is $\hat{U}$.

$$Q_v = \frac{1}{8} \hat{U}^2 \sqrt{\frac{\omega \rho \mu}{2}} \qquad (16)$$

When the heat transfer is to the fluid from the pipe walls, one would expect the heat transfer rate to be reduced at the velocity antinodes due to viscous dissipation, but for the latter to have little effect on the heat transfer at the velocity nodes, where the local value of $\hat{U}$ is small. We first consider the heat transfer data presented in Section 3 of this report. Surveying Figures 36-43, we see that in almost all cases, the maxima and minima of heat transfer are so located as not to support the hypothesis that viscous dissipation is an important effect in explaining the observed heat transfer deviations. In the data of Figure 37 ($\check{U}_A/\bar{U} \approx .8$, the lowest amplitude at which noticeable effects on heat transfer were produced by the oscillations) however, the locations of the maxima and minima, though somewhat downstream of those predicted by the viscous dissipation effect, lend some slight support to the hypothesis that viscous effects may be important. [If the variations of heat transfer (as one moves downstream) shown in Figure 37 were in fact caused by viscous dissipation, it would be necessary to postulate another mechanism to raise the general level of heat transfer under oscillating conditions, since viscous dissipation predicts only decreases in heat transfer, and at some axial position in Figure 37, increases of heat transfer are observed. This overall increase in level of heat transfer might be caused by an increase in the turbulence exhange rates of the flow under oscillating

conditions, see Section 1]. We now estimate the magnitude of the dissipation effects to see if they might explain the fluctuations in heat transfer shown in Figure 37. To get an idea of the order of magnitude of the eddy viscosity in the regions of the high A. C. shear (see Section 1) causing dissipation, we locate the value of the A. C. boundary layer thickness (δ_A defined by Equation (12), Section 1, and the following text) on the eddy viscosity plot across the pipe diameter as determined from the steady-state universal velocity profile. There are, of course, many possible causes for error in this simple analysis: one is the fact that δ_A defined by Equation (12), et cetera, is derived for laminar flow; another is the fact that the eddy viscosity profile is not expected to be the same as that in steady flow, indeed, changes in the eddy viscosity are proposed as another mechanism for producing the deviations of heat transfer observed under oscillating conditions. However, as the analysis proceeds, it will be shown that such errors are not serious for order of magnitude estimates. We first estimate the value of δ_A using the following equation obtained from Equation (12) and the succeeding text.

$$\delta_A = \sqrt{\frac{2\nu}{\omega}} \tag{67}$$

Rather than use exact values appropriate for the data of Figure 37, we evaluate μ and ρ for air under typical conditions of temperature and pressure - 70° F and 54.7 psia (see Section 3.1). The frequency of oscillation at the 9th harmonic, at which the heat transfer data of Figure 37 was taken was $\sim$ 270cps. Inserting these values in Equation (67), yields δ_A = .00272 in. From Equation (11), Section 1, and from the fact that the dissipation per unit volume varies as U_y^2, it can be seen that the mean distance from the wall at which the dissipation takes place is 1/2 δ_A = .00136 in. To estimate the eddy viscosity in the region of the flow near the wall, we use the universal velocity profile in the form given in Reference 29, p. 157. This is given in Equation (68).

$$y^+ = 0 - 5 \quad , \quad u^+ = y^+ \qquad (a)$$

$$y^+ = 5 - 30 \quad , \quad u^+ = -3.05 + 5.00 \ln(y^+) \qquad (b)$$

$$y^+ = 30 \quad , \quad u^+ = 5.5 + 2.5 \ln(y^+) \qquad (c)$$

$$y^+ = \frac{y}{\nu}\sqrt{\frac{\tau_w}{\rho}} \qquad (d) \qquad (68)$$

$$u^+ = u\sqrt{\frac{\rho}{\tau_w}} \qquad (e)$$

where τ_w = shear stress at wall.

We also set

$$y_1^+ = 5 \qquad (69)$$

$$y_2^+ = 30 \qquad (70)$$

We now assume that $\tau = \tau_w$ in the region that we are interested in. (Our values of δ_A will turn out to lie at such small values of y^+, that they are well within the 'constant-stress' layer.) We have plotted in Figure 95, the values of $\frac{\varepsilon * \nu}{\nu}$ versus y^+ that would be obtained from Equation (68) if $\tau = \tau_w$ everywhere. The discontinuity is between the two lower equations for $u^+ = f(y^+)$ at $y^+ = 30$ in Equation (68). Figure 95 is, of course, correctly related to Equation (68) only insofar as $\tau = \tau_w$ out to $y^+ = 50$.

Since the heat transfer section in which the measurements presented in Figure 37 is preceeded by a calming section 32.7 diameters long (Section 3.1), we shall estimate the value of τ_w from the standard curve of the friction factor, λ, versus Re given in Schlicting (Reference 28, p. 504). λ is defined as given below:

$$\tau_w = \frac{1}{8}\lambda\rho\bar{u}^2 \qquad (71)$$

By combining Equations [68(d)], (69) and (71), we obtain

$$\frac{y_1}{D} = \frac{14.14}{\sqrt{\lambda}}\,\frac{1}{Re} \qquad (72)$$

182
50
40
30
20
10
0
y^+
y_2^+
y_1^+
$\frac{\delta_{AI}^+}{2}$
35
30
25
20
15
10
5
0
$\frac{u}{u+v}$

Figure 95

where

$$5 = y_1^+ = \frac{y_1}{\nu}\sqrt{\frac{\tau_w}{\rho}} \tag{73}$$

Taking the values of Re and D from Figure 37 as $\sim$ 100,000 and 1.5 in., we obtain from Equation (72), $y_1 = .001582$. This means that the average wall distance at which the viscous dissipation takes place, non-dimensionalized as y is in Equation [68(d)] is given by:

$$\frac{\delta_A^+}{2} = y_1^+ \left(\frac{\delta_A}{2\,y_1}\right) \tag{74}$$

$$\frac{\delta_A^+}{2} = 5\left(\frac{.00136}{.001582}\right) = 4.30$$

This value of $\delta_A^+/2$ is shown in Figure 95 as δ_{A1}^+. Since, from the location of $\delta_A^+/2$ on Figure 95 in this case, most of the viscous dissipation should be occuring with $(\epsilon + \nu)/\nu$ values near unity, Q_v calculated from the laminar flow formula Equation (16) should be a good estimate of the true value. From Figure 37, $\tilde{U}_A/\bar{U} = .770$. From mass flow calculations (see Section 3.4) the mean velocity in this case was computed as 33.7 ft/sec. Hence, approximately

$$\hat{U}_A = 2\sqrt{2} \times .770 \times 33.7$$

$$= 73.7 \text{ ft/sec}$$

Substituting this value of $\hat{U}$ into Equation (16) along with values of ρ, μ and ω approximated as discussed on p. 180, yields

$$Q_v \text{ (vel. antinode)} = Q_{v,A} = .001445 \text{ BTU/ft}^2 \text{ sec.}$$

From the data reduction associated with Run 22 (Figure 37) (i.e. the table corresponding to Table 14, for Run 27), a typical value of heat transferred to a condensate collection chamber of area .0654 ft^2 was $\sim$200 BTU/hr. Hence, a typical total heat transfer rate for the run in question (Q_c) is

$$Q_c = \frac{200}{3600 \times .0654} = .848 \text{ BTU/ft}^2 \text{ sec.}$$

From Figure 37, the fractional difference between the maximum and minimum deviations of the heat transfer under oscillating conditions from the steady state curve is about .118. Hence, the difference between the deviations of heat transfer at the maxima and minima is ΔQ_c .118 x .848 $\approx$ .100 BTU/ft^2 sec. The amount of viscous dissipation ($Q_{v,A}$) appears to be about 70 times too small to account for the observed fluctuations of the deviations of heat transfer (ΔQ_c).

We shall now estimate the value of Q_v for the case of maximum amplitude oscillations (Run 16, Figure 42) although the location of the maxima and minima of heat transfer in this case do not support the

hypothesis that viscous dissipation is an important phenomena. From Figure 42, $\tilde{U}_A/\bar{U} = 2.31$. We estimate $Q_{v,A}$ (Run 16) as follows.

$$Q_{v,A}\ (\text{Run 16}) \approx \left[\frac{\left(\frac{\tilde{U}_A}{\bar{U}}\right)_{\text{Run 16}}}{\left(\frac{\tilde{U}_A}{\bar{U}}\right)_{\text{Run 22}}}\right]^2 Q_{v,A}\ (\text{Run 22}) \qquad (75)$$

$$\approx \left(\frac{2.31}{770}\right)^2 \quad .001445$$

$$Q_{v,A}\ (\text{Run 16}) \approx .01030 \quad \text{BTU/ft}^2\ \text{sec}$$

Since the previous value of Q_c is also roughly applicable for Run 16, we see that at maximum amplitude, the viscous dissipation at the velocity antinodes is only slightly more than 1% of the typical total heat transfer rate through the pipe wall, and certainly could not explain the heat transfer deviations shown in Figure 42, even ignoring the fact that the maxima and minima of heat transfer in Figure 42 are in the wrong locations to be explained by viscous dissipation.

We now consider the possibility of applying viscous dissipation theory to explain some of the heat transfer data presented in References 1, 2, 3, 21, 22 and 23 which refer to the work done at the Georgia Institute of Technology (see Section 2). Surveying the experimental data presented in these references, bearing in mind the nature of the effects which viscous dissipation should produce, as discussed earlier in this section, leads the present author to select the data of Reference 23, p. 29 as typical of that most suitable for possible interpretation in terms of viscous dissipation effects. In the data selected from Reference 23 (The reader may refer to Figure 21, which is very similar to the selected data, and is extracted from the same reference.), the maxima of heat transfer are located at the velocity nodes and differs little from the steady-state heat transfer values. The minima of heat transfer occur at the velocity antinodes. Hence, with regard to the location of the maxima and minima of heat transfer and the level of the maxima, this data agrees perfectly with that to be expected on the basis of

viscous dissipation. However, we now estimate whether the dissipation effects can account for the magnitudes of the heat transfer deviations shown in the data selected from Reference 23. For this data (see Section 2) the air conditions are roughly 70° F and atmospheric pressure, and the frequency of oscillation is 222 cps. Under these conditions, δ_A computed as described earlier in this section is .00650 in. Since hydrodynamic development in these experiments started essentially at the inlet to the heat transfer section and since the latter was $\sim$ 31 diameters long, τ_w was estimated from a formula for a flat plate taking x = 16 diameters $\approx$ 60 in. The formula used is taken from Schlicting, (Reference 28, p. 537) and is:

$$C_f' = \frac{\tau_w}{\frac{1}{2}\rho \bar{U}^2} = \frac{.0576}{(Re_x)^{.2}} , \qquad (76)$$

$$5 \times 10^5 < Re_x < 10^7$$

Schlicting states that this formula, derived from the 1/7 power velocity distribution in the boundary layer and the Blasius law for the skin-friction coefficient, is in excellent agreement with experiment for flat plates whose boundary layers are turbulent from the leading edge onwards. References 5, 19 and 4 (see Section 2) indicate that under oscillating conditions, flow over flat plates may transition at as low as $Re_x = 10^4$. Hence, for the case now being discussed, we shall assume that transition takes place essentially at the leading edge, and use Equation (76) to estimate τ_w. Combining Equations (73) and (76) yields

$$\frac{y_1}{x} = \frac{29.4}{Re_x^{.9}} \qquad (77)$$

For the data of Reference 23, Re = 43,000, D = 3.86 in. and x = 60 in. as mentioned above. Hence,

$$Re_x = 43{,}000 \times \frac{60}{3.86} = 668{,}000 \ .$$

and $y_1 = .01009$ in.

Again, non-dimensionalizing $\delta_A/2$ as y is non-dimensionalized in Equation [68(J)], we have

$$\frac{\delta_A^+}{2} = y_1^+ \left(\frac{\delta_A}{2y_1}\right)$$

$$= 5 \left(\frac{.00325}{.01009}\right)$$

$$\frac{\delta_A^+}{2} = 1.61$$

Hence, referring to Figure 95, the viscous dissipation in this case should be very nearly entirely in regions where $(\epsilon+\nu)/\nu \approx 1$. Hence again the use of Equation (16) to estimate Q_v should be justified. The μ, ρ and ω values used in Equation (16) are those taken previously to compute δ_A. The value of $\hat{U}_A$ is computed from the appropriate sound pressure level given in Reference 23 (see Equation 8, Section 1) as 80.2 ft/sec. Substituting these values in Equation (16) yields,

$$Q_{v,A} = .000800 \quad BTU/ft^2\text{-sec.}$$

From a table in Reference 23, typical values of the heat transfer coefficient and wall-air temperature difference for the case of interest are $h = 5.45$ BTU/ft^2-hr-$^\circ$R and $\Delta T = 68.2^\circ$R. Hence, a typical value of Q_c is

$$Q_c = \frac{5.45 \times 68.2}{3600} = .1033 \quad BTU/ft^2\text{-sec.}$$

Now, the fractional difference between the deviations of heat transfer at the maxima and minima for the case in point was .1414. Hence, the difference between the deviations of heat transfer at the maxima and

minima is

$$\Delta Q_c = .1414 \times .1033 = .01460 \quad BTU/ft^2 \text{ sec.}$$

Thus, while in this case, the form of the heat transfer deviations corresponds closely to that expected on the basis of viscous dissipation, the magnitude of the deviations observed are $\sim$ 18 times too large to be explained by dissipation effects. Other experimental data in References 1, 2, 3, 21, 22, and 23 does not offer any stronger evidence of the importance of viscous dissipation effects. At Reynolds numbers greater than $\sim$ 30,000 (see the discussion of these references in Section 2), the data is similar to that discussed above, and for lower Reynolds numbers, the locations of the maxima and minima of heat transfer disagree with those predicted from dissipation theory.

Finally, we attempt to explain deviations in heat transfer observed in a rocket engine (Reference 24) using the viscous dissipation theory. The heat transfer data used is that shown in Figure 27 taken from Reference 24. In this case, the heat transfer is from the gas to the wall, and the effect of viscous dissipation would be to increase the heat transfer at the velocity antinodes and to have little effect at the velocity nodes. From Figure 27, it can be seen that, again, the form of the observed heat transfer deviations agree with that predicted by viscous dissipation theory. We now estimate the magnitude of $Q_{v,A}$ as was done in the two previous cases. Computing the appropriate values of ρ, μ, and ω as described in the discussion of Reference 24 in Section 2, and substituting these values into Equation (16) yields δ_A = .00430 in. In the case now being discussed, the length of the 'heat transfer section' (the rocket motor chamber) is $\sim$11 diameters (32 inches), and the flow starts to develop (in some fashion) at the beginning of this section. Hence, we again use the flat plate formula [Equations (76) and (77)] to estimate τ_w. From Section 2, Re and D are 161,000 and 3 in. respectively. We take a typical value of x as 16 in. (= half the chamber length). Hence, we have:

$$Re_x = 161{,}000 \times \frac{16}{3} = 860{,}000$$

Substituting the values of x and Re_x into Equation (77) yields y_1 = .0216. Hence,

$$\frac{\delta_A^+}{2} = y_1^+ \left(\frac{\delta_A}{2y_1}\right)$$

$$= 5 \left(\frac{.00215}{.0216}\right) \qquad (74)$$

$$\frac{\delta_A^+}{2} = .50$$

and again referring to Figure 95, we see that the dissipation regions should, in this case, lie almost entirely within the region where $\frac{\epsilon+\nu}{\nu} \approx$ 1. Using the values of ρ, μ, ω and $\hat{U}_A$ computed as stated in the discussion of Reference 24 in Section 2, we compute $Q_{v,A}$ from Equation (16).

$$Q_{v,A} = 1.208 \quad BTU/ft^2\text{-}sec.$$

The value of ΔQ_c can be read directly from Figure 27 at

$$\Delta Q_c = 3.5 \quad BTU/in^2\text{-}sec$$

$$\Delta Q_c = 144 \times 3.5 = 504 \quad BTU/ft^2\text{-}sec.$$

Thus, in this case, the deviations of heat transfer, again of the correct <u>form</u> to be explained by viscous dissipation, are very much larger in magnitude than those predicted by dissipation theory. In this last case, the large temperature differences across the boundary layer may introduce errors into the values of ρ and μ used in the calculations, but these errors are not large enough to alter the above conclusion. (Especially in the calculation of $Q_v \propto \sqrt{\rho\mu}$, the temperature effects on ρ and μ being in opposite directions, and the presence of the square

root, should make the value of Q_v relatively weakly affected by the temperature variations across the boundary layer.)

On the basis of the results obtained above for the three cases investigated, it appears that in most cases of interest, viscous dissipation effects should be unimportant in explaining deviations of heat transfer observed under oscillating flow conditions. In all three cases discussed above the oscillations were very strong and hence, in general, for dissipation effects to become important, it would appear that Q_c values would have to be very low which could occur if the time-average flow velocities ($\bar{U}$) and/or temperature differences between the air and the pipe wall (ΔT) were very low. In cases where $\bar{U}$ and/or ΔT are small enough, $Q_{v,A}$ may become appreciable compared to Q_c, and in this case dissipation effects would be important.

5.2 Acoustic Streaming

We use the theoretical analysis presented in Reference 1 (see Section 2) for acoustic streaming in laminar channel flow with superimposed standing wave oscillations. We use the results of Reference 1 which are for channel flow rather than those of Reference 2 for pipe flow on account of the extreme complexity of the latter. However, examination of plots of the acoustic streaming velocities given in References 1 and 2 indicate that the nature and magnitude of the streaming velocities are very similar for the corresponding cases in pipe and channel flow. Hence, comparison will be made between the streaming velocities predicted in Reference 1 for laminar channel flow, and the $\bar{v}'$ velocity profiles (see Section 4.13) measured in the present author's test rig for turbulent pipe flow. Reference 1 (see Section 2, pp. 50-53) shows that, except for the very thin wall vortices, the acoustic streaming velocities normalized by the time mean velocity in the channel ($\bar{U}$) depend only on $(\hat{U}_A/\bar{U})^2$ M, and, in particular, are independent of Re. The object of the comparison being made here is to see whether the acoustic streaming velocities in turbulent flow are similar to those predicted by the laminar flow theory using the values of $\hat{U}_A/\bar{U}$ and M

applicable to the turbulent flow case. The nature of the acoustic streaming velocities predicted from Reference 1 are shown in Figure 96, ignoring the thin wall vortices.

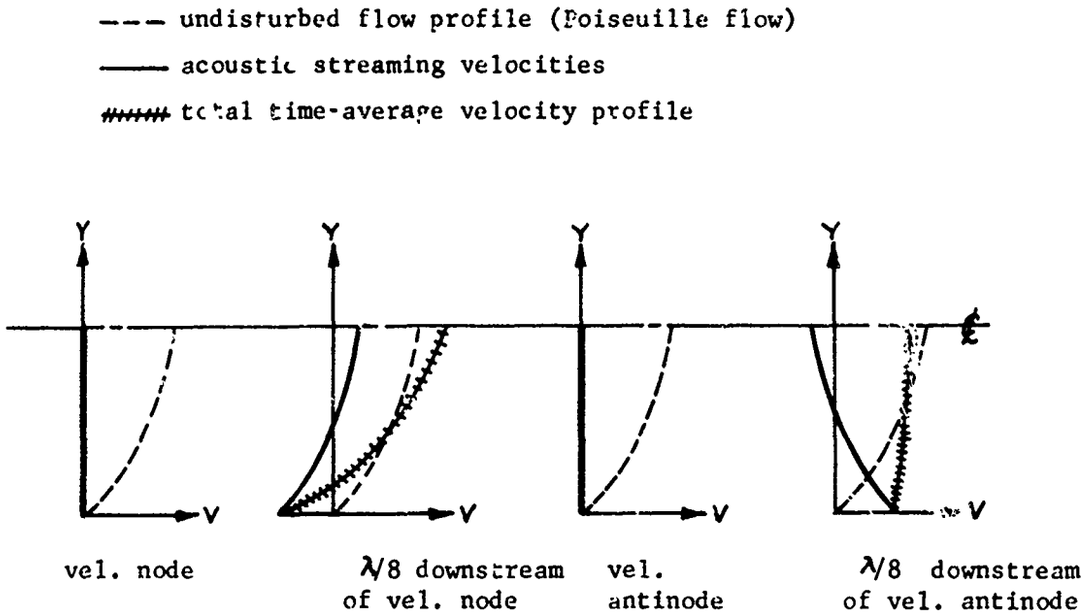

FIGURE 96

We compare these theoretically predicted profiles with the experimental profiles given in Section 4.13 (Figures 71-74). The latter profiles are of $\bar{v}' = \overline{\rho v}/\bar{v}$, whereas the former profiles are $\bar{v}$ profiles. However, as discussed in Section 4.13, it appears that the experimentally obtained profiles of $\bar{v}'$ and $\bar{v}$ have almost identical shapes and hence, we should be able to use the $\bar{v}'$ profiles for the above comparison.

In Table 20, we relate the theoretical and experimental profiles.

TABLE 20

			EXPERIMENTAL PROFILES		
LOCATION	THEORETICAL PROFILE	x-POSITION	x-POSITION	RUN NO.	FIG. NO.
		%	%		
Vel. Node	Fig. 96(a)	71	(71)	AS-19	Fig. 72
$\lambda/8$ Down. of Vel. Node	Fig. 96(b)	35	(35)	AS-23	Fig. 73
Vel. Antinode	Fig. 96(c)	-2	(0)	AS-24	Fig. 74
$\lambda/8$ Down. of Vel. Antinode	Fig. 96(d)	107	(100)	AS-22	Fig. 71

Note: The bracketed x-positions were those where the experimental profiles were taken. Where the desired location (column 1) lay outside the range of the travelling test section, (see Section 4.2) velocity profiles were taken at the nearest attainable location.

From Figure 96, we see that the acoustic streaming velocities are theoretically predicted to be zero at the velocity nodes and antinodes, and hence, we do not search for streaming velocities in Figures 72 and 74 but rather in Figures 73 and 71, at which locations, according to theory, the streaming velocities should be of maximum amplitude and in opposite directions.

The limitations of the theory given in Reference 1 [see Section 2,pp.50-53,Equations (26), (27) and (28)] require that

$$\frac{2\bar{U}}{\hat{U}_A} = o(\delta) \tag{26}$$

$$\frac{\hat{U}_A}{2c} = \frac{\hat{U}_A}{2\bar{U}} \times \frac{\bar{U}}{c} = o(\delta) \tag{27}$$

$$2\left(\frac{D}{\lambda}\right) = o(\delta) \tag{28}$$

where δ = a small number.

The theoretical calculation to be made will be done at the values of M and $\hat{U}_A/\bar{U}$ of the experimental tests to which the theoretical results will be compared. These data are given in Table 21 (p. 195) Also, from Figure 73 and 71, D = 1.46 in. λ at the 9th harmonic frequency of $\sim$ 270 cps is 49.5 in. Hence, we have corresponding to the above Equations (26), (27), (28):

$$\frac{2\bar{U}}{\hat{U}_A} = \frac{2}{6.15} = .325$$

$$\frac{\hat{U}_A}{2c} = \frac{6.15}{2} .0322 = .0990$$

$$2\left(\frac{D}{\lambda}\right) = 2\frac{1.46}{49.5} = .0590$$

Because the large value of the first term, $2\bar{U}/\hat{U}_A$, the theoretical laminar flow analysis applied to the case with $\hat{U}_A/\bar{U}$ and M as given above will only give a rough idea of the acoustic streaming velocity field (errors of the order of 30% may occur). However, this is sufficiently accurate to allow some comparisons with experiment to be made.

Reference 1 gives the time average non-dimensionalized U-velocity profile in the channel with acoustic streaming as:

$$\bar{U}' = \frac{6\bar{U}}{\hat{U}_A}\left(\gamma - \frac{\gamma^2}{2}\right) - \frac{\hat{U}_A}{16c}\sin\left(\frac{4\pi x}{\lambda}\right)\left\{\left(9 - \frac{54\delta_A}{D}\right)\left(\gamma - \frac{\gamma^2}{2}\right) - 3 + e^{-\left(\frac{y}{\delta_A}\right)}\left(2\cos\left(\frac{y}{\delta_A}\right) + 6\sin\left(\frac{y}{\delta_A}\right) + e^{-\left(\frac{y}{\delta_A}\right)}\right)\right\} \quad (78)$$

where $\gamma = \frac{2y}{D}$

x = dimension measured downstream from a velocity antinode.

We consider the region well outside the wall vortices, hence $e^{-\left(\frac{y}{\delta_A}\right)}$ is very small. (see Section 2, p. 53 , Figure 24) Also, for our case, δ_A/D is very small (see Section 1, p. 6 , Equation (13), and associated text). Neglecting these terms Equation (78) simplifies to:

$$\bar{U}' \left(\frac{\hat{U}_A}{6\bar{U}}\right) = \left[\left(\gamma - \frac{\gamma^2}{2}\right) - \frac{1}{96}\left(\frac{\hat{U}_A}{\bar{U}}\right)^2 M \sin\frac{4\pi x}{\lambda}\left\{9\left(\gamma - \frac{\gamma^2}{2}\right) - 3\right\}\right] \tag{79}$$

Undisturbed flow profile — Acoustic streaming velocities

In the new non-dimensionalization of Equation (79), the mean flow velocity is 1/3. We consider the location where $\sin\left(4\pi x/\lambda\right) = 1$ in Equation (79). This corresponds to the position $\lambda/8$ downstream of a velocity antinode [Figure 96(d)]. In this case the acoustic streaming velocity near the wall (but well outside of the wall vortex) is, from Equation (79):

$$\frac{3}{96}\left(\frac{\hat{U}_A}{\bar{U}}\right)^2 M$$

At the same location the acoustic streaming velocity at the center of the channel is, from Equation (79):

$$-\frac{1.5}{96}\left(\frac{\hat{U}_A}{\bar{U}}\right)^2 M$$

The streaming velocities at the location $\lambda/8$ downstream of a velocity node would just be the negatives of those given above. For the experimental velocity profiles being compared with theory, we have (taking $\hat{U}_A/\bar{U} \approx 2\sqrt{2}\ \tilde{U}_A/\bar{U}$) from Figures 73 and 71 and associated mass flow measurements, the data shown in Table 21.

TABLE 21

Run No.	M_a	$\bar{U}$	$\tilde{U}_A/\bar{U}$	$\hat{U}_A/\bar{U}$
	—	ft/sec	—	—
AS-22	.0321	36.2	2.12	6.00
AS-23	.0323	36.1	2.23	6.30
Average	.0322	36.15	—	6.15

We substitute the average values of $\hat{U}_A/\bar{U}$ and M_a into the previously given non-dimensional expressions for the acoustic streaming velocities near the wall and at the channel center-line. The resulting velocities, together with the same, made dimensional using the average mean velocity for the cases of the two experimental profiles are shown in Table 22.

TABLE 22

Mean Flow Velocity	Acoustic Streaming Velocities $\lambda/8$ Downstream of Velocity Antinode		Units
	Near Wall	At Channel Center-line	
.333	.0382	- .0191	non-dimensional
36.15	4.15	-2.08	ft/sec

The theoretical prediction, then, for the difference between the profiles taken at x = 100% and x = 35% is 2 x 4.15 = 8.30 ft/sec near the wall, and 2x (-2.08) = -4.16 ft/sec at the pipe center-line. The theoretically predicted shape of the $\bar{v}$(x - 100%) - $\bar{v}$(x = 35%) profile is shown in Figure 97.(The wall vortices are not shown.) We shall compare this profile with the experimentally obtained profile of $\bar{v}'$(x - 100%) - $\bar{v}'$(x = 35%) taken from the data of Figures 73 and 71. As discussed in Section 4.13, the data of Figures 73 and 71 show a blockage effect of the hot-wire probe, but if acoustic streaming velocities such as those shown in Figure 97 were present one would expect them to be superimposed on the blockage

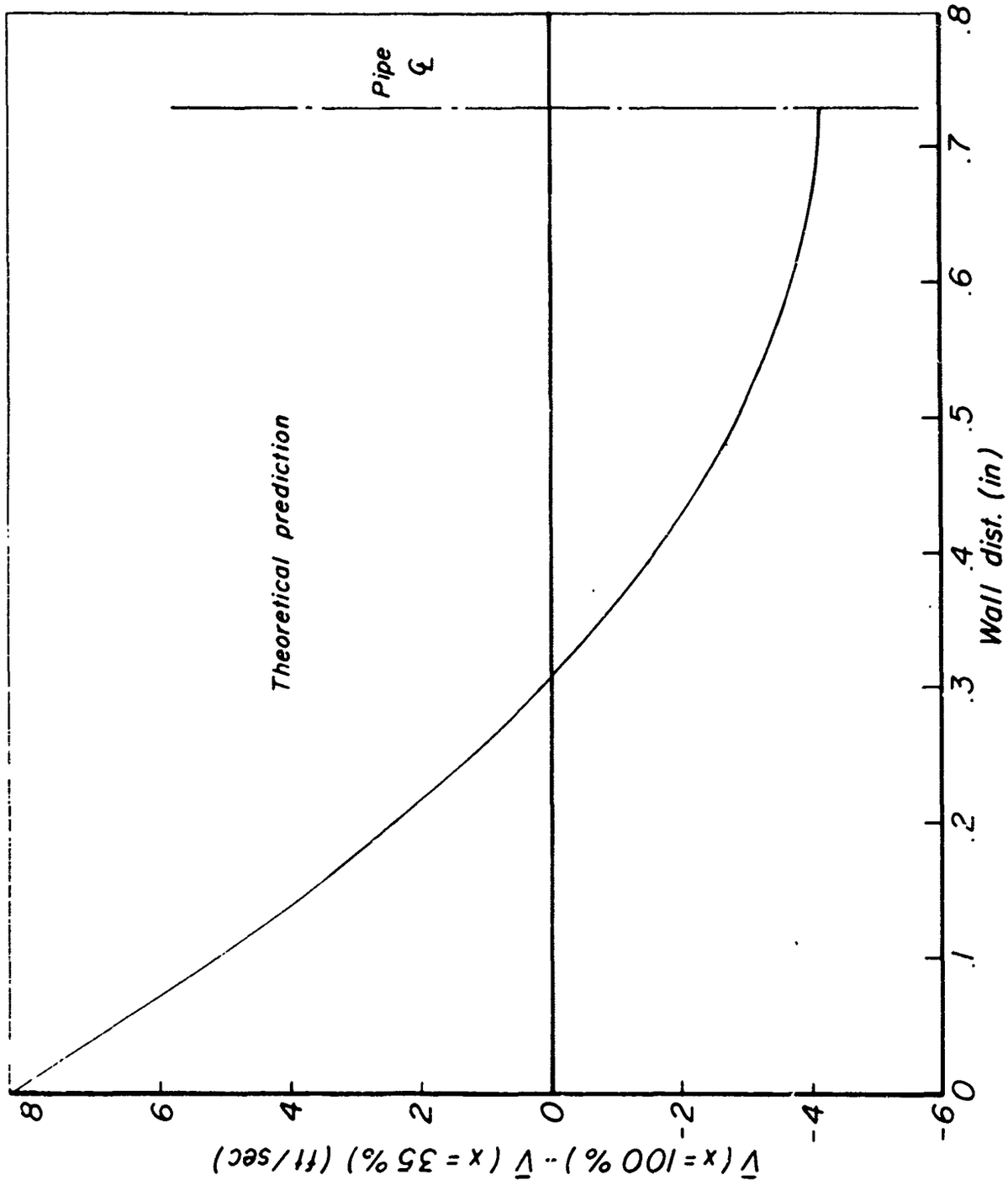

Figure 97

effect and to be readily discernable when one computes $\bar{v}'(x = 100\%) - \bar{v}'(x = 35\%)$. Also, as discussed in Section 4.13, there are level shifts among the various hot-wire profiles which are unexplained, but there are reasons for believing that the shapes of these profiles are accurate, except for blockage effects. Hence, if there are different level shifts in the experimental profiles of $\bar{v}'(x = 100\%)$ and $\bar{v}'(x = 35\%)$, there will be a corresponding level shift in the plot of $\bar{v}'(x = 100\%) - \bar{v}'(x = 35\%)$, but the shape of the latter should still show the acoustic streaming velocities, if present. The experimental profile of $\bar{v}'(x = 100\%) - \bar{v}'(x = 35\%)$ is shown in Figure 98. As discussed in Section 1 (pp. 10,11) the velocity profiles of Figures 73 and 71, will be distorted both by acoustic streaming velocities and effects due to variation in the eddy viscosity profile (turbulence exhange properties). Hence, both these effects might be responsible for the profile shown in Figure 98. The author believes that the very low section of the profile near the wall is an effect of variations in the eddy viscosity (see Section 5.3). The remainder of the profile only suggests the acoustic streaming profile (Figure 97) very weakly, and if interpreted as indicating streaming, would yield streaming velocities at least 4 times smaller than predicted theoretically (Figure 98). It is possible that effects of eddy viscosity variation almost cancel the acoustic streaming velocities in Figure 98, and that acoustic streaming is, in fact, as important as indicated in Figure 97 (the theoretical prediction). This is very unlikely since the eddy viscosity effects necessary to cancel the acoustic streaming velocities shown on Figure 97 would have to be exceedingly strong, and should produce very strong distortions of the velocity profiles of Figures 72 and 74 (where the acoustic streaming velocities should be zero, theoretically). The profiles Figures 72 and 74 do not show distortions of this magnitude. Hence, the tentative conclusion is that, at least in this case, for turbulent flow, the acoustic streaming velocities are much less (at least 4 times) than those predicted from the laminar flow theory using the $\hat{U}_A/\bar{U}$ and M values appropriate for the turbulent flow case. In Section 2, p. 51 , it was noted from References 1 and 2 that the acoustic streaming flow fields, normalized with respect

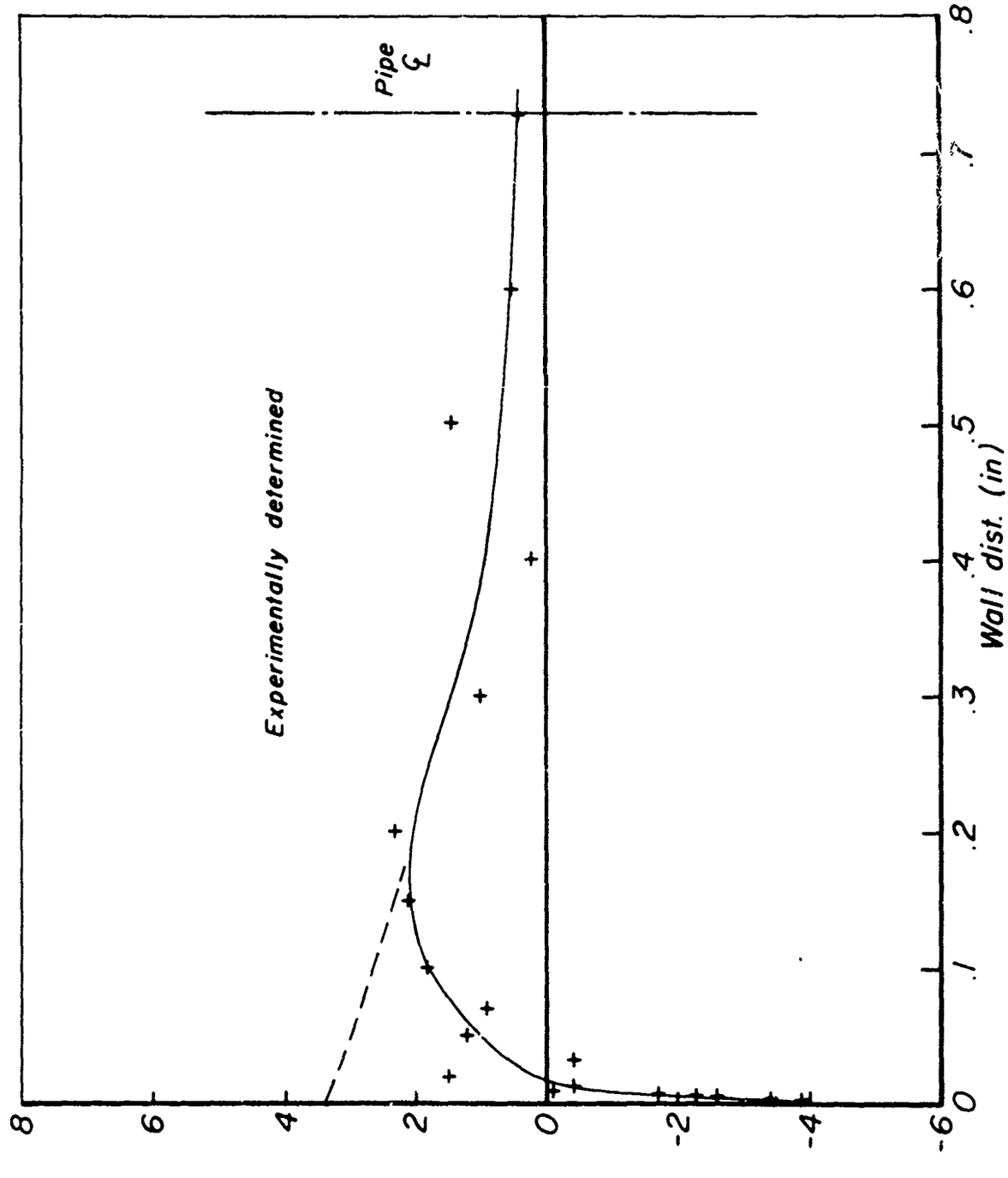
Pipe
℄
Experimentally determined
Wall dist. (in)
0
.1
.2
.3
.4
.5
.6
.7
.8
8
6
4
2
0
-2
-4
-6
$\bar{V}'(x=100\%) - \bar{V}'(x=35\%)$ (ft./sec.)

Figure 98

to the mean flow velocity depend only on $(\hat{U}_A/\bar{U})^2$ M, and not on Re (except for the wall vortices). Hence, the author feels that the fact that acoustic streaming velocities appear, in the case investigated above, to be much smaller in turbulent flow than predicted from the laminar flow analysis, is due to the variation of the 'total' (eddy + molecular) viscosity $(\epsilon + \nu)$ across the diameter of the pipe. In the laminar flow case, of course, $\epsilon = 0$ throughout the flow field. It might be possible to show this reduction of the streaming velocities by performing the theoretical analysis of Reference 1 using the steady turbulent pipe flow values of $\epsilon + \nu$ (as an approximation to the true values of $\epsilon + \nu$) in place of ν in the equations.

In Section 2, pp.50-53, we discussed the theoretical solution for heat transfer in laminar channel flow with superimposed standing wave oscillations presented in Reference 3. From this solution, Reference 3 presents the following correlation between the maximum fractional heat transfer deviation and Re, $\hat{U}_A/\bar{U}$ and M. (This is shown in Figure 26 taken from Reference 3.)

$$\left[\frac{Nu - Nu_o}{Nu_o}\right]_{max} \frac{1}{Re^{1/3}} = .0833 \left(\frac{\hat{U}_A}{\bar{U}}\right)^2 M \qquad (80)$$

The term $(\hat{U}_A/\bar{U})^2$ M represents the magnitude of the acoustic streaming velocities as compared to the average flow velocity $(\bar{U})$ (see Equation (79), p. 194). The reason for the appearance of Re in Equation 80 is as follows. Let T be a representative bulk temperature of the gas, and T_w the pipe wall temperature (here assumed constant). Then the amount of heat conducted to the walls per unit area is of order

$$\frac{K(T - T_w)}{D} .$$

The amount of heat transported towards the wall by convection per unit area, taking the velocity to be represented by $\bar{U}$, is of order

$$\rho\bar{U}C_p(T - T_\infty) \quad .$$

The ratio of these two quantities is

$$\frac{\rho\bar{U}C_p(T - T_w)}{K(T - T_w)/D} = \frac{\rho\bar{U}C_pD}{K} = \frac{\rho\bar{U}D}{\mu} \cdot \frac{\mu C_p}{K} = RePr \qquad (81)$$

As mentioned in Section 2, p. 54 , Reference 3 does not state the value of Pr used in the analysis; however, since the analysis is done for compressible flow, we assume that Pr = O[1], and hence, the ratio in Equation (81) may be represented by Re alone. We shall be using Equation (80) to predict heat transfer deviations to be expected in the case of turbulent flows. In this case, the heat transfer by conduction is not represented by $K(T - T_w)/D$ but rather, by the same expression with an 'average' 'eddy thermal conductivity' substituted for K. We estimate the ratio of the 'average' 'eddy thermal conductivity' to the molecular value by assuming that this ratio is given by the ratio of the experimentally observed Nusselt number to the theoretically predicted value of Nu for fully developed laminar pipe flow with constant wall temperature. From Reference 29, p. 194, this latter value is 3.65. Hence, when using Equation (80) to predict heat transfer deviations in turbulent flow, we shall evaluate Re based on an eddy viscosity which is larger than the molecular value by the ratio of the thermal conductivities discussed above This is, of course, assuming that the ratio of 'average' eddy to molecular viscosities is the same as the ratio of 'average' eddy to molecular thermal conductivities. This method of predicting heat transfer deviations due to acoustic streaming in turbulent flow is very uncertain for the following two reasons. The first is the fact that we assume that the streaming velocities are as given in Reference 1 (see pp. 50-53) in spite of the flow being turbulent. We have evidence from the first part of this section that in one case, at least, in turbulent flow, the acoustic streaming velocities are, in fact, considerably smaller than those predicted in Reference 1. The second point would introduce

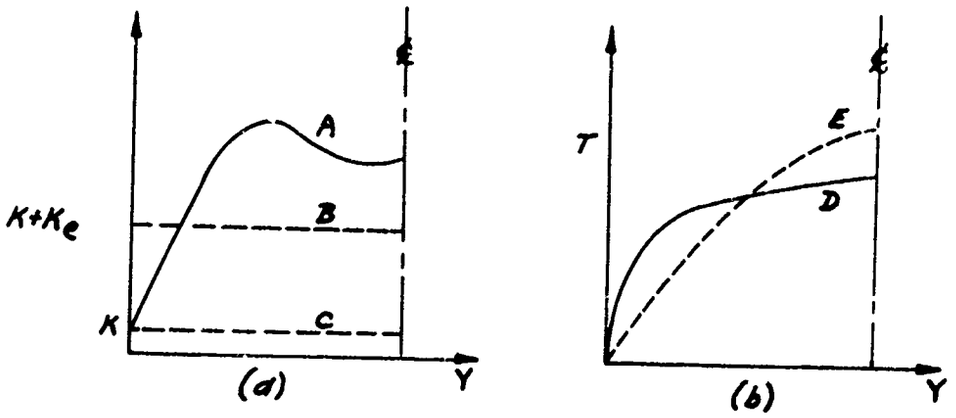

K_e = 'eddy thermal conductivity'

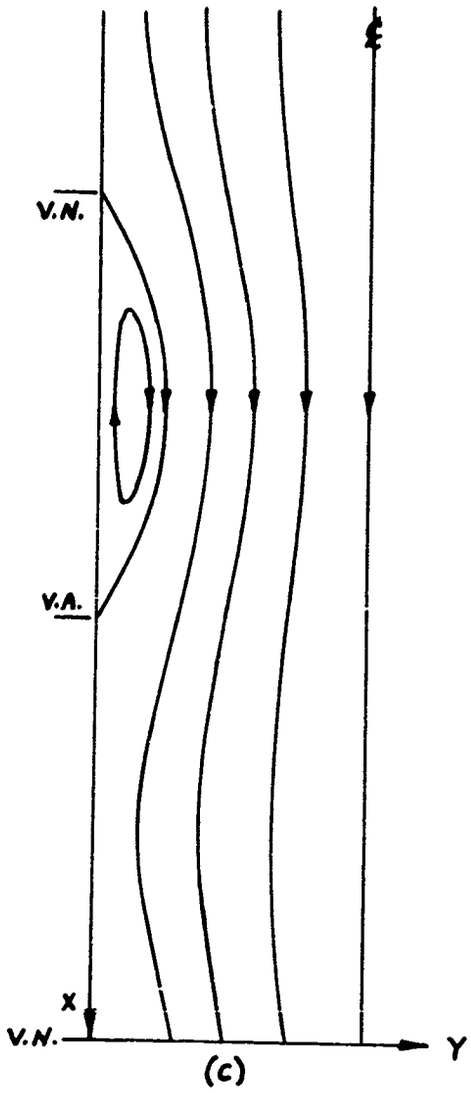

FIGURE 99

uncertainties, even if the acoustic streaming velocities were given by the analysis of Reference 1, as follows. We refer to Figure 99. In Figure 99 (a) and (b), the 'eddy thermal conductivity' and temperature profiles in steady fully developed turbulent pipe flow at the Reynolds number of interest are shown by curves A and D respectively. However, the way we have set up our theoretical analysis for turbulent pipe flow, we are actually investigating the effects of acoustic streaming on the flow situation shown in Figure 11 (a) and (b), curves B and E; that is, a laminar flow with the thermal conductivity replaced by an 'average eddy thermal conductivity' for the Reynolds number of interest computed from the steady-flow Nusselt number as described earlier in this section. The effects of the acoustic streaming velocities [a typical time average velocity field with acoustic streaming is shown in Figure 99 (c)] may be considerably different when acting upon the actual profiles of $K + K_\epsilon$ and T (represented by the steady-state curves A and D) than when acting on the form of these profiles assumed in the theoretical analysis (represented by curves B and E).

The effect of the difference in the acoustic streaming velocities from those predicted from the laminar flow analysis would be a decrease in the effect of acoustic streaming on heat transfer if the streaming velocities investigated by the present author (pp. 190-199) are representative of those in turbulent flows in general. The effect of the second point discussed above is not obvious but might increase the effect of streaming on heat transfer because near the wall, the y-velocities are convecting heat through a region of higher temperature gradient in the actual situation than in the situation theoretically modelled.

Because of these effects, the application of the heat transfer analysis of Reference 3 to predict the effects of streaming in turbulent flows is very uncertain, but some comparisons with experiment will be made. Any conclusions from these comparisons will be very tentative.

From Figure 25, Section 2 (taken from Reference 3), we see that acoustic streaming predicts that the maxima of heat transfer are

slightly downstream of the velocity antinodes, that the minima are slightly downstream of the nodes, and that there is little change in the overall heat transfer. We first consider the possible application of acoustic streaming theory to partially explain the deviations in heat transfer observed by the present author (see Section 3.5, Figure 36-43). Of Figures 36-43, Figure 42 seems to be in the best agreement, regarding general shape of the curve, with the acoustic streaming theory. The maxima and minima of heat transfer are roughly in the locations predicted by acoustic streaming theory, but there is an overall increase in heat transfer which would have to be otherwise explained, if acoustic streaming were responsible for the oscillations of the heat transfer curve in Figure 42. This overall increase in heat transfer, one might suppose to be caused by increases in the 'eddy thermal conductivity' (turbulence exchange properties) (see Section 1, pp. 10,11). From Figure 42, the deviations of the Nusselt number at the first minima, second maxima (at about chamber number 15), and second minima are 15, 92 and - 11 respectively. The mean steady-state Nusselt number in this region is 161. The value to be compared with the $[(Nu - Nu_o)/Nu_o]_{max}$ value in Equation (80) is then:

$$\frac{92 - \frac{[15 + (-11)]}{2}}{2(161)} = .279$$

We define

$$w = \left[\frac{Nu - Nu_o}{Nu_o}\right]_{max}, \qquad (82)$$

and w_e as the w value estimated from experimental data (in the above case $w_e = .279$). From Figure 42, for this case,

$$\frac{\hat{U}_A}{\bar{U}} = 2\sqrt{2}\,\frac{\tilde{U}_A}{\bar{U}} = 2\sqrt{2} \times 2.31 = 6.55$$

$$M_a = .0302$$

$$Re_a = 99{,}000$$

Hence, w based on Re evaluated with the molecular viscosity (w_ν), is from Equation (80)

$$w_\nu = (99{,}000)^{1/3} \quad (.0833) \quad (6.55)^2 \quad .0302$$

$$w_\nu = .499$$

Now, the ratio of viscosities, evaluated as discussed on p. 200, is

$$\frac{\bar{\epsilon}}{\nu} = \frac{161}{3.65} = 44.1$$

Hence, the value of w, based on Re evaluated sith the 'average eddy viscosity' ($w_{\bar{\epsilon}}$), is

$$w_{\bar{\epsilon}} = \frac{.499}{(44.1)^{1/3}} = .1414 \quad .$$

Hence, if the acoustic streaming velocities in this case were as given by the laminar flow analysis of Reference 1, the heat transfer analysis of Reference 3, modified as discussed above to allow for 'eddy thermal conductivity' effects predicts that about 1/2 of the observed oscillations of the heat-transfer deviations could be accounted for by acoustic streaming effects (since $w_{\bar{\epsilon}} \approx 1/2\ w_e$). However, as discussed earlier in this section (pp. 190-199) it appears that the actual acoustic streaming velocities in this turbulent flow case are at least 4 times smaller than those predicted by the theoretical analysis. Thus, based upon the maximum allowable streaming velocities consistant with the experimental observation, and the heat transfer analysis of Reference 3,

it appears that acoustic streaming could account for, at most, about 1/8 of the oscillations of the heat transfer deviations shown in Figure 42. Hence, despite the uncertainty of the heat transfer analysis, it appears fairly likely that acoustic streaming is not the major factor causing the oscillations of the heat transfer deviations in Figure 42.

We now consider the possible application of the modified acoustic streaming analysis of Reference 3 to explain some of the experimental heat transfer data presented in References 1, 2, 3, 21, 22, 23 describing the work done at the Georgia Institute of Technology. Reviewing the discussion of these references presented in Section 2, pp.42-56, we see that, ignoring the data taken at Re $\approx$ 2000, where natural convection effects may complicate the situation, only data in the Reynolds number range 10,000 - 20,000 shows locations of the maxima and minima of the heat transfer deviations which correspond roughly to those predicted by acoustic streaming. We compare the heat transfer deviations predicted by the theory discussed earlier in this section with experiment for the two cases of Reference 22, Figure 10, and Reference 23, Figure 6. The first set of data referred to is that reproduced in Figure 20 of this paper. In this case, the data shows an overall heat transfer increase as well as oscillations which might be attributable to acoustic streaming. In the data of Reference 23, Figure 6, there is no overall change in heat transfer. In both cases data are presented in the references for various sound pressure levels; we apply our analysis only to the maximum sound pressure level in each case. The calculations are gone through in essentially the same way as done earlier in this section for the present author's data (pp.200-204). The relevent data are presented in Table 23.

TABLE 23

	THEORETICAL CALCULATIONS							EXPERIMENTAL DATA
	Re	M	$\hat{U}_A/\bar{U}$	w_ϕ	Nu	$\frac{\bar{\epsilon}}{\nu}$	$w_{\bar{\epsilon}}$	w_e
Ref. 22, Fig. 10	11,600	.00553	9.23	.0885	28.2	7.72	.0448	.360
Ref. 23, Fig. 6	16,000	.00763	7.32	.0860	38.7	10.60	.0392	.166

Re was taken directly from the references; M and $\hat{U}_A/\bar{U}$ were computed as described in Section 2, p. 43 . w_ν , $\bar{\epsilon}/\nu$ and w_ℓ were computed as described earlier in this section (pp. 200-204), and a typical value of Nu was read off the curve of the reference. The value of $[(Nu - Nu_o)/Nu_o]_{max}$ estimated from experimental data (w_e) is computed essentially as done on p. 203, although different maxima and minima were used. In these cases we see that the observed oscillations in the heat transfer deviations are about 8 and 4 times larger than those predicted by the modified theoretical analysis of Reference 3. On the basis of these numbers, it might appear unlikely that acoustic streaming is a major cause of the oscillations of the heat transfer deviations which are experimentally observed in these two cases. This argument would be further strengthened if the observation by the present author (see pp. 190-199) that the acoustic streaming velocities experimentally observed in turbulent flow are (in one case) considerably less than those predicted by the laminar flow analysis applied (though perhaps less strongly) also to the two cases now being considered. Another argument against the importance of streaming in these two cases is the observation that the maximum (minima) of heat transfer are observed to be almost exactly located at the velocity antinodes (nodes), whereas in the theoretical analysis of Reference 3 (see Section 3, Figure 25), the locations of these extrema are $\sim \lambda/12$ farther downstream. However, bearing in mind the uncertainty of the heat transfer analysis, the possible importance of acoustic streaming in the above two cases is not completely eliminated, especially for the case of Reference 23 where $w_e/w_\ell \approx 4$. An argument which favors the importance of acoustic streaming in the cases selected from References 22 and 23 more strongly than in the data of the present work (Section 3.5, Figure 42) is now given. In the latter case, as was mentioned on p. 203, if acoustic streaming was responsible for the oscillations of the heat transfer deviations, one would have to propose another mechanism to explain the overall increase in heat transfer. In the case taken from Reference 23, the overall change in heat transfer is essentially zero, and in the case from Reference 22 (see Figure 20), the overall increase of heat transfer is much smaller compared to the amplitude of oscillations

of the heat transfer deviations than in the case of the data of Figure 42. Hence, in these cases from References 22 and 23, acoustic streaming could predict the form of the heat transfer deviations more closely without the assumption of any other mechanism, provided that the amplitude of the streaming-produced oscillations of the heat transfer deviations were large enough.

The conclusions of this section are now reviewed. For the case investigated by the present author (Re $\approx$ 100,000), it appears that the measured acoustic streaming velocities are at least 4 times lower than those predicted by the laminar flow theory of Reference 1. Applying the heat transfer analysis of Reference 3 modified as described previously to some of the experimental heat transfer results of the present author seems to indicate that acoustic streaming is not important in explaining the heat transfer deviations observed on account of: (1) the low heat transfer deviations (compared to observed values) predicted by the theoretical analysis (allowing for the largest streaming velocities consistent with experimental observation) and (2) the need to postulate another mechanism to explain the observed overall increase in heat transfer. However, due to the uncertainty of the heat transfer analysis, these conclusions are uncertain. Finally, the heat transfer analysis was applied to data selected from References 22 and 23, to attempt to explain the heat transfer deviations there observed experimentally by means of acoustic streaming. In these cases, facts favoring the possible importance of acoustic streaming are the ability of acoustic streaming to roughly predict the observed form of the heat transfer deviations without postulating any other mechanism, whereas facts arguing against the importance of streaming, are the low heat transfer deviations (compared to observed values) predicted by the theoretical analysis based on the streaming velocities which would occur in laminar flow (these values would be further lowered, if the streaming velocities were less than those predicted for laminar flow, as was observed by the present author for one case in turbulent flow) and the variation of the locations of the maxima and minima of the heat transfer deviations from the exact values predicted by the theoretical analysis. In view of the uncertain nature of the theoretical heat transfer analysis used here, no

definite conclusion can be reached about the importance of acoustic streaming in the cases taken from References 22 and 23.

5.3 Effects of Oscillations on Turbulence Exchange Properties

We first present an 'eddy viscosity' calculation based on the $\bar{v}'$ profiles presented in Section 4.13 (Figures 71-78). Under the conditions of the present experiment, there are many possible causes for error in such a calculation. These will be discussed in some detail after the method of calculation is given.

Because of the blockage effect of the hot-wire probe (see Section 4.13, pp.170,171), the $\bar{v}'$ profiles (Figures 71-78) were corrected as shown below before being used in the 'eddy viscosity' calculation. We refer to Fig. 93, which gives pitot and hot-wire velocity profiles across the duct in steady flow, and shows the blockage effect as discussed in the associated text. From these profiles, we construct a correction factor (F_v) as given below

$$F_v(y) = \frac{v_{p,ss}(y)}{v_{hw,ss}(y)} \tag{83}$$

where $v_{p,ss}(y)$ = velocity from pitot profile, steady flow (Fig. 93)

$v_{hw,ss}(y)$ = " " hot-wire " " " " " "

The pitot probe itself showed blockage effects for $y < .020$ in., and the $v_{p,ss}(y)$ profile was extended for $y < .020$ in. using the 'law of the wall'. A corrected value of $\bar{v}'(\bar{v}_c')$ was then computed as

$$\bar{v}_c'(y) = \bar{v}'(y)\, F_v(y) \tag{84}$$

There is a slight error in the factor $F_v(y)$ due to the fact that the average flow velocities for the two tests in which the profiles of Fig. 93 were taken were not quite the same. Because there are much more serious causes for error which will be discussed next, this error was ignored. The value of μ_t ('eddy' plus molecular viscosity) was calculated from a balance of pressure and shear forces as given on the next page.

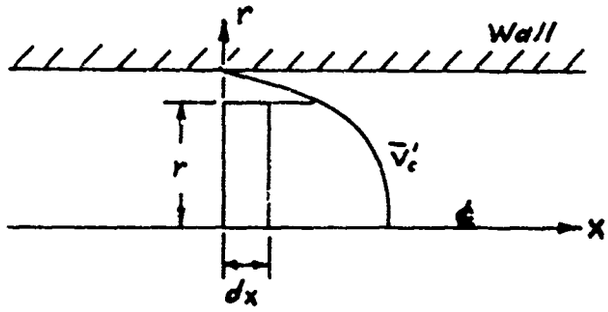

FIGURE 100

$$-\pi r^2 P_x \, dx + 2\pi r \, dx \mu_t \frac{\partial \bar{v}_c'}{\partial r} = 0 \qquad (85)$$

$$-\frac{\mu_t}{P_x} = -\frac{r}{2} \frac{1}{\frac{\partial \bar{v}_c'}{\partial r}} \qquad (86)$$

The resulting profiles of $-\mu_t/P_x$ versus y are given in Figures 101-108. $-\mu_t/P_x$ profiles obtained from the steady-state pitot profile of Fig. 93 are shown for comparison in Figures 109 and 110. Since this steady-state profile was extended using the 'law of the wall' for $y < .020$ in. as mentioned earlier, the $-\mu_t/P_x$ values for $y < .020$ in. are those assumed in the wall law; however, for $y \geq .020$ in., the $-\mu_t/P_x$ values are those determined from experiment. The x-position, location with respect to the node-antinode system on the duct, and Figure number of the related $\bar{v}'$ profile, are given for the $-\mu_t/P_x$ profiles in Table 24. Even assuming that the $-\mu_t/P_x$ profiles of Figures 101-110 are correct, the absolute value of μ_t is not known, since no measurements of P_x were taken. Hence, in the further discussion of the $-\mu_t/P_x$ profiles, comparison of the absolute levels of one profile with another to determine changes in the absolute value of μ_t cannot easily be made, however, some attempts to do this will be presented in the later discussion.

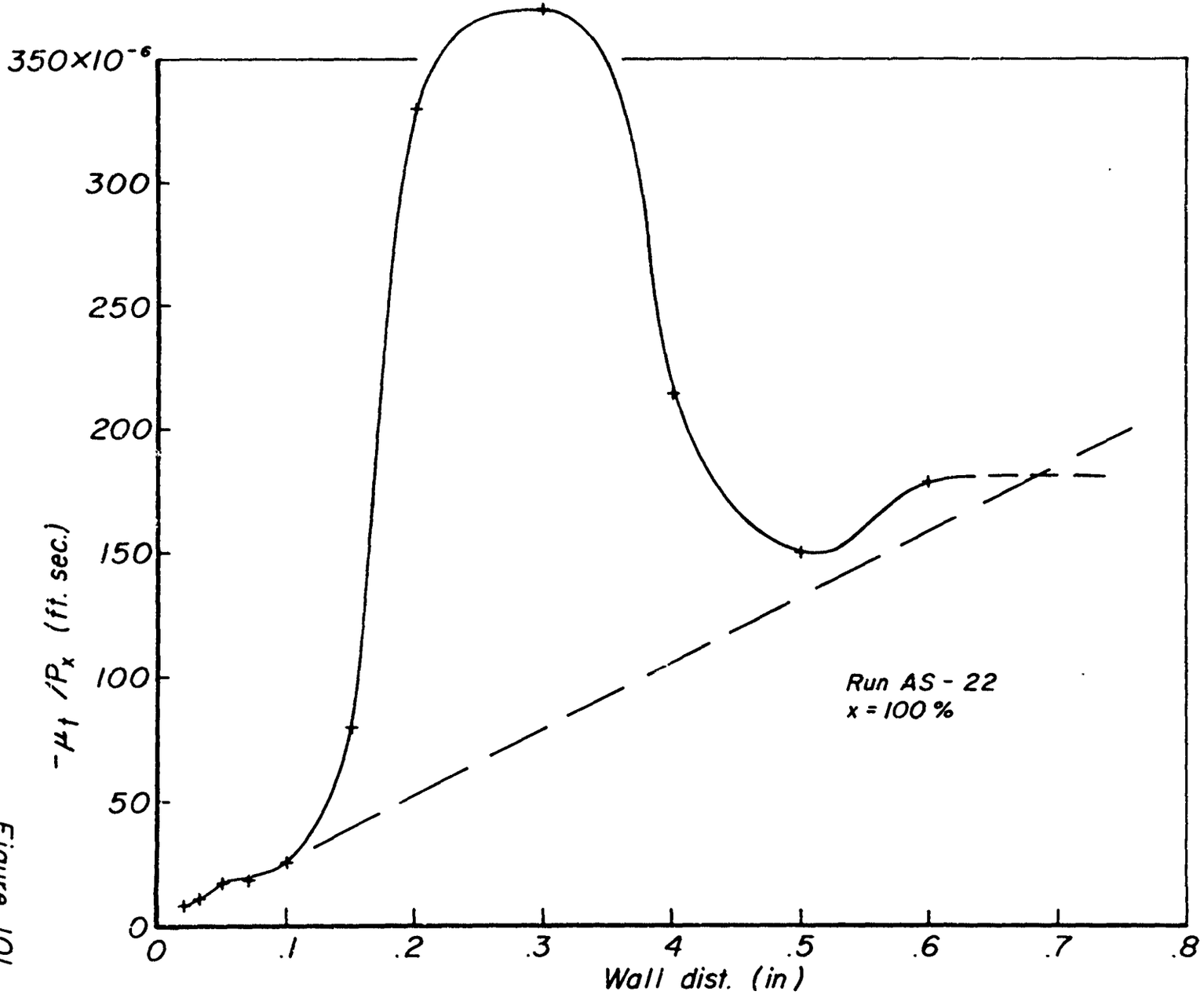
350×10⁻⁶
300
250
200
150
100
50
0
0
.1
.2
.3
.4
.5
.6
.7
.8
$-\mu_t / P_x$ (ft. sec.)
Wall dist. (in)
Run AS - 22
x = 100 %

Figure 101

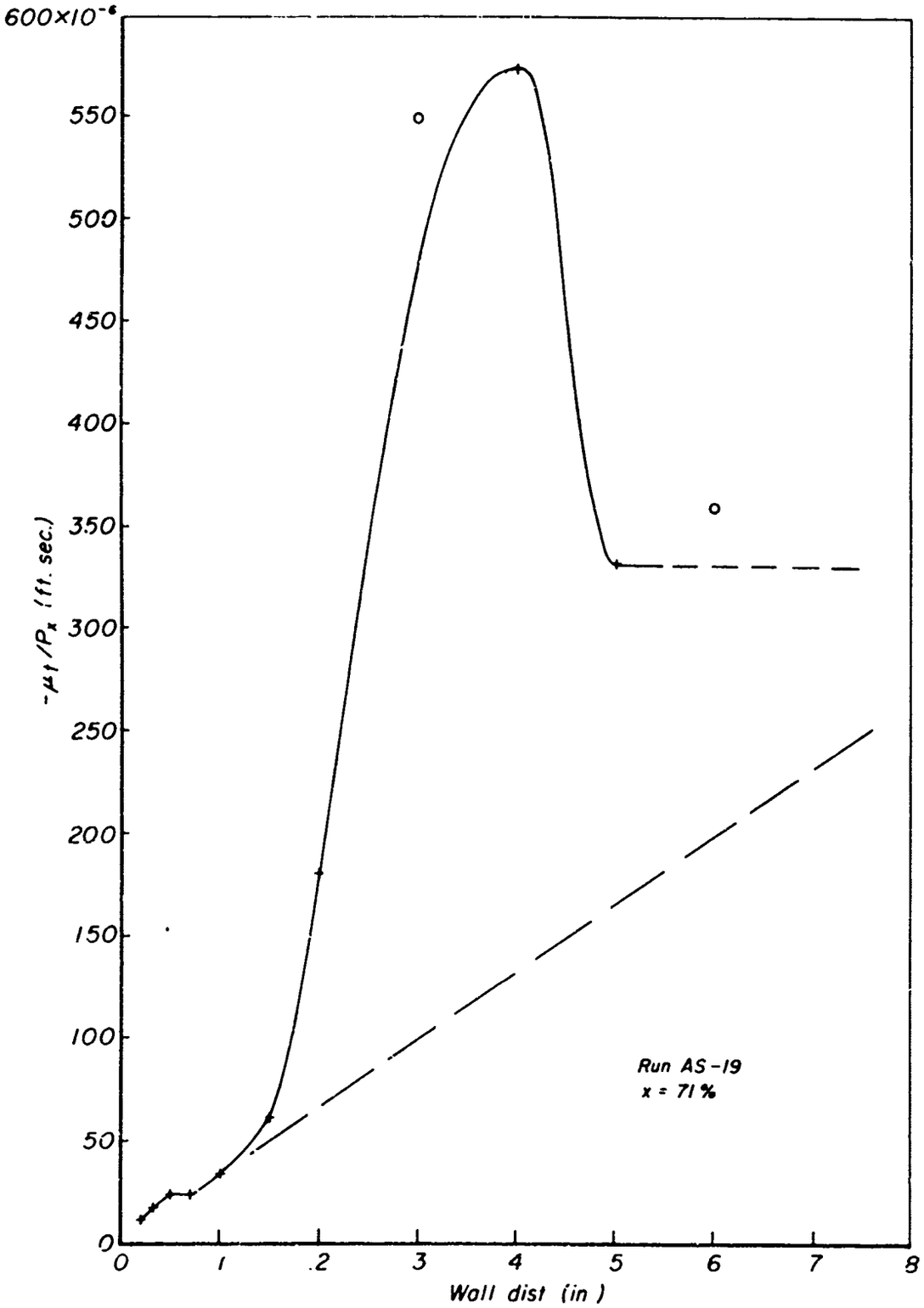
600×10⁻⁶
550
500
450
400
350
300
250
200
150
100
50
0
-μ₁/Pₓ (ft. sec.)
0
1
2
3
4
5
6
7
8
Wall dist (in.)
Run AS-19
x = 71%

Figure 102

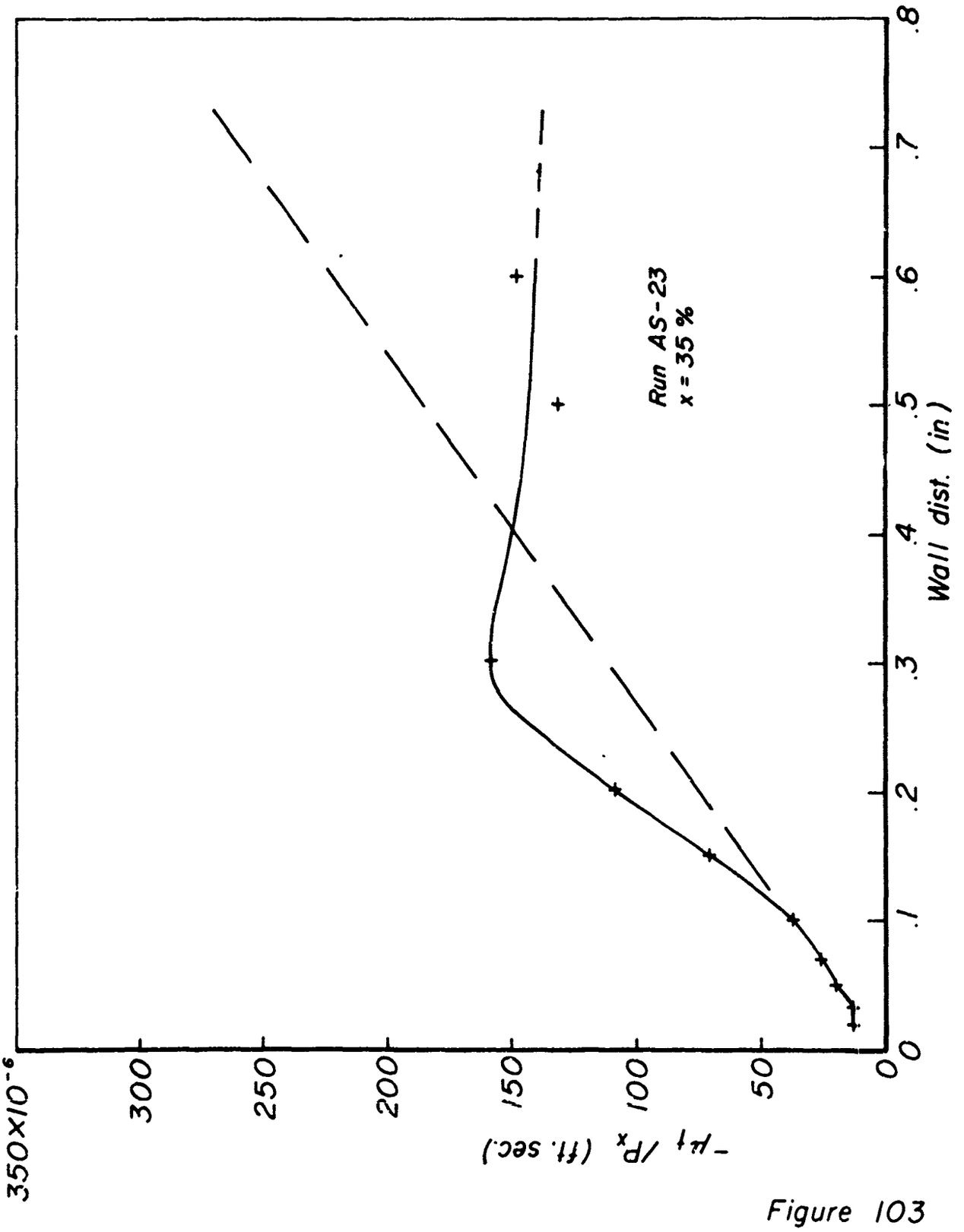
350x10⁻⁶
300
250
200
150
100
50
0
$-\mu_t/P_x$ (ft. sec.)
0
.1
.2
.3
.4
.5
.6
.7
.8
Wall dist. (in.)
Run AS-23
x = 35 %

Figure 103

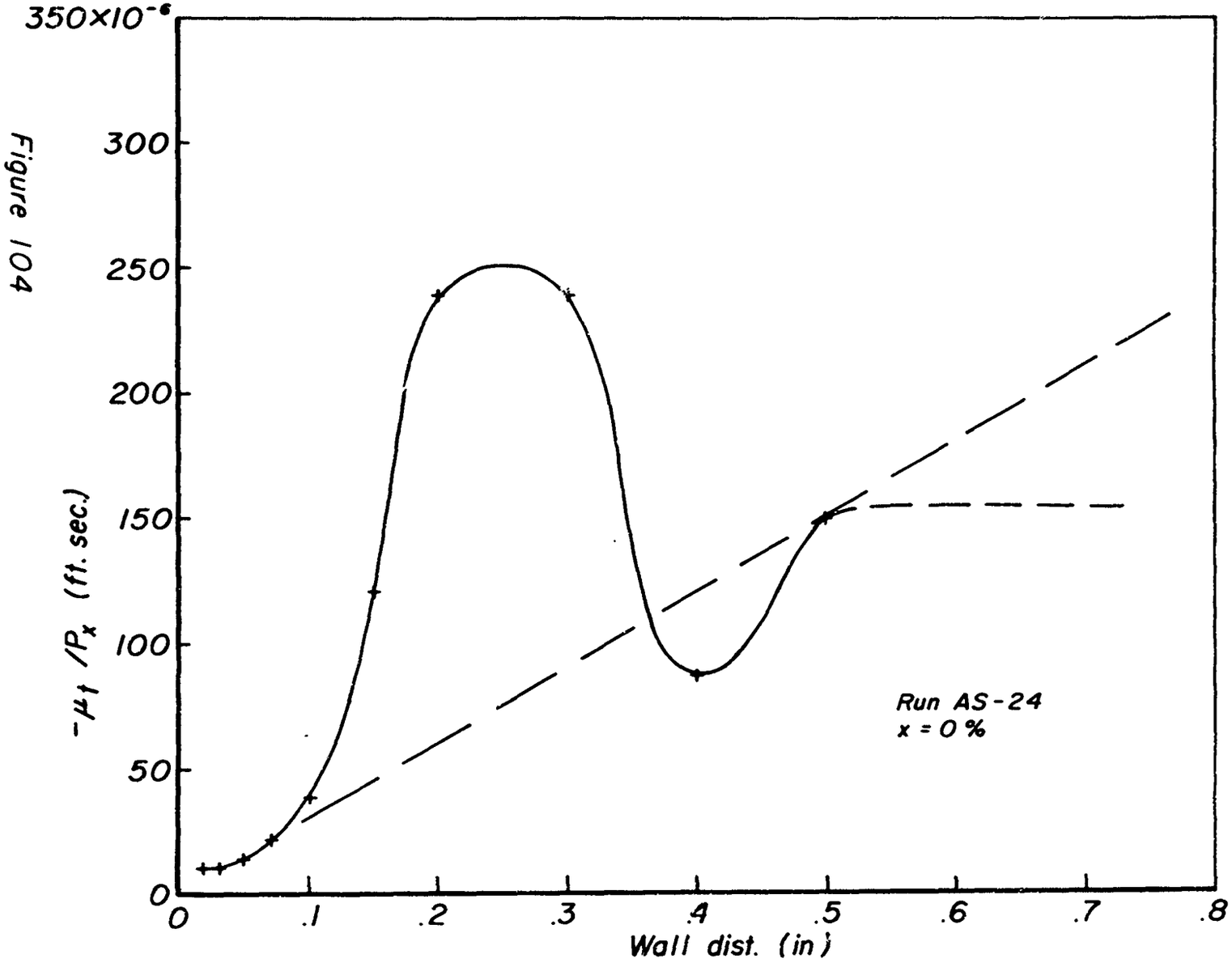
350×10⁻⁶
300
250
200
150
100
50
0
$-\mu_t / P_x$ (ft. sec.)
0
.1
.2
.3
.4
.5
.6
.7
.8
Wall dist. (in)
Run AS-24
x = 0 %

Figure 104

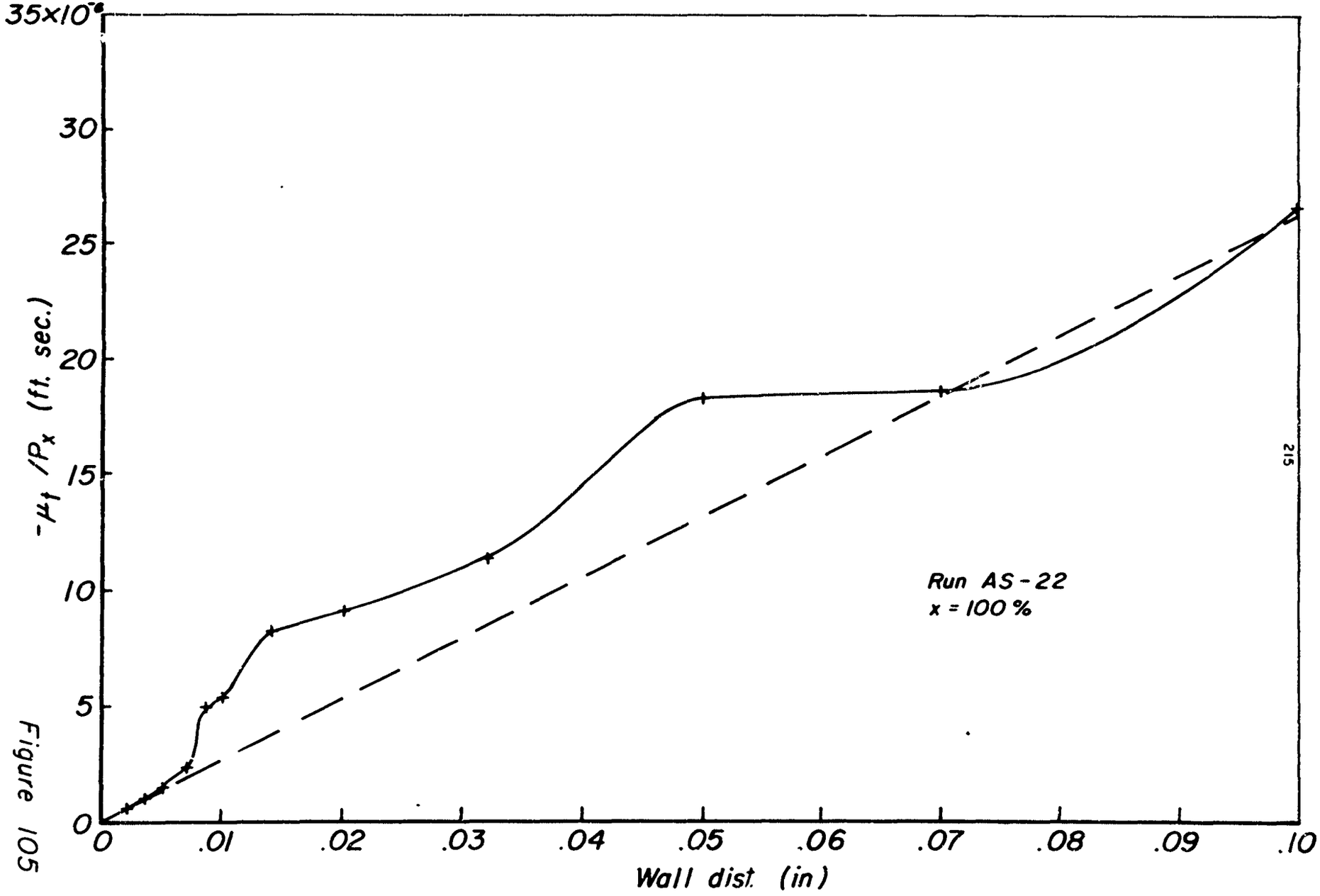
35x10⁻⁶
30
25
20
15
10
5
0
$-\mu_t / P_x$ (ft. sec.)
0
.01
.02
.03
.04
.05
.06
.07
.08
.09
.10
Wall dist. (in)
Run AS-22
x = 100 %

Figure 105

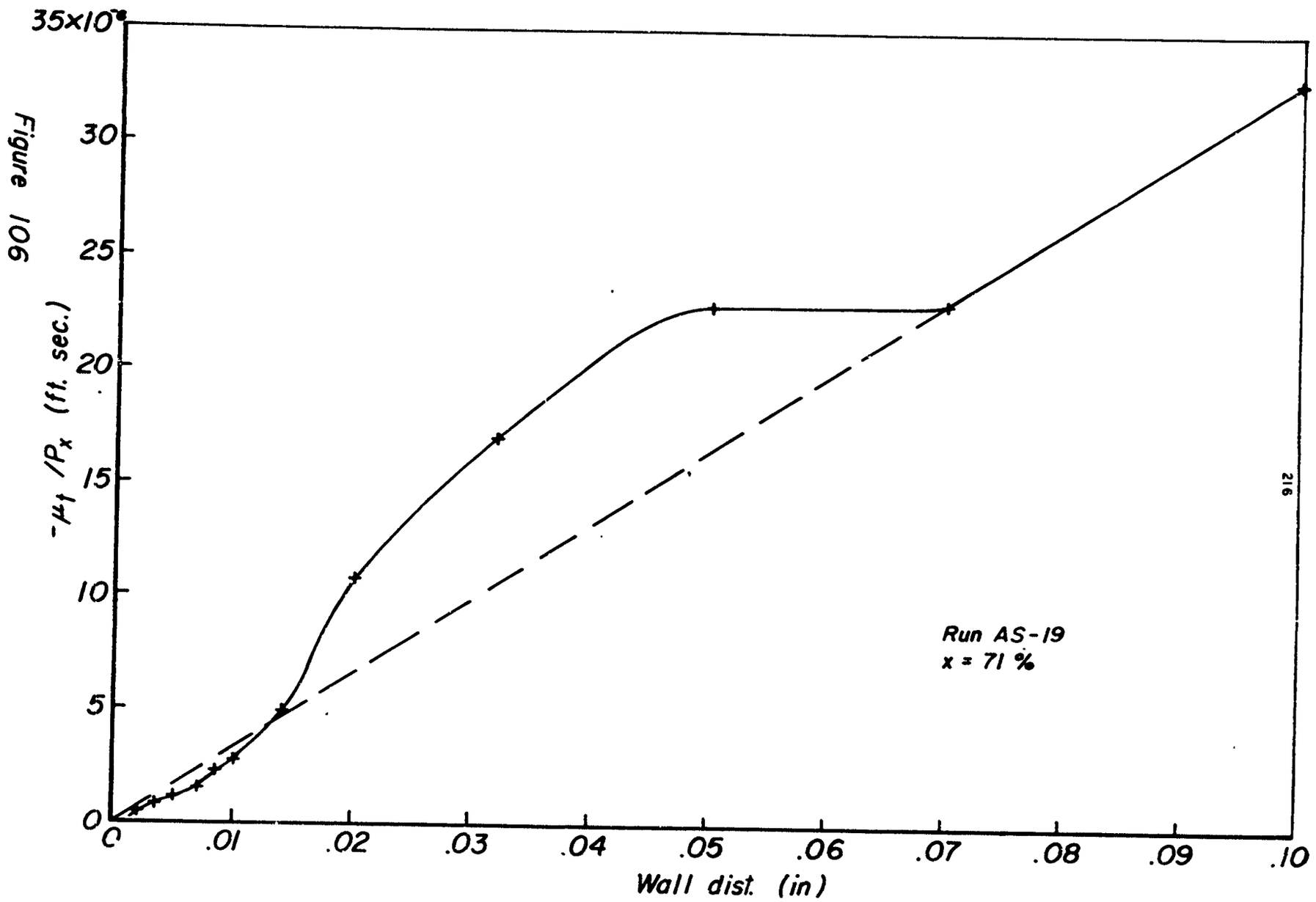

Figure 106

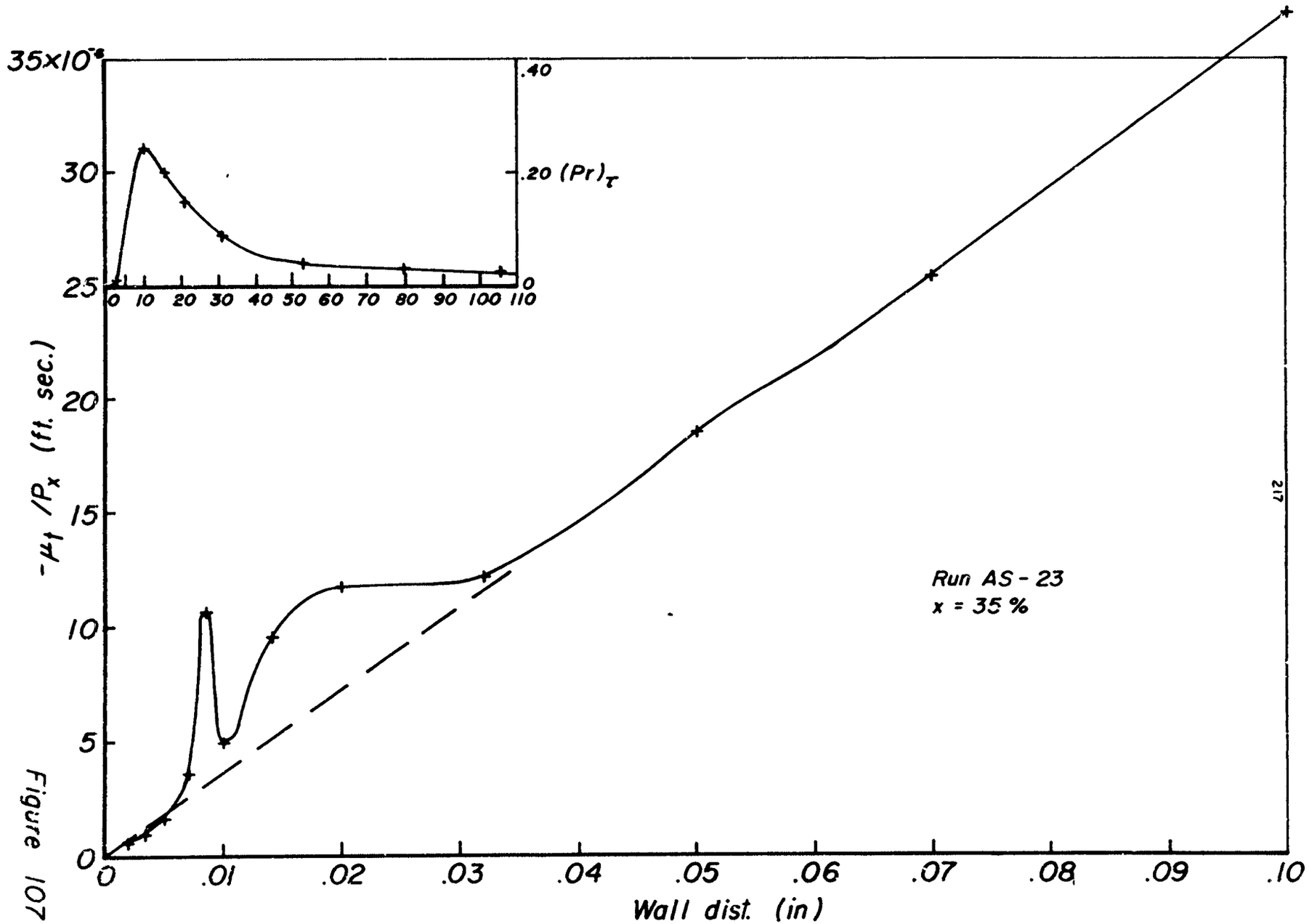
35x10⁻⁶
30
25
20
15
10
5
0
$-\mu_t / P_x$ (ft. sec.)
0 10 20 30 40 50 60 70 80 90 100 110
.40
.20 $(Pr)_T$
0
0 .01 .02 .03 .04 .05 .06 .07 .08 .09 .10
Wall dist. (in)
Run AS - 23
x = 35 %
217

Figure 107

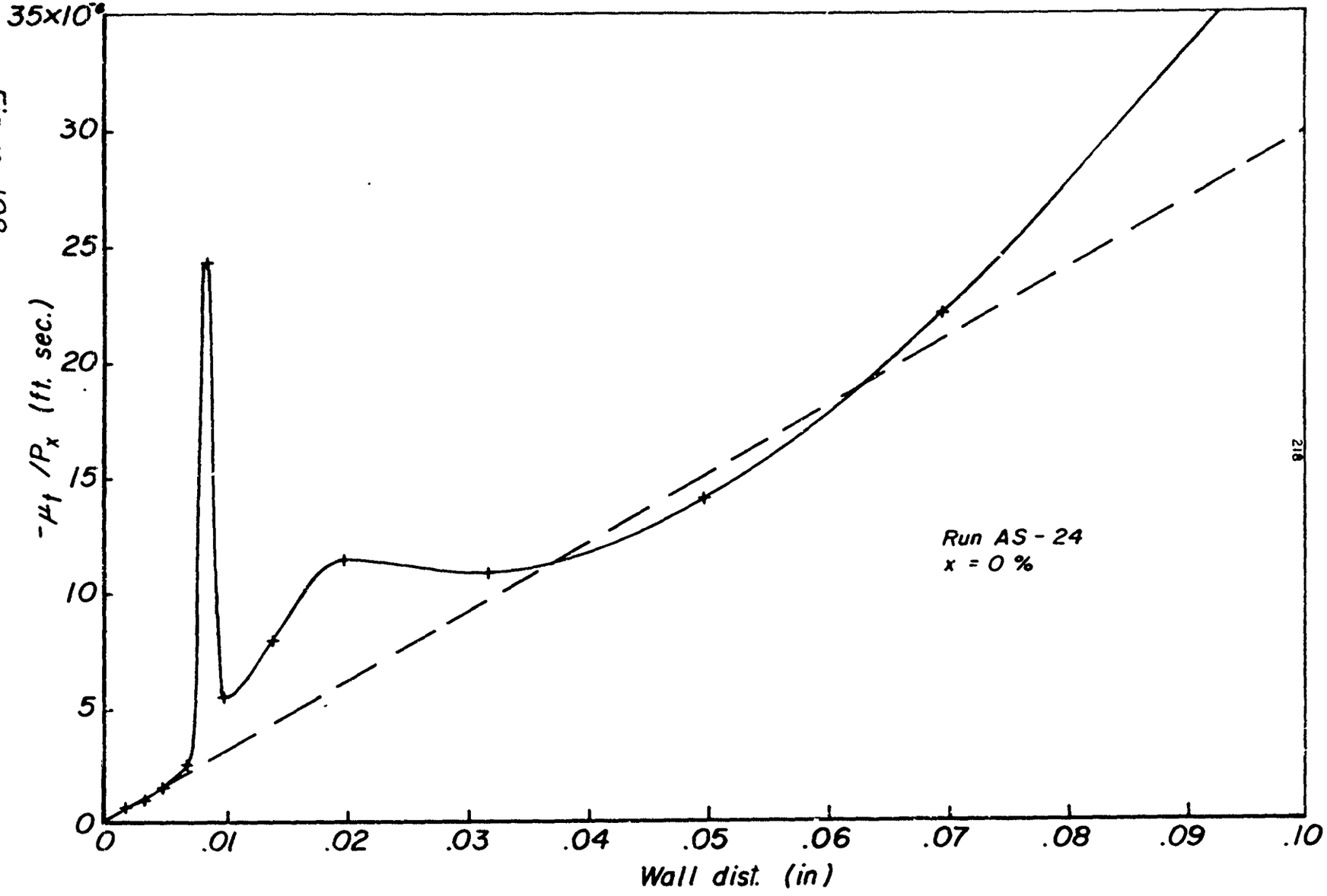
35x10⁻⁶
30
25
20
15
10
5
0
$-\mu_f / P_x$ (ft. sec.)
0
.01
.02
.03
.04
.05
.06
.07
.08
.09
.10
Wall dist. (in)
Run AS - 24
x = 0 %

Figure 108

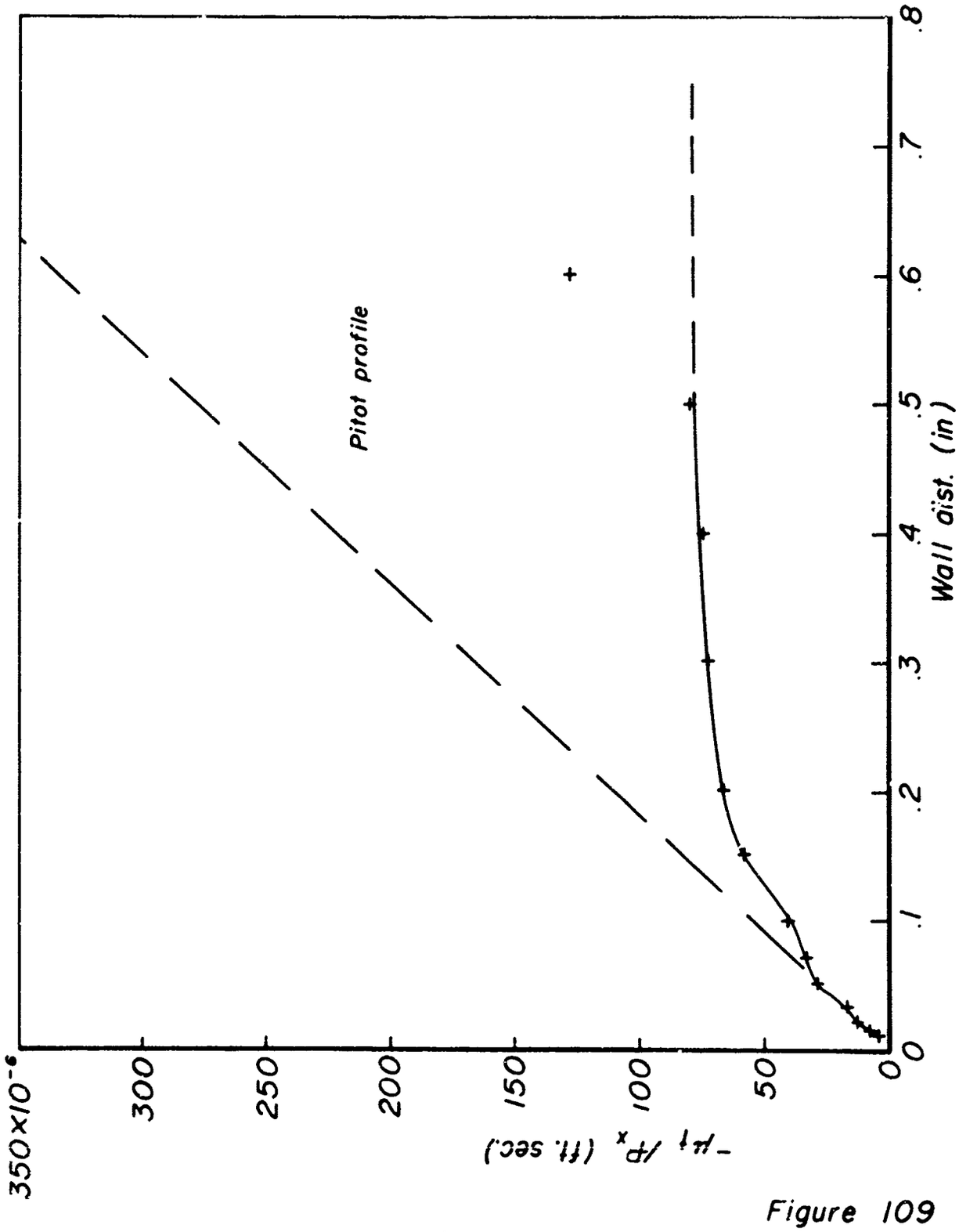

Figure 109

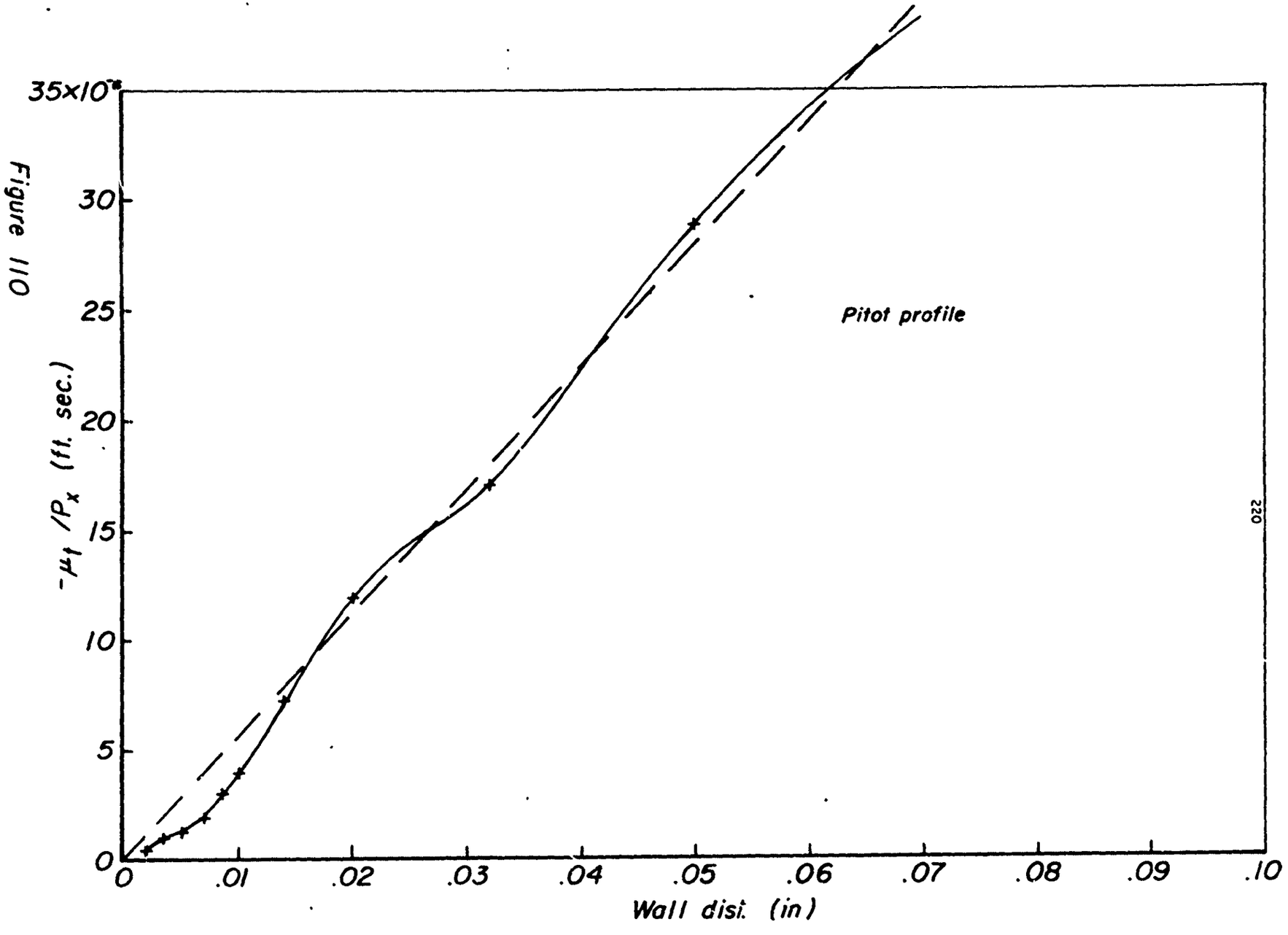
35x10⁻⁶
30
25
20
15
10
5
0
-μ1 /Px (ft. sec.)
Pitot profile
0
.01
.02
.03
.04
.05
.06
.07
.08
.09
.10
Wall dist. (in)

Figure 110

TABLE 24

FIGURE NO.	LOCATION	RUN NO.	x-POSITION	FIGURE NO. OF RELATED $\bar{v}'$ PROFILE
			%	
101, 105	$\frac{\lambda}{8}$ downstream of velocity antinode	AS-22	100	71, 75
102, 106	velocity node	AS-19	71	72, 76
103, 107	$\frac{\lambda}{8}$ downstream of velocity node	AS-23	35	73, 77
104, 108	velocity antinode	AS-24	0	74, 78
109, 110	STEADY-STATE			

Before discussing the $-\mu_t/P_x$ profiles further, some of the possible causes of error in the computation of $-\mu_t/P_x$ (these were mentioned earlier) should be discussed. These are listed below.

(1) The correction for the probe blockage effect mentioned earlier in this section was computed from steady flow data. In fact, we should allow for the probe blockage effect as follows. At each point in the ensemble-averaged cycle at a given y-position (see Section 4.11, Section 4.12, p.135), an (unknown) unsteady blockage correction should be applied to the computed instantaneous velocity; then, from these corrected instantaneous velocities, the values of $\bar{v}'$ should be calculated. The blockage correction technique actually used essentially assumes that the unsteady blockage correction is the same as the (measured) steady correction. There is some support for this assumption as follows. The magnitude of a typical unsteady velocity component is $\sim$ 50 ft/sec. At this velocity, the flow will traverse the 1/8 in. thickness of the hot-wire probe in

$$\frac{1}{8 \times 12 \times 50} = .00021 \text{ sec.}$$

A cycle time at the 9th harmonic frequency of 270 cps is:

$$\frac{1}{270} = .0037 \text{ sec.}$$

Hence, it appears that the blockage effect around the probe should be roughly established in about .06 of a cycle time, and thus the true blockage correction should approximate the quasi-steady blockage correction for the relevant instantaneous profile. The fact that these latter differ somewhat in shape from the steady profile will introduce some errors in using corrections computed from steady profile data for unsteady profiles, but at most instants in the cycle, the unsteady profiles are similar to the steady profile in a very coarse sort of way, and these errors may not be too large. This was the philosophy behind the application of the blockage correction computed from steady flow data to the $\bar{v}'$ profiles. Errors may thus be introduced into the $-\mu_t/P_x$ profiles as discussed above.

(2) We note that any acoustic streaming velocities (see Section 5.2) present will be interpreted in the 'eddy viscosity' analysis as erroneous variations in $-\mu_t/P_x$. However, from Figure 96 and Table 20 (Section 5.2) we note, that, theoretically, the x-components of the acoustic streaming velocities should be almost zero at $x = 0\%$ and 71%, and hence the eddy viscosity calculations at these locations should not be subject to this error. Again referring to Figure 96 and Table 20, we see that at $x = 35\%$ and 100%, the acoustic streaming velocities are theoretically of maximum value. However, following the discussion of Section 5.2, pp.190-199, it is shown that the features of the experimentally observed profile of $\bar{v}'(x = 100\%) - \bar{v}'(x = 35\%)$ (Figure 98) for $y < .15$ in. are not explainable in terms of acoustic streaming, and hence, very likely represent a true eddy viscosity effect. However, for $y > .15$ in., the shape of the profile $\bar{v}'(x = 100\%) - \bar{v}'(x = 35\%)$ agrees fairly well with that predicted by streaming theory, and hence any eddy viscosities computed in this region must be regarded as extremely uncertain. Hence, at x-positions of $x = 35\%$ and 100%, we feel that eddy viscosity data at, say $y < .10$ in. may be fairly free from streaming effects, but that for $.10 \text{ in.} < y < .73$ in. may be affected by streaming. This tentatively follows from the fact that slopes of the $\bar{v}'(x = 100\%) - \bar{v}'(x = 35\%)$ profile (Figure 98) possibly due to acoustic stream-

ing (dotted line, Figure 98) rapidly become small compared to those likely due to eddy viscosity effects for $y < .1$ in.

(3) Another possible cause for error is the use of

$$\bar{v}' = \frac{\int_0^T \rho v dt}{\int_0^T \rho dt}$$

profiles to compute $-\mu_t/P_x$ instead of

$$\bar{v} = \frac{1}{T}\int_0^T v dt$$

profiles.* However in Section 4.13, pp. 172, 173, evidence is given which indicates that the $\bar{v}'$ profiles are very similar in shape to the $\bar{v}$ profiles. Hence, calculation of $-\mu_t/P_x$ from the $\bar{v}'$ profiles should be as satisfactory as calculations from the $\bar{v}$ profiles.

(4) Another possible effect may result from the time-varying 'total' viscosity (μ_t). To explain this effect, we consider a periodic laminar pipe flow as sketched below. We consider μ to vary 'magically' with r and t and consider the flow field to be independent of x and incompressible.

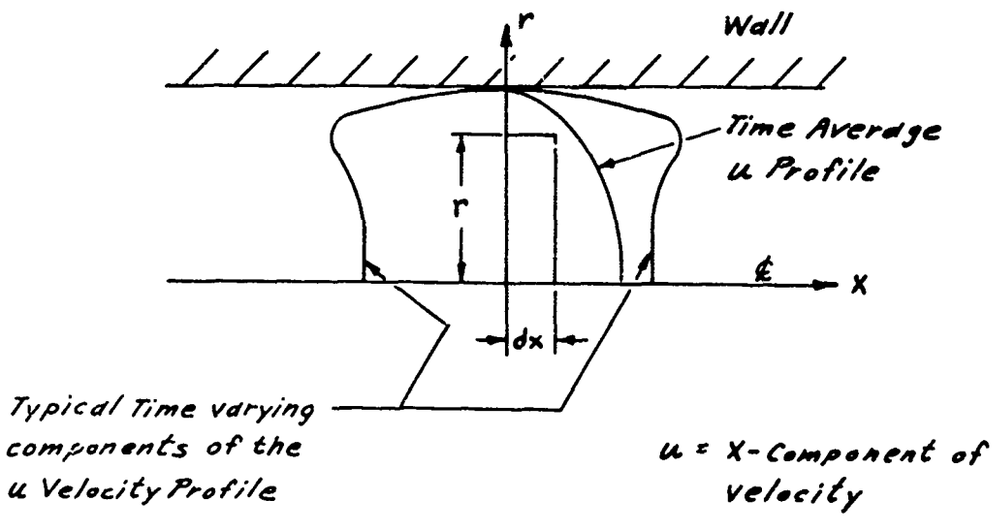

FIGURE 111

* For lack of time, $\bar{v}$ profiles were not calculated in most cases.

Then the time-average force balance on the fluid element is

$$- \pi r^2 \bar{P}_x dx + 2\pi r dx \overline{\mu u_r} = 0 \quad , \tag{87}$$

or

$$- \frac{r}{2} \bar{P}_x + \overline{\mu u_r} = 0 \quad . \tag{88}$$

We divide μ and u_r into time-average and time-varying components as given below:

$$\mu = \bar{\mu} + \mu' \tag{89}$$

$$u_r = \bar{u}_r + u_r' \tag{90}$$

Substituting Equations (89) and (90) into Equation (88) yields:

$$- \frac{r \bar{P}_x}{2} + \bar{\mu} \bar{u}_r + \overline{\mu' u_r'} = 0 \tag{91}$$

The equation for $-\bar{\mu}/\bar{P}_x$ corresponding to Equation (86) can be written as:

$$- \frac{\bar{\mu}}{\bar{P}_x} = - \frac{r}{2} \frac{1}{\bar{u}_r} \frac{1}{\left(1 + \dfrac{\overline{\mu' u_r'}}{\bar{\mu} \bar{u}_r} \right)} \tag{92}$$

If μ' does not vary with time ($\mu' = 0$), Equation (92) corresponds exactly to Equation (86) which was in fact used to compute $-\mu_t/P_x$. However, if μ varies with time and is correlated with u_r ($\overline{\mu' u_r'} \neq 0$), in general the profile of $-\bar{\mu}/\bar{P}_x$ will differ from that of $-r/(2\bar{u}_r)$. Thus, if the correlation $\overline{\mu' u_r'}/(\bar{\mu} \bar{u}_r)$ varies with r, the calculation of $-\mu_t/P_x$ from Equation (86) will not give a true profile of the average 'total' viscosity. Unfortunately, we have no method to estimate the seriousness of this error in the data presented in this report.

(5) In the balance of forces taken leading to Equation (85), we tacitly assumed that the momentum flux through the two faces of the disk was the same, and that there was zero momentum flux through the edge of the disk. We now discuss the errors which may be caused by these assumptions. We consider a steady laminar pipe flow with a viscosity (μ) 'magically' varying in x and y. We denote the x-component of velocity by u. Equation (86) could be written, replacing μ_t by μ and $\bar{v}'_c$ by u as:

$$\frac{\mu}{\rho} ru_r - \frac{r^2 P_x}{2\rho} = 0 \qquad (93)$$

The corresponding equation allowing for the neglected momentum fluxes is:

$$\frac{\mu}{\rho} ru_r - \frac{r^2 P_x}{2\rho} = \left[\int_0^r ru^2 dr\right]_x - u\left[\int_0^r rudr\right]_x \qquad (94)$$

However, because of the fact that the scale distance for x-variations (= distance between a velocity node and the next velocity antinode $= \frac{\lambda}{4} \approx 12$ in.) is much greater than the scale distance for y-variations (= boundary layer thickness = half-diameter of pipe = .73 in.), the terms on the R.H.S. of Equation (94) should be small compared to the terms on the L.H.S. and thus Equations (93) or (86) should be satisfactory to compute $-\mu_t/P_x$ in this respect.

We now begin discussion of the $-\mu_t/P_x$ profiles as presented in Figures 101 - 110 (see Table 24). First to be discussed are the steady-state $-\mu_t/P_x$ profiles obtained from the pitot traverse (Figures 109-110). For the moment we will ignore the dotted line in Figure 110. As mentioned earlier in this section, the pitot probe showed blockage effects for $y < .02$ in., and for this region the velocity profile obtained from the pitot probe was extended using the 'law of the wall'. Hence, the $-\mu_t/P_x$ values shown in Figures 109-110 for $y < .02$ in. are merely those assumed in the 'law of the wall'. However, for $y \geq .02$ in., the $-\mu_t/P_x$ values are legitimately obtained from experimental data. Figures 109-110 show the usual roughly linear increase in $-\mu_t/P_x$ out to $\frac{2y}{D} \approx \frac{2 \times .07}{1.46} \approx .10$,

and a roughly constant value of $-\mu_t/P_x$ for $\frac{2 \times .2}{1.46} = .27 \leq \frac{2y}{D} \leq 1$. The anomalous point at $y = .6$ in Figure 109 was determined from a very small slope in the pitot velocity profile curve and hence a slight error in the pitot tube measurement at this point would account for the anomalous value of $-\mu_t/P_x$.

For comparison purposes, we present in Figure 112 the $-\frac{\mu_t}{\rho\nu}$ variations for steady flow as computed using the 'law of the wall' in the form given in Section 5.1, Equations (68). Here, we have assumed constant shear stress from $0 \leq y \leq .10$ in.; this is in error, of course, by $\sim 14\%$ at $y = .10$ in.; however this error should only produce a gentle bend in the curve of Figure 111, and we shall use the straight line for rough comparisons with experiment. The degree of bend which might occur is shown in the $-\mu_t/P_x$ data obtained from the steady flow pitot profile (Figures 109-110). The kinks in these curves are likely due to experimental errors, and errors in reading the derivative off the velocity profile curves. In Figure 112, the solid curve gives the $-\mu_t/P_x$ values computed directly from Equation (68). (The discontinuity is between Equations (68b) and (68c) at $y^+ = 30$, and is faired in with the dashed curve.) The dotted line merely extends that part of the solid curve where $-\mu_t/P_x$ is proportional to y. We note particularly that in the buffer region ($5 < y^+ < 30$, $.0016$ in. $< y <$ $.0095$ in.) the $-\mu_t/P_x$ values fall below those lying on the extension of the $-\mu_t/P_x \propto y$ curve through zero. This sort of behavior is not as apparent in Figure 110 for the steady-state data due to experimental scatter, but when the line of $-\mu_t/P_x \propto y$ is drawn through the mean of the points in the region $.02$ in. $< y <$ $.07$ in. in Figure 110 (dashed line), we see that the $-\mu_t/P_x$ values lie below this line for $y \leq .01$ in. Of course, this must be so, since we extended the steady-state pitot profile for $y < .02$ in. using the 'law of the wall'.

The $-\mu_t/P_x$ profiles obtained under oscillating conditions are now discussed. Because of the previously enumerated possible causes of error in the $-\mu_t/P_x$ profiles, the following discussion is quite tentative in nature; however, the picture which develops is consistent with heat transfer data which will be discussed later, and is thus more likely to be correct than if based on the $-\mu_t/P_x$ data alone. During the first part of this

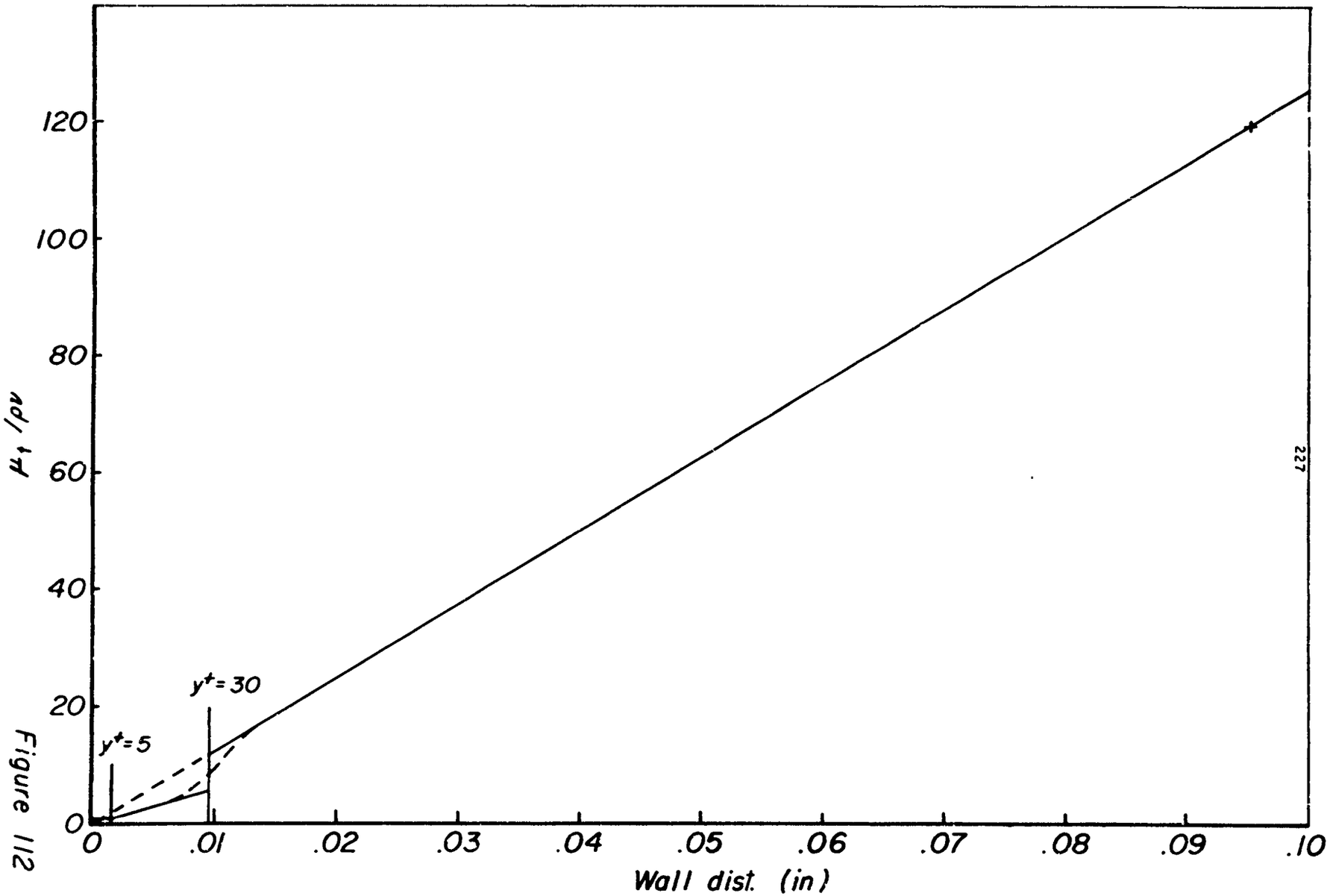
120
100
80
60
40
20
0
$\mu_t/\rho\nu$
$y^+=30$
$y^+=5$
0
.01
.02
.03
.04
.05
.06
.07
.08
.09
.10
Wall dist. (in)
227

Figure 112

discussion, we confine ourselves mainly to the data for $y \leq .1$ in., where the $-\mu_t/P_x$ values should be more accurate than for $y > 1$ in., since they were obtained from greater slopes of the $\bar{v}'$ profiles, and also because the latter contained a higher density of data points for $y \leq .1$ in. We first refer to the data taken at $x = 35\%$ (Figures 103 and 107). For the moment we ignore the small graph superimposed on Figure 107. This data was taken $\frac{\lambda}{8}$ downstream of a velocity node, and hence the flow has just left the region of minimum disturbance by the oscillation. The interpretation of Figure 107 by the author is that during passage of the flow through the nodal region, the $-\mu_t/P_x$ values almost settled down into typical steady flow values. The indications of this are the portion of the $-\mu_t/P_x$ curve which is closely proportional to y for $.03$ in. $< y <$ $.10$ in., and the fact that the $-\mu_t/P_x$ values drop below the $-\mu_t/P_x \propto y$ curve extended to zero for $.002$ in. $< y$ $.005$ in., as they should in steady flow according to the 'law of the wall' (Figure 112). However, for $.005$ in. $< y <$ $.03$ in., the $-\mu_t/P_x$ values appear to be anomalously high, and the author attributes this to the generation of abnormally high turbulence levels in this region due to the high A.C. shear values at these y distances. We point out again that for Figures 103 and 107, the flow is leaving the region of minimum disturbance (minimum local $\hat{U}$) and is moving into regions with increasing $\hat{U}$. We note here that we have no guarantee that the μ_t values shown in Figure 107, $.03$ in. $< y <$ $.1$ in., are 'normal' (as in steady flow) since we have no P_x measurements. The $-\mu_t/P_x$ values in this region merely appear to be 'normal' because they are proportional to y . Against the background of the above-mentioned 'normal-appearing' $-\mu_t/P_x$ values (in Figure 107), the values of $-\mu_t/P_x$ for $.005$ in. $\leq y \leq .03$ appear to be abnormally high. Apparently, the region of maximum generation of 'abnormal' turbulence is that of the spike at $y \approx .0085$ in. We note that, while the exact details of the 'double-peaked' curve of Figure 107, especially the deep minimum of $-\mu_t/P_x$ at $y \approx .01$ in., should not be taken too seriously, due to the previously enumerated possible causes of error, the spike at $y \approx .0085$ in. appears to be fairly well defined and corresponds to the negative slope region in Figure 77. At this point, we point out that the negative slope regions of Figures 77 and 78 (and other figures) become positive slope regions when the factor F_v (p. 209) correcting for the block-

age effect of the hot-wire probe is applied to the hot-wire $\bar{v}'$ profiles. Hence, the negative slope regions of Figures 77 and 78 do not represent a true feature of the flow, but rather a probe blockage effect. Thus, all $-\mu_t/P_x$ values calculated in these negative slope regions will be positive, giving some support for the approximate validity of the hot-wire probe blockage correction procedure discussed on p. 209 and 221,222. Returning to the discussion of the $-\mu_t/P_x$ profile of Figure 107, the author feels, as mentioned above, that the deep minimum at $y \approx .01$ in. may be a product of experimental error and likely, the two regions of abnormally high $-\mu_t/P_x$ centered on $y \approx .0085$ in. and $y \approx .02$ in. should be more smoothly joined. We now plot on the same scale, the non-dimensionalized turbulence energy production as measured in steady pipe flow by Laufer (Reference 30). This data is shown in the upper left-hand part of Figure 107, and was taken at $Re = 40{,}500$. We have selected the scales so that the values of $y^+ = \frac{y}{\nu}\sqrt{\frac{\tau_w}{\rho}}$ correspond in our data (for our data, y^+ is computed for steady flow at the relevant Reynolds number) and the data of Laufer. To explain the form in which Laufer's data is presented, we define:

a = velocity in x-direction

b = velocity in r-direction

$\bar{a}$, $\bar{b}$ = time-average components

a', b' = time-varying components (turbulence)

$\rho a_\tau^2 = \tau_w$ = wall shear stress

Then, Laufer gives the turbulent-energy production rate, $(Pr)_\tau$ as:

$$(Pr)_\tau = \nu \frac{\overline{a'b'}}{a_\tau^4} \frac{d\bar{a}}{dr} \qquad (95)$$

Because of the non-dimensionalization, this form of the turbulent-energy production should be equally applicable for our reference steady flow. From Figure 107 it appears that the region of maximum production of 'abnormal' turbulence under unsteady flow conditions is somewhat further from the wall

($y^+ \sim 26$) than the peak of turbulence production in the reference steady flow (at $y^+ \sim 10$). Due to the many possible causes of experimental error discussed earlier, such conclusions are not certain. Whether the region of abnormally high $-\mu_t/P_x$ from .01 in. $<$ y $<$ .03 in. represents also regions of high turbulence production under oscillating conditions, or whether these high values of $-\mu_t/P_x$ represent mainly diffusion of turbulence energy from a restricted region of abnormal turbulence production .005 in. $<$ y $<$ .01 in. cannot be determined from the present meager data. However, the possibility of a relatively narrow zone of 'abnormal' turbulence production under oscillating conditions is supported by the very rapid fall off of the oscillating shear component with y. From Equation (11), Section 1, we see that for laminar flow the unsteady shear falls off as e^{-y/δ_A} where δ_A = .00272 in. (from Section 5.1, p.180) for our conditions of frequency, density and viscosity. In the actual case with turbulent flow, the shear may not fall as rapidly as e^{-y/δ_A}, but still, the fall off is very rapid as compared to the roughly $\frac{1}{y}$ fall off of shear in the reference steady flow (this follows since $-\mu_t/P_x$ is roughly $\propto y$ for much of the flow region .001 in. $<$ y .1 in. in the steady flow case). Hence, the possibility that the zone of 'abnormal' turbulence production under oscillating conditions is mainly the peak from .005 in. $<$ y .010 in. in Figure 107, and is thus much narrower than the broad peak of turbulence production in the reference steady flow cannot be disregarded.

We now give some discussion of the possible effects of the 'abnormal' turbulence on heat transfer. We give an estimate of the thermal resistances of various regions of the flow under steady flow conditions. Since the Prandtl number of the airflow is near unity, the velocity profile should be very similar in shape to the temperature profiles if the duct was heated (for fully developed flow). Hence, we could represent the shape of the hypothetical temperature profile across the duct by the shape of the pitot profile of Figure 93, extended using the 'law of the wall' as discussed on p. 209 . Pitot profile data taken under slightly different conditions of mass flow and mean velocity are shown in Figure 113. Using the analogy of the shapes of the velocity and hypothetical temperature profiles, fractional thermal resistances of various regions were computed, and are shown on

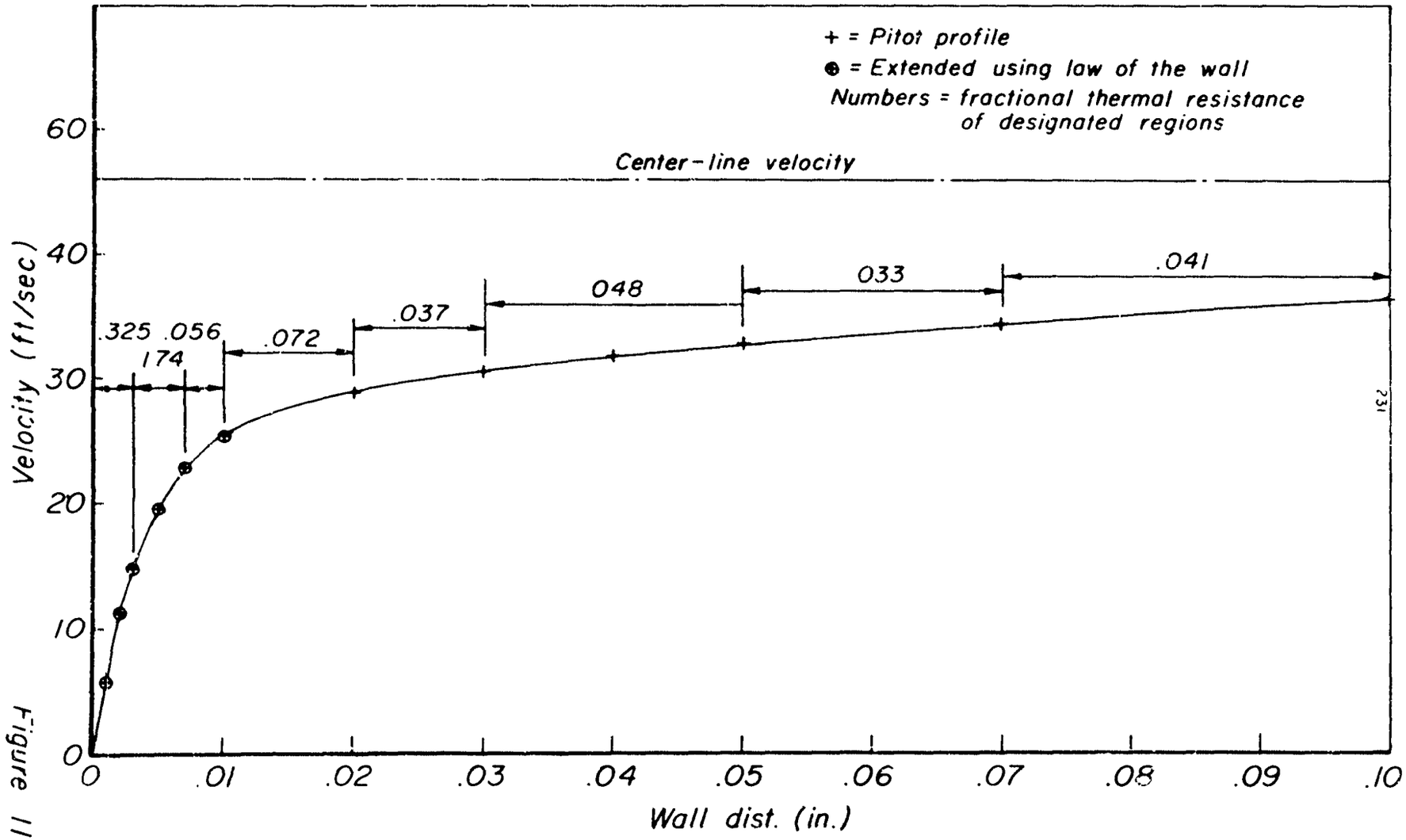

Figure 113

Figure 113. We see that the region of 'abnormally' high $-\mu_t/P_x$ in Figure 107 ($.005$ in. $< y <$ $.03$ in.) includes a fairly substantial fraction of the thermal resistance in the steady flow case ($\sim .24$, see Figure 113), which is in keeping with the proposed importance of increased turbulence exchange properties with respect to heat transfer in the duct. We also note the great importance in the steady flow case of the region $y <$ $.005$ in., which contains .42 of the thermal resistance. Before discussing the $-\mu_t/P_x$ profiles at other x-positions, we introduce the idea of the 'steady flow reference line'. For a given plot of $-\mu_t/P_x$ values under oscillating conditions, this line would be determined as follows. μ_t values from steady flow data, and the P_x value taken from the relevant unsteady flow data would be combined to yield a set of $-\mu_t/P_x$ which could be plotted on the graph along with the oscillating flow values of $-\mu_t/P_x$. Since we have no P_x measurements, this cannot in practice be done. If the steady flow μ_t data could be closely represented using the 'law of the wall', the resulting plot would look like Figure 112 except for a slight bend in the main portion of the curve due to the varying shear stress for $0 < y <$ $.1$ in. as discussed on p.226. The line corresponding to the straight line through the origin in Figure 112 then represents the μ_t values in steady flow, (properly scaled as compared to the unsteady flow data), except in the buffer and laminar sub-layer regions for $y <$ $.01$ in., and for the slight bend mentioned above. We call this line the 'steady flow reference line'. The assumption made in the previous discussion of the data of Figure 107, that the $-\mu_t/P_x$ values for $.03$ in. $< y <$ $.10$ in. are 'normal' is equivalent to assuming that the nearly straight line defined by the data points in the region $.03$ in. $\leq y \leq$ $.10$ in. is identical to the 'steady flow reference line'. If the $-\mu_t$ values in this region, in spite of appearing 'normal' (lying on a straight line through the origin), were in fact greater than the corresponding steady flow values by, say 30% (which value would have to be uniform over the region $.03$ in. $< y <$ $.10$ in., to explain the fact that the $-\mu_t/P_x$ values there do lie on a straight line through the origin), the 'steady flow reference line' would lie $\sim$30% below the line defined by the points with $.03$ in. $\leq y \leq$ $.10$ in. If this were true, in our previous discussion of the data of Figure 107, we should have pointed out the abnormally high $-\mu_t/P_x$ values for $.03$ in. $< y <$ $.1$ in.

However, even if the data of Figure 107, .03 in. $\leq$ y $\leq$ .1 in. does not correspond exactly to the 'steady flow reference line', much of the arguments presented on generation and diffusion of the turbulence still apply, because whatever the (unknown) location of the 'reference line' the $-\mu_t/P_x$ values in the region .005 in. $<$ y $<$ .03 in. divided by the 'reference line' values are much higher than similar values computed for .03 in. $<$ y $<$ .1 in. In discussing data at other x-positions, we shall make tentative assignments of the position of the 'steady flow reference line' using regions of 'normal-appearing' (α y) $-\mu_t/P_x$ values as was done for Figure 107. As discussed above however, much of the discussion of regions of generation and diffusion of turbulence would still be applicable even if the tentative assignment of the position of the 'steady flow reference line' is somewhat incorrect.

We now discuss the $-\mu_t/P_x$ profiles Figures 104 and 108 computed at an x-position of 0%. At this x-position, we are $\lambda/8$ downstream from the point at which the data of Figures 103 and 107 was taken and are located at a velocity antinode (the position of maximum disturbance of the velocity flow field by the oscillations). At this point, we discuss mainly the data of Figure 108 (y $<$ .1 in.). We first note that the $-\mu_t/P_x$ profile in Figure 108 gives much less evidence of any regions with 'normally varying' (similar to the variations occuring in the steady-state, see Figures 110 and 112) $-\mu_t/P_x$ than Figure 107. This is in part due to the shoulder of the peak in $-\mu_t/P_x$ at y $\approx$ .25 in. (we note that these phenomena for y $>$ .1 in. will be discussed later). The $-\mu_t/P_x$ values in Figure 108 at y = .032, .05 and .07 in., seem roughly to fall on a straight line through the origin and we very tentatively take this line to be the 'steady flow reference line'. Using this 'reference line', we see that the peak of $-\mu_t/P_x$ at y $\approx$ .0085 in. in Figure 108 is much higher than the same peak in Figure 107 which is consistent with the former being in a region of much greater disturbance of the flow by the oscillations. Although it is not immediately apparent, the $-\mu_t/P_x$ values divided by the reference line values are larger for most of the region .01 in. $<$ y $<$ .03 in. for the data of Figure 108 compared to the data of Figure 107. This, also, is consistent with the greater opportunity for generation of turbulence in the former case. A most important feature of the data of Figure 108, due to the very high thermal resistance of that region, (see Figure 113) is the apparently greater values,

in the region $y < .005$ in., of $-\mu_t/P_x$ divided by the tentatively assigned 'reference line' values in Figure 108 as compared to Figure 107. This last statement, unlike the earlier statement about the high peak of $-\mu_t/P_x$ at $y \approx .0085$ in., is quite sensitive to the location of the true 'steady flow reference line'. If the tentatively assigned 'reference lines' for Figures 107 and 108 are substantially in error, the above statement about the region $y < .005$ in. may be completely incorrect. However, as there is some support for the correctness of the locations of the tentatively assigned 'reference line' in Figures 107 and 108 from heat transfer data, (which will be described later), we make the following statement on the assumption that these lines are correctly located. If this is so, it appears that the higher values $-\mu_t/P_x$ compared to the 'reference line' values for $y < .005$ in. in Figure 108 (as compared to Figure 107) are due to either increased generation of turbulence in this region or to diffusion of turbulence from the higher main generation region centered at $y \approx .0085$ in. Both hypotheses are consistent with the fact that the data of Figure 108 was taken in the region of maximum local $\hat{U}$.

We now discuss the $-\mu_t/P_x$ profiles of Figures 101 and 105, taken at an x-position of 100%. While this data was in fact taken about $3\lambda/8$ upstream of the data of Figures 104 and 108, because the node-antinode pattern repeats itself every $\lambda/2$, the data corresponds to that which would be obtained $\lambda/8$ downstream of $x = 0\%$ (Figures 104 and 108). Hence, at this point, the flow is leaving the region of maximum disturbance by the oscillation. (The location is $\lambda/8$ downstream of a velocity antinode.) Referring to Figures 101 and 105, we see that, again, there is little resemblance of the $-\mu_t/P_x$ profile to the 'normal' (steady flow) profile. Based somewhat on the y positions where we previously (Figures 107 and 108) used unsteady $-\mu_t/P_x$ data to tentatively locate 'reference lines', we very tentatively use the data at $y = .07$ and $.10$ in. to define a 'reference line' (dashed) in Figure 105. Using this reference line, we now discuss some aspects of Figure 105. The peak of $-\mu_t/P_x$ at $y \approx .0085$ in. in Figure 108 has shrunk to a small bump in Figure 105. If this peak represents the main region of generation of 'abnormal' turbulence, as postulated earlier, this behavior is consistent with the fact that Figure 105 refers to conditions of weaker flow disturbance by the oscillation than Figure 108. Also, it appears that some

of the 'abnormal' turbulence (indicated by $-\mu_t/P_x$ values above the 'steady flow reference curve') located at $y < .03$ in. in Figure 108, has diffused outwards as far as $y = .07$ in. by the time the flow reaches $x = 100\%$ (Figure 105)). Finally, it is noted that $-\mu_t/P_x$ values divided by the reference lines values are much the same in Figure 105 as in Figure 108 for $y < .005$ in. If the 'reference lines' in Figures 108 and 105 are in error, the first two observations(referring to the postulated main region of 'abnormal' turbulence generation, and the diffusion outwards of turbulence between the locations of Figures 108 and 105) are still quite significant. The last observation, referring to the $-\mu_t/P_x$ values for $y < .005$ in., may, of course, be completely erroneous if the 'reference lines' are substantially in error.

We now consider the $-\mu_t/P_x$ profiles taken at $x = 71\%$ (Figures 102 and 106). This data was taken $\lambda/8$ downstream of the location of the data of Figures 101 and 105, and at the region of minimum disturbance of the flow by the oscillation (velocity node). Examining the data of Figures 101 and 105, again we see somewhat more evidence of regions of 'normal' (as in steady flow) variation of $-\mu_t/P_x$ than in Figures 104 and 108 and Figures 101 and 105. This is as follows: the $-\mu_t/P_x$ values at $y = .07$ and $.10$ in. lie closely on a straight line through the origin, and the point at $y = .15$ in. lies much closer to this line extended in Figure 102 ($x = 71\%$) than the corresponding points in Figures 104 and 101 do to the tentatively assigned 'reference lines' in those cases. In the latter cases the points at $y = .15$ in. lie on the steeply rising shoulder of the $-\mu_t/P_x$ peak located centered at $y \approx .25$ in. Hence, we take the dashed line in Figure 106 as the tentatively assigned 'reference line'. Using this reference line, we briefly discuss some features of the data of Figure 106. Comparing Figures 105 and 106, we see that the $-\mu_t/P_x$ values divided by the reference line values are much lower in Figure 106 than in Figure 105 for $y < .02$ in. This is consistent with the interpretation that on entering the zone of minimum disturbance of the flow by the oscillation the smaller scale ($y < .02$ in.) 'abnormal' turbulence caused by high A.C. shear in the antinodal regions rapidly decays towards the steady flow values. The fact that the $-\mu_t$ values for $y < .01$ in. are approaching the steady-state values in Figure 106 is suggested by the observation that the $-\mu_t/P_x$

values in this region are considerably below the 'reference line' and in this respect Figure 106 shows a resemblance to the steady flow $-\mu_t/P_x$ profiles of Figures 110 and 112. Again comparing Figures 105 and 106, it appears that the 'abnormal' $-\mu_t/P_x$ values divided by the 'reference line' values are quite similar for the region .02 in. $<$ y $<$ .07 in. The following tentative interpretation is advanced for this fact. The 'abnormal' turbulence in range .02 in. $<$ y $<$ .07 in. is of larger scale than that for y $<$ .02 in. Hence, it is postulated that, when the flow has arrived at x = 71% in the weakly disturbed region, sufficient time has elapsed for the small scale 'abnormal' turbulence to decay considerably (for y $<$ .02 in.). The larger scale 'abnormal' turbulence for .02 in. $<$ y $<$ .07 in. has had insufficient time to decay.

We now make a few remarks comparing the $-\mu_t/P_x$ profiles at x = 100% (Figures 101 and 105) and x = 71% (Figures 102 and 106) with those at x = 35% (Figures 103 and 107). The latter profiles have been described previously earlier in this section and were taken $\lambda/8$ downstream of those at x = 71%. The data at x = 71% is at the region of minimum disturbance of the flow by the oscillation, while that at x = 35% is further downstream in the region of increasing disturbance. We present now a very tentative history of the development of the 'abnormal' turbulence from x = 100% (Figure 105) to x = 71% (Figure 106) to x = 35% (Figure 107). Referring to Figure 105, we see that on entering the region of minimum disturbance the flow apparently has a wide spread band of 'abnormal' turbulence, 0 $<$ y $<$ .07 in. By the time the flow reaches the center of the region of minimum disturbance (Figure 106) the smaller scale 'abnormal' turbulence for y $<$ .02 in. has decayed considerably towards the steady-state values. At this point, however, the larger-scale 'abnormal' turbulence for .02 in. $<$ y $<$ .07 in. present in Figure 105 has decayed very little. Finally, when the flow passes the end of the minimum-disturbance region (Figure 107), sufficient time has passed for even the larger-scale 'abnormal' turbulence for .03 in. $<$ y $<$ .07 in. to decay towards the steady-state values. At this last x-position, we are, of course entering the region of greater flow disturbance and we see also, the generation of new 'abnormal' turbulence in the region .005 in. $<$ y $<$ .03 in. At this point, we have returned to the location (x = 35%) at which we began to discuss the $-\mu_t/P_x$ profiles (see p. 228).

We now make some very tentative estimates of P_x for the case of oscillating flow. If the locations of the tentatively assigned 'steady flow reference lines' in Figures 105-108 were in fact correct, the values of P_x for these cases as compared to that for the steady flow case (Figure 110) could be determined by dividing the slope of these 'reference lines' into the slope of the dashed line in Figure 110 which approximates the $-\mu_t/P_x$ data there for .02 in. $<$ y $<$ .07 in. The values of $P_x/P_{x,\text{steady flow}}$ so obtained are plotted versus x-position in Figure 114. The positions of velocity nodes and antinodes are shown. Since the flow pattern repeats itself every $\lambda/2$ along the duct, the 4 experimentally obtained values of $P_x/P_{x,\text{steady flow}}$ were reproduced at this interval in Figure 114 to allow a better picture of the variation of $P_x/P_{x,\text{steady flow}}$ versus x-position to be obtained. We compare this curve with the heat transfer data of Figure 42, to see if any evidence of analogy between heat and momentum transfer is apparent. By examining Figures 71-78 which show the $\bar{v}'$ data from which the $-\mu_t/P_x$ data of Figures 101-108 were calculated, and thence the $P_x/P_{x,\text{steady flow}}$ data of Figure 114, we see that the mean values of the flow parameters for the data of Figure 114 are

$$Re_a = 100{,}400$$

$$M_a = .0322$$

$$S_a = 5.80$$

$$\tilde{U}_A/\bar{U} = 2.16$$

From Figure 42, the values of the same parameters for the heat transfer data are

$$Re_a = 99{,}100$$

$$M_a = .0304$$

$$S_a = 6.41$$

$$\tilde{U}_A/\bar{U} = 2.31$$

The author feels that the slight differences in these parameters are quite

Figure 114

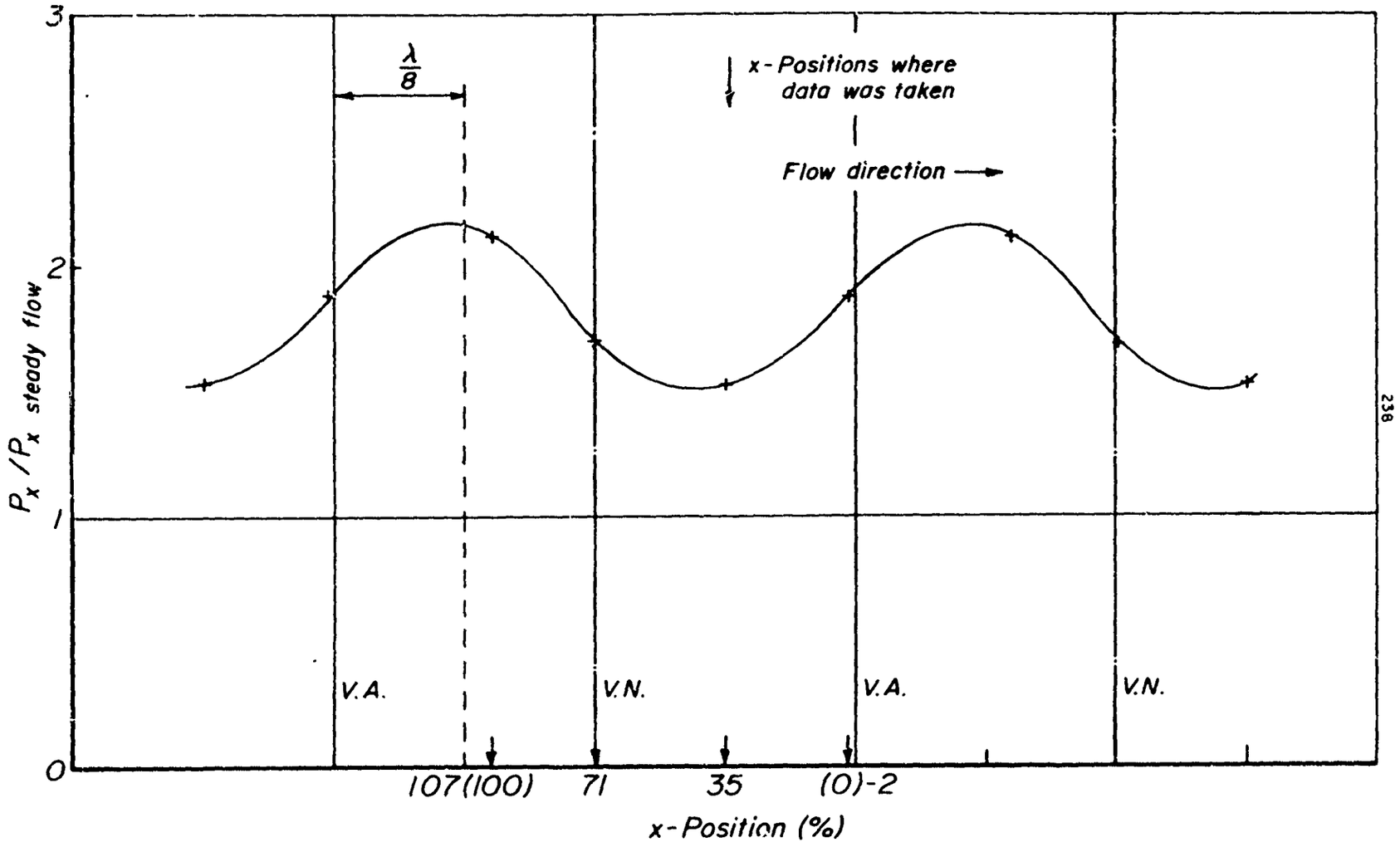
3
2
1
0
P_x / P_x steady flow
$\frac{\lambda}{8}$
x - Positions where data was taken
Flow direction
V.A.
V.N.
V.A.
V.N.
107(100)
71
35
(0)-2
x-Position (%)

unimportant for the comparison being made. Hence we regard the $P_x/P_{x,\text{steady flow}}$ data of Figure 114 and the heat transfer data of Figure 42 as taken under essentially the same flow conditions. We note that the resemblance between the Nu_n values taken from Figure 42 as compared to the steady flow values and the $P_x/P_{x,\text{steady flow}}$ values of Figure 114 is quite crude. From Figure 114, we see that the average fractional increase in P_x (under oscillating conditions, as compared to steady flow conditions) is about .85, while from Figure 42 the average fractional increase of Nu_n is $\sim .30$. The fractional amplitude of the oscillations of P_x from Figure 114 is $\sim .55$ and the corresponding number from the heat transfer data of Figure 42 is $\sim .56$. Finally the extrema of P_x in Figure 114 are located about $0.8(\lambda/8)$ downstream of the nodes and antinodes, whereas the extrema of Nu_n divided by the steady flow values are roughly located at $0.1(\lambda/8)$ downstream of the nodes and antinodes. The author feels that further comparison of the P_x and Nu_n data referred to above is not profitable for the following reasons. First, there are the many possible causes of error in the calculations of $-\mu_t/P_x$ as enumerated near the beginning of this section. Perhaps more important is the fact that even if the $-\mu_t/P_x$ profiles were correct, the plot of $P_x/P_{x,\text{steady flow}}$ depends strongly on the locations of the 'steady flow reference lines' in the unsteady flow $-\mu_t/P_x$ profiles. If these are substantially in error, the shape and level of the $P_x/P_{x,\text{steady flow}}$ curve in Figure 114 would be strongly effected. For instance, it is possible that because of the presumably greater overall generation of turbulence in the oscillating flow case, the regions of the $-\mu_t/P_x$ profiles (mainly $.03 \text{ in.} < y < .10 \text{ in.}$) in Figures 105-108 used to locate the 'reference lines' do not, in fact, have μ_t values similar to those in the reference steady flow but rather considerably higher values. If this is so, the true location of the 'steady flow reference lines' in Figures 105-108 would be lower than the tentatively assigned 'reference lines' actually used, and the average level of $P_x/P_{x,\text{steady flow}}$ in Figure 114 would be considerably increased. We note that these possible errors in the locations of the 'steady flow reference lines' while strongly affecting the $P_x/P_{x,\text{steady flow}}$ data of Figure 114, still leave much of the earlier discussion of turbulence generation, diffusion and decay roughly valid. However, of course, the

possible causes of error in the determination of the $-\mu_t/P_x$ profiles enumerated near the beginning of this section mean that the earlier discussion of turbulence generation, etc., is tentative in nature.

We discuss the heat transfer data, which, as mentioned on p. 226, tends to support the picture of the development of turbulence described on pp. 226-236. The heat transfer data appears to be roughly consistent with the $-\mu_t/P_x$ profiles using the tentatively assigned 'reference lines'; this is a point supporting the location of these lines. For the following discussion, we regard the location of these lines as correct and we shall see that a fairly consistent qualitative agreement is obtained between the $-\mu_t/P_x$ profiles and the heat transfer data. On p. 237 , we compared the average flow parameters of the data of Figure 114 (which are the same as the average flow parameters for Figures 105-108) with those of Figure 42, and pointed out that the differences are small. Hence, in the following discussion, we regard the flow conditions under which the $-\mu_t/P_x$ data of Figures 105-108 was taken as identical to those of Figure 42 (the heat transfer data). From Figure 42 we see that the minima of heat transfer at about chamber 10 is considerably higher than that at chamber 22. This may be due to thermal development of the boundary layer between chambers 10 and 22, (see Section 5.4) and will be ignored for the present discussion. At this point we again refer to Figure 113 to obtain some idea of the thermal resistances of the various regions of the flow. The resistances of Figure 113 assume similarity of the velocity and temperature profiles and hence apply strictly only for fully-developed steady flow. However, these values should still give some idea of the thermal resistances for the oscillating flow case, and will be used in the discussion below. From Figure 113, we take the following fractional thermal resistances (see Table 25 next page). We first refer to Figure 106 (x = 71%) which corresponds to the velocity node in Figure 42 between chambers 8 and 9, and Figure 107 (x = 35%) which corresponds to position midway between the V.N. and V.A. lines between chambers 11 and 12 in Figure 42. From Figure 42, we see that the unsteady heat transfer is about .19 above the steady flow value at x = 71% and about .32 above the steady flow value at x = 35%. From Figures 106 and 107, we see that μ_t is apparently higher at x = 35% than at x = 71% for the region .005 in. < y < .02 in. However, from Table 25, we see that this region contains

TABLE 25

y-POSITION (in.)	FRACTIONAL THERMAL RESISTANCE
0 - .005	.43
0 - .01	.56
0 - .02	.63
.005 - .01	.13
.01 - .02	.07
.005 - .02	.20
.02 - .1	.16

only roughly .20 of the fractional thermal resistance, whereas the region $0 < y < .005$ in., containing roughly .43 of the thermal resistance, has quite similar μ_t values at $x = 35\%$ and $x = 71\%$. Because of the latter fact, the relatively small increase of heat transfer from $x = 71\%$ to $x = 35\%$, in spite of the large increases in μ_t between $y = .005$ in. and $y = .02$ in. appears fairly consistent. We now refer to Figure 108 ($x = 0\%$) which corresponds to a location just upstream of the V.A. line between chambers 14 and 15 in Figure 42, and at which location Figure 42 shows a fractional increase in heat transfer of $\sim .56$. This relatively large increase in heat transfer from $x = 35\%$ to $x = 0\%$ is consistent with the substantially higher values of μ_t shown in Figure 108 as compared to Figure 107 almost throughout the region $0 < y < .01$ in., which includes roughly .56 of the thermal resistance (from Table 25). These increases in μ_t (from $x = 35\%$ to $x = 0\%$) include both the increase in the height of the peak at $y \approx .0085$ in., and the rise in μ_t for $y < .005$ in., which latter is especially important as it includes roughly .43 of the thermal resistance. The values of μ_t are apparently quite similar for $.01 \text{ in.} < y < .02$ in. at $x = 35\%$ and $x = 0\%$, but this is not inconsistent with the difference in heat transfer at these two locations since the fractional thermal resistance of this region is only roughly .07 (Table 25). We now refer to Figure 105 ($x = 100\%$) which corresponds to a location just downstream of chamber 18 in

Figure 42. At this location, the heat transfer under oscillating conditions is fractionally about .23 higher than that under steady flow conditions. The drop in heat transfer from $x = 0\%$ to $x = 100\%$ is the least consistent part of the present attempt to correlate heat transfer and $-\mu_t/P_x$ data, since the μ_t values for $0 < y < .02$ in. in Figures 108 and 105 are much the same except for the great reduction of the peak at $y \approx .0085$ in. However, the region of this peak ($.007$ in. $< y < .010$ in.) only contains a fractional thermal resistance of $\sim .06$ (Figure 113) and the reduction of this peak alone is not sufficient to account for the heat transfer reduction from $x = 0\%$ to $x = 100\%$. Finally, we refer again to Figure 106, which represents conditions at the velocity node located roughly at chamber 21 in Figure 42 (as well as that located between chambers 8 and 9). The heat transfer at this location is .97 of the steady flow value. The drop in heat transfer from $x = 100\%$ to $x = 71\%$ is consistent with the drop in μ_t throughout the region $0 < y < .02$ in. from Figure 105 to Figure 108. From Table 25, we see that this region contains roughly .63 of the thermal resistance. Especially important with respect to the drop in heat transfer from $x = 100\%$ to $x = 71\%$ is the drop in μ_t from Figures 105 to Figure 108 in the region $0 < y < .005$ in., which contains roughly .43 of the thermal resistance. Thus, a fair correlation can be established between the μ_t values for $0 < y < .02$ in. (which region, from Table 25 should contain roughly .63 of the thermal resistance of the flow), assuming the tentatively assigned 'reference lines' to be correctly located, and the heat transfer data taken under essentially the same flow conditions.

A slight further confirmation of the $-\mu_t/P_x$ data can be obtained from the $\hat{v}$ profiles (Figures 83-90). Before presenting this, we give a brief discussion of the $\hat{v}$ profiles. We compare the observed behavior of $\hat{v}$ with that predicted for laminar flow. For laminar incompressible flow in a pipe with the oscillations driven by a sinusoidally time-varying pressure gradient, the unsteady flow velocity is given by Equation (11), Section 1. The analysis is done on pp. 5,6 , Section 1. An important parameter in this analysis in the A.C. boundary layer thickness

$$\delta_A = \sqrt{\frac{2\nu}{\omega}} \qquad (67)$$

calculated on p.180, Section 5.1 for the 9th harmonic frequency and typical conditions of duct temperature and pressure as .00272 in. In Reference 28, p. 231 a graph of the mean square velocity $(\tilde{U}^2)$ divided by the same far from the wall $(\tilde{U}_o^2)$ versus y/δ_A is given. For this system $\hat{U}/\hat{U}_o$ ($\hat{U}_o = \hat{U}$ value far from the wall) is simply given by

$$\frac{\hat{U}}{\hat{U}_o} = \sqrt{\left(\frac{\tilde{U}}{\tilde{U}_o}\right)^2} \qquad (96)$$

The graph in Reference 28 shows that $\hat{U}/\hat{U}_o$ reaches a maximum value of about 1.068 at $y = 2.28\,\delta_A$ and essentially falls off to 1 by $y = 5\,\delta_A$. For our case, then, based on laminar flow theory the maxima of $\hat{U}(\hat{v})$ should occur at $2.28 \times .00272 = .00620$ in., and $\tilde{U}$ should essentially reach a constant value for y $5x.00272=.0136$ in. We see that the location of the peak of $\hat{U}/\hat{U}_o$ in the theoretical laminar flow analysis varies as $\sqrt{\nu}$. Hence, for this constant-viscosity analysis, the peak of $\hat{U}/\hat{U}_o$ is located farther from the wall, the greater the viscosity (ν). In the actual flow situation, with turbulent flow, the total kinematic viscosity (molecular plus eddy viscosities, μ_t/ρ) is varying rapidly near the wall, so the laminar flow solution of Equation (11), Section 1 does not strictly apply, but one would still expect the peak of $\hat{U}/\hat{U}_o$ to be farther from the wall in a case where the μ_t values were larger at most y-positions of interest (in the region of the peak of $\hat{U}/\hat{U}_o$). From the data of Figures 83-90, we prepare the following table of the maximum value of $\hat{U}/\hat{U}_o$ $\left[= (\hat{U}/\hat{U}_o)_{max.}\right]$ and the y- value at which this maximum occurred.

TABLE 26

x-POSITION	FIG. NO.	$\left(\frac{\hat{U}}{\hat{U}_o}\right)_{max.}$	y-POSITION AT WHICH $\left(\frac{\hat{U}}{\hat{U}_o}\right)_{max.}$ OCCURS
%	–	–	in.
100	87,83	1.11	.006
71	88,84	1.19	.007
35	89,85	1.22	.008
0	90,86	1.11	.014
LAMINAR FLOW THEORY		1.068	.00620

Note: for the experimental data of Table 26, $\hat{U}$ in the table is equivalent to $\hat{v}$ in Figures 83-90.

The fact that the maxima of $(\hat{U}/\hat{U}_o)$ are considerably larger than predicted by the laminar flow theory and the much slower experimentally observed fall-off of $\hat{U}$ with increasing y as compared to that predicted by the theory are almost certainly due to the blockage effect of the hot-wire probe which tends to make the probe indicate abnormally high velocity values near the wall. No explanation can be given for the wide variations in the amount by which the experimental values of $(\hat{U}/\hat{U}_o)_{max.}$ exceed the theoretical laminar flow values. This blockage effect can be seen in Figure 93, Section 4.13 which shows steady flow hot-wire and pitot traverses of the duct. The pitot profile, as discussed on p. 170, appears likely to be very close to the true velocity profile. While the blockage effect shown in Figure 93 was observed in steady flow, as discussed on pp.221,222, a similar blockage effect should apply in unsteady flow. Because the effects of probe blockage vary rapidly in the region of the $\hat{v}$ peaks shown in Figures 87-90, the forms of these peaks are likely considerably modified when the unsteady blockage corrections, which are not known exactly, are applied. However, the greater distance from the wall of the peak of $\hat{v}$ at $x = 0\%$ (Figure 90) as compared to the corresponding distances at other x-positions (see Table 26) does give some slight evidence of greater total viscosity (μ_t) at that location. This is consistent with the fact that the maximum of heat transfer occurs very near this x-position, which nearly corresponds to the velocity antinode located between chambers 14 and 15, Figure 42. It is also roughly consistent with the $-\mu_t/P_x$ data of Figures 105-108, which shows (assuming the tentatively assigned 'reference lines' to be correctly located) that the maximum average μ_t level over $0 < y < .02$ in. (which includes the region of the peaks of $\hat{v}$) occurs at $x = 0\%$. Mainly because of the unsteady blockage effects, which are not known exactly, the support which the $\hat{v}$ profiles lend to the picture of the development of turbulence outlined from the $-\mu_t/P_x$ profiles is fairly weak.

We now discuss briefly, the $-\mu_t/P_x$ profiles for $y > .1$ in. (Figures 101-104). Examining the $\bar{v}'$ profiles of Figures 71-74, from which the $-\mu_t/P_x$ profiles of Figures 101-104 were derived, we see that in the region $y > .1$ in., the slopes of the $\bar{v}'$ curves are very low and and the density of data points is small, both these factors compared to

those in the region $y < .1$ in. These two factors tend to make the $-\mu_t/P_x$ data in the region $y > .1$ in. much less accurate relative to that in the region $y < .1$ in. For instance, considering Figure 71, we refer to the data points at $y = .4$ and .5 in. which apparently show a scatter compared to the smooth curve drawn for $\bar{v}'$ of $\sim .6$ ft/sec . If the smooth curve were raised or lowered in this region, say, .3 ft/sec, $-\mu_t/P_x$ would there be changed 100% or more. Referring now to the $-\mu_t/P_x$ profiles of Figures 101-104, we note first that since τ in Equation (86) from which $-\mu_t/P_x$ is calculated is zero at $y = .73$ in., no $-\mu_t/P_x$ value can be calculated there. Secondly, the $-\mu_t/P_x$ values calculated at y-positions indicated by circles in Figures 102 and 104 are more than twice the neighboring values, and are hence regarded by the author as even more untrustworthy than the remaining $-\mu_t/P_x$ data for $y > .1$ in. These values of $-\mu_t/P_x$ were computed from locations on the $\bar{v}'$ profiles with slopes near zero, which value would yield an infinite value of $-\mu_t/P_x$ if the probe blockage correction factor, F_v (see beginning of this section) were 1 in this region. Another possible cause of error for the $-\mu_t/P_x$ profiles at $x = 35\%$ and $x = 100\%$, is the possible presence there of acoustic streaming velocities, which would be interpreted as erroneous variations in $-\mu_t/P_x$ (see pp.222,223). Also, relatively slight variations of the true (unsteady) (unknown) blockage correction applied to the $\bar{v}'$ profiles to enable $-\mu_t/P_x$ to be calculated (see pp.209,221)from the assumed form of this correction obtained from steady flow data could cause substantial errors in the $-\mu_t/P_x$ values in the region $y > .1$ in., since the slopes of the $\bar{v}'$ profiles are very low there.

If the peak in $-\mu_t/P_x$ observed between $y = .25$ in. and $y = .4$ in. in Figures 101, 102 and 104 is a true feature of the flow, presumably it would represent another region of generation of 'abnormal' turbulence by the oscillation. If this was so, it is difficult to see why the greatest height of this peak compared to the tentatively assigned 'reference line' occurs at $x = 71\%$ (Figure 102) which is the location of minimum disturbance of the flow by the oscillation. Related to this fact is the fact that unlike the apparent μ_t variations for $y < .1$ in., the apparent μ_t variations for $y > .1$ in., are not supported by the heat transfer data. (Under any

conditions it would be difficult to support indicated μ_t variations for .1 in. < y < .73 in. by heat transfer data, since from Table 25, this region contains only about 21 of the thermal resistance of the flow.) Because of the facts discussed above, any conclusions made on the basis of the $-\mu_t/P_x$ data for $y > .1$ in. are extremely tentative.

There is some slight support for the possibility that another region of generation of 'abnormal' turbulence exists away from the duct wall which may be obtained from power spectrum data of the turbulence in the pipe. For this reason and for use in Section 5.5, we examine power spectrum data for steady turbulent pipe flow taken from Reference 30. This data was taken in fully developed airflow in a pipe of 9.72 in. inside diameter at a Reynolds number of 4.25×10^5. The airflow was essentially at room temperature and pressure. Since we are interested in transfer of heat in the r-direction, we examine the power spectrum of the r-component of turbulence. Here, we let $\bar{a}(\bar{b})$ and $a'(b')$ be the time-average and time-varying components of the x(r)-velocity respectively. The data of Reference 30 is given in the form of the amount of $\overline{b'^2}$ energy per unit wave number interval versus wave number (k) . We refer to this function as E_r, the units of which in Reference 30 are cm^3/sec^2. $\overline{b'^2}$ is related to E_r as follows

$$\overline{b'^2} = \int_0^\infty E_r dk \tag{97}$$

Now, the data was actually taken with a frequency analyzer which measured the signal energy content per unit frequency interval as a function of ω . No statement is given in Reference 30 about the relation between ω and k . We assume that

$$\omega = k\bar{a} \quad . \tag{98}$$

The data of Reference 30 is presented as graphs of

$$E_r = f(k) \tag{99}$$

We now make some transformations and finally, present this data in another form. Let E_{1r} be the amount of $\overline{b'^2}$ energy per unit frequency interval. Then, we can write:

$$E_{1r} = \frac{E_r}{\bar{a}} \tag{100}$$

Non-dimensionalizing E_{1r} using the mean flow velocity in the pipe $(\bar{\bar{a}})$ and a characteristic frequency $\bar{\bar{a}}/D$, we obtain

$$E_{2r} = \frac{E_{1r}}{\bar{\bar{a}}^2} \frac{\bar{\bar{a}}}{D} = \frac{E_{1r}}{\bar{\bar{a}}D} \tag{101}$$

Non-dimensionalizing ω in the same way yields

$$\omega_2 = \frac{\omega D}{\bar{\bar{a}}} = \frac{k\bar{a}D}{\bar{\bar{a}}} \quad . \tag{102}$$

The power spectrum in the form $E_{2r} = g(\omega_2)$ is, of course, independent of D and $\bar{\bar{a}}$, providing the Reynolds number is unchanged. Finally, we introduce logarithmic representation as follows

$$\nu_2 = \log_{10} \omega_2 = \log_{10} \frac{k\bar{a}D}{\bar{\bar{a}}} \tag{103}$$

$$F_{2r} = \omega_2 \ln(10)\, E_{2r} = \frac{k\bar{a}D}{\bar{\bar{a}}} \ln(10) \frac{E_r}{\bar{\bar{a}}\bar{a}D} = \ln(10) \frac{kE_r}{\bar{\bar{a}}^2} \tag{104}$$

We note that

$$\int_{\nu_{21}}^{\nu_{22}} F_{2r} d\nu_2 = \int_{\nu_{21}}^{\nu_{22}} \ln(10) \frac{kE_r}{\bar{\bar{a}}^2} \frac{1}{\ln(10)} \frac{\bar{\bar{a}}}{k\bar{a}D} \frac{\bar{a}Ddk}{\bar{\bar{a}}} = \frac{1}{\bar{\bar{a}}^2} \int_{k_1}^{k_2} E_r dk \tag{105}$$

so that, with linear scales for F_{2r} and ν_2, in the plot of $F_{2r} = h(\nu_2)$, the area under the F_{2r} curve, between the two values of ν_2 corresponding to k_1 and k_2, when multiplied by $\bar{\bar{a}}^2$ gives the b'^2 energy between k_1 and k_2. We present the data of Reference 30 plotted in the form $F_{2r} = h(\nu_2)$ for $2y/D = .691$ and $.074$ in. in Figure 115. Since this data was taken at $Re = 4.25 \times 10^5$ and the present author's data at $Re \approx 10^5$, the data of Figure 115 does not correspond exactly to that to be expected under our reference steady flow conditions, but should give a rough approximation. The values of y in our apparatus corresponding to the $2y/D$ values of the F_{2r} data are .505 and .054 in. These y-values are shown in Figure 115. We note that

$$\nu_2 = \log_{10} \frac{k\bar{a}D}{\bar{\bar{a}}} = \log_{10} \frac{\omega D}{\bar{\bar{a}}} = \log_{10} \; [illegible] \tag{106}$$

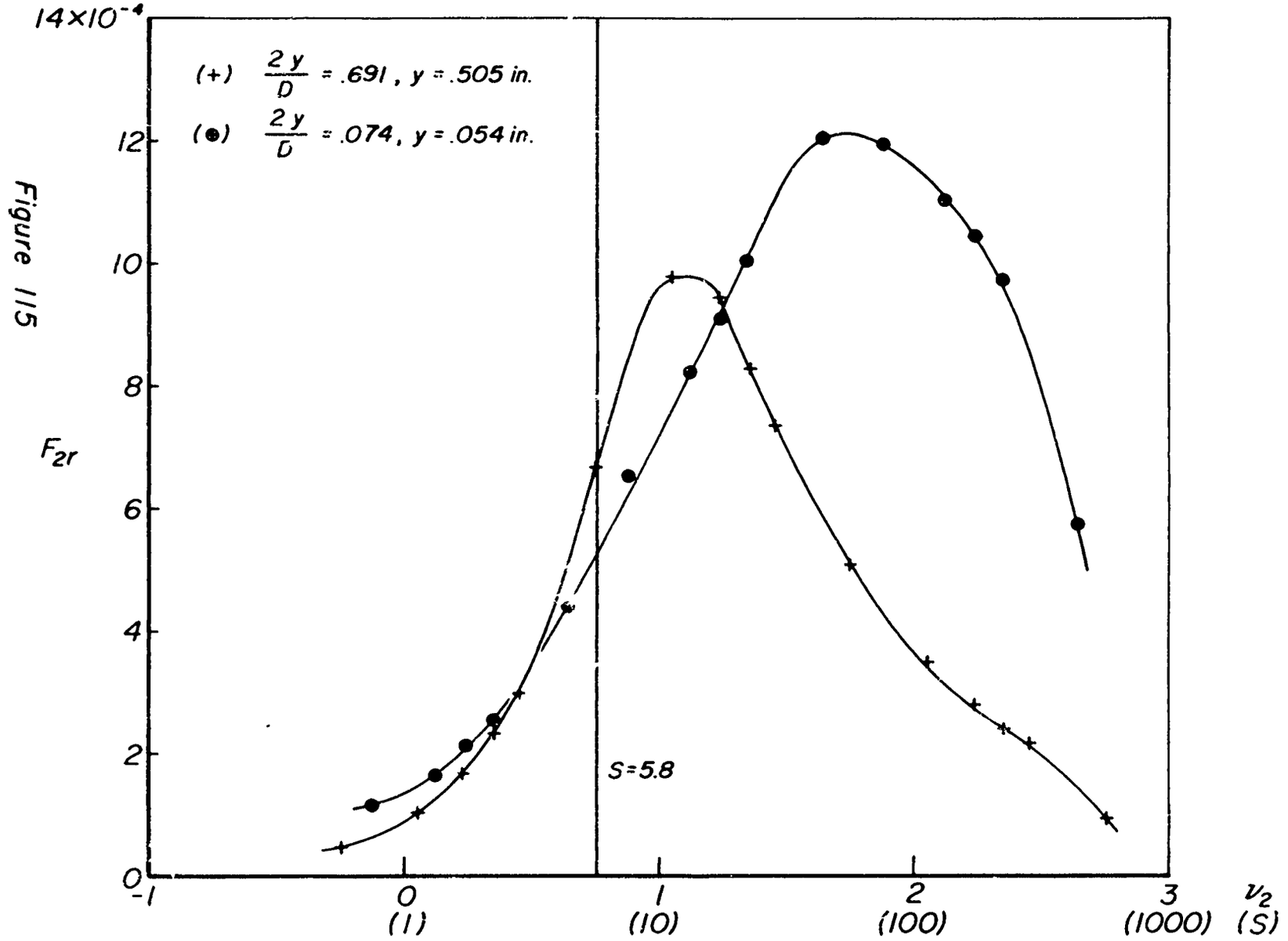

Figure 115

where S is the Strouhal number of the turbulence. We can thus add the Strouhal number scale shown in brackets on the abscissa of Figure 115. Referring to the $\bar{v}'$ profiles of Figures 71-74, we see that the average oscillation Strouhal number for these tests is 5.80. This value is shown on Figure 115. Thus, one could use Figure 115 to very roughly compare the frequencies of the oscillation and of the r-component of turbulence at the two y-positions shown under oscillating conditions. (The comparison is very rough because the power spectrum data was taken under steady flow conditions, and at a somewhat different Re value.) From Figure 115, it appears that, for the present author's tests, in the central regions of the duct, the turbulence energy is mainly in a band centered at about twice the oscillation frequency, whereas at $y \sim .05$ in., the band is centered at ~ 10 times the oscillation frequency.

Because the oscillation frequency is close to the center of the energy-containing band of turbulence frequencies in the central regions of the duct, but is farther from this frequency band near the wall, it is possible that the oscillation would be more effective in generating 'abnormal' turbulence in the central regions of the duct than nearer the wall (excepting the region of very high A.C. shear values ($y < .03$ in.) discussed earlier). This would, of course, be because the oscillation is more likely to be near resonance with an eddy in the central regions of the duct, than in the wall regions. This mechanism could be speculated as a possible 'explanation' of the nature of the peak of $-\mu_t/P_x$ shown in Figures 101, 102 and 104 in the region $.25 \text{ in.} < y < .4 \text{ in.}$ -- if this peak is a true characteristic of the flow and not a product of experimental error (see pp. 244, 245). If this speculation did correspond to the facts, the lower levels of $-\mu_t/P_x$ in the region $.45 \text{ in.} < y < .73 \text{ in.}$ as compared to the peak at $y \sim .3$ in. might be explained as due to the lower steady component of shear in those regions. The unsteady component of shear is likely very small beyond $y \approx 20\sigma_A \approx .06$ in. on account of the exponentially decaying nature of unsteady x-velocities indicated by the laminar flow solution, Section 1, Equation (11), despite the fact that actual flow has large variations of μ_t near the wall. Our very speculative explanation of the location of the peak of $-\mu_t/P_x$ at $y \sim .3$ in. would then be that nearer the center of the duct, the steady shear values are too low for large 'abnormal'

turbulence production although many of the eddies are near resonance with the oscillation, while nearer the wall, the steady shear values are large, but the turbulence frequencies are, for the most part, too far removed from resonance for large 'abnormal' turbulence production.

Lest the reader attach too great a significance to the above speculations on the generation of 'abnormal' turbulence in the region of the $-\rho_t/P_x$ peak at $y \sim .3$ in. shown in Figures 101, 102 and 104, we refer him back to pp.244,245,where the reasons for the extreme uncertainty of the $-\rho_t/P_x$ data taken for $y > .1$ in. are outlined.

We now discuss some possible improvements in experimental technique and possible additional measurements which might in the future be made on the author's apparatus. A most important improvement, in the author's opinion would be a reduction of the hot-wire probe blockage effect, which introduces great difficulties in the interpretation of the experimental data as mentioned in many places in Sections 5.2 and 5.3. From Figure 49, it is apparent that the large size of the wire support needles and the closeness of the 1/8 in. diameter body of the probe of the wire are likely the cause of the probe blockage effect. In Figure 116, we have sketched two of the hot-wire probes obtained from Thermo-Systems, Inc., Minneapolis, Minnesota, Figure 116(a) being the probe which was used to obtain all hot-wire data presented in this paper. The probe illustrated in Figure 116(b) should produce much smaller blockage effects, since the 1/8 in. diameter body of the probe is much farther from the wire and, also, the support needles are of much smaller diameter near the wire than for the probe of Figure 116(a). However, when the probe of Figure 116(b) was tried under typical conditions of oscillating flow, extremely large oscillations were observed on the output of the hot-wire amplifier (superimposed on the velocity signal). As discussed previously, in Section 4.6, with respect to the probe of Figure 116(a), these oscillations are suspected by the author to be due to vibration of the wire support needles causing the hot-wire to act as a strain guage. However, the oscillations observed for the probe of Figure 116(b) were much larger than those observed for the probe Figure 116(a), and could not be much reduced by the use of a slackly mounted wire, which was successful in reducing similar vibrations for the latter probe (Section 4.6). Hence, probes of the type shown in Figure 116(b) could not

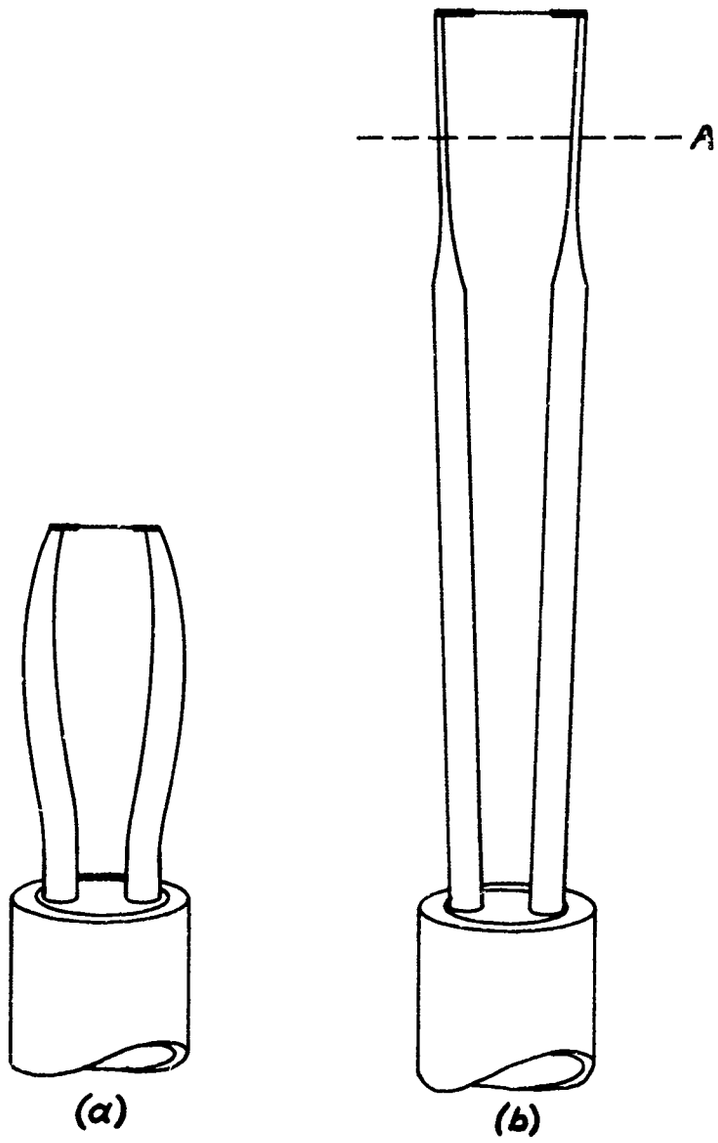

FIGURE 116

be used. If the excitation of the wire support needle vibrations is primarily by vibrations of the duct assembly caused by the siren wheel drive system, the former could be reduced as follows. When hot-wire measurements are taken on the apparatus, the configuration is as sketched in Figure 31, with the steam-heated section shown there replaced by the traversing test section shown in Figure 44, which mounts the hot-wire probe. At present, the siren wheel drive system (see Section 3.1) is rigidly connected to an I-beam running parallel to the duct which also mounts the latter. Hence, the severe vibrations produced by the siren wheel drive system are directly transmitted to the duct. If the duct and the siren wheel drive system were independently mounted on the floor, the vibration transmission to the duct could be much reduced. Since the gap between the downstream surface of the variable area nozzle (Figure 31) and the siren wheel is very small, the variable area nozzle and the last foot or so of the duct would have to be rigidly connected to the siren wheel drive system, necessitating a flexible joint in the duct about 1 foot upstream of the siren wheel.

If, however, the main cause of excitation of the wire support needle vibration is the oscillation of the airflow, of course, the above described modifications will have little effect on the support needle vibrations. In this case, the strain-guage effect produced by the support needle vibrations for the probe of Figure 116(b) might be greatly reduced by joining the needles with a thin metal bar at about point A (Figure 116(b)). The bar would have to be thin, so as not to introduce significant blockage effects itself, and would have to be insulated from the needles so as not to short out the wire.

It should be possible, perhaps using some of the ideas outlined above, to obtain velocity data much freer from probe blockage effects than that of the present author. Any probe configuration intended to reduce probe blockage effects could be checked in steady flow against pitot profiles and fully developed pipe flow data from the literature as discussed in Section 4.13, pp.170,171.If a probe configuration essentially free of blockage effects could be constructed, data so obtained corresponding to that of the $\bar{v}'$, $\bar{v}$, $\hat{v}$ and $-\mu_t/P_x$ profiles discussed in Sections 4.13, 5.2 and 5.3 would carry much greater weight than the present author's data.

A measurement of great importance which might be made in the future is that of pressure drop along the duct. For instance, the increases in heat transfer and pressure drop produced by the oscillations could be compared to investigate the analogy between heat and momentum transfer. We make a few brief estimates on the size of the pressure drops that might be expected as compared to the peak-to-peak time-varying pressure in the duct. We base our pressure drop estimates on fully-developed, steady pipe flow corresponding to the mean flow parameters under oscillating conditions. From Figure 42, the value of $\tilde{P}_N/\bar{P}$ under roughly maximum amplitude oscillations of which the apparatus is capable is $\sim .1030$. Since $\bar{P} = 54.7$ psia, and assuming that $\hat{P}_N \approx 2\sqrt{2}\ \bar{P}$, we obtain a $\hat{P}_N$ value of

$$.1030 \times 54.7 \times 2\sqrt{2} = 15.96 \text{ psi}$$

Typical mean velocities ($\bar{U}$), densities ($\bar{\rho}$), and Re values are as follows:

$$\bar{U} = 34.1 \text{ ft/sec}$$

$$\bar{\rho} = .288 \text{ lbm/ft}^3$$

$$Re = 101{,}000$$

The inside diameter of the duct is 1.50 in., and the maximum length available for pressure drop measurements is $\sim$98 in. (see Figure 32). In Reference 28, pp. 503-504, the pressure gradient in steady flow is given as

$$P_x = \frac{\lambda}{D}\ \frac{1}{2}\bar{\rho}\bar{U}^2 , \qquad (107)$$

and λ for $Re = 100{,}000$ is $\sim .018$.

Hence,

$$P_x = .018\ \frac{12}{1.46}\ \ \frac{1}{2}\ \frac{(.288)(34.1)^2}{32.2}$$

$$P_x = .769 \text{ lbf/ft}^3$$

$$P_x = \frac{.769}{144} = .00534 \text{ psi/ft} .$$

The pressure drop which would be observed over the 98 in. length available is

$$= \frac{98}{12} \times .00534$$

$$= .0435 \text{ psi}$$

Hence the pressure drop to be measured is of the order of 1/400 of $\hat{P}_N$. The ratio of the peak-to-peak fluctuating pressure at the two pressure taps to the time-average pressure difference between these taps could be reduced perhaps ten-fold, by locating both pressure taps at velocity anti-nodes (pressure nodes). Presumably, the pressure difference would be measured on a manometer, and perhaps small chambers and flow restrictions as sketched in Figure 117, if properly designed, would allow the pressures over the manometer fluid to be, very closely, a true linear time-average of the adjacent duct pressure. This is, of course, necessary if the manometer is to measure the time-average pressure drop in the duct, and not some spurious effect of the very large time-varying pressures in the duct.

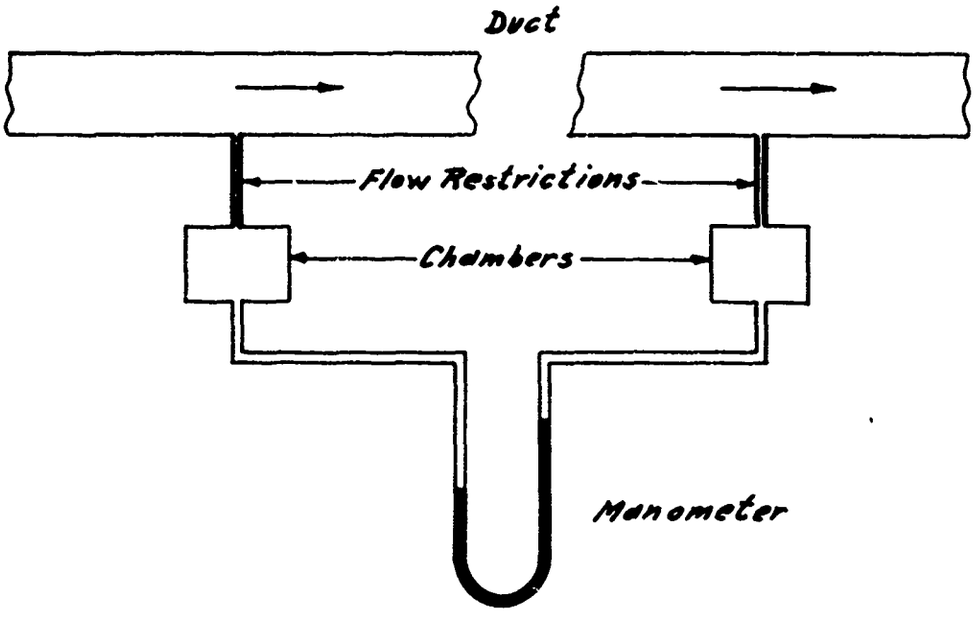

FIGURE 117

Earlier in this section, we discussed the fact that even if the $-\mu_t/P_x$ profiles obtained in the present investigation were correct, it would be difficult to compare μ_t values from one profile to the next, since the P_x values were unknown. We attempted to make this comparison by locating regions of the $-\mu_t/P_x$ profiles where the variations of μ_t appeared 'normal' (similar to that in steady flow, roughly $\propto y$) and locating the 'reference line' through these regions. If local P_x data could be obtained using the manometer system discussed above, the correct 'steady flow reference line' could be immediately drawn on each $-\mu_t/P_x$ profile without regard to the unsteady flow $-\mu_t/P_x$ data. However, if the future $-\mu_t/P_x$ data was obtained at roughly the same x-position interval that the author used ($\sim \frac{\lambda}{8} \approx 6$ in.) the pressure taps would appear to have to be at most ~ 6 in. apart to obtain satisfactory 'local' P_x data. The ratio of the peak-to-peak time-varying pressure at the pressure taps to the time-average pressure difference between the taps would be increased by a factor of $98/6 \approx 16$ for this reason, and also because the pressure taps could not now be located at pressure nodes as was possible when the overall pressure drop only was measurement. In this case, the ratio of the peak-to-peak time-varying pressure at the pressure taps to the time-average pressure difference might be as high as $16 \times 400 = 6400$. Hence, it may prove possible to obtain the overall P_x data referred to above, but not the 'local' P_x data. However, even the former would be quite valuable, and the latter should be attempted, especially since the equipment and apparatus modifications necessary are quite simple.

Finally, it is suggested that direct measurement of some turbulence quantities can be obtained using the hot-wire. It appears that the power spectrum of the x-component of velocity (a) can be obtained, as well as the mean square value of the random component of a, (equivalent to $\overline{a'^2}$ in steady flow) in spite of the large periodic component of a present due to the oscillation. If data on the power spectrum of a was obtained at various x-positions, it would very likely furnish much more positive information on the generation, diffusion and decay of 'abnormal' turbulence than $-\mu_t/P_x$ data which was used for this purpose in the present investigation. This data could be obtained as follows. Essentially, the same techniques described in Section 4 for obtaining one 'ensemble-averaged' cycle of the

x-velocity component would now be used to obtain, say,10 or 20 consecutive cycles of x-velocity values (not ensemble-averaged). The author started to develop this technique, but was forced to halt for lack of time. Essentially, the only important difference from the data handling technique described in Section 4, is in the obtaining of the original photographic record of the output voltage of the hot-wire amplifier. Rather than using a Polaroid camera with a 5 sec exposure and a synched 'scope trace of one cycle of the hot-wire output signal, as was done to obtain the 'ensemble-averaged' data, the horizontal sweep in the scope was turned off and a continuous-film-motion 35 mm camera was mounted on the 'scope. Thus, as many cycles as were desired could be recorded on the 35 mm film. From this photographic record, data reduction could proceed essentially as outlined in Section 4, until finally a continuous list of x-velocity values over the 10 or 20 cycles of interest (with $\sim$ 40 velocity values per cycle) were obtained. Taking this data, choosing a length T_1 (Figure 118) equal to an integral number of cycles, as nearly as possible, a Fourier analysis could then be performed. Plotting the amplitudes of the Fourier components versus frequency,we would obtain data as shown in Figure 119 (for the case shown in Figure 118). The Fourier components at frequencies of $n(6)\frac{2\pi}{T_1}$, $n = 1, 2, 3 \ldots$, represent the periodic components of the time-varying velocity and the remaining Fourier components represent the random components of the time-varying velocity (turbulence). The form of the power spectrum of the x-component of turbulence would be represented by a graph of the amplitudes squared of the latter Fourier components plotted versus frequency. The behavior in various regions of the flow of the power spectrum of a so obtained would, as discussed at the beginning of this paragraph, very likely yield data on the development of 'abnormal' turbulence much superior to that obtained by the present author.

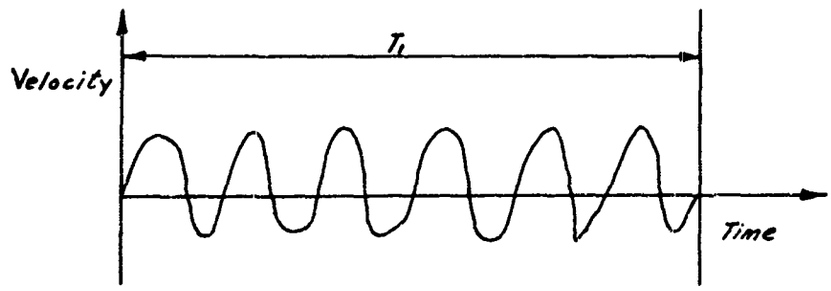

FIGURE 118

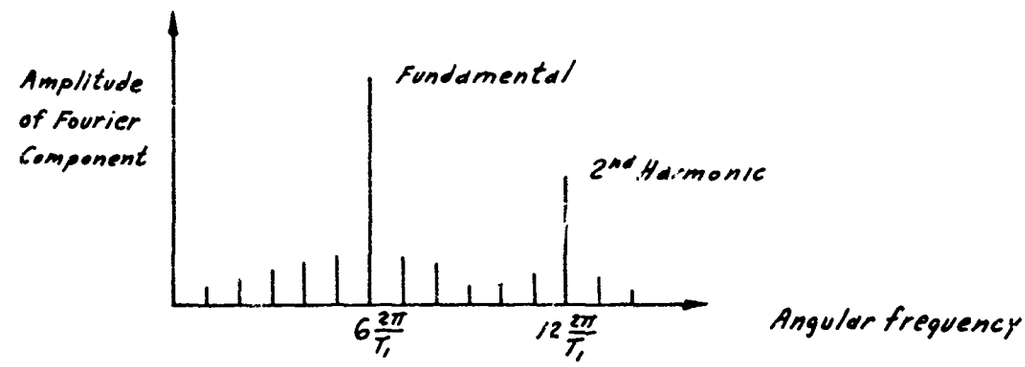

FIGURE 119

5.4 Brief Discussion of Certain Features of the Heat Transfer Data of this Report

We refer to the heat transfer data of Figures 36-43. In addition to the oscillations of the heat transfer deviations and the general shifts of the heat transfer levels shown in Figures 36-43 (and discussed in Sections 5.1, 5.2, 5.3 and 5.5) the following additional features may be observed.

(1) There is, in general, a gradual lowering of the unsteady heat transfer data with respect to the steady flow data as one moves downstream. For example, in Figures 41 and 42, the minima in the region of chamber 22 are lower with respect to the steady flow values than the corresponding minima near chambers 9 and 10. Also in Figures 38 and 39, the maxima near chamber 23 is lower with respect to the steady flow values than the corresponding maxima near chambers 11 and 12.

(2) For about the first three chambers, in Figures 37, 38 and 39, there is an additional increase in heat transfer with respect to the steady flow values and with respect to the values $\lambda/2$ further downstream. This effect may also be present to a slight degree in the other figures. In Figures 38, 39, and perhaps 37 (the No. 1 chamber point being likely in error makes the conclusion uncertain for Figure 37) the difference is such to make the deviations positive for the first three chambers whereas, $\lambda/2$ further downstream the deviations are negative.

To aid in discussing these features we now replot the heat transfer data of Figure 42 in the form of the oscillating flow Nusselt number ($Nu_{n,u}$) divided by the steady flow Nusselt number ($Nu_{n,s}$). This data is shown in Figure 120 (curve No. 1). In order to compare the data $\lambda/2$ apart, the downstream half of curve No. 1 in Figure 120 has been reproduced $\lambda/2$ farther upstream as curve No. 2. The gradual decrease of the unsteady heat transfer values with respect to the steady flow values as one moves downstream here appears as the overall difference in level of curves (1) and (2). The additional increase in heat transfer for the first three chambers as compared to the steady flow values and as compared to data from $\lambda/2$ further downstream is not as apparent in Figure 120 as it would in a similar plot prepared from Figures 38 and 39, but is slightly suggested by

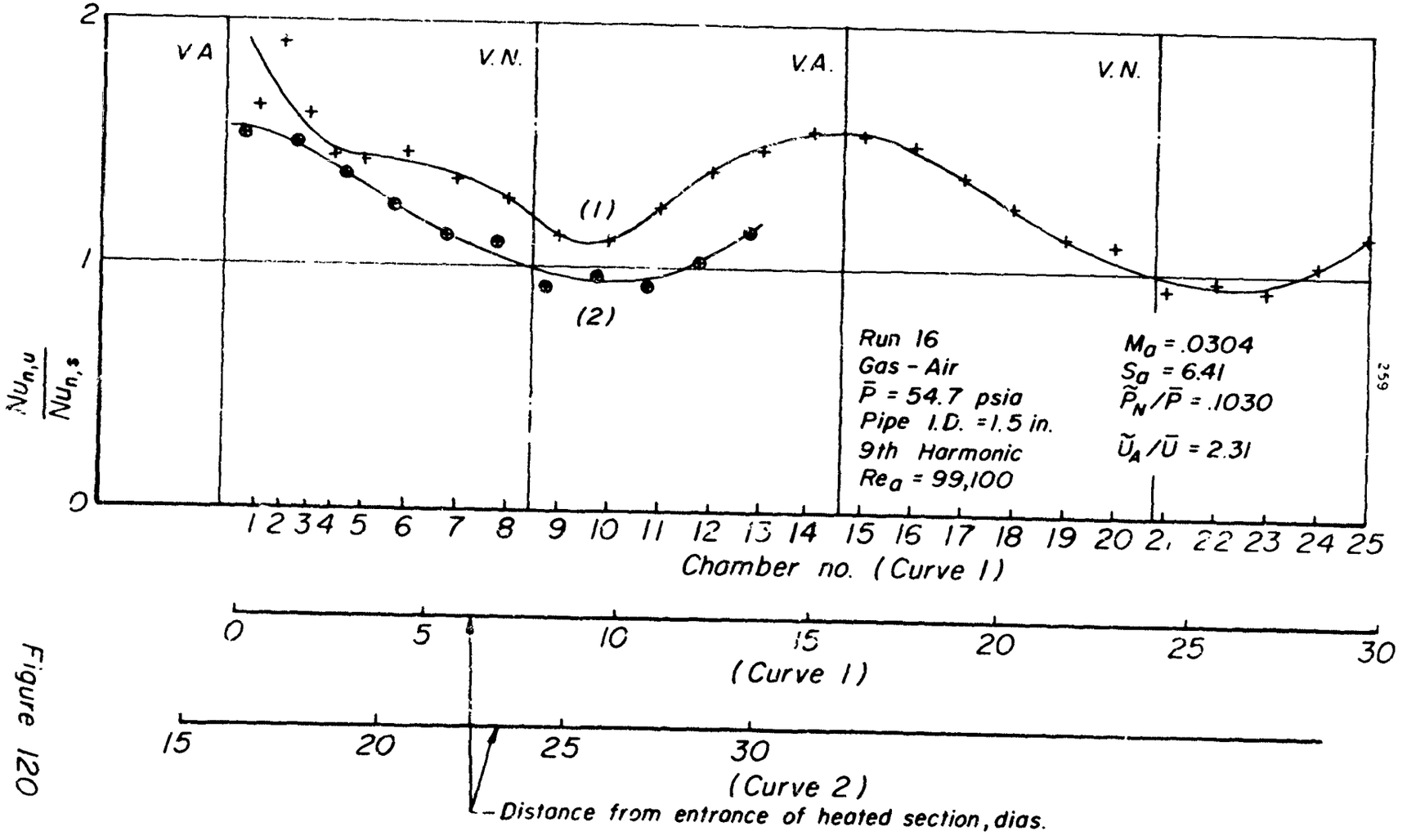
V.A
V.N.
V.A.
V.N.
(1)
(2)
Run 16
Gas - Air
$\bar{P}$ = 54.7 psia
Pipe I.D. = 1.5 in.
9th Harmonic
Re_a = 99,100
M_a = .0304
S_a = 6.41
$\tilde{P}_N/\bar{P}$ = .1030
$\tilde{U}_A/\bar{U}$ = 2.31
$\frac{Nu_{n,u}}{Nu_{n,s}}$
Chamber no. (Curve 1)
(Curve 1)
(Curve 2)
Distance from entrance of heated section, dias.

Figure 120

data of chambers 1 and 2 (curve No. 1).

We first discuss possible explanations for the gradual decrease in the unsteady heat transfer values with respect to the steady flow values as one moves downstream. From Figure 120, the unsteady heat transfer values divided by the steady flow values seems to average about .2 lower over the range 15-30 diameters downstream of the entrance to the heated section as compared to over the range 0-15 diameters downstream of same. We first investigate the question of whether experimental error may have caused these results. From Section 3.4, Table 15, the fractional heat balance errors of the runs yielding the data of Figures 36-43 (including the steady-state run) are .04-.08. This would seem to imply that no experimental errors in the calculation of the amount of heat transferred to each chamber large enough to cause the overall deviations of curve 1 in Figure 120 occurred. Further, as discussed in Section 3.4, the average fractional heat balance error of $\sim$ .06 is likely due to conduction effects in thermocouple B, Figure 31, and applies almost uniformly to all runs, leaving the random error contribution to the fractional heat balance error in the range $\pm$.02. If this is the case, it is even more unlikely that experimental error is responsible for the overall deviation of curve 2 from curve 1 in Figure 120.

Next, we investigate the possibility that the strength of the oscillation (say, $\hat{U}_A$) varies significantly from velocity antinode to velocity antinode, and hence, the possibility that the different values of the unsteady heat transfer divided by the steady flow heat transfer in the regions of, say chambers 6 and 18, 19 in Figure 120, are caused by different local values of $\hat{U}$ at these points, despite the fact that they are located similarly with respect to the node-antinode pattern. In Table 19, Section 4.13 pp. 176,177, we compared $\hat{U}_A/\bar{U}$ computed (1) from $\tilde{P}_N/\bar{p}$ just upstream of the siren wheel and (2) from hot-wire velocity data at $x = 0\%$, $\sim$36 in. further upstream. We found that the $\hat{U}_A/\bar{U}$ values so computed agreed within 3 and 8% in the two cases compared, the values further upstream being greater. [This latter was likely due to the fact that the hot-wire value of $\hat{U}_A/\bar{U}$ was a true peak-to-peak measurement while the pressure transducer value of $\hat{U}_A/\bar{U}$ was based on a r.m.s. value of pressure $(\tilde{P}_N)$ and the oscillation waveform was

only roughly sinusoidal , see pp. 176-177] Hence, it appears unlikely that the strength of the oscillation (say, $\hat{U}$) could be sufficiently different at two points $\lambda/2$ ($\sim$ 24 in.) apart to explain the overall deviation of curve 1 from curve 2 in Figure 120. Further support for the above statement is obtained as follows. From Figure 41 and 42 any reduction in oscillation strength in this range of $\hat{U}_A/\bar{U}$ values seems always to result in a decrease in the fractional heat transfer deviations. From Figure 120, the fractional heat transfer deviations are larger $\lambda/2$ further upstream, where the oscillations should be weaker, if substantial changes in oscillation strength occur over a distance of $\lambda/2$, since this is farther from the siren wheel.

Since, from the previous 2 paragraphs, it appears that the overall deviation of curve 1 from curve 2 in Figure 120 is likely not caused by experimental error or variations in the oscillation strength down the duct, we now search for other possible explanations of this deviation. We examine possible effects of development of the thermal boundary layer on the fractional heat transfer deviations. Two effects will be discussed here. To discuss the first effect, we assume that the fluid properties (μ, K, ρ) are unaffected by the heat transfer. In particular, we assume that all turbulence quantities, eddy viscosities and thermal conductivities, are independent of heat transfer. Let us assume that the total conductivity (K_t = molecular plus 'eddy' conductivity) at a certain point in the node-antinode pattern divided by the corresponding steady flow values is as sketched in Figure 121(b), which shows very crudely, some of the features of the $-\mu_t/P_x$ profiles discussed in section 5.3. Very near the entrance to the heated section, the thermal boundary layer may be very thin and a substantial fraction of the temperature drop across the thermal boundary layer may take place within the region of high K_t(unsteady) / K_t(steady) [see curve 1, Figure 121(a)]. At this point the fractional heat transfer deviation would be expected to be large. However, $\lambda/2$ further downstream, where the curve of Figure 121(b) again applies, the thermal boundary layer, being much thicker, may have only a small portion of its temperature drop in the region of high K_t(unsteady) / K_t(steady) [see curve 2, Figure 121(b)]. Here the fractional heat transfer deviation would be much smaller. From the $-\mu_t/P_x$ profiles

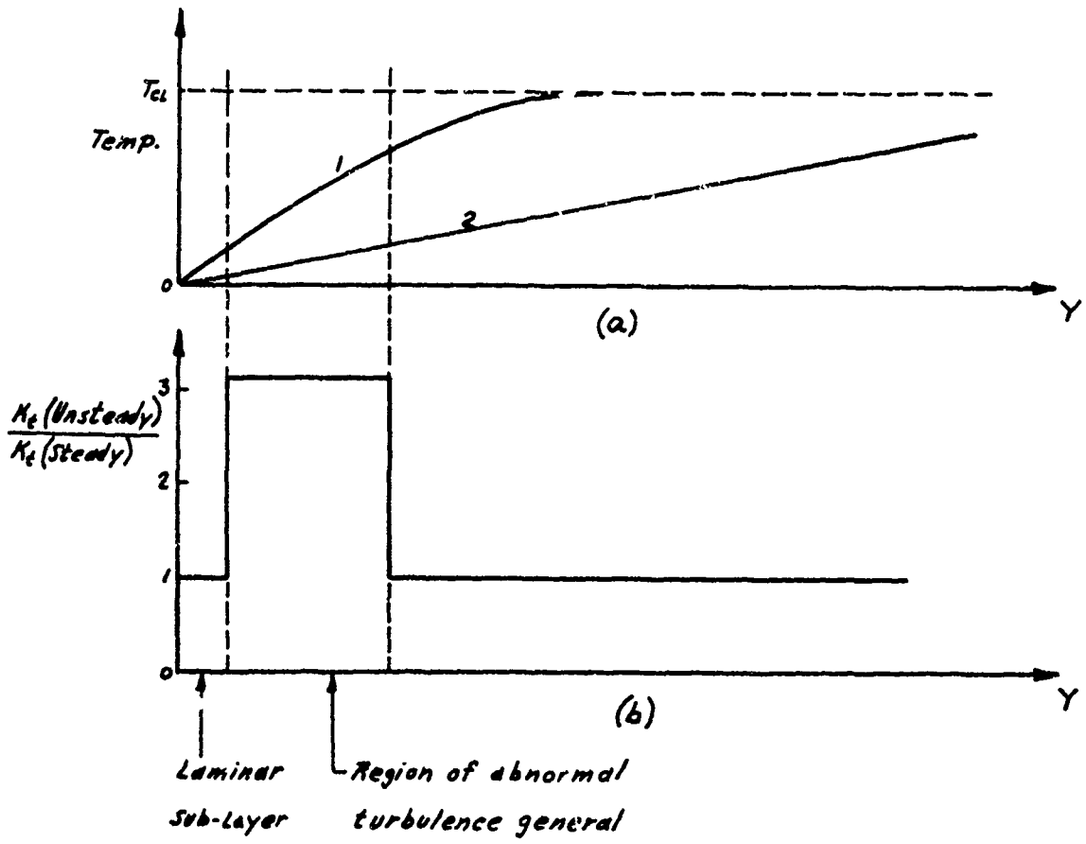

FIGURE 121

and thermal resistance change [Figure 1 3] of Section 5.3 it is apparent that, an effect as strong as that implied in Figure 121 does not, in fact, exist; but to a lesser extent, such an effect is quite possible. The second effect depends upon possible variations in the structure of turbulence at similar points in the node-antinode pattern, due to differences in the fluid properties (μ and ρ) at the same y-positions caused by the different temperature profiles at varying stages in the development of the thermal boundary layer. For example, since the flow near the wall has a lower density, due to the locally higher temperature, there is a tendancy for the air in this region to oscillate with a larger $\hat{U}$ than the flow further from the wall. This can introduce additional A.C. shear into the

flow over and above that expected from a constant-density flow analysis. The nature of this additional A.C. shear will depend upon the density gradient near the wall and hence upon the thickness of the thermal boundary layer. If this additional A.C. shear contributes significantly to the generation of 'abnormal' turbulence, then the latter will depend upon the thickness of the thermal boundary layer. Thus, another mechanism by means of which the development of the thermal boundary layer can affect the fractional heat transfer deviations at similar points in the node-antinode system is apparent. We now consider the possible application of these effects to explain the overall deviation of curve 1 from curve 2 in Figure 120. From Reference 3, Figure 22, we take steady flow heat transfer data in air at Re = 64,600, and replot it (Figure 122) in the form of local Nusselt number (Nu) divided by Nusselt number at $x/D = 25$ (where the flow is presumably thermally fully developed) versus distance from the entrance to the heated section in diameters. (The flow is hydrodynamically fully developed upstream of the heated section). The points corresponding to the location of the chambers in the present author's apparatus in diameters is shown in the scale at the bottom of Figure 122. Taking the data of Reference 3, as roughly typical of that under steady-flow conditions in the present author's apparatus, despite the difference in Re values ($\sim$ 65,000 versus $\sim$ 100,000), we see that the Nusselt number is within about 10% of its final value at $x/D = 5$, and within about 4% of its final value at $x/D = 10$.

Thus, it seems very likely that the inner part of the thermal boundary layer, say, $y < .1$ in, containing almost all of its thermal resistance (see Figure 113) is nearly fully developed at $x/D = 10$ or even at $x/D = 5$. Then, since both the previously advanced possible mechanisms by which development of the thermal boundary layer could affect the fractional heat transfer deviations at similar points in the node-antinode pattern depend upon substantial differences in the shape of the temperature profiles for $y < .1$ in, these effects should be quite small more than $\sim$ 5 diameters downstream of the entrance to the heated section. Thus, it appears likely that these effects are incapable of explaining the overall deviation of

Figure 122

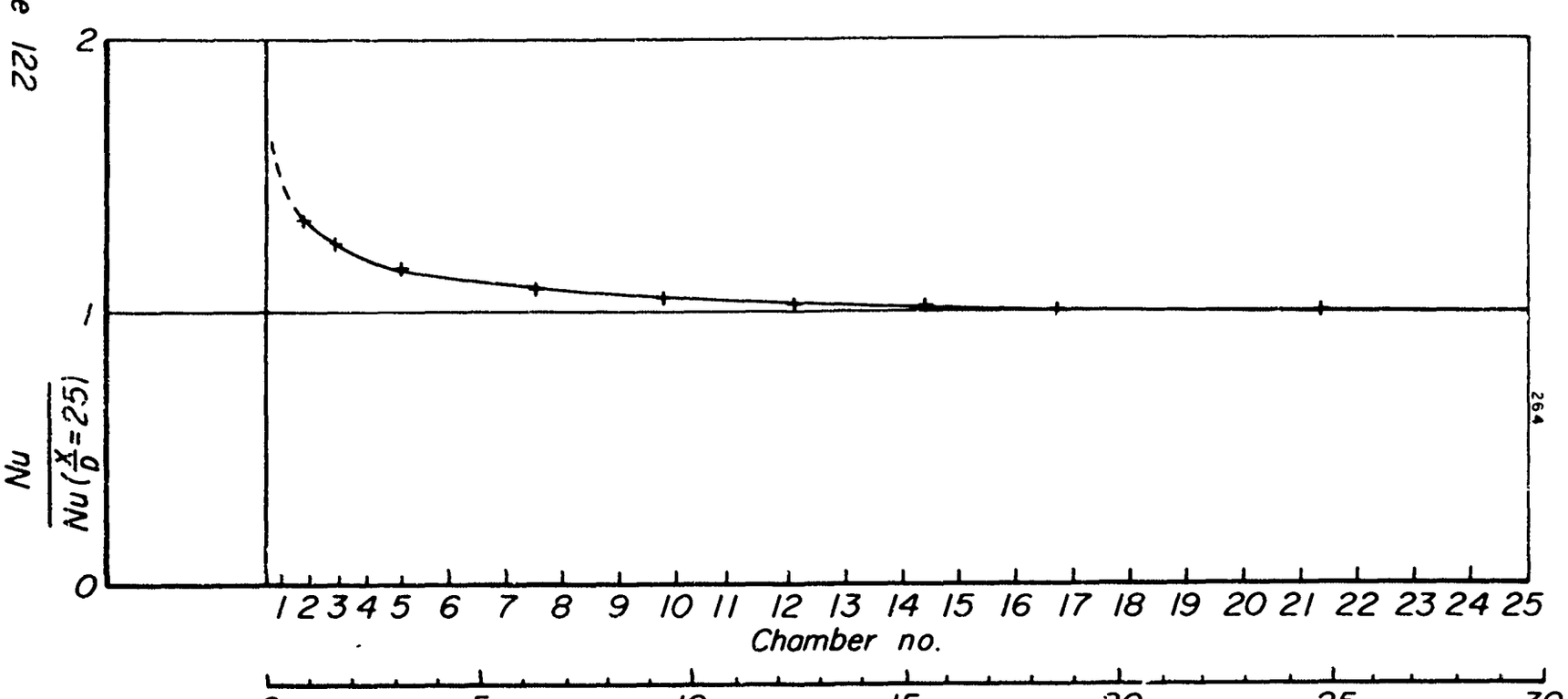

264

JP 17 R 4057 67

curve (1) from curve (2) in Figure 120. Hence, no satisfactory explanation can be found for the gradual decrease of the unsteady heat transfer data with respect to the steady flow data generally observed in Figure 36-43 as one moves downstream. This apparent characteristic of heat transfer under oscillating conditions should be further investigated.

We now discuss the second feature of the heat transfer data of Figures 36-43 listed at the beginning of this section - the additional increase in heat transfer with respect to the steady flow values and with respect to the values $\lambda/2$ further downstream observed for the first three chambers. [This is in addition to feature (1) discussed at the beginning of this section]. In this region, referring to Figure 122, we note that the Nu values are considerably different than the thermally fully developed values, and hence also are the temperature profiles near the wall. Hence, both the mechanisms discussed on pp. 261-263, might contribute to the effect now being discussed. [Because the description of this effect is so long, we hereafter refer to it as 'effect No. 2', the description of which is given at the beginning of this section, and more briefly at the beginning of this paragraph.] We now refer to Figure 38 and 39, where 'effect No. 2' is sufficient to make the heat transfer deviations positive for the first 3 chambers, while the deviations are negative $\lambda/2$ further downstream. The mechanism discussed on pp. 262,263, by means of which the steeper temperature gradient close to the wall nearer the beginning of the thermal boundary layer may cause additional 'abnormal' turbulence generation, may be of especial importance for these cases since, if $K_t(\text{unsteady})/K_t(\text{steady})$ were $\leq$ 1 near the wall as is implied at the locations $\lambda/2$ downstream of chambers 1 - 3 by the data there obtained, the effect discussed on pp. 261, 262, which is not dependent on any change of fluid or turbulence properties near the beginning of the thermal boundary layer, could not produce any additional heat transfer increases at that location.

Finally, we point out that the 'effects directly due to the time-varying velocity profiles' discussed in Section 1, pp. 12-18, may contribute to 'effect No. 2' discussed above. In Section 1, we pointed that these effects should disappear beyond a distance $\hat{x} = \hat{U}/\omega$ downstream from the

entrance to the heated section. Since the chambers of interest are quite close to a velocity antinode, we shall compute $\hat{x}$ as $\hat{U}_A/\omega$. Taking $\hat{U}_A/\bar{U}$ data from Figures 36-43, a typical $\bar{U}$ value as 34.0 ft/sec, and the 9th harmonic frequency as $\omega = 2\pi \times 270$ rad/sec, we compute $\hat{x}$ values as shown in Table 27. Since chambers 1 and 2 are each 1 in. long, these effects appear likely to be mainly limited to chamber No. 1, with perhaps some effect in chamber No. 2 at the larger amplitudes.

This 'effect No. 2' observed in the first three chambers should also be further investigated, to ascertain which, if any, of the above-mentioned phenomena are important in its production and to see if any other phenomena are involved.

TABLE 27

Run No.	$\hat{U}_A/\bar{U}$	$\hat{x}$
-	-	in.
23	.435	.296
22	.770	.525
17	1.159	.789
26	1.430	.974
21	1.560	1.063
18	1.691	1.152
16	2.31	1.574
27	1.929	1.315

5.5 Correlation of Heat Transfer Data

For the case of heat transfer in pipe flow with superimposed standing-wave oscillations, in the situation described in Section 1, we found that the Nusselt number distribution along the pipe [$\hat{Nu} = \hat{Nu}\left(\frac{x}{D}\right)$] was given as follows.

$$\hat{Nu} = \hat{Nu}\left(\frac{x}{D}\right) = f\left(M,\ Re,\ T_w/T,\ S,\ \hat{U}_A/\tilde{U},\ x_A/D\right) \qquad (7)$$

On pp. 1 - 7, we observed that likely T_w/T may be dropped from Eqn. (7) when the variations of the fluid properties throughout the flow field and the effects of viscous dissipation are unimportant. We shall make this approximation here, although as discussed in Section 5.4, pp. 262,263, the fluid density variation through the boundary layer (which depends on T_w/T) may have some effect on the generation of 'abnormal' turbulence. In Equation (7), the dependence of the flow upon x, the distance downstream of the entrance to the heated section, and x_A, the distance of a velocity antinode downstream of the entrance to the heated section is due to thermal development of the boundary layer. If the boundary layer is fully thermally developed downstream of a certain point, in that region Nu should no longer depend on $\frac{x}{D}$ and x_A/D separately but only upon $\frac{x - x_A}{D}$, i.e., the distance of the point of interest downstream of a velocity antinode. Under these conditions, Eqn. (7) may be replaced by

$$\hat{Nu} = \hat{Nu}\left(\frac{x - x_A}{D}\right) = f\ (M,\ Re,\ S,\ \hat{U}_A/\tilde{U}) \qquad (108)$$

- for fully developed flow, when T_w/T may be dropped as a parameter.

We now discuss the importance of the parameters of Eqn. 108. $\hat{U}_A/\tilde{U}$ represents the magnitude of the oscillation velocity as compared to the mean flow velocity and from typical heat transfer data seems to be the most important parameter as is to be expected.

We next present arguments which support the selection of a certain function of S and Re as the most important parameter (after $\hat{U}_A/\tilde{U}$) with which to correlate heat transfer data. We begin by examining

some aspects of fully developed steady pipe flow.

Let $\bar{U}$ = mean flow velocity in pipe

U_m = centre-line velocity in pipe

U_τ = skin friction velocity defined by

$$\tau_w = \rho U_\tau^2 \tag{109}$$

From Section 5.1, we have Eqn. (71) as follows.

$$\tau_w = \frac{1}{8}\lambda\rho\bar{U}^2 \tag{71}$$

In Eqn. (71), λ is the friction factor given as a function of Re in Reference 28, p. 504.

From Eqns. (109) and (71), we have

$$\frac{\bar{U}}{U_\tau} = \sqrt{\frac{8}{\lambda}} \tag{110}$$

In Reference (25), p. 155, a graph of $\bar{U}/U_m$ is given as a function of Re. Hence, we can prepare the following table of U_m/U_τ as a function of Re.

TABLE 28

Re	U_m/U_τ
10^4	20.3
3×10^4	22.5
10^5	25.7
3×10^5	28.0
10^6	30.7

In Reference 32, p. 12, steady flow flat plate boundary layer profiles are presented as plots of U/U_τ versus yU_τ/ν for various

values of Re_δ (Reynolds number based on the boundary layer thickness). To proceed with the discussion, we make the approximation of assuming that these profiles are also applicable to fully developed pipe flow with $Re = 2\ Re_\delta$. Examining the data of Reference 32, we see that at $Re = 10^4$ ($Re_\delta = 5 \times 10^3$) the velocity profile begins to deviate from the universal velocity profile at $U/U_\tau \approx 14$. For higher Re values, the deviation takes place at larger U/U_τ values. Also, we note that at $Re = 10^4$, the above-mentioned deviation starts at $yU_\tau/\nu \approx 45$, whereas the edge of the boundary layer (corresponding to the center of the pipe) is at $yU_\tau/\nu \approx 230$. Hence, for the region $U/U_\tau < 14$, we are within .1D of the wall and the geometry difference between the flat plate and the pipe should not be serious. Since, for $Re > 10^4$ the yU_τ/ν values at the edge of the boundary layer ($\sim$ center of the pipe) are higher than for $Re = 10^4$, in these cases, the region $U/U_\tau < 14$ will be closer to the wall, and the geometry difference mentioned above should be still smaller. From the above discussion, it appears that throughout the Reynolds number range of Table 28, $10^4 < Re < 10^6$, the flow regions $U/U_\tau < 14$ should be similar. The scale lengths and scale velocities for these similar regions are, of course ν/U_τ and U_τ. Now, we restrict ourselves to gas flows, so that $Pr \approx 1$. Hence, if there was a fully developed thermal boundary layer in the flow (the temperature differences are presumed not to affect the properties of the fluid sufficiently to significantly affect the velocity field of the flow), the temperature profile would be similar in shape to the velocity profile. Thus, the fractional thermal resistance of a region between the wall and a certain y - position would be roughly given by U/U_m at that point. Hence, using the data of Table 28 we see that the similar regions of the flow mentioned above ($U/U_\tau < 14$) include about $14/20.3 = .69$ of the thermal resistence at $Re = 10^4$, and $14/30.7 = .46$ of the thermal resistance at $Re = 10^5$. Thus, the similar region, often containing more than half the thermal resistance of the flow, is very important in determining heat transfer. As will be

shown later, it appears that, under oscillating conditions, the interaction of the oscillation and the similar region of the flow, is largely dependent upon a certain function of Re and S, which will be used to attempt correlation of various heat transfer data. Before discussing this, we show some reasons why other combinations of the parameters $\hat{U}_A/\bar{U}$, S, Re and M are important. We refer to Figure 122A.

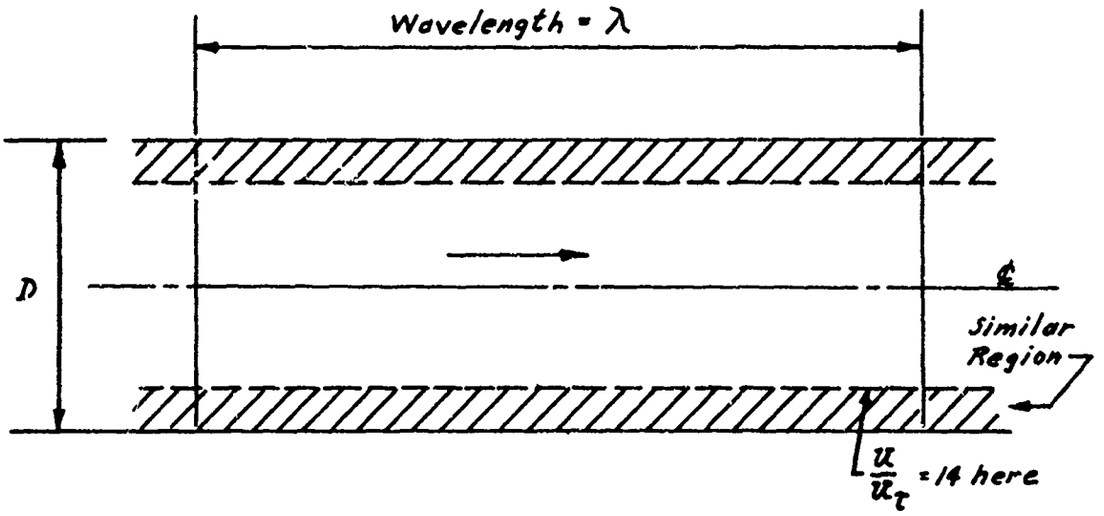

FIGURE 122A

Even if the effect of the oscillation on the similar region of the flow is completely determined, from the previous discussion we see that a substantial part of the thermal resistance of the flow occurs for $U/U_\tau > 14$, and hence this region also carries considerable weight in determining the heat transfer. Clearly, a factor bearing on the relative importance of the two regions $U/U_\tau < 14$, and $14 < U/U_\tau < U_m/U_\tau$ is the fractional thermal resistance of the former region, which may be estimated as above as $\approx 14U_\tau/U_m$. As discussed earlier, this is a function of Re only; Thus this indicates one reason for the importance of the parameter Re alone. However, from Table 28, we notice that the change of $14U_\tau/U_m$

is only $\sim$ 50% while Re changes by a factor of 100; hence the effect of Re alone through $14U_\tau/U_m$ appears to be fairly weak. However, other effects of Re alone may be more important. We now discuss reasons for the importance of the Mach number, M. At the beginning of Section 5.2, we point out that the laminar channel flow analysis of Reference 1 indicates that the acoustic streaming velocities normalized with respect to the time mean velocity in the channel depend only upon $(\hat{U}_A/\bar{U})^2 M$ except for the regions of the very thin wall vortices. From this indication, if acoustic streaming takes place in the actual flow situation (turbulent pipe flow) one would expect M to be an important parameter. Even if acoustic streaming is not a important mechanism, M still cannot be neglected, since it partially determines the ratio of wave length (λ) to pipe diameter as shown in Eqn. (111).

$$\frac{\lambda}{D} = \frac{2\pi c}{\omega}\,\frac{1}{D} = 2\pi\,\frac{c}{\bar{U}}\,\frac{\bar{U}}{\omega D} = \frac{2\pi}{M S} \tag{111}$$

Further, from p.269, we see that the edge of the similar region of the flow occurs at $yU_\tau/\nu \approx 45$. Let us designate the y-coordinate at this point as y_s. Thus

$$y_s = 45\,\frac{\nu}{U_\tau} \tag{112}$$

Now, the ratio of y_s to D is given by

$$\frac{y_s}{D} = \frac{45\nu}{U_\tau D} = 45\sqrt{8}\,\frac{1}{\sqrt{\lambda_1(\mathrm{Re})}\,\mathrm{Re}}, \tag{113}$$

which is obtained using Eqn. 110 (replacing the friction factor λ in Eqn. 110 by λ_1 to here distinguish it from λ, the wavelength of the oscillation). Hence, we have

$$\frac{\lambda}{y_s} = \frac{2\pi}{45\sqrt{8}}\,\frac{\sqrt{\lambda_1(\mathrm{Re})}\,\mathrm{Re}}{MS}\,. \tag{114}$$

Thus M partially determines λ/y_s as well as λ/D. One reason for

the importance of λ/D (and λ/y_s; for the rest of this paragraph, everywhere λ/D is written λ/y_s could also be read, except where numerical values are given for λ/D) is as follows. For very large λ/D values (say $\lambda/D \approx 1000$ or more) one would expect the 'abnormal' turbulence to come into 'equilibrium' with the local oscillating flow field. In other words, if λ/D is long enough, the 'abnormal' turbulence should be dependent (ignoring heat transfer effects, see Section 5.4 pp.262,263) upon the local $\hat{U}/\bar{U}$ value instead of upon $\hat{U}_A/\bar{U}$ and the position of the point of interest with respect to the node-antinode pattern. However, for decreasing λ/D values the 'abnormal' turbulence at a given point should tend to be progressively further out of 'equilibrium' with the relevant local oscillating flow field.

From the discussion of the $-\rho_t/P_x$ profiles presented in Section 5.3, it can be seen that for the case of the present author's experimental work with $\lambda/D \approx 30$, considerable evidence of 'non-equilibrium' between the 'abnormal' turbulence and the oscillating flow field at that point is present.

Finally, we present the arguments as to why the certain function of Re and S referred to earlier should, under oscillating conditions, largely control the interaction between the similar region of the flow and the oscillation. First, under oscillating conditions, we compare the length scale of the regions of the time-mean boundary layer which would be similar under steady flow conditions as approximated by that of these regions under steady flow conditions, $y' = \frac{\nu}{U_\tau} = \frac{y_s}{14}$, with the length scale of the time-varying boundary layer, approximated using the laminar flow analysis of p. 56 as $\delta_A = \sqrt{\frac{2\nu}{\omega}}$. Thus

$$\frac{\delta_A}{y'} = \sqrt{\frac{2\nu}{\omega}} \quad \frac{U_\tau}{\nu} \tag{115}$$

Reproducing Eqn. 110, we have

$$\frac{\bar{U}}{U_\tau} = \sqrt{\frac{8}{\lambda}} \tag{110}$$

Combining Equations (115) and (110), we have:-

$$\frac{\delta_A}{y'} = \frac{1}{2}\sqrt{\frac{\lambda(Re)\,Re}{S}} = \frac{1}{2\sqrt{\zeta}} \qquad (116)$$

Now, we compare the frequency scales of the time-mean and time-varying boundary layers in an exactly analogous way to that of the length comparison done above. The frequency scale of the 'similar' (the word similar, used in quotation marks here, indicates the regions that would be similar in the reference steady flow) regions of the time-mean boundary layer is

$$\omega_s = \frac{U_\tau}{y'} = \frac{U_\tau^2}{\nu} \qquad (117)$$

The frequency scale of the time varying boundary layer is ω . Comparing ω_s and ω, we get

$$\frac{\omega}{\omega_s} = \frac{\omega\nu}{U_\tau^2} = \frac{\omega\nu}{\bar{U}^2}\,\frac{8}{\lambda} = \frac{\omega D}{\bar{U}}\,\frac{\nu}{\bar{U}D}\,\frac{8}{\lambda} = \frac{8S}{Re\,\lambda(Re)} = 8\zeta \quad , \qquad (118)$$

using Equation (110). Hence, we see that the location of the regions of high A.C. shear (represented by δ_A) with respect to the turbulence structure of the 'similar' regions of the time-mean boundary layer (represented by y') is determined by ζ (Eqn. 116). Also, the value of the oscillation frequency as compared to the turbulence frequencies in the 'similar' region of the boundary layer is likewise determined by ζ (Eqn. 118). Thus, it appears that ζ should be a very important parameter in determining the effect of oscillations on heat transfer in the flow. Therefore, we shall tentatively regard $\zeta = \zeta(S, Re)$ as the most important parameter (after $\hat{U}_A/\bar{U}$) in the succeeding correlation attemps, and Re and M as less important.

We now briefly review factors that may affect the flow system, but which were eliminated in the simplifying assumptions that lead to Eqn. 108. First, at the beginning of this section, we discussed the elimination

of T_w/T as a parameter affecting Nu. Also, at that point, we assumed that the flow was fully developed thermally, thus eliminating the independent parameters $\frac{x}{D}$ and $\frac{x_A}{D}$ affecting Nu and introducing instead only $\frac{x-x_A}{D}$. Including again, these two additional parameters in the equation for $\hat{Nu}$ would return us to Eqn. (7), see beginning of this section. Even for Eqn. (7), derived in Section 1, the assumptions listed on p. 1 are made, and differences (1)-(6), pp. 7,8, of the actual flow situation from that assumed in the derivation of Eqn. (7) must be borne in mind. We refer again to these points affecting the validity of Eqn. (108) in succeeding paragraphs where correlation of certain experimental data is attempted.

We now attempt correlation of heat transfer data of several sources with the parameter $\hat{U}_A/\bar{U}$ and the parameters $\hat{U}_A/\bar{U}$ and f. The first set of data used is that obtained from the references of the work done by T. W. Jackson et.al. at the Georgia Institute of Technology, which were discussed in Section 2, pp. 42-56. We refer to Table 10, p. 43. All data there listed is used in the correlation except for that taken at $Re \approx 2000$. As discussed on p. 49, the data at $Re \approx 2000$ likely involves free convection effects which may greatly complicate the effect of the oscillations on the flow. Hence, this data is not used in the correlation attempts. We now examine the points affecting the validity of Equation (108) discussed at the end of the preceding paragraph, and judge to what extent the data in question corresponds to the model leading to Equation (108). These are only two significant points of difference of the actual experimental situation from this model. The first is the fact that the data of References 22 and 23 is taken with the flow beginning both hydrodynamic and thermal development at the entrance to the heated section. (The data of Reference 3 is taken with hydrodynamically developed flow at the entrance to the heated section as in the model). Secondly, all the heat transfer data used in the correlation was taken between distances of 11 and 31 diameters downstream of the entrance to the heated section so that the flow is there not thermally fully developed as is required for strict application of Eqn. (108). To proceed with the correlation attempt we make the assumption that the data of References 22, 23 and

3, roughly represents that of fully hydrodynamically and thermally developed flow. We have some support for this assumption as follows. The unsteady flow data of References 22 and 23 divided by the relevant steady flow data seems to repeat itself at $\lambda/2$ intervals fairly well beyond a distance of ~ 13 diameters from the entrance of the heated section. The data is typified by that of Figures 20 and 21 taken from References 22 and 23 representively.

We now describe the elements of the heat transfer data used in the correlation attempt, referring to Figure 123 taken from Figure 21. All data are taken at the 'maxima' 3Λ and 4Λ and the 'minima' $3V$ (Figure 123). These 'extrema' are obtained by finding the points at which a line parallel to the steady flow curve at a given x-coordinate is tangent to the oscillating flow curve at that same x-coordinate. The z-values are steady flow Nusselt numbers subtracted from the corresponding unsteady flow Nusselt numbers. Hence all the z-values in Figure 123 are negative as indicated. $\overline{Nu}$ is an average steady flow Nusselt number in the x-coordinate range of interest. The y-values are either the distance of a 'maxima' downstream of the indicated node of the distance of 'minima' downstream of the indicated antinode. Thus all y-values in Figure 123 are also negative as shown in Figure 123, since the 'extrema' are there upstream of the reference points. We define the 'level' (L), 'amplitude' (A), and 'phase' (ϕ) of the unsteady flow heat transfer data as:

$$L = \frac{\frac{z_{3\Lambda} + z_{4\Lambda}}{2} + z_{3V}}{2\,\overline{Nu}} \tag{115}$$

$$A = \frac{\frac{z_{3\Lambda} + z_{4\Lambda}}{2} - z_{3V}}{\overline{Nu}} \tag{116}$$

$$\phi = \frac{y_{3\Lambda} + y_{3V} + y_{4\Lambda}}{3\left(\frac{\lambda}{4}\right)} \tag{117}$$

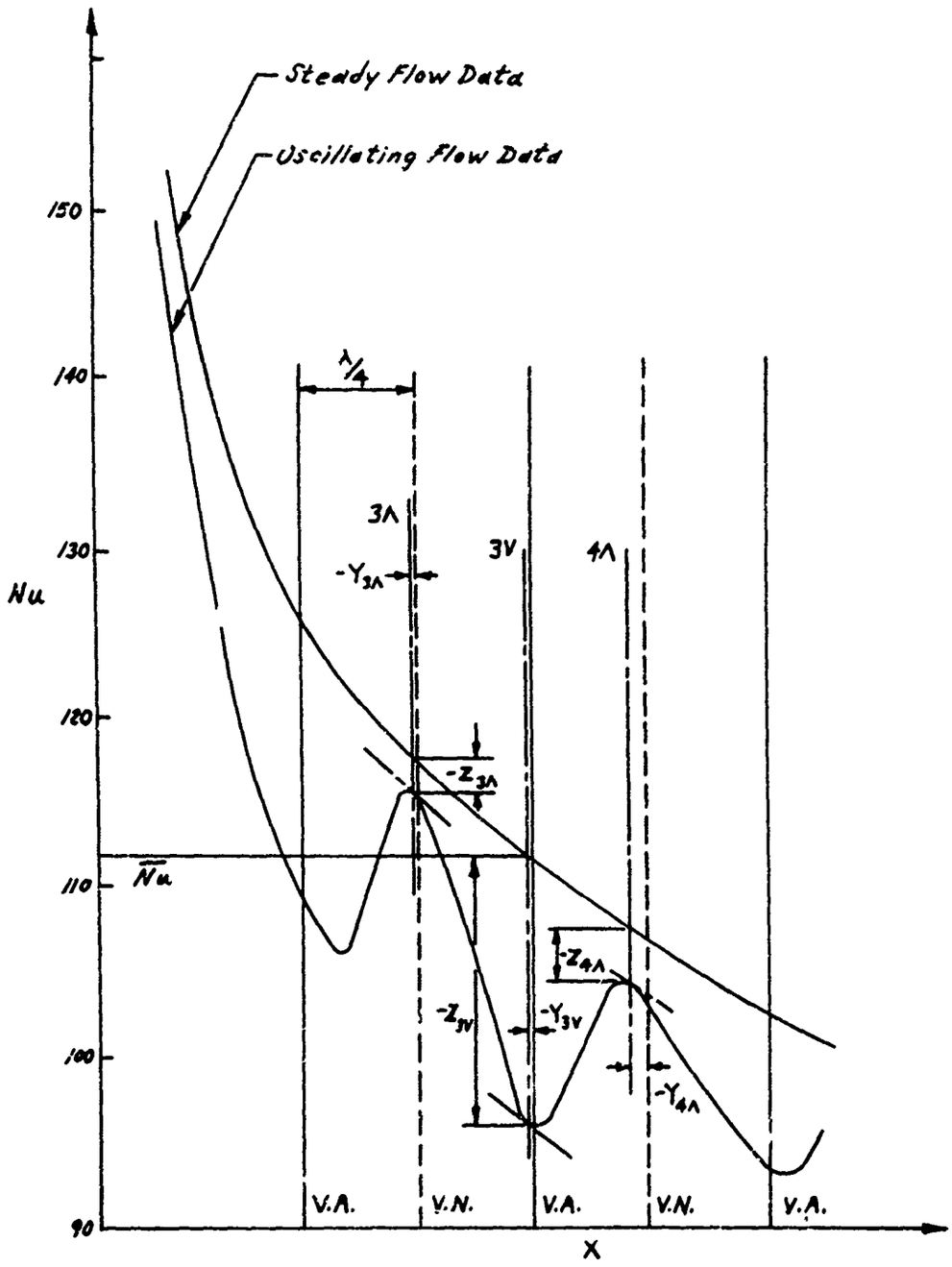
Steady Flow Data
Oscillating Flow Data
150
140
130
120
110
100
90
Nu
$\bar{Nu}$
λ/4
3Λ
3V
4Λ
$-Y_{3\Lambda}$
$-Z_{3\Lambda}$
$-Z_{4\Lambda}$
$-Z_{3V}$
$-Y_{3V}$
$-Y_{4\Lambda}$
V.A.
V.N.
V.A.
V.N.
V.A.
X

FIGURE 123

Thus L represents roughly the overall fractional heat transfer deviation of the oscillating flow data. A represents the fractional amplitude of the oscillations of the oscillating flow data, and ϕ locates the 'extrema' of these oscillations, $\phi = 0$ corresponding to the 'maxima' being located at the velocity nodes, and the 'minima' being located at the velocity antinodes, and $\phi = 1$ corresponding to the reversed situation. We note that the 'extrema' used in Figure 123 to compute A, L, and ϕ are not always the ones so used; in some cases two 'minima' and one 'maxima' are used, and in the data of Reference 3 (See Figure 22, taken from this reference), because of the large value of λ , only one 'minima' and one 'maxima' are used. In these cases, the equations used for calculation L, A, and ϕ would be slightly different than Equations 115, 116 and 117 respectively.

The second set of data used in the correlation attempt is the heat transfer data of the present author, Figures 36-43. Again, we examine the data in question to see to what extent it corresponds to the model leading to the correlation Eqn. (108). The heat transfer data used in the correlation was taken between distances of 7 and 30 diameters downstream of the entrance to the heated section. There is only one significant point of difference of the actual experimental situation from that of the model of Eqn. (108). This is the fact that the flow is not thermally fully developed throughout the region where the correlation heat transfer data was taken, as is required for strict application of Eqn. (108). Again, to proceed with the correlation, we make the assumption that the data of the present author roughly represents that under fully developed flow conditions. This should not be too bad an assumption, since on entering the heated section, the flow is already hydrodynamically fully developed, and hence, thermal development in the heated section will proceed much more rapidly than if hydrodynamic development also started at the entrance to the heated section. However, the discussion of Section 5.4 suggests that some thermal development may still be taking place throughout the heated section. Hence, the assumption made above must be borne in mind in the succeeding correlation attempts. The parameters L, A, and ϕ for the present author's data are calculated from equations completely analogous to Equations 115, 116 and 117 presented previously.

The data of Reference 31 could have also been included in these correlations, if Reynolds number and time-average pressure data corresponding to the given heat transfer data were presented in the paper (see Section 2, pp.60-62). Since this data was not given, the heat transfer data of Reference 31 could not be included in the present correlation.

The variables L, A and ϕ for the heat transfer data of References 22, 23 and 3 and the present author are plotted versus $\hat{U}_A/\bar{U}$ in Figures 124, 125 and 126 and versus $\hat{U}_A/\bar{U}$ and $\int$ in Figures 127, 128, and 129. For the moment, we ignore the point marked (▽) in Figure 127.

The curves labeled Q-S in Figures 124, 125 and 126 are calculated on a quasi-steady basis as follows. The unsteady flow Nusselt number (Nu) divided by the steady flow value (Nu_0) at every point in the node-antinode system is assumed to be related to the local value of $\hat{U}/\bar{U}$ as presented in the second part of the quasi-steady discussion of Section 1 (pp.20-22). To form the parameters L, A and ϕ under these assumptions we examine Nu/Nu_0 at a velocity node and at a velocity antinode. Under the quasi-steady assumption Nu/Nu_0 at a velocity node is always 1. Nu/Nu_0 at a velocity antinode would merely be the value read off Figure 14 for the relevant abscissa value ($\hat{U}_A/\bar{U}$). We estimate L, A and ϕ as follows (subscript A denotes values at a velocity antinode).

$$L = \frac{\left(\frac{Nu}{Nu_0}\right)_A + 1}{2} \tag{119}$$

$$A = \left| \left(\frac{Nu}{Nu_0}\right)_A - 1 \right| \tag{120}$$

$$\begin{aligned} \phi &= 1 \quad , \left(\frac{Nu}{Nu_0}\right)_A > 1 \\ &= 0 \quad , \left(\frac{Nu}{Nu_0}\right)_A < 1 \end{aligned} \tag{121}$$

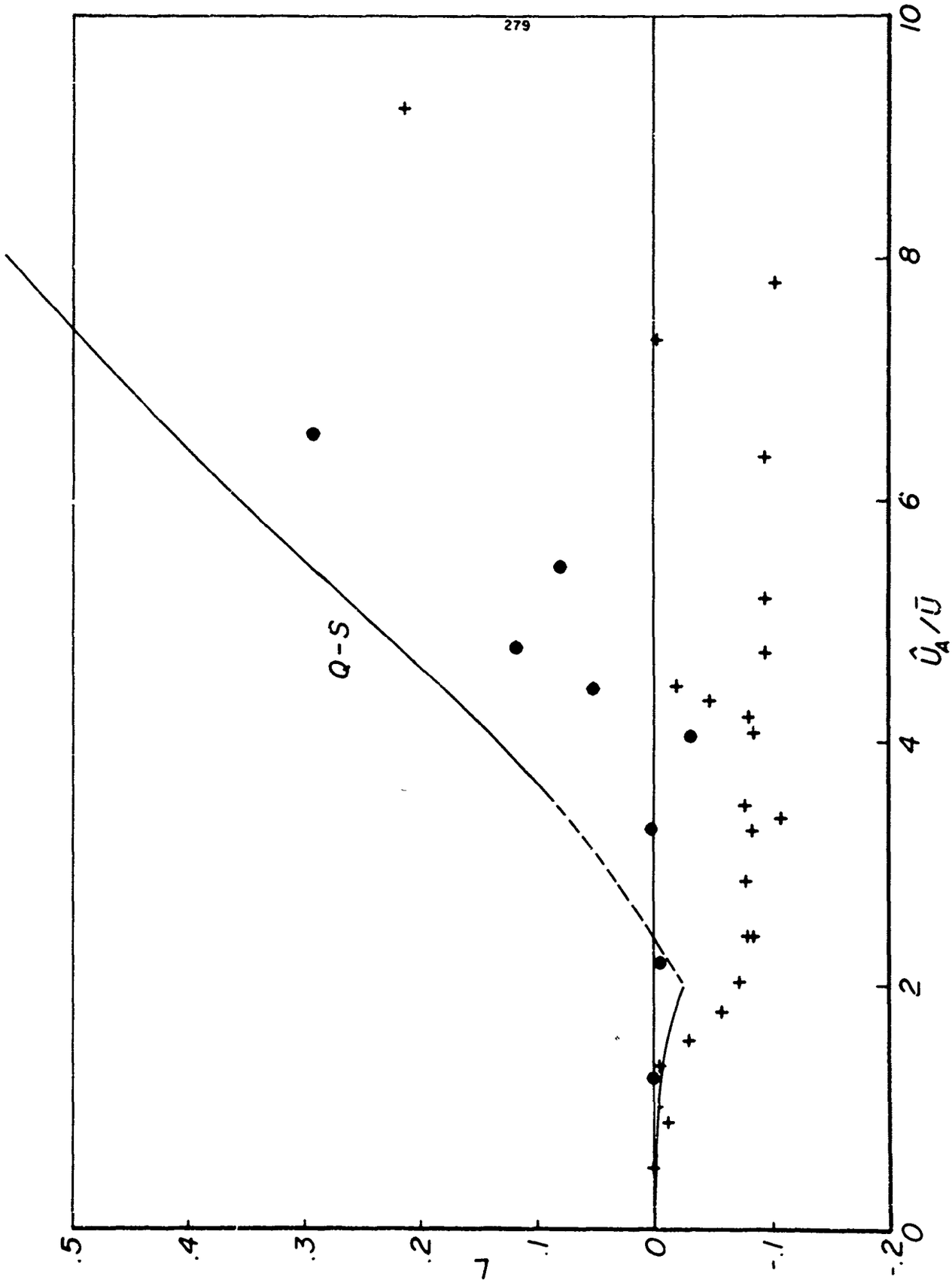

Figure 124

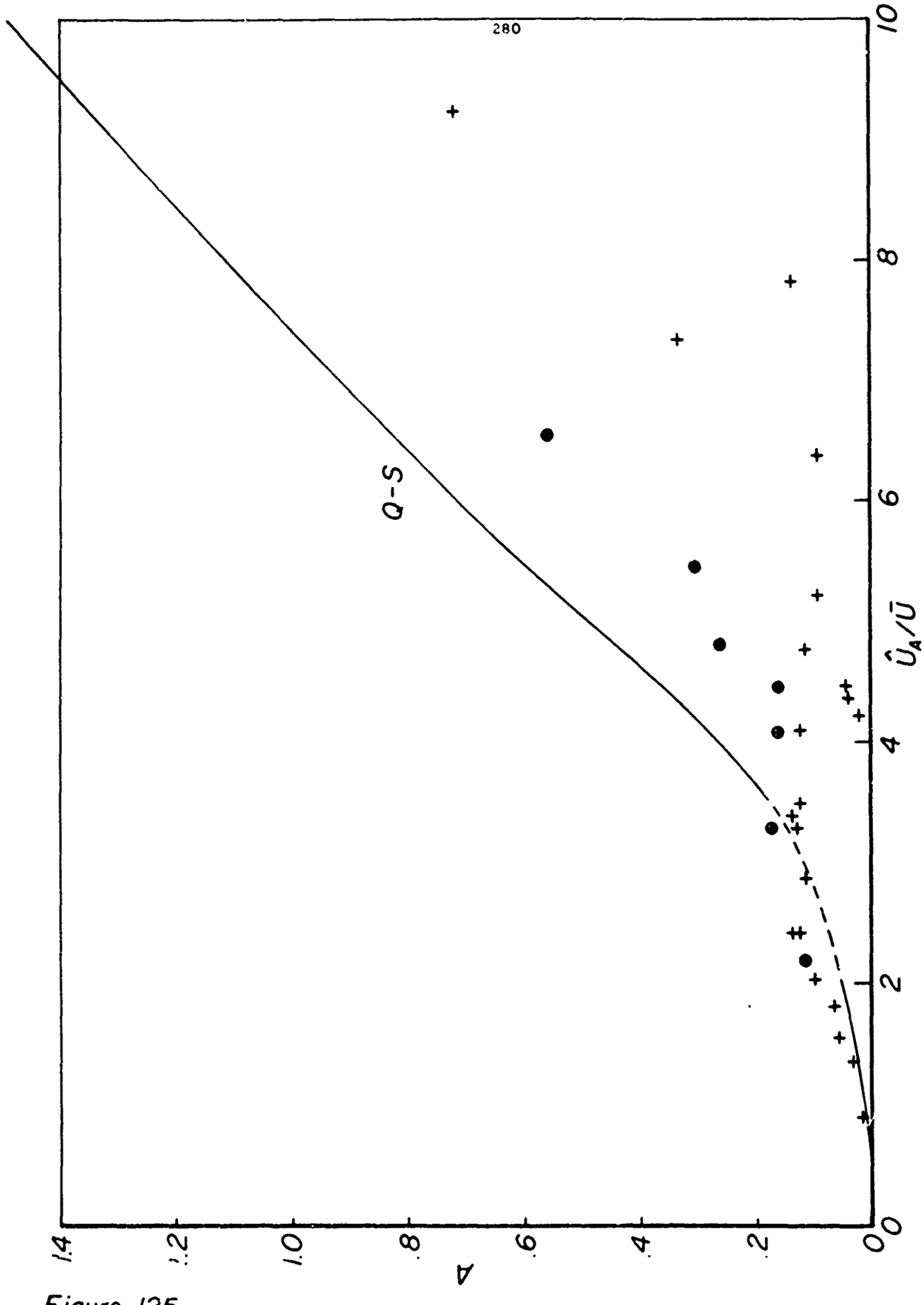

Figure 125

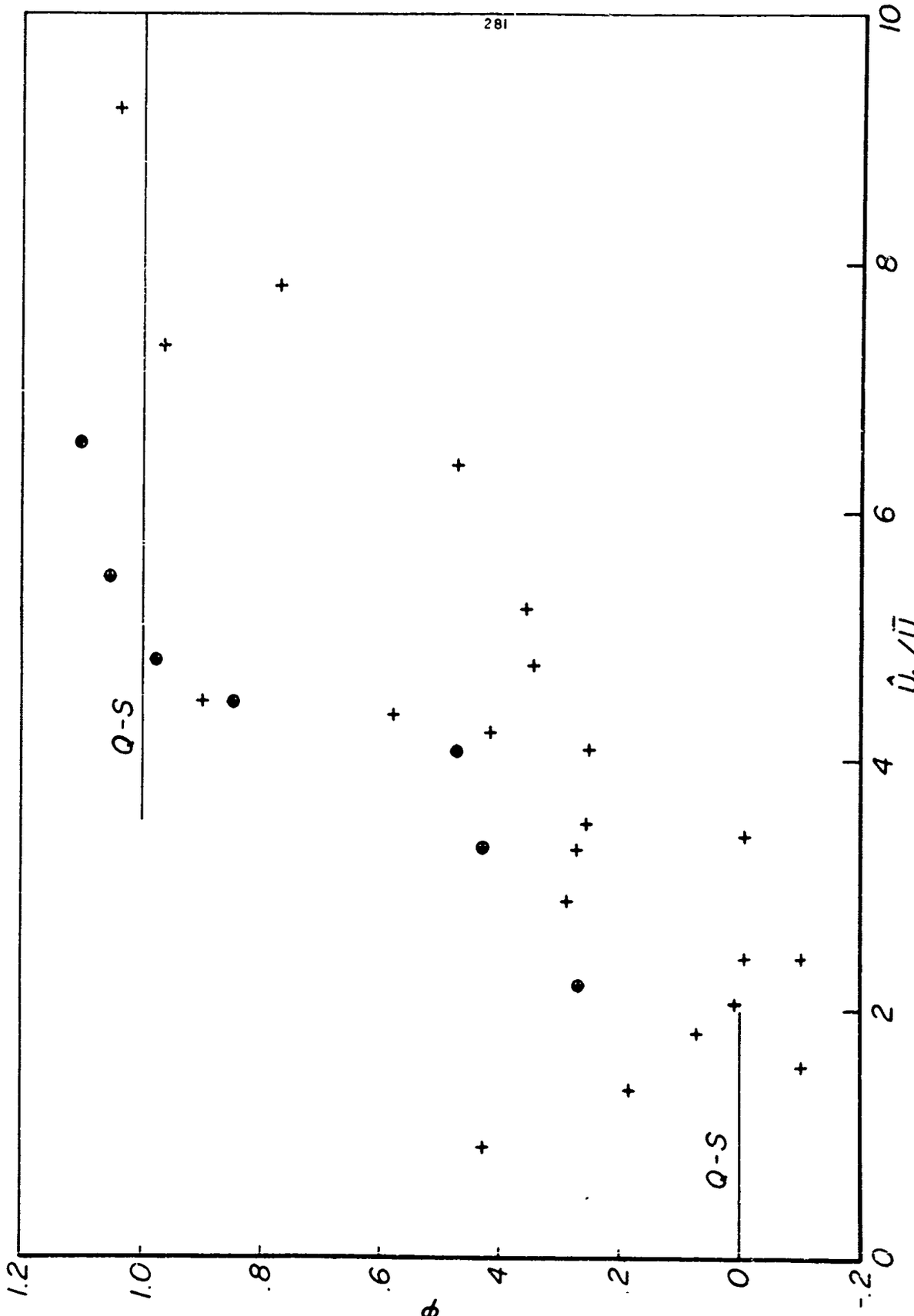

Figure 126

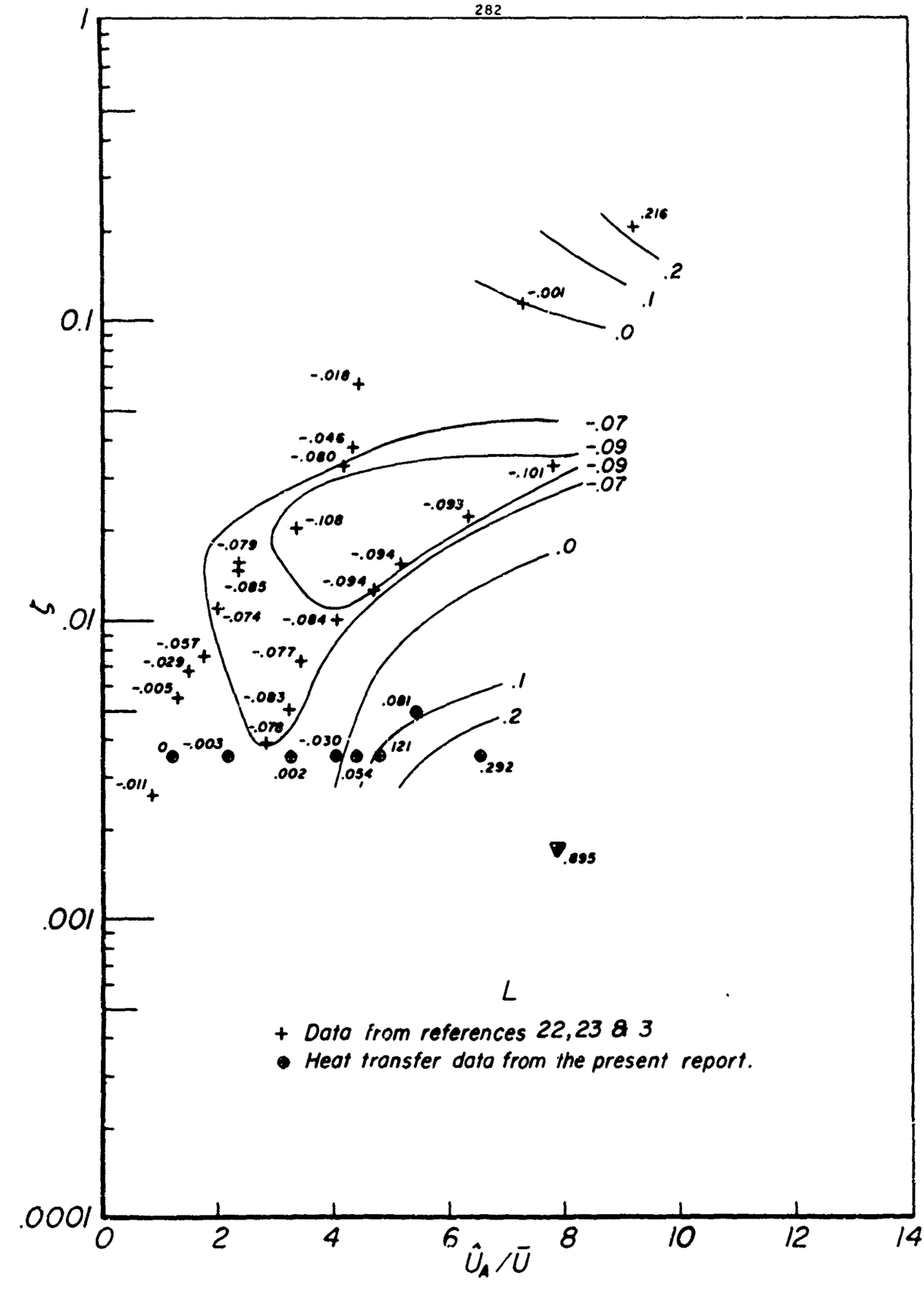
1
0.1
.01
.001
.0001
ζ
0
2
4
6
8
10
12
14
$\hat{U}_A/\bar{U}$
.216
.2
.1
.0
-.001
-.018
-.046
-.080
-.07
-.09
-.09
-.07
-.101
-.093
-.108
-.079
-.094
-.085
-.094
-.074
-.084
.0
-.057
-.029
-.005
-.077
-.083
-.078
.081
.1
.2
0
-.003
-.030
.121
.002
.054
.292
-.011
.695
L
+ Data from references 22,23 & 3
● Heat transfer data from the present report.

Figure 127

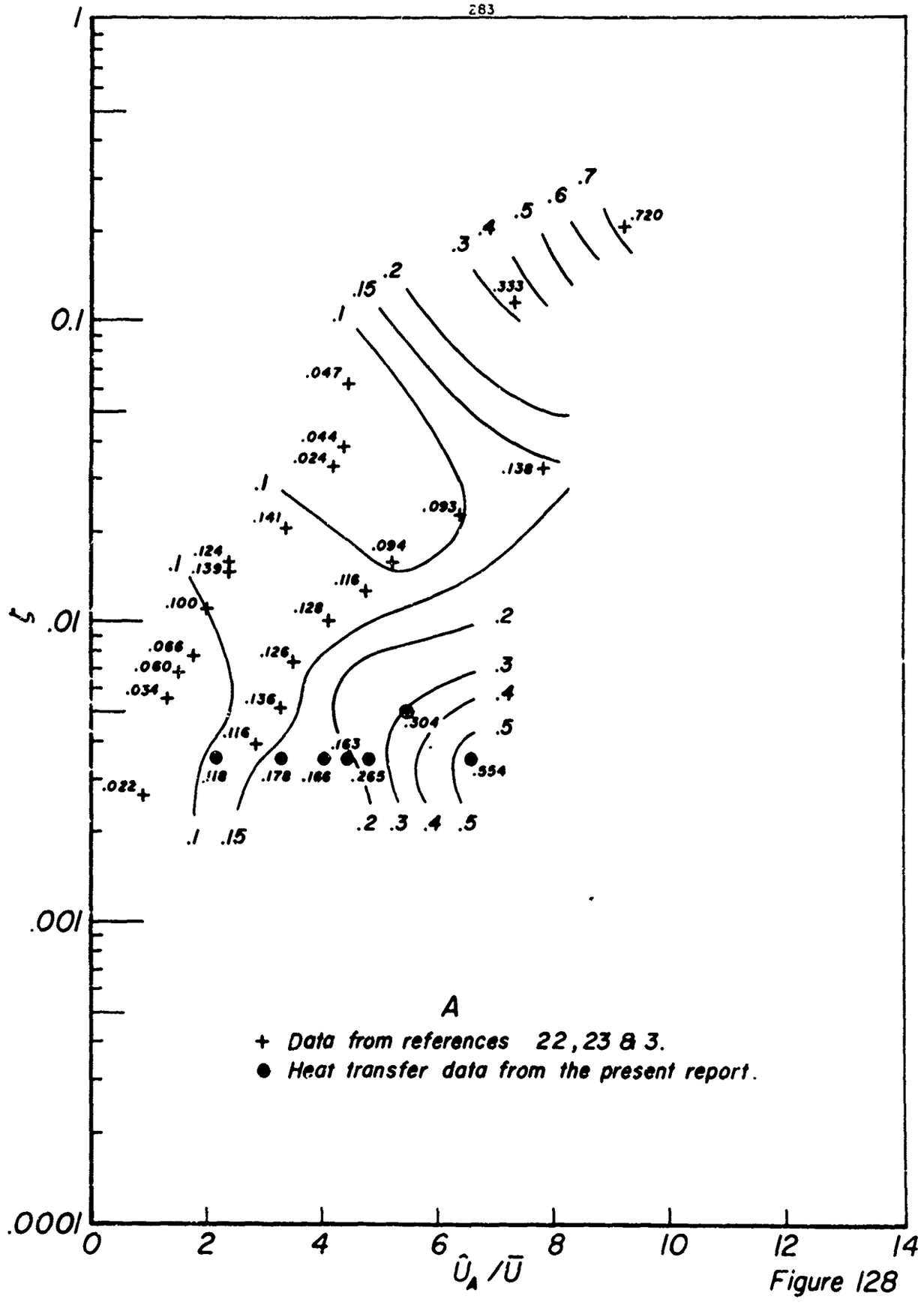
1
0.1
.01
.001
.0001
ζ
0
2
4
6
8
10
12
14
$\hat{U}_A/\bar{U}$
.7
.6
.5
.4
.3
.2
.15
.1
.720
.333
.047
.044
.024
.138
.093
.141
.094
.124
.139
.116
.100
.128
.066
.060
.034
.126
.136
.116
.304
.163
.554
.118
.178
.166
.265
.022
A
+ Data from references 22, 23 & 3.
● Heat transfer data from the present report.

Figure 128

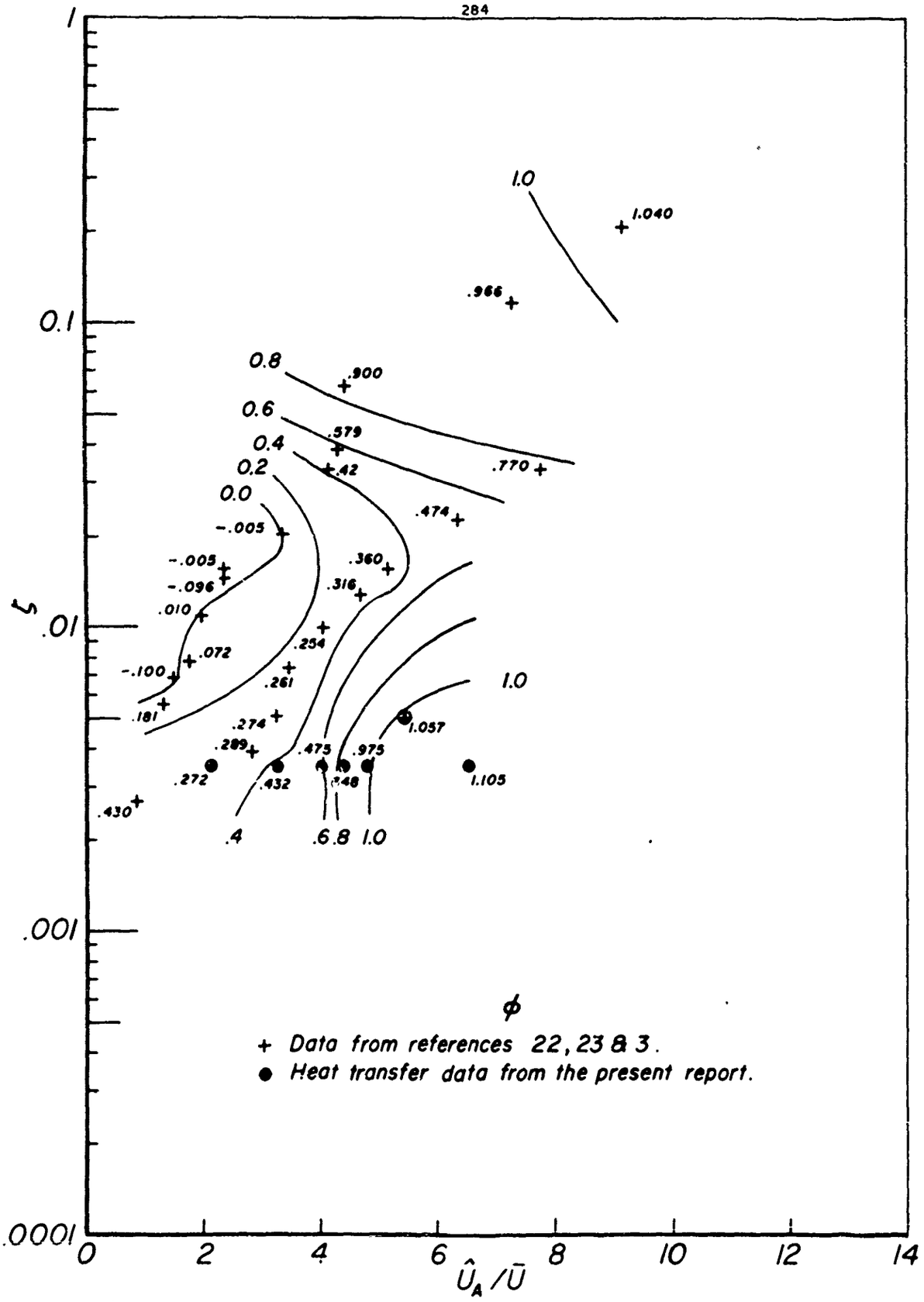

Figure 129

Now, when $2 < \hat{U}_A/\bar{U} <\sim 3.5$, the values of Nu/Nu_0 predicted by the quasi-steady calculation present a complicated picture, as roughly sketched below.

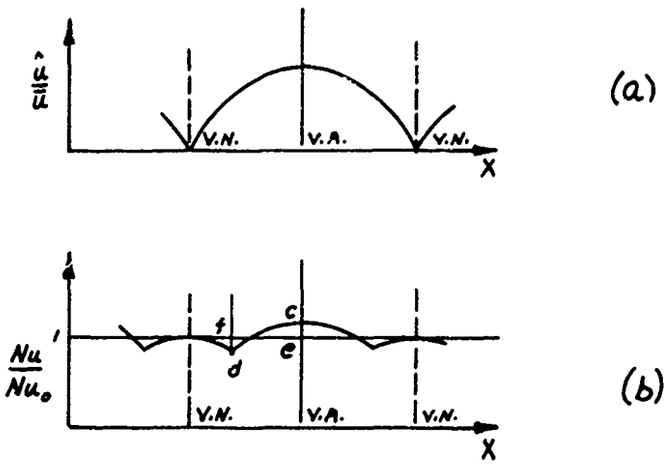

FIGURE 130

In this case, L, A and ϕ as calculated in Equations 118, 119, and 120 have a meaning which corresponds poorly with the meaning of L, A, and ϕ calculated from the experimental data. When $\hat{U}_A/\bar{U} > 3.5$, the Nu/Nu_0 values predicted by the quasi-steady calculation still look qualitatively as sketched in Figure 130(b) but now the distance ce is more than 3 times the distance fd and the point f is much closer to the V.N. line, so that the meaning of L, A and ϕ calculated from Equations 118, 119 120, again corresponds closely to that calculated from the experimental data. Then, for $\hat{U}_A/\bar{U} < 2$ and $\hat{U}_A/\bar{U} > 3.5$, we can use Equations 118, 119 and 120 to approximately predict L, A and ϕ on the basis of the quasi-steady calculation. Because of the aspects of the quasi-steady calculation discussed above, the sections of the Q-S curve in Figures 124 and 125 for $\hat{U}_A/\bar{U} < 2$ and $\hat{U}_A/\bar{U} > 3.5$ are shown joined by a dotted curve indicating

the uncertain meaning of the quasi-steady predictions in this area, and for Figure 126, the Q-S curve is omitted completely for $2 < \hat{U}_A/\bar{U} < 3.5$.

We now discuss the L, A and ϕ data of Figures 124-129. From Figures 124-126, that is, the plots of L, A and ϕ versus $\hat{U}_A/\bar{U}$ we see immediately that L, A and ϕ cannot, even in the crudest approximation, be regarded as a function of $\hat{U}_A/\bar{U}$ along. We now refer to Figures 127-129, which plot L, A and ϕ as functions of $\hat{U}_A/\bar{U}$ and ζ . At first glance, especially in view of the contours which we have plotted on Figures 127-129, it appears that these figures offer considerable evidence that L, A, and ϕ may be regarded as mainly dependent on $\hat{U}_A/\bar{U}$ and ζ . However, this is not the case as discussed below. First, we note that the data of References 22, 23 and 3 falls roughly along two lines; the upper (lower) of these lines corresponds to data taken at a frequency of $\sim$ 220(90) cps. From the discussion of Section 2, pp.49,50, it can be seen that as we move along either of these lines S changes, and also $Re \propto \frac{1}{S}$ and $M \propto \frac{1}{S}$. Hence, the variations in L, A and ϕ that occur as we move along one of these lines could quite possibly be due to Re and M effects as well as to ζ (and $\hat{U}_A/\bar{U}$, of course) effects. Thus, in order to establish whether L, A, and ϕ were even approximately dependent on $\hat{U}_A/\bar{U}$ and ζ only, we would require much more data than that given in Figure 127-129, and in particular, we would require large amounts of data at similar values of $\hat{U}_A/\bar{U}$ and ζ but widely varying values of Re and M in order to allow one to attempt to show that the effect of the latter parameters on L, A and ϕ was relatively small.

We now discuss which of the effects of the oscillation on the flow mentioned in Section 1, pp. 10-19, are likely responsible for the variations in L, A and ϕ shown in Figures 124-129. On the basis of the discussion of Section 5.1, it appears very likely that visious dissipation is quite unimportant in the regime of the data of Figures 124-129. Also, as pointed out in Section 1, p. 15 , the 'effects directly due to the time-varying velocity profiles' should rapidly disappear beyond a distance $\hat{x} = \hat{U}/\omega$ downstream of the entrance to the heated section. It may

readily be shown that the heat transfer data used in the correlations was taken at much further downstream from the entrance to the heated section than $\hat{x}$. Hence, these effects also should produce unimportant contributions to the L, A, and ϕ variations shown in Figures 124-129. Thus, the remaining mechanisms presented in Section 1, pp. 10-19, by means of which the oscillation can likely produce contributions to the L, A and ϕ variations of interest are:

(1) Acoustic streaming

(2) Variation in the turbulence exchange properties of the fluid due to the imposed oscillations.

We are mainly interested here in tentatively applying the data of Figures 124-129 to examine some aspects of the effects on turbulence of the oscillations [effect (2) listed above]. Therefore, we ask the following questions. Is acoustic streaming likely to be a factor in any of the data presented in Figures 124-129 and if so, what is its effect? We discuss these questions with reference to the acoustic streaming discussion of Section 5.2. In that section, we discussed the possible importance of acoustic streaming in explaining the heat transfer deviations observed for the data of References 22 and 23 corresponding to the points ($\hat{U}_A/\bar{U} \approx 9.2$, $\zeta \approx .2$) and $\hat{U}_A/\bar{U} \approx 7.3$, $\zeta \approx .11$) in Figures 127-129 and the data of the present paper corresponding to the poin.. ($\hat{U}_A/\bar{U} \approx 6.5$, $\zeta \approx .0035$). For the latter case, it appeared likely that acoustic streaming was unimportant. For the former two cases, the evidence was controversial and uncertain, some of it tending to support the idea that acoustic streaming was here important. As stated in Section 5.2, the heat transfer data obtained from References 22, 23 and 3, except for the two cases mentioned above, shows little resemblence in form to that predicted by the acoustic streaming theory. On the basis of this fact and the tentative conclusions reached with respect to the data point ($\hat{U}_A/\bar{U} \approx 6.5$, $\zeta \approx .0035$) in Section 5.2, we tentatively assume that acoustic streaming effects are unimportant in Figures 127-129, except possibly for the two points at the highest ζ values.

We now examine briefly, the effects on heat transfer which would occur, if acoustic streaming effects were important, and superimposed on

other effects in a certain piece of heat transfer data. The effect of acoustic streaming on L, A and ϕ is indicated by examining the form of the heat transfer deviations produced by streaming as predicted by the theoretical laminar flow analysis of Reference 3. (See Section 2, pp. 51-56, and Fig. 25). Examining Figure 25, we see, that a first approximation, acoustic streaming should not affect L. A could be either raised or lowered by the presence of streaming effects depending on their phasing with respect to any other effects present. The presence of streaming effects would always tend to shift ϕ towards the value that would occur if only streaming effects were present. From Figure 25, this value would be about $\phi = 1.3$.

We now make some comparisons of the L, A and ϕ data of Figures 124-129 with those predicted using the quasi-steady analysis (which predictions are the Q-S lines shown on Figures 124-126). As discussed on p. 273 , ζ gives a rough measurement of the ratio of the oscillation frequency to the turbulence frequencies in the 'similar' portion of the boundary layer. Hence, it would appear that ζ should be the most important factor in determining the degree to which a given flow approaches the quasi-steady state as described in Section 1, pp. 20-22. The other factors $\hat{U}_A/\bar{U}$, Re and M very likely also affect the above-mentioned degree of approach to the quasi-steady state, but less strongly than ζ . Accordingly, we should examine the plots of Figures 127-129, select those data points with the lowest values of ζ , replot the L, A and ϕ values of these data points versus $\hat{U}_A/\bar{U}$ and compare the latter plots with the quasi-steady curves. This would isolate the data most likely to approach the quasi-steady state. Examining Figures 127-129, we see that, by pure accident, the 9th harmonic data of the present paper is approximately, the data of lowest ζ value as mentioned above. Hence, to compare the lowest ζ value data of L, A and ϕ with the quasi-steady values, we merely have to refer to Figures 124-126, restricting ourselves to the data from the present report, excepting the 13th harmonic data point at $\hat{U}_A/\bar{U} \approx 5.4$. Examining the relevant data in Figures 124-126, we see that there is quite a strong tendency for this data to approach the quasi-steady curve. On the other hand, the data at higher ζ values shows much poorer agreement with the Q-S curve. The fact that the low ζ data tends to approach the quasi-steady curves for the cases of <u>all three variables</u> L, A and ϕ,

suggests to the author, that for these experimental conditions, some regions of the flow are in truth approaching quasi-steady conditions to some extent. Referring to Section 5.3, and in particular to the $-\mu_t/P_x$ profiles there (Figures 105-108 and 110), the attendent discussion and also the discussion correlating the $-\mu_t/P_x$ and heat transfer data, seems to indicate that the region of flow most likely to be approaching the quasi-steady situation to some degree would be that for $o < y < .015$ in, which, being adjacent to the wall, should, of course, have the shortest response time. This region also apparently includes the main region of 'abnormal' turbulence generation. While this is a very restricted region of the flow, referring to the thermal resistance plot of Figure 113, we see that this region includes $\sim .60$ of the thermal resistance of the flow and hence, could quite conceivably account for the approach of the relevant L, A and ϕ data in Figure 124-126 to the quasi-steady curves. We now refer to the power spectrum data of Figure 115. Here, we see that in the central regions of the flow, the energy of the r-component of turbulence is mainly in a band centered at about twice the oscillation frequency, and hence, one would certainly not expect the flow in these regions to be quasi-steady. However, from Figure 115, we see that at $y=.054$ in the center of the band containing the r-component of turbulence energy has shifted to about 10 times the oscillation frequency, and presumably for $o < y < .015$ in., the band of turbulence energy would shift to still higher frequencies. Thus, it appears that in the region $o<y<.015$ in., the band containing the r-component of turbulence energy may be centered at as high as 20-30 times the oscillation frequency, and it is turbulence in this frequency range that the author suggests may approach the quasi-steady state to some degree and thus be responsible for the behaviour of the L, A and ϕ data as discussed above.

We now discuss some possible reasons for the sharp fall off of the L and A values for $\hat{U}_A/\bar{U} > 4$ and $.0035 < \zeta < .025$ (See Figures 127,128). A possible partial explanation of the effect is as follows. For $\zeta \gtrsim .0035$, the turbulence frequencies in the 'similar' region of the flow ($y^+ < 45$, $o<y< .014$ in. in the case of the present authors apparatus) are sufficiently high, compared to the oscillation frequency, to allow the turbulence there to approach the quasi-steady situation to a significant degree. Hence, the high values of L and A follow from the quasi-steady predictions. On

the other hand for $\zeta \gtrsim .025$, the turbulence frequencies in the 'similar' region may be low enough compared to the oscillation frequency so that the turbulence, as a rough approximation, does not respond to the unsteady shear components, but only to the time-average shear. Another effect, possibly contributing to the fall off of L and A for $\hat{U}_A/\bar{U} > 4$ and $.0035 < \zeta < .025$ is as follows. As ζ increases, not only does the oscillation frequency become higher compared to the turbulence frequencies in the 'similar' region of the flow (Eqn. 118), but the region of high A.C. shear moves closer to the wall as compared to y' (Eqn. 110). Hence, as ζ increases in the range .0035-.025, it is possible that the region of high A.C. shear is tending to become submerged in the 'laminar sub-layer' where its capability for generating 'abnormal' turbulence is likely greatly reduced. Reiterating, the two proposed effects possibly contributing to the fall-off of L and A for $\hat{U}_A/\bar{U} > 4$ and $.0035 < \zeta < .025$ are: (1) that the oscillation frequency is becoming too high for the turbulence to respond to, and (2) that the regions of high A.C. shear are becoming submerged in the 'laminar sub-layer' thus reducing their effectiveness in generating 'abnormal' turbulence. If these two proposed effects are, in fact, present then, for $\zeta \gtrsim .025$, one would expect L and A to decrease to small values, which is what is observed, except for the data points at the two highest values of ζ. As mentioned on p. 287, acoustic streaming may be an important mechanism for these two points. Acoustic streaming effects of sufficient strength could explain the high A values at these two points, but could not explain the high L value at the data point at highest ζ. Thus, if the above suggested explanation for the sharp fall-off of L and A for $\hat{U}_A/\bar{U} > 4$ and $.0035 < \zeta < .025$ is correct, we have no satisfactory explanation for the high L value at the point ($\hat{U}_A/\bar{U} \approx 9.2$, $\zeta \approx .2$).

We now attempt to correlate some of the data of Reference 24, taken in rocket motors, with the plot of L versus $\hat{U}_A/\bar{U}$ and ζ of Figure 127. The data which we attempt to correlate with Figure 127 is that described in Section 2, pp. 56-59. (See Figure 27, taken from Reference 24.) We first note that there are several ways in which the experimental set-up in which this data was taken differs from the model leading to

Eqn. (108); which is the basis of the correlation attempt (see p. 267). The readily apparent significant differences from that model are:

(1) The flow is not hydrodynamically developed at the entrance to the heat-transfer section (in which, in this case, the gas is cooled rather than heated).

(2) The flow is not thermally developed at the point at which the heat-transfer measurements are taken.

(3) $T_w/T \neq 1$.

(4) The center-line fluctuating velocity waveshapes (as a function of time) are not even approximately sinusoidal; rather they are shocks followed by exponential rarefactions.

To proceed with the correlation attempt, we make the approximation that differences (1) and (2) can be circumvented as follows. We refer to Figure 131, which shows the flow situation of interest in the rocket motor and a fully developed pipe flow situation which we shall approximate it by.

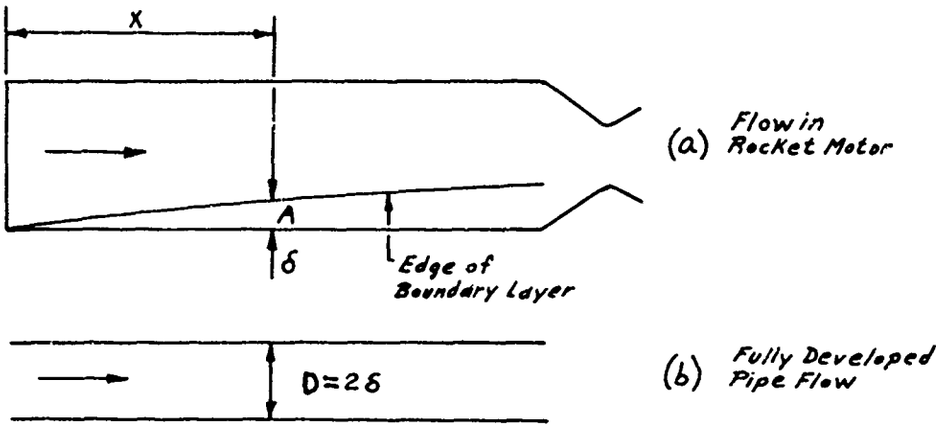

FIGURE 131

We consider heat transfer data taken at point A (corresponding to the data of Figure 27 at a distance of $\sim$ 16 in. from the

injector face) which is essentially located at the velocity antinode of the fundamental longitudinal mode of oscillation of the motor (which is the mode in which the unsteady flow heat transfer data was taken). The boundary layer thickness at this point is estimated roughly using the following formula for a turbulent boundary layer on a flat plate from Reference 28, p. 537.

$$\frac{\delta}{x} = .37\ Re_x^{-.2} \tag{122}$$

We feel that this formula may be used to roughly estimate δ, in spite of the fact that Re_x (computed in a way analogous to Re, p. 56) has the relatively low value of $.835 \times 10^6$, from the following arguments. The flow inside a rocket motor even under non-oscillating conditions is subject to very strong random disturbances. (e.g. peak-to-peak pressures under the conditions leading to the steady flow data of Figure 27 are typically about 5 psi). In the discussion of References 5, 19 and 4 (Section 2, pp. 35-37 and pp. 38-42) evidence from these references is given which shows that oscillations are effective in reducing the transition Reynolds number on a flat plate. In Reference 5, longitudinal oscillations with $\hat{U}/\bar{U} \approx 2.5$ reduced the transition Re_x value from 1.8×10^4 to 0.9×10^4. In Reference 4, longitudinal oscillation with $\hat{U}/\bar{U} = 1.4\text{-}1.8$ reduced the transition Re_x value from 10^5 to 10^4. Hence, the author feels that transition of the boundary layer, even for the steady flow data in the extremely disturbed flow in the rocket motor, likely takes place at $Re_x < 10^5$, and hence, Eq. (122) may be used to give a rough estimate of δ. We assume that the fully developed pipe flow of Figure 131(b), described by the parameters $\hat{U}_A/\bar{U}$ and M relevant to the actual experimental situation, Figure 131(a), and the parameters $S' = \omega D'/\bar{U}$ and $Re' = \rho \bar{U} D'/\mu$ calculated from the values of ρ, μ, $\bar{U}$ and ω relevant to the actual experimental situation and $D' = 2\delta$, is approximated by the actual experimental situation in the region where $\delta \approx \frac{D}{2}$. From Section 2, p. 58, we see that for the actual experimental situation

$$\hat{U}_A/\bar{U} = 7.90$$

$$M = .050$$

$$Re = 161{,}000$$

$$S = 6.0$$

Referring to the previous discussion, and using Eqn. (122), we can easily show that the parameters of the fully developed pipe flow used to approximate the actual flow situation in the region of the antinodal point are

$$Re' = 40,500$$

$$S' = 1.51$$

Taking λ' , the friction factor based on Re', from Reference 28, p. 504, we can compute

$$\zeta' = \frac{S'}{\lambda' Re'} = .001699$$

We now make an estimate of the level, L, from the heat transfer data of Figure 27. Directly from Figure 27, the fractional change in heat transfer at the 'maxima' (see p.275)

$$\frac{5.3 - 1.9}{1.9} = \frac{3.4}{1.9} = 1.790 .$$

From the behaviour of the heat transfer data of Figure 27, we make a very rough estimate of zero as the fractional change in heat transfer at the 'minima' (again see page 275). This estimate is very rough because the δ values at the locations in Figure 27 where data is given near velocity nodes (which is the basis of the above mentioned estimate of zero fractional heat transfer change at the 'minima') are not the same as the δ value used to set up the fully developed pipe flow used to approximate the actual flow situation near the velocity antinode. However, since the data of Figure 27 shows a strong tendency for the fractional change in heat transfer to approach zero in the region of the velocity nodes at δ values both smaller and larger than those used to set up the 'analogous' pipe flow, the above estimate of zero fractional change in heat transfer at the 'minima' in the 'analogous' pipe flow should be satisfactory as a rough approximation. Referring to the discussion of pp. 275-277, we see that the value of L is merely the mean of the fractional changes in heat transfer

at the 'maxima' and 'minima'. Thus, for our case, from the data of Figure 27, we estimate

$$L = \frac{1.790 + 0}{2} = .895 .$$

Thus, the data point from this rocket motor data used to see if the plot of L versus $\hat{U}_A/\bar{U}$ and ζ (Figure 127) obtained from pipe flow data predicts the former with any degree of success is ($\hat{U}_A/\bar{U} = 7.90$, $\zeta = .001699$, $L = .895$) which is the point shown thus (▼) on Figure 127. While this point falls somewhat outside the range of the remaining data of Figure 127, making comparisons more uncertain, it appears likely from the slope of the surface $L = L(\hat{U}_A/\bar{U}, \zeta)$ shown in Figure 127, that the L value of the rocket motor data will fall considerably above the corresponding L values from hypothetical pipe flow data at the same $\hat{U}_A/\bar{U}$ and ζ values. In the author's opinion, the most likely cause for this assumed disagreement is the fact that in the rocket motor the oscillation involves shock waves, whereas for the remaining data of Figure 127, the waves are roughly sinusoidal. In other words, all other things being equal, the author feels that a shock wave will be much more effective in producing 'abnormal' turbulence than a smooth wave (even if not strictly sinusoidal) of the same $\hat{U}_A/\bar{U}$ value. Of course, because of the crudeness of the comparison between the rocket motor data and the pipe flow data of Figure 127, there are many other possible causes for the assumed disagreement of L data, which, however, the author feels are less important than the presence of shock waves in the rocket motor as discussed above. These are listed below.

(1) the fact that $T_w/T \neq 1$ in the rocket motor.

(2) the errors involved in approximating the 'flat plate' flow in the rocket motor by the fully developed pipe as done above.

(3) The differences in Re' and M of the rocket motor data from the Re and M values of the nearest pipe flow data of Figure 127 (note, however, that these differences are not too large; i.e. from pp. 292,293, for the rocket motor data $Re' = 40{,}500$, $M = .050$, and from Figure 42, for the nearest pipe flow data of Figure 127, $Re = 99{,}000$ and $M = .030$).

We now make some recommendations for further heat transfer measurements (both in the apparatus used by the author, and in possible future apparatus). To start the discussion, we list the parameters used in the correlation attempt. These are

$$\hat{U}_A/\bar{U}$$

$$\zeta = \frac{S}{\lambda(Re)\ Re}$$

$$Re$$

$$M$$

The first recommendation (See Figures 127-129) is that the $\hat{U}_A/\bar{U}$ - ζ plane shown in these figures be explored further using the present author's apparatus. Simply by keeping the time-average duct pressure and mass flow roughly constant and using different resonances of the duct (Fundamental, 3rd, 5th, 7th, 9th, 11th ... harmonics) Re and M can be kept nearly constant and the effects of ζ and $\hat{U}_A/\bar{U}$ alone can be studied. At the two lowest resonances, the present steam-heated section is not sufficiently long to cover the distance of $\frac{\lambda}{2}$ needed to completely survey one cycle of repetition of the heat-transfer pattern. At these two resonances one would thus be limited to incomplete heat-transfer data; however, for the 3rd harmonic case, extending the heat-transfer section could allow data to be obtained over a distance of $\frac{\lambda}{2}$. Using the same Re and M values used by the present author, heat transfer data could be obtained over a range of ζ values of .00039 - .064 (the lower limit being the ζ value at the fundemental frequency of the duct, and the upper limit the value at the maximum operating frequency of the siren wheel, 5000 cps - See Section 3.1). Some further extension of the range of ζ could be obtained by altering Re . Also, of course, the effects of Re and M (in each case, with the other 3 parameters kept constant) should be investigated. This can be accomplished readily in the existing apparatus, since the 3 parameters ζ , Re , and M are in our apparatus essentially determined by 3 variables $\bar{p}$, $\bar{U}$ and ω , which can be independently varied. The first two of these variables can

be controlled by using the various available calibrated sonic orifices (See Figure 31) and changing the pressure on the upstream side of these orifices, and by changing the size of the opening at the variable area nozzle. ω can be varied, of course, by selecting different resoncances of the duct. This proposed investigation of the effects of ζ, Re, M, in each case with the remaining parameters held constant (for varying $\hat{U}_A/\bar{U}$ values in each case, of course) would confirm or negate the author's earlier proposal, that under the conditions of the model leading to Eqn. (108), the parameters most important in determining the heat transfer variables L, A and ϕ are $\hat{U}_A/\bar{U}$ and ζ.

From the discussion of pp. 290-294, it appears likely that shock waves produce a considerably different effect on the boundary layer with respect to the generation of 'abnormal' turbulence than smooth waves (even if not exactly sinusoidal) of the same peak-to-peak amplitude. Since the present apparatus, using a siren to generate the oscillations, does not produce shock waves, new apparatus would have to be built to investigate their effect. The apparatus might be constructed as sketched on Figure 132 using a piston to generate the oscillations. Reference 33 indicates that shock waves can be generated by a piston oscillating at the end of a closed tube (no time-average through flow). Hence, it appears quite likely that shock waves can be generated using the apparatus sketched in Figure 132.

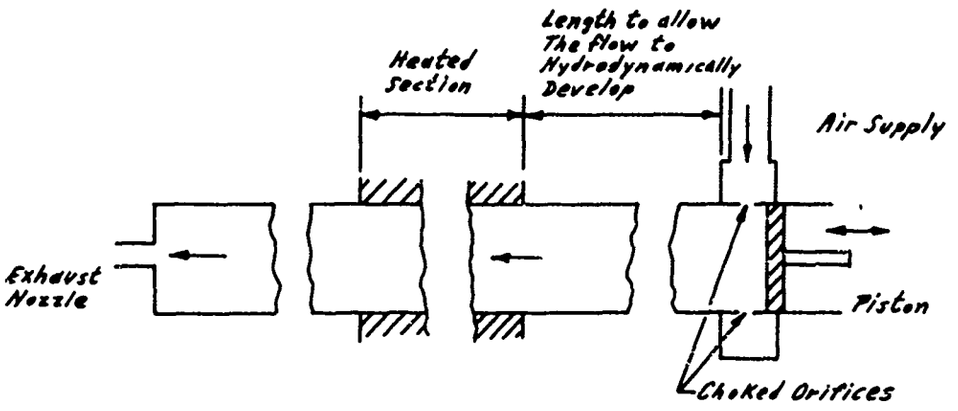

FIGURE 132

5.6 Some Recommendations for Further Work

The recommendations given here are merely those presented at various points in Sections 5.1-5.5; we collect them together in this section, giving section number, page numbers and a very brief description for each recommendation.

Section 5.2, p. 199 , the suggestion that an acoustic streaming analysis be done using eddy plus molecular viscosity instead of molecular viscosity only.

Section 5.3, pp. 250- 257, suggestions for reducing the blockage effect of the hot-wire probe, for making pressure drop measurements in the duct, and for making certain direct measurements of turbulence quantities using the hot-wire anemometer.

Section 5.4, pp. 258 - 266 , in this section we discuss several effects that appeared in the heat transfer data of the present author, and for which explanations are lacking or are merely postulated, and unsupported by additional experimental data. In this case, the suggestion is merely the general one for further investigation of these effects, rather than specific suggestions as given elsewhere in this section.

Section 5.5, pp. 295 - 296 , suggestions are made that the dependence of the heat transfer variables L, A and ϕ upon the parameters $\hat{U}_A/\bar{U}$, ζ, Re and M be further investigated using the author's apparatus, and that the effect of shock waves (as opposed to smooth time variations of pressure and velocity) upon heat transfer in pipe flow be investigated (this would require new apparatus).

5.7 Possible Applications of the Effects of Longitudinal Oscillations Upon Heat Transfer Observed in this Report.

We consider the possibility of the application of oscillations to improve the performance of a heat exchanger with gas flow inside pipes. We define the following quantities:

Δp_o	=	pressure drop in steady flow
Δp	=	pressure drop in oscillating flow
ΔQ_o	=	heat transferred in steady flow
ΔQ	=	heat transferred in oscillating flow

We consider the following possible form for the relation of heat transfer and pressure drop in steady and oscillating pipe flows. (The steady and oscillating flows compared are, of course, identical, except for the presence of oscillations in one case).

$$\frac{\Delta P}{\Delta P_o} = \left(\frac{\Delta Q}{\Delta Q_o}\right)^n \tag{128}$$

We now discuss what value n is liable to take. If the oscillation increases the eddy viscosity and eddy thermal conductivity by the same factor at all points in the flow (i.e., the turbulent Prandtl number is unchanged by the oscillations) since the turbulent and molecular Prandtl numbers are then near unity throughout both the oscillating and reference flows, the fractional increase in heat transfer should be roughly the same as the fractional increase in skin friction. In this case, $n \approx 1$. However, the very uncertain experimental data presented below seems to indicate that n is considerably greater than 1. From the very tentative estimates of pressure drop made in the author's apparatus (Section 5.3, pp. 237- 240), it is seen that with an overall oscillating flow heat transfer coefficient of ~ 1.30 times the steady flow value, the overall pressure drop under similar oscillating flow conditions is estimated as ~ 1.85 times the steady flow value. Hence, in this case n may be estimated from

$$(1.30)^n = 1.85$$
$$n = 2.35.$$

In Reference 9 (Section 2, pp. 24 - 25) heat transfer and pressure drop data in oscillating air flow in a pipe are given (a description of the experiment is given in the quoted pages in Section 2). In Section 2, we pointed out that essentially no data on the amplitude, waveshape, etc. of the oscillation was given in Reference 9; hence that data could not be used in the correlation attempts of Section 5.5. However, to estimate n we need only heat transfer and pressure drop data under the same (partially unknown) oscillation conditions; this data is given in Reference 9. This data was taken at 4 different frequencies in the range 2.5-15 cps and over a Reynolds number range of 7,000-200,000. In Table 28A, we give the M and f values of the flow as functions of Re and f.

TABLE 28A

	freq.(cps)	2.66	4.66	7.17	15
Re	M	f	f	f	f
5,000	.00172	$32.0X10^{-4}$	$56.0X10^{-4}$	$86.0X10^{-4}$	$180.0X10^{-4}$
10,000	.00344	9.54	16.70	25.7	53.6
20,000	.00688	2.84	4.98	7.65	16.0
50,000	.0172	.561	.985	1.514	3.16
100,000	.0344	.164	.287	.441	.924
200,000	.0688	.0462	.0811	.1244	.260

In Figures 134-137, the fractional increases in heat transfer $\left(\frac{Nu-Nu_o}{Nu_o}\right)$ and pressure drop $\left(\frac{\Delta P - \Delta P_o}{\Delta P_o}\right)$ are plotted versus Re (at a different frequency in each of the four figures). In each figure, each pair of points at a given Re value was taken under the same oscillating conditions. Examining these figures, we see wide variations in the relation between the heat-transfer and pressure drop increases. For instance, in Figures 135 and 136, below Re = $3X10^4$, the fractional pressure drop increases are typically 6-8 times

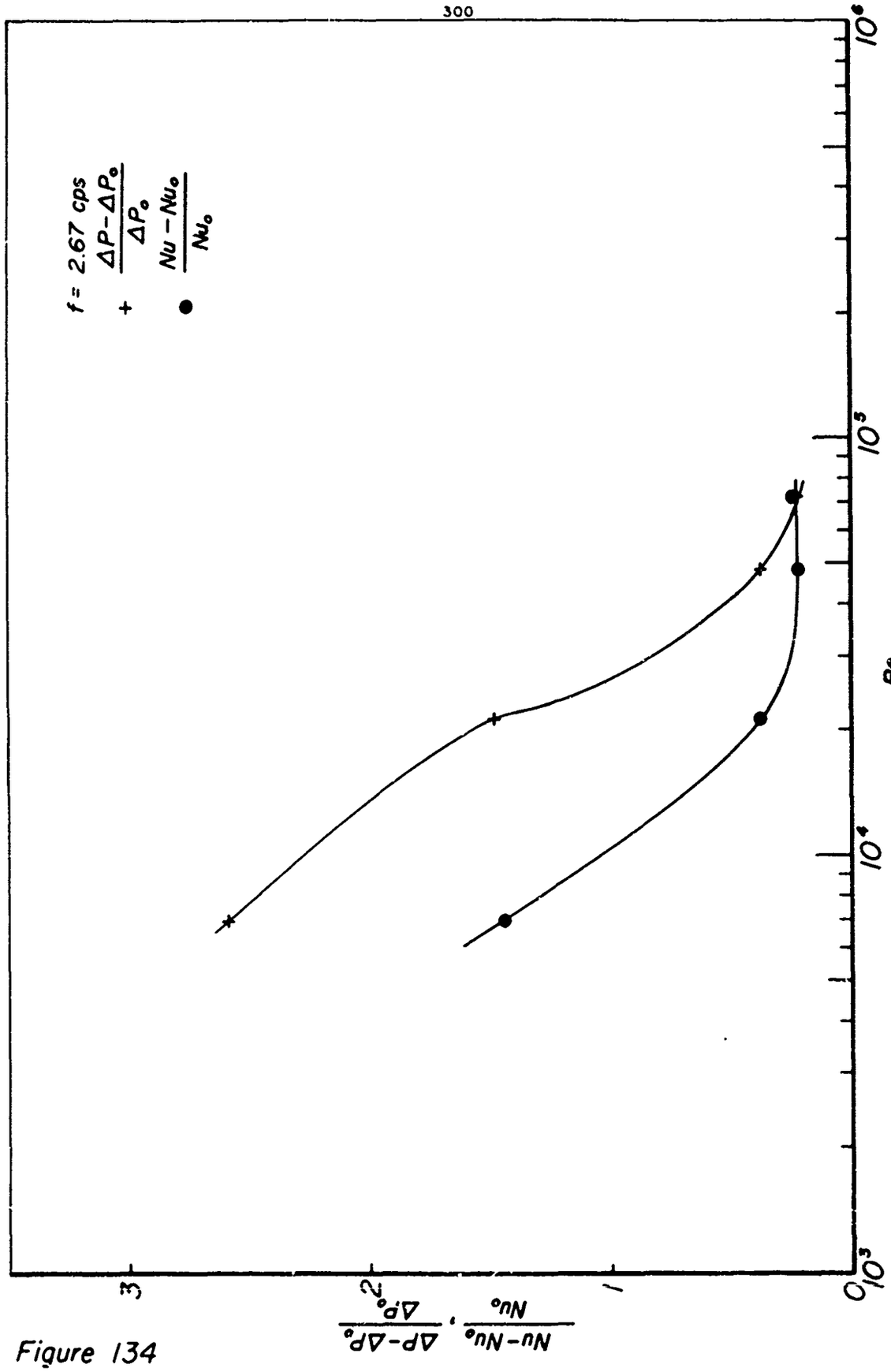
f = 2.67 cps
+ ΔP-ΔP₀ / ΔP₀
● Nu-Nu₀ / Nu₀
10⁶
10⁵
10⁴
10³
Re
3
2
1
0
Nu-Nu₀ / Nu₀ , ΔP-ΔP₀ / ΔP₀

Figure 134

JP ITR 4067 61

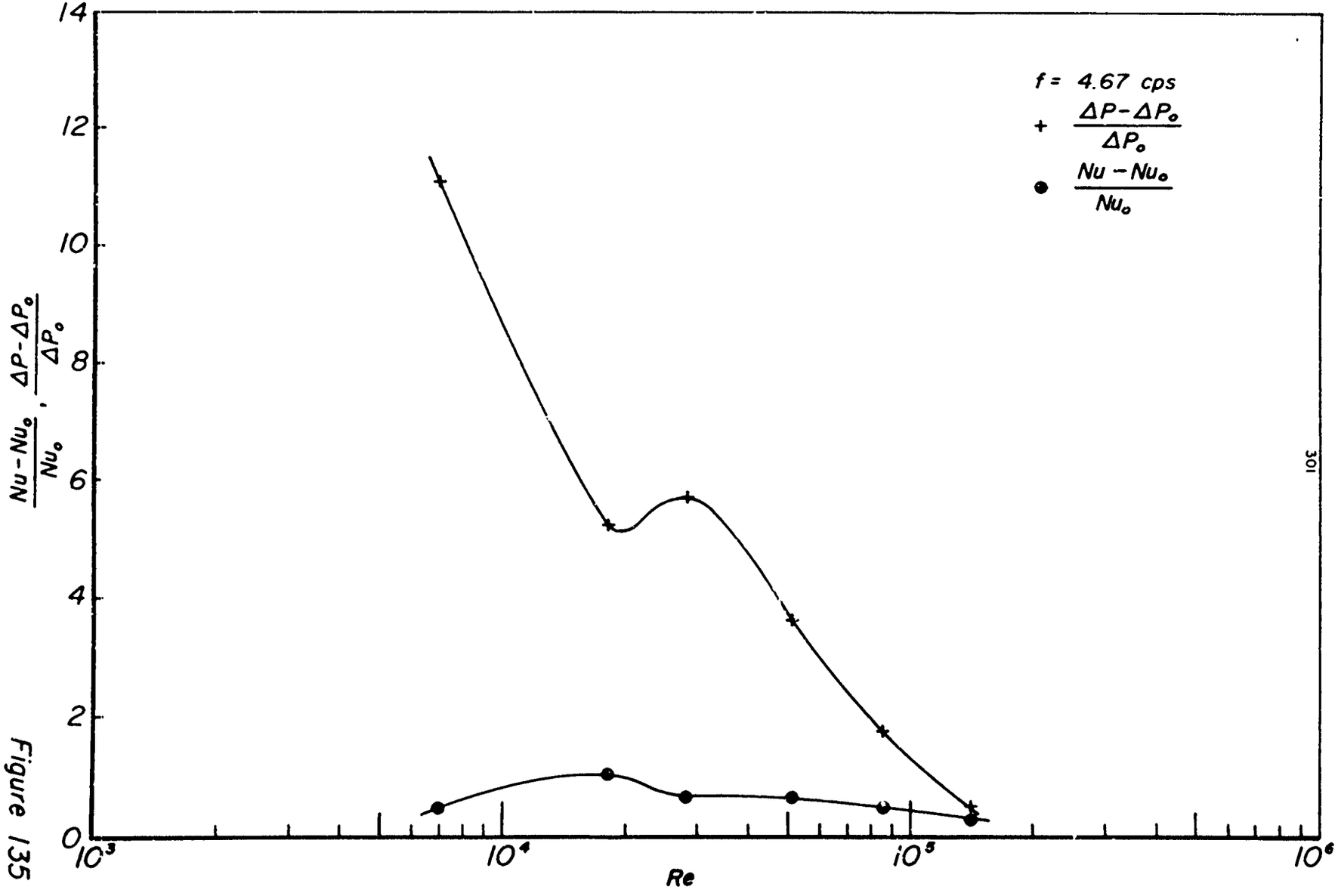

Figure 135

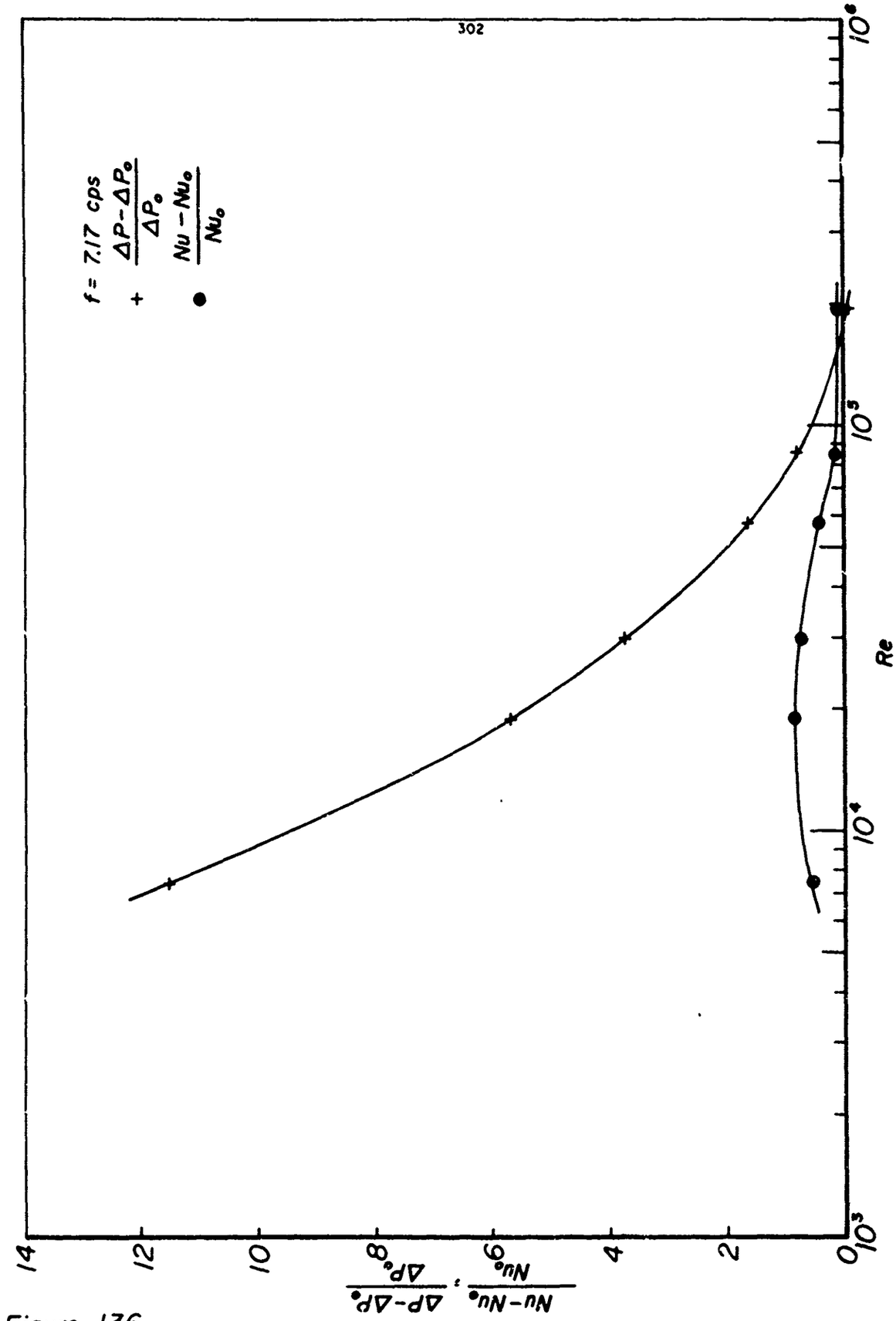

Figure 136

JP 17R 4066 67

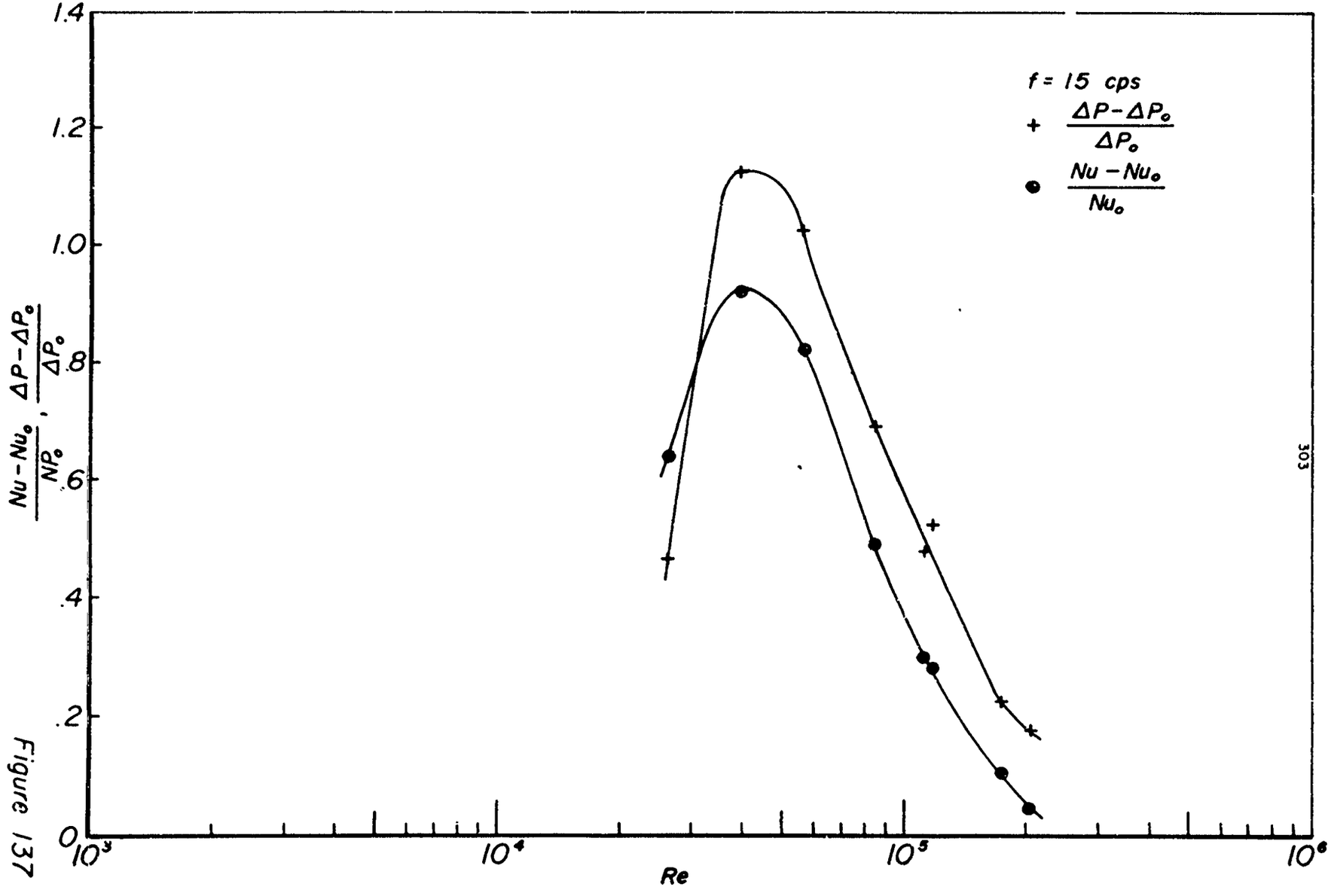

Figure 137

the fractional heat transfer increases, while in Figure 137, below Re = 10^5, the fractional heat transfer increases are roughly equal to the fractional pressure drop increases. While some variation of n with Re and f is expected, it is likely that the extreme apparent variations shown in Figures 134-137 are partially produced by experimental errors in the pressure drop measurements. The discussion of the pressure drop measurements in Reference 9 indicates the likelihood of these errors; for example, it is pointed out that under some conditions, the indicated pressure drop was negative. Despite the likely severe errors in the pressure drop measurements, we make a crude attempt to estimate n by plotting the data of Figures 134-137 in the form $\Delta P/\Delta P_o$ versus Nu/Nu_o on logarithmic paper (Figure 138). The lines n=1, 2 and 3 are also shown in Figure 138. The extreme variation of the apparent n values of the data of Figures 134-137 is indicated in Figure 138, but the best 'average' value of n appears to be ~ 2. This value of n very roughly agrees the value estimated earlier from the present author's data (n = 2.35).

At this point, we point out that excitation of the oscillations by a siren, as done in the present author's apparatus would very likely introduce such a large pressure drop at the siren (over and above that needed to generate the wave of the oscillations) due to separation effects, etc., as the siren ports open and close, that this pressure drop effect would greatly outweigh the effect of increased pressure drop in the pipe due to increased turbulence caused by the oscillating flow velocities. In this case, the siren losses would probably make the heat exchanger operation very poor on a pressure drop basis. Perhaps the non-wave-producing pressure drops at the oscillation generation can be reduced by using a piston to generate the oscillations as sketched below:

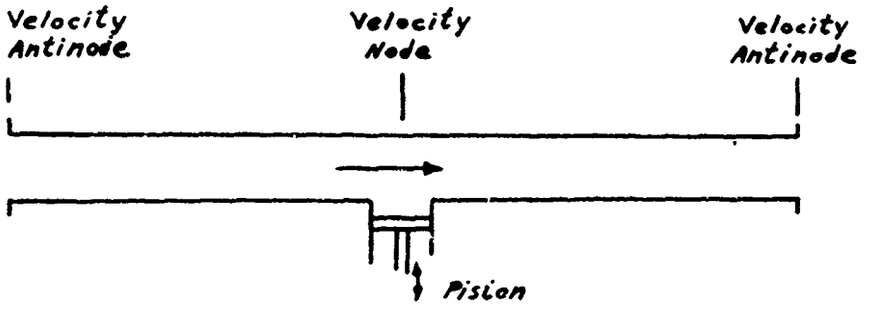

Note: Other Nodes and Antinodes may or may not be present in between those shown.

FIGURE 133

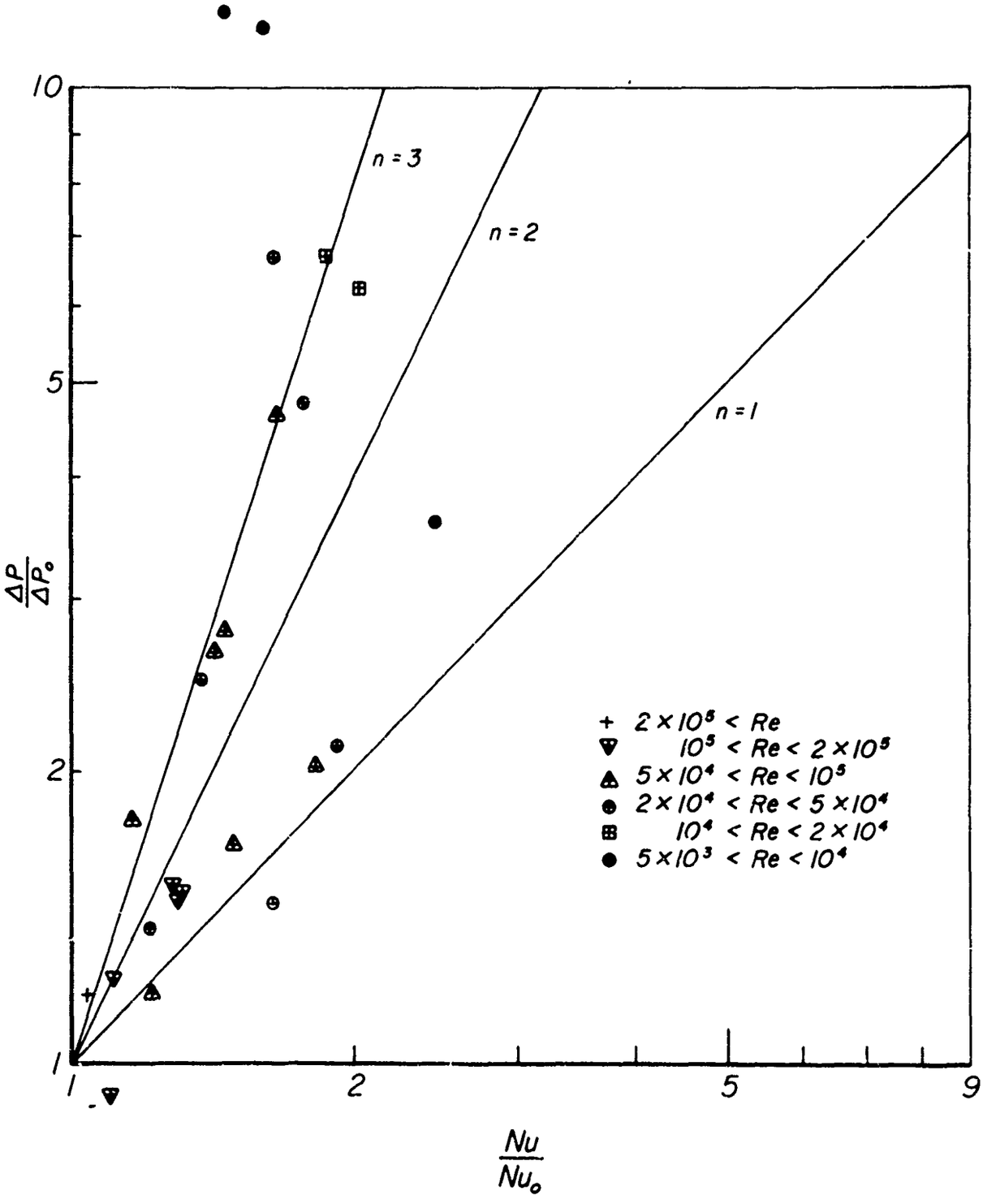

JP 17 R 4070 67

Figure 138

[Of course, it is apparent that the additional mechanical complexity necessary to generate oscillations in a heat exchanger is a strong factor against the application of oscillations to improve heat transfer (Obviously, this does not apply to the case where oscillations may be obtained directly from the flow - e.g. combustion driven oscillations as described in References 24, 13 and 14). However, we ignore this point temporarily and see what other factors appear from the present flow analysis].

We first present a brief very simplified discussion of the effect of certain variables on the 'design' of a steady flow heat exchanger. Our reference heat exchanger contains N pipes of inside diameter D and length L through which the gas flows with average velocity V and pressure drop ΔP_o. We are to transfer a total amount of heat ΔQ_T BTU/hr to a gas mass flow of $\dot{m}$ lbm/sec. We consider only the gas thermal resistance, that the gas flow is always fully-developed and turbulent, and that the log-mean temperature difference is the same for all cases considered. From Reference 23, p. 219, for fully-developed pipe flow, $Nu \propto Re^{0.8}$ ($Re = 10^4 - 1.2 \times 10^5$). We assume that this formula applies to all cases of interest here and thus $h \propto D^{0.2} V^{0.8}$. From Reference 28, p. 503 the fraction factor $\lambda \propto Re^{-.25}$ in the range $4 \times 10^3 < Re < 10^5$. We assume that this formula also applies to all cases of interest here and thus $\lambda \propto V^{-.25} D^{-.25}$. Using the preceding simplifying assumptions, the effect on the pressure drop and volume of the heat exchanger of changing the mean flow velocity and pipe diameter (in steady flow) are shown in Table 29 in the first 6 rows of data. From row 2, we see that doubling the flow velocity reduces the size of the exchanger almost by a factor of 2, but almost quadruples the pressure drop. Conversely (row 3), halving the flow velocity almost reduces the pressure drop by a factor of 4, but nearly doubles the size of the exchanger. From row 4, we see that halving the size of the tubes produces the same reduction in exchanger size as doubling the mean flow velocity, but with only a very modest pressure drop penalty, as opposed to the severe pressure drop penalty which occurs if the same exchanger size reduction is achieved by increasing the mean flow velocity. From rows 1, 2 and 3, we see that changing the value of V without changing D, allows one to reduce the volume of the exchanger, but only at the expense of increasing ΔP_o (or vice-versa). However, from rows 4 and 5 (especially the latter), we

TABLE 29

	Diameter of Pipes	Mean Flow Velocity	Number of Pipes	Length of Pipes	Pressure Drop	Number Proportional to Volume of Exchanger
Steady Flow (1)	D	V	N	L	ΔP_o	NLD^2
(2)	D	2V	$\frac{N}{2}$	1.15L	$3.87\Delta P_o$	$.575\ NLD^2$
(3)	D	$\frac{V}{2}$	2N	.870L	$.258\Delta P_o$	$1.740\ NLD^2$
(4)	$\frac{D}{2}$	V	4N	.575L	$1.367\Delta P_o$	$.575\ NLD^2$
(5)	$\frac{D}{2}$	.852V	4.70N	.555L	ΔP_o	$.453\ NLD^2$
(6)	$\frac{D}{2}$	1.188V	3.37N	.595L	$1.913\Delta P_o$	$.500\ NLD^2$
Osc. Flow (See Text) (7)	D	V	N	$\frac{L}{2}$	$\Delta P_o(n=1)$ $2\Delta P_o(n=2), 4\Delta P_o(n=3)$	$.500\ NLD^2$

see that reducing D (and changing V) allows a definite improvement in exchanger performance to be obtained; i.e. in row 5, the volume of the exchanger has been reduced without increasing ΔP_o (the opposite situation could also be obtained easily by suitably altering V after D had been reduced). Returning to the case when V is altered and D remains unchanged, it may easily be shown that in this case

$$\Delta P_o \propto (NLD^2)^{-2.44} . \tag{129}$$

In row (7), Table 29, we have considered the oscillating flow case where D and V (and N) are the same as in the reference steady flow but the average heat transfer coefficient has been doubled by the oscillation. We see that the volume of the exchanger has been halved and the pressure drop is 1, 2, or 4 times ΔP_o for the cases n = 1, 2 and 3 respectively. For the use of oscillating flow where D, V and N are as in the steady flow case, it may easily be shown that the changes in pressure drop and exchanger volume produced by the use of oscillating flow are related by (assuming Eqn. (128) to be valid)

$$\Delta P_o \propto (NLD^2)^{-(n-1)} . \tag{130}$$

Comparing Equations (129) and (130) shows that if $n < 3.44$, the use of oscillations together with changes of V will allow lower exchanger volumes for a given ΔP_o (or vice-versa) to be obtained. If $n > 3.44$, such improved performances cannot be obtained. Our earlier very tentative estimates of n from experimental data give $n \approx 2$, which, if correct, makes such improvements in heat transfer possible. In row (6), Table 29, we have computed steady flow results for halving the diameter of the tubes and adjusting V so that the volume of the exchanger is halved. The latter was done simply to make the exchanger volumes equal for the steady flow case of row (6) and the oscillating flow case of row (7). Examining these two rows of data, we see that if $n \approx 2$, as tends to be indicated by the experimental data discussed earlier, then doubling the heat transfer coefficient by the use of oscillations is about as effective in improving exchanger performances as halving the tube size (using steady flow). However, we point out another point against the possible use of oscillations to improve heat exchanger performance is as follows: The improvement in performance obtainable by reducing the tube size can in many cases be made very large by decreasing the size much more than a factor of 2 as in the example discussed above; however, the local fractional heat transfer increases due to the application of oscillations noted by the author in surveying the literature appear to be limited to ~ 2 at most. Hence the exchanger performance increases obtainable through the use of oscillations appears very limited compared to that obtainable by reducing the size of the tubes.

We now leave the question of the relation of the effects on heat transfer and pressure drop of the oscillation, and make some estimates of the work required to maintain the oscillation as compared to the pressure drop work in the pipe in the reference steady flow. The damping coefficient (α, ft^{-1}) for a wave travelling in a circular tube based on <u>molecular</u> viscosity and thermal conductivity effects only is given in Reference 34 as:

$$\alpha = \frac{2}{Dc}\sqrt{\frac{\omega\mu}{2\rho}\left(1 + \frac{K}{\mu C_p}\right)} \qquad (131)$$

Reference 34 also presents experimental data from Reference 35 taken under the following conditions. Oscillations were set up at an organ-pipe resonance in a tube of 6.7 cm inside diameter at a frequency of 50 cps. The gases used were CO_2 and air and the mean pressure range was 1 - 2.2 atm. The maximum value of $\hat{P}_N/\bar{P}$ obtained in air at 1 atm pressure was .0647. The through flow of gas was zero or very small. In air at one atmosphere pressure, experimental damping coefficients as much as 2.7 times the theoretical value from Eqn. (131) are shown in Reference 34 (from the data of Reference 35) at the largest $\hat{P}_N/\bar{P}$ values. These values decrease towards the theoretical value of Eqn. (131) at lower values of $\hat{P}_N/\bar{P}$. Reference 35 points out that turbulence produced by the oscillation is likely the mechanism explaining the high values of α observed at large $\hat{P}_N/\bar{P}$ values. From this discussion it can be seen that the wave energy lost per unit time computed from Eqn. (131) is very likely to be considerably too small when applied to our case of interest; that is, turbulent time-average through flow in a pipe, with superimposed oscillations. Nevertheless, we shall use Eqn. (131) in computing the work necessary to maintain the oscillation, bearing in mind that this is a lower limit and that the true value may be several times higher. From Eqn. (131), it can easily be shown that the wave energy lost per unit time, per unit area of the pipe, is

$$E_o = \frac{1}{8}\,\hat{U}^2\sqrt{\frac{\omega\rho\mu}{2}\left(1+\frac{K}{\mu C_p}\right)}, \qquad (132)$$

where $\hat{U}$ is the local peak-to-peak velocity.

Hence, the total wave energy lost per unit time in a pipe of length L, diameter D, with standing waves of antinodal peak-to-peak velocity $\hat{U}_A$ set up inside is

$$E_{o,1} = \pi DL \times \frac{1}{2} \times \frac{1}{8}\,\hat{U}_A^2\sqrt{\frac{\omega\rho\mu}{2}\left(1+\frac{K}{\mu C_p}\right)}. \qquad (133)$$

Now, the pressure drop work done per unit time in the flow in the reference steady flow is

$$E_{s,1} = \bar{U}\Delta P_o = \bar{U}\,\frac{1}{2}\lambda\,\frac{L}{D}\,\rho\bar{U}^2 \tag{134}$$

Forming the ratio of $E_{o,1}$ and $E_{s,1}$ from Equations (133) and (134), we get

$$\frac{E_{o,1}}{E_{s,1}} = \frac{1}{2\lambda}\left(\frac{\hat{U}_A}{\bar{U}}\right)^2\sqrt{\frac{\omega\nu}{\bar{U}^2}\left(1+\frac{K}{\mu C_p}\right)}$$

$$= \frac{1}{2}\left(\frac{\hat{U}_A}{\bar{U}}\right)^2\sqrt{\frac{1}{\lambda^2}\,\frac{\omega D}{\bar{U}}\,\frac{\nu}{\bar{U}D}\left(1+\frac{K}{\mu C_p}\right)}$$

$$= \frac{1}{2}\left(\frac{\hat{U}_A}{\bar{U}}\right)^2\sqrt{\frac{1}{\lambda^2}\,\frac{S}{Re}\left(1+\frac{1}{Pr}\right)}$$

$$\frac{E_{o,1}}{E_{s,1}} = \frac{1}{2}\left(\frac{\hat{U}_A}{\bar{U}}\right)^2\sqrt{\frac{\zeta}{\lambda}\left(1+\frac{1}{Pr}\right)} \tag{135}$$

First, we apply Equation (135), to the maximum amplitude oscillation heat transfer data of the present author (Figure 42). From Figure 127, the overall fractional heat transfer increase in this case is $\sim .29$, $\hat{U}_A/\bar{U} \approx 6.50$, and $\zeta \approx .0035$. Pr for air is .73 and from Schlicting (28) p. 504, for $Re \approx 10^5$, $\lambda = .018$. Substituting these values in Equation (135) yields

$$\frac{E_{o,1}}{E_{s,1}} = 14.5\ . \tag{136}$$

Referring to the earlier discussion of the effect of oscillations on pressure drop and volume of heat exchangers, and remembering that: (1) $\frac{E_{o,1}}{E_{s,1}}$ may well

be several times larger than given in Equation (136) due to the effects of turbulence, and (2) that this value of $\frac{E_{o,1}}{E_{s,1}}$ is for a overall heat transfer increase of only $\sim$ 30% , it appears, if the case calculated above is fairly typical, that the principal additional power requirement associated with the use of oscillations, is not that due to the increased pressure drop in the pipe, but that necessary to maintain the oscillation. Referring to Equation (135), $Pr \approx .73$ is typical for gases, and the λ value of .018 (at $Re = 10^5$) may be used over the range $10^4 < Re < 10^6$ with a maximum error of $\sim$ 35% since it appears in the square root. Hence, the lower limit of the ratio $\frac{E_{o,1}}{E_{s,1}}$ is given for gases in the range $10^4 < Re < 10^6$ within $\sim$ 35% by substituting these two values into Equation (135), yielding

$$\frac{E_{o,1}}{E_{s,1}} \approx 5.73 \left(\frac{\hat{U}_A}{\bar{U}}\right)^2 \sqrt{\zeta} \quad . \tag{137}$$

Referring to Equation (137), as far as can be seen from Figure 127, it appears that substantial increases in overall heat transfer will always be associated with large $\frac{E_{o,1}}{E_{s,1}}$ values (say, 10 or more). Because of the large power requirements necessary to maintain the oscillation, it appears that wherever heat exchanger flow power requirements are an important factor, oscillations will be of no use in improving exchanger performance. On the other hand, if power requirements are of no importance, it appears, referring to Table 29 that the exchanger size reductions achievable by the use of oscillations can more easily be achieved by increasing the flow velocity (or decreasing the pipe size). Thus it appears likely that the only cases where applications might be found for the use of oscillations to improve heat transfer would be those where the oscillations can be generated by the flow itself without absorbing very large amounts of pressure and kinetic energy of the time-average flow. The obvious examples of this are combustion-driven oscillations, where the wave energy source is not the pressure and kinetic energy of the time-average flow but the combustion reaction. If one had a burner, say at the end of a boiler tube (i.e. a case unlike that of unstable combustion in jet and rocket engines, where improved heat transfer to the duct wall is <u>not</u> desired) as sketched in Figure 139, it might be useful to set up a combustion-driven oscillation at an organ-pipe resonance of the tube

to increase the heat transfer coefficient at the tube wall.

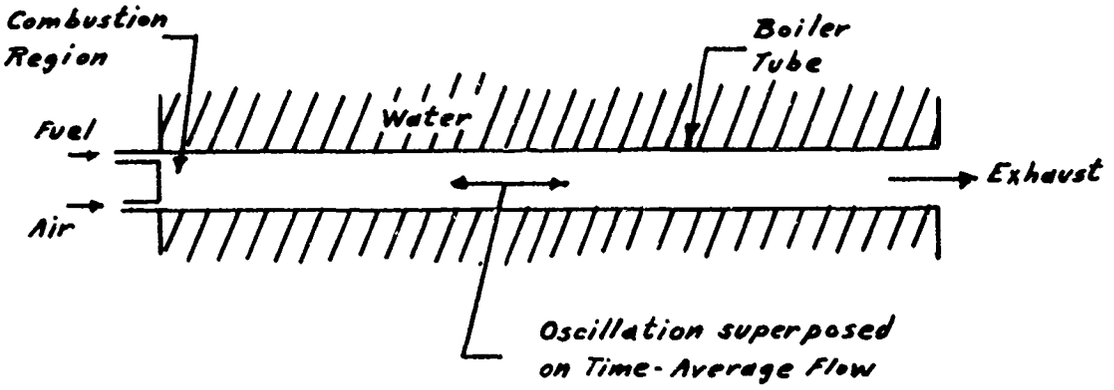

FIGURE 139

However, even here we note that it would still be possible to make similar increases in the heat transfer coefficient by the simpler means of increasing the flow velocity, and as the boiler volume could be reduced by the use of oscillations, it could also be reduced by decreasing the pipe size.

From the above discussion, it appears that the opportunities to apply longitudinal fluid oscillations to improve the performance of heat exchangers with turbulent gas flow in pipes are very limited.

REFERENCES

1. Purdy, K. R., et al., "Viscous Fluid Flow Under the Influence of a Resonant Acoustic Field", ASME paper No. 62-WA-116, 1962.

2. Purdy, K. R., et al., "The Effect of a Resonant Acoustic Field on Laminar Flow in a Circular Tube", ARL Report No. ARL65-96, May, 1965.

3. Jackson, T. W., et al., "Investigations of the Effect of Acoustic Vibrations on Convective Heat Transfer", ARL Report No. ARL-65-97, May, 1965.

4. Feiler, C. E., "Experimental Heat-Transfer and Boundary-Layer Behavior with 100 cps Flow Oscillations" NASA TN D-2521, Dec., 1964.

5. Bayley, F. J., et al., "The Effect of Flow Pulsations on Heat Transfer by Forced Convection From a Flat Plate", paper presented at the 1961 International Heat Transfer Conference, 28 Aug. - 1 Sept., 1961, Univ. of Colorado, Boulder, Colorado, U.S.A.

6. Lemlich, R., and Hwu, C. K., "The Effect of Acoustic Vibration on Forced Convective Heat Transfer", A. I. Ch.E. Journal, V. 7, March, 1961, pp. 102-106.

7. Lévêque, M. A., "Les Lois de la Transmission de Chaleur par Convection", Annales des Mines, Series 12, Vol. 13, 1928, p. 283-287.

8. Havemann, H. A., et al., "Studies for a New Hot Air Engine", J. Indian Inst. of Sci., Vol. 38, No. 3, Sect. B, July, 1956, pp. 172-202.

9. Chalitbhan, V., "Effect of Longitudinal Oscillations on Heat Transfer", PhD Thesis, University of Texas, Jan., 1959.

10. Lemlich, R., "Vibration and Pulsation Boost Heat Transfer", Chem. Eng., Vol. 68, 15 May, 1961, pp. 171-174, 176.

11. West, F. B., & Taylor, A. T., "The Effects of Pulsations on Heat Transfer", Chem. Eng. Prog., Vol. 48, No. 1, pp. 39-43, Jan. 1952.

13. Zartmann, W. N. & Churchill, S. W., "Heat Transfer From Acoustically Resonating Gas Flames in a Cylindrical Burner", A. I. Ch.E Journal, Vol. 7, No. 4, Dec., 1961, pp. 588-592.

14. Linke, W. & Hufschmidt, W., "Heat Transfer in Pulsating Flow", Chemie Ing. Tecnn., Vol. 30, No. 3, 1958, pp. 159-165.

15. Shirotsuka, T., et al., "Analogy of Mass, Heat and Momentum Transfer to Pulsation Flow from Inside Tube Wall", Chem. Eng. (Japan), Vol. 21, No. 10, pp. 638-644, 1957.

16. Romie, F. E., "Heat Transfer to Fluids Flowing With Velocity Pulsations in a Pipe", PhD Thesis, UCLA, June, 1956.

18. Evans, N.A., "Experimental Laminar Heat Transfer From an Oscillating Flat Plate", PhD Thesis, Princeton University, Princeton, N.J., 1963.

19. Feiler, C.E. & Yeager, E.B., "Effect of Large-Amplitude Oscillations on Heat Transfer", NASA TR R-142, 1962.

21. Jackson, T.W., et al, "The Effects of Resonant Acoustic Vibrations on the Local and Overall Heat Transfer Coefficients for Air Flowing Through an Isothermal Horizontal Tube", ARL Report No. ARL 60-322, Oct., 1960.

22. Jackson, T.W., et al, "The Effects of Resonant Acoustic Vibrations on the Nusselt Numbers for a Constant Temperature Horizontal Tube", paper presented at the 2nd. International Heat Transfer Conference, 28 Aug.-1 Sept., 1961.

23. Eastwood, I., et al, "Heat Transfer Threshold Values for Resonant Acoustic Vibrations in a Horizontal Isothermal Tube", ARL Report No. ARL 62-236, Apr., 1962.

24. Harrje, D.T., Condomines, A., & Crocco, L., "Combustion Instability in Liquid Propellant Rocket Motors", 29th Quarterly Progress Report, Aeronautical Engineering Report No. 216-cc, Department of Aeronautical Engineering, Princeton University, 15 Sept., 1959.

25. McAdams, W.H., "Heat Transmission", 3rd. Edition, McGraw-Hill, New York, 1954.

26. Collis, D.C. & Williams, M.J., "Two-Dimensional Forced Convection From Cylinders at Low Reynolds Numbers", Report A. 105, Aeronautical Research Laboratories, Commonwealth of Australia

27. Kronauer, R.E., "Survey of Hot-Wire Theory and Techniques", Pratt & Whitney Research Report No. 137, Dec., 1953.

28. Schlicting, H., "Boundary Layer Theory", McGraw-Hill, New York 1960.

29. Eckert, E.R.G., & Drake, R.M., "Heat and Mass Transfer", McGraw-Hill, New York, 1959.

30. Laufer, J., "The Structure of Turbulence in Fully Developed Pipe Flow", NACA Report 1174, 1954.

31. Koshkin, V.K., et al, "Unsteady Heat Transfer in Tubes Resulting From Changes in Heat Flow, Gas Mass Flow Rate and Acoustic Resonance", paper presented at the 3rd. International Heat Transfer Conference, Chicago, Ill., 7-12 Aug., 1966.

32. Dryden, H.L. & von Kármán, T., Editors, "Advances in Applied Mechanics", Academic Press, New York, 1956.

33. Saenger, R.A. & Hudson, G.E., Journal of the Acoustical Society of America, 32, 961.

34. Binder, R.C., "The Damping of Large Amplitude Vibrations of a Fluid in a Pipe", Journal of the Acoustical Society of America, Vol. 15, No. 1, July, 1943, pp. 41-43.

35. Lehmann, K.O., "Die Dämpfungsverluste bei starken Schallschwingungen in Rohren", Annalen der Physik, Ser. 5, Vol. 21, 1934, pp. 533-546.

DISTRIBUTION LIST

GOVERNMENT AGENCIES

Chief of Naval Research
Navy Department
Washington, D.C. 20360
Attn: R.O. Jackel, 429 (5)

Chief, Bureau of Weapons
Department of the Navy
Washington, D.C. 20360
Attn: RMMP-1
Attn: RAPP-1

Chief, Bureau of Ships
Department of the Navy
Washington, D.C. 20360
Attn: Code 335

Office of Naval Research
Branch Office
495 Summer Street
Boston, Mass. 02210

Commanding Officer
Office of Naval Research
Branch Office
John Crear Library Building
86 E. Randolph Street
Chicago, Illinois 60607

Commanding Officer
Area Office
Office of Naval Research
346 Broadway
New York, New York 10001
via
Office of Naval Research
Research Representative
Princeton University
Princeton, New Jersey 08540

Commanding Officer
Office of Naval Research
Branch Office Navy No. 100
Fleet Post Office
New York, New York 10001

Commanding Officer
Office of Naval Research
Branch Office
1030 E. Green Street
Pasadena, California 91102

Commanding Officer
Office of Naval Research
Area Office
1000 Geary Street
San Francisco, California 94101

Naval Engineering Exp. Station
Annapolis, Maryland 21401
Attn: Arthur Senner

Naval Ordnance Station
Research & Development Dept.
Indian Head, Maryland 20640
Attn: Lionel A. Dickinson

U.S. Naval Ordnance Test Station
China Lake
California 93555
Attn: D. Couch
Attn: Technical Librarian

Director
Naval Research Laboratories
Washington, D.C. 20360
Attn: Code 2028

U.S. Naval Postgraduate School
Monterey, California 93940

Air Force Office of Scientific Research
1400 Wilson Boulevard
Arlington, Virginia 22209
Attn: B.T. Wolfson

Air Force Rocket Propulsion Laboratory
Research & Technology Division
Air Force Systems Command
Edwards, California 93523
Attn: R. Bornhorst, RPRR
Attn: Technical Librarian

ARL (ARC)
Wright-Patterson Air Force Base
Dayton, Ohio 45433
Attn: K. Scheller

Aeronautical Systems Division
Air Force Systems Command
Wright-Patterson Air Force Base
Dayton, Ohio 45433
Attn: Technical Librarian

Unclassified

Security Classification

DOCUMENT CONTROL DATA - R & D

(Security classification of title, body of abstract and indexing annotation must be entered when the overall report is classified)

1 ORIGINATING ACTIVITY (Corporate author)	2a. REPORT SECURITY CLASSIFICATION
Princeton University Guggenheim Laboratories, Forrestal Campus Princeton, New Jersey 08540	Unclassified 2b. GROUP

3 REPORT TITLE

A STUDY OF THE MECHANISMS OF HEAT TRANSFER IN OSCILLATING FLOW

4. DESCRIPTIVE NOTES (Type of report and inclusive dates)

Technical Report 15 July 1963 - September 1967

5 AUTHOR(S) (First name, middle initial, last name)

David W. Bogdanoff

6 REPORT DATE	7a. TOTAL NO. OF PAGES	7b. NO. OF REFS
September 1967	314	35

8a. CONTRACT OR GRANT NO.	9a. ORIGINATOR'S REPORT NUMBER(S)
USN Nonr 1858(29) b. PROJECT NO. NR 094-200 c. d.	Department of Aerospace and Mechanical Sciences Report 483-f 9b. OTHER REPORT NO(S) (Any other numbers that may be assigned this report)

10. DISTRIBUTION STATEMENT

Distribution of this document is unlimited.

11. SUPPLEMENTARY NOTES	12. SPONSORING MILITARY ACTIVITY
	Office of Naval Research Power Branch, Washington, D.C. 20360

13. ABSTRACT

This detailed technical report covers an extensive research on the mechanisms responsible for the heat transfer effects associated with oscillating flow. Measurements were made in a turbulent, unsteady environment provided within a duct which was placed in longitudinal mode resonance by a siren arrangement. Importance of the velocity antinode locations and the degree of flow reversal in the enhancement of heat transfer was indicated. Measurement techniques utilized a steam-heated axially-segmented test section which covered more than one wave length of the imposed oscillations; and constant-temperature hot-wire probe surveys of the core and boundary layer in both the steady-state and unsteady duct environments. Measurements were compared with other applicable research. The important parameters were outlined together with a quasi-steady analysis. The mechanism which best correlated the experimental measurements and analyses was the effect of the oscillations on the turbulence exchange properties, while viscous dissipation and acoustic streaming appeared to be unimportant for many cases of interest. Total (eddy plus molecular) viscosity plots indicated regions of generation of 'abnormal' turbulence and subsequent diffusion and decay. Recommendations for further work are given and possible applications of oscillations to heat exchanger design is discussed; the latter appear very limited.

DD FORM 1 NOV 65 1473 (PAGE 1)

S/N 0101-807-6801

Unclassified

Security Classification

3ND PPSO 13152

14 KEY WORDS	LINK A		LINK B		LINK C	
	ROLE	WT	ROLE	WT	ROLE	WT
Unsteady heat transfer						
Heat transfer mechanisms						
Resonating duct						
Acoustic streaming						
Viscous dissipation						
Turbulence structure						
Total viscosity						
Velocity profiles						
Constant-temperature hot-wire						
Velocity antinodes						
Flow reversal						
Application of unsteady heat transfer						